

Low-thrust horizontal Lyapunov orbits in the Earth-Moon restricted three body problem

A numerical exploration towards the planar periodic solution structure of a combined low-thrust multi-body dynamical model

S.H.F. Martens



This page is intentionally left blank.

Low-thrust horizontal Lyapunov orbits in the Earth-Moon restricted three body problem

A numerical exploration towards the planar periodic
solution structure of a combined low-thrust multi-body
dynamical model

by

S.H.F. Martens

to obtain the degree of Master of Science
at the Delft University of Technology,
to be defended publicly on Friday Month XX, 2020 at 14:00.

Student number: 4149610
Project duration: October 1, 2018 – Month XX, 2020

Thesis committee: Prof. dr. ir. T.B Determined Committee Chair
Ir. K.J. Cowan MBA Supervisor
Ir. T.B. Determined External examiner

An electronic version of this thesis is available at <http://repository.tudelft.nl/>.



This page is intentionally left blank.

Contents

List of Figures	v
List of Tables	viii
Nomenclature	ix
List of symbols	x
List of acronyms	x
1 Journal Article	1
A Physical constants and algorithm parameters	31
A.1 Physical constants	31
A.2 Algorithm settings for orbit generation	32
A.2.1 Integrator settings	32
A.2.2 Settings for equilibria generation	33
A.2.3 Settings for orbit generation	33
B Numerical Integration	35
B.1 Runge-Kutta Fehlberg 7(8) method	35
B.2 12 th order Legendre-Gauss-Lobatto collocation method	36
B.2.1 Numerical integration through Gauss-Legendre-Lobatto quadrature	36
B.2.2 Error control via Boor's method	38
C Root-finding algorithms	41
C.1 Multivariate Newton's method	41
C.2 Equilibria root-finding procedure	42
C.3 Floquet targeter	43
C.3.1 Velocity correction via Floquet analysis	43
C.3.2 Construction of approximate periodic solutions	44
C.3.3 Effect of the velocity correction interval	45
C.4 Two-level targeter algorithm	45
C.4.1 Two-level targeter correction scheme	46
C.4.2 Two-level targeter performance analysis	50
C.4.3 Hamiltonian path constraints	51
C.5 Collocation root-finding scheme	52
C.5.1 General collocation root-finding scheme	52
C.5.2 Additional constraints	53
D Extended analysis of acceleration-varying families	55
D.0.1 a_{lt} -varying families at $H_{lt} = -1.55$	55
D.0.2 a_{lt} -varying families at $H_{lt} = -1.50$	57
E Verification and Validation	59
E.1 Equilibria contour verification	59
E.2 Floquet targeter verification	60
E.3 Two-level targeter verification	62
E.4 Collocation method verification	63
E.5 Libration point orbit families verification	65
E.5.1 H_{lt} -varying families	66
E.5.2 a_{lt} -varying families	82
E.5.3 α -varying families	91

F Recommendations	101
F.1 Technical recommendations	101
F.2 Scientific recommendations	102
Bibliography	105

List of Figures

B.1	Node placement strategy of the 12 th order Legendre-Gauss-Lobatto collocation method	37
C.1	The effect of the correction interval parameter of the Floquet targeter	45
C.2	A schematic representation of a discretised input trajectory for the two-level targeter	46
C.3	Sensitivity of the two-level targeter with respect to the number of nodes	50
D.1	Planar projections of a_{lt} -varying families at $H_{lt} = -1.55$ emanating from E_1	55
D.2	Evolution of Saddle stability indices and orbital period $E_1 H_{lt} = -1.55$ a_{lt} -varying families	56
D.3	Planar projections of a_{lt} -varying families at $H_{lt} = -1.55$ emanating from E_2	56
D.4	Evolution of Saddle stability indices and orbital period $E_2 H_{lt} = -1.55$ a_{lt} -varying families	56
D.5	Planar projections of a_{lt} -varying families at $H_{lt} = -1.50$ emanating from E_1	57
D.6	Evolution of Saddle stability indices and orbital period $E_1 H_{lt} = -1.50$ a_{lt} -varying families	57
D.7	Evolution of Saddle stability indices and orbital period $E_2 H_{lt} = -1.50$ a_{lt} -varying families	57
D.8	Planar projections of a_{lt} -varying families at $H_{lt} = -1.50$ emanating from E_2	58
E.1	Verification of the equilibria root-finding procedure	59
E.2	Validation of the equilibria root-finding procedure	60
E.3	Error evolution of the Floquet targeter as a result of in-plane amplitude variation	60
E.4	Error evolution of the Floquet targeter as a result of a change in acceleration orientation	61
E.5	Error evolution of the Floquet targeter as a result of a change in acceleration magnitude	61
E.6	Convergence behaviour of the two-level targeter correction procedure	62
E.7	Visualization of the first cycle of the two-level targeter	62
E.8	Visualization of the second cycle of the two-level targeter	63
E.9	Visualization of the third cycle of the two-level targeter	63
E.10	Visualization of the collocation procedure	64
E.11	Explanation of the mesh refinement process	65
E.12	$L_1 (a_{lt} = 0.0, \alpha = 0.0 \text{ rad}) H_{lt}$ -varying family periodicity verification	67
E.13	$L_1 (a_{lt} = 0.0, \alpha = 0.0 \text{ rad}) H_{lt}$ -varying family monodromy matrix eigensystem validation	67
E.14	$L_1 (a_{lt} = 0.0, \alpha = 0.0^\circ) H_{lt}$ -varying family numerical continuation verification	68
E.15	$L_1 (a_{lt} = 0.0, \alpha = 0.0^\circ) H_{lt}$ -varying family numerical spatial evolution	68
E.16	$L_2 (a_{lt} = 0.0, \alpha = 0.0 \text{ rad}) H_{lt}$ -varying family periodicity verification	69
E.17	$L_2 (a_{lt} = 0.0, \alpha = 0.0 \text{ rad}) H_{lt}$ -varying family monodromy matrix eigensystem validation	69
E.18	$L_2 (a_{lt} = 0.0, \alpha = 0.0 \text{ rad}) H_{lt}$ -varying family numerical continuation verification	70
E.19	$L_2 (a_{lt} = 0.01, \alpha = \frac{2}{3}\pi \text{ rad})$ Horizontal Lyapunov family periodicity verification	70
E.20	$L_1 (a_{lt} = 0.01, \alpha = \frac{2}{3}\pi \text{ rad}) H_{lt}$ -varying family monodromy matrix eigensystem validation	71
E.21	$L_1 (a_{lt} = 0.01, \alpha = \frac{2}{3}\pi \text{ rad}) H_{lt}$ -varying family numerical continuation verification	71
E.22	$L_1 (a_{lt} = 0.01, \alpha = \frac{4}{3}\pi \text{ rad}) H_{lt}$ -varying family periodicity verification	72
E.23	$L_1 (a_{lt} = 0.01, \alpha = \frac{4}{3}\pi \text{ rad}) H_{lt}$ -varying family monodromy matrix eigensystem validation	72
E.24	$L_1 (a_{lt} = 0.01, \alpha = \frac{4}{3}\pi \text{ rad}) H_{lt}$ -varying family numerical continuation verification	73
E.25	$L_1 (a_{lt} = 0.05, \alpha = \frac{1}{3}\pi \text{ rad}) H_{lt}$ -varying family periodicity verification	73
E.26	$L_1 (a_{lt} = 0.05, \alpha = \frac{1}{3}\pi \text{ rad}) H_{lt}$ -varying family monodromy matrix eigensystem validation	74
E.27	$L_1 (a_{lt} = 0.05, \alpha = \frac{1}{3}\pi \text{ rad}) H_{lt}$ -varying family numerical continuation verification	74
E.28	$L_1 (a_{lt} = 0.05, \alpha = \frac{5}{3}\pi \text{ rad}) H_{lt}$ -varying family periodicity verification	75
E.29	$L_1 (a_{lt} = 0.05, \alpha = \frac{5}{3}\pi \text{ rad}) H_{lt}$ -varying family monodromy matrix eigensystem validation	75
E.30	$L_1 (a_{lt} = 0.05, \alpha = \frac{5}{3}\pi \text{ rad}) H_{lt}$ -varying family numerical continuation verification	76
E.31	$L_1 (a_{lt} = 0.10, \alpha = \frac{2}{3}\pi \text{ rad}) H_{lt}$ -varying family periodicity verification	76
E.32	$L_1 (a_{lt} = 0.10, \alpha = \frac{2}{3}\pi \text{ rad}) H_{lt}$ -varying family monodromy matrix eigensystem validation	77
E.33	$L_1 (a_{lt} = 0.10, \alpha = \frac{2}{3}\pi \text{ rad}) H_{lt}$ -varying family numerical continuation verification	77

E.34 $L_1 (a_{lt} = 0.10, \alpha = \frac{4}{3}\pi \text{ rad}) H_{lt}$ -varying family periodicity verification	78
E.35 $L_1 (a_{lt} = 0.10, \alpha = \frac{4}{3}\pi \text{ rad}) H_{lt}$ -varying family monodromy matrix eigensystem validation	78
E.36 $L_1 (a_{lt} = 0.10, \alpha = \frac{4}{3}\pi \text{ rad}) H_{lt}$ -varying family numerical continuation verification	79
E.37 $L_2 (a_{lt} = 0.10, \alpha = \frac{1}{3}\pi \text{ rad}) H_{lt}$ -varying family periodicity verification	79
E.38 $L_2 (a_{lt} = 0.10, \alpha = \frac{1}{3}\pi \text{ rad}) H_{lt}$ -varying family monodromy matrix eigensystem validation	80
E.39 $L_2 (a_{lt} = 0.10, \alpha = \frac{1}{3}\pi \text{ rad}) H_{lt}$ -varying family numerical continuation verification	80
E.40 $L_2 (a_{lt} = 0.10, \alpha = \frac{5}{3}\pi \text{ rad}) H_{lt}$ -varying family periodicity verification	81
E.41 $L_2 (a_{lt} = 0.10, \alpha = \frac{5}{3}\pi \text{ rad}) H_{lt}$ -varying family monodromy matrix eigensystem validation	81
E.42 $L_2 (a_{lt} = 0.10, \alpha = \frac{5}{3}\pi \text{ rad}) H_{lt}$ -varying family numerical continuation verification	82
E.43 $L_1 (H_{lt} = -1.55, \alpha = \frac{1}{3}\pi \text{ rad}) a_{lt}$ -varying family periodicity verification	83
E.44 $L_1 (H_{lt} = -1.55, \alpha = \frac{1}{3}\pi \text{ rad}) a_{lt}$ -varying family monodromy matrix eigensystem validation	83
E.45 $L_1 (H_{lt} = -1.55, \alpha = \frac{1}{3}\pi \text{ rad}) a_{lt}$ -varying family numerical continuation verification	84
E.46 $L_1 (H_{lt} = -1.55, \alpha = \frac{5}{3}\pi \text{ rad}) a_{lt}$ -varying family periodicity verification	84
E.47 $L_1 (H_{lt} = -1.55, \alpha = \frac{1}{3}\pi \text{ rad}) a_{lt}$ -varying family monodromy matrix eigensystem validation	85
E.48 $L_1 (H_{lt} = -1.55, \alpha = \frac{5}{3}\pi \text{ rad}) a_{lt}$ -varying family numerical continuation verification	85
E.49 $L_2 (H_{lt} = -1.55, \alpha = \frac{1}{3}\pi \text{ rad}) a_{lt}$ -varying family periodicity verification	86
E.50 $L_2 (H_{lt} = -1.55, \alpha = \frac{1}{3}\pi \text{ rad}) a_{lt}$ -varying family monodromy matrix eigensystem validation	86
E.51 $L_2 (H_{lt} = -1.55, \alpha = \frac{1}{3}\pi \text{ rad}) a_{lt}$ -varying family numerical continuation verification	87
E.52 $L_2 (H_{lt} = -1.55, \alpha = \frac{5}{3}\pi \text{ rad}) a_{lt}$ -varying family periodicity verification	87
E.53 $L_2 (H_{lt} = -1.55, \alpha = \frac{5}{3}\pi \text{ rad}) a_{lt}$ -varying family monodromy matrix eigensystem validation	88
E.54 $L_2 (H_{lt} = -1.55, \alpha = \frac{1}{3}\pi \text{ rad}) a_{lt}$ -varying family numerical continuation verification	88
E.55 $L_2 (H_{lt} = -1.50, \alpha = \frac{1}{3}\pi \text{ rad}) a_{lt}$ -varying family periodicity verification	89
E.56 $L_2 (H_{lt} = -1.50, \alpha = \frac{1}{3}\pi \text{ rad}) a_{lt}$ -varying family monodromy matrix eigensystem validation	89
E.57 $L_2 (H_{lt} = -1.50, \alpha = \frac{1}{3}\pi \text{ rad}) a_{lt}$ -varying family numerical continuation verification	90
E.58 $L_2 (H_{lt} = -1.50, \alpha = \frac{5}{3}\pi \text{ rad}) a_{lt}$ -varying family periodicity verification	90
E.59 $L_2 (H_{lt} = -1.50, \alpha = \frac{5}{3}\pi \text{ rad}) a_{lt}$ -varying family monodromy matrix eigensystem validation	91
E.60 $L_2 (H_{lt} = -1.50, \alpha = \frac{5}{3}\pi \text{ rad}) a_{lt}$ -varying family numerical continuation verification	91
E.61 $L_1 (a_{lt} = 0.05, H_{lt} = -1.55) \alpha$ -varying family periodicity verification	92
E.62 ($L_1 (a_{lt} = 0.05, H_{lt} = -1.50)$ α -varying family monodromy matrix eigensystem validation	93
E.63 $L_1 (a_{lt} = 0.05, H_{lt} = -1.50) \alpha$ -varying family numerical continuation verification	93
E.64 $L_1 (a_{lt} = 0.10, H_{lt} = -1.55) \alpha$ -varying family periodicity verification	94
E.65 ($L_1 (a_{lt} = 0.10, H_{lt} = -1.55)$ α -varying family monodromy matrix eigensystem validation	94
E.66 $L_1 (a_{lt} = 0.10, H_{lt} = -1.55) \alpha$ -varying family numerical continuation verification	95
E.67 $L_1 (a_{lt} = 0.10, H_{lt} = -1.525) \alpha$ -varying family periodicity verification	96
E.68 ($L_1 (a_{lt} = 0.10, H_{lt} = -1.525)$ α -varying family monodromy matrix eigensystem validation	96
E.69 $L_1 (a_{lt} = 0.10, H_{lt} = -1.525) \alpha$ -varying family numerical continuation verification	97
E.70 $L_1 (a_{lt} = 0.10, H_{lt} = -1.50) \alpha$ -varying family periodicity verification	98
E.71 ($L_1 (a_{lt} = 0.10, H_{lt} = -1.50)$ α -varying family monodromy matrix eigensystem validation	98
E.72 $L_1 (a_{lt} = 0.10, H_{lt} = -1.50) \alpha$ -varying family numerical continuation verification	99

This page is intentionally left blank.

List of Tables

A.1	Physical constants of the Earth-Moon CR3BP-LT	32
A.2	Dimensionless quantities of the CR3BP-LT	32
A.3	Runge-Kutta-Fehlberg7(8) integrator settings	32
A.4	12 th order Legendre Gauss Lobatto collocation settings	33
A.5	Equilibria root-finder parameter settings	33
A.6	Floquet targeter parameter settings	33
A.7	Two-level targeter corrector parameter settings	34
A.8	Numerical continuation procedure parameter settings	34
B.1	The Butcher tableau of the embedded Runge-Kutta-Fehlberg7(8) method	36
B.2	Normalized mesh times of the 12 th order Legendre-Gauss-Lobatto collocation method	37
B.3	Constants for the 12 th order Legendre-Gauss-Lobatto collocation defect computation	38
C.1	Pseudo-code of the orbital period approximation	44
C.2	Partial derivatives of the level-II corrector of the two-level targeter	48
C.3	Partial derivative elements of the level-II corrector of the two-level targeter	48
C.4	Evaluation of the Hamiltonian path constraints	52
E.1	Comparison between Richardson third order method and the Floquet targeter scheme	61
E.2	Validation of the two-level targeter correction procedure	63
E.3	Validation of the 12 th order Legendre-Gauss-Lobatto collocation procedure	64
E.4	An exhaustive list of the termination causes of the continuation procedure	66
E.5	Termination causes of the numerical continuation procedure of the H_{lt} -varying families.	66
E.6	Termination causes of the numerical continuation procedure of the a_{lt} -varying families.	82
E.7	Termination causes of the numerical continuation procedure of the α -varying families.	91

Nomenclature

The entirety of acronyms and symbols used in the Appendices A-F is presented in the lists below. The nomenclature used in Chapter 1 is presented in the article itself.

List of acronyms

Acronym	Definition	Chapter
BVP	Boundary value problem	B
CR3BP	Circular restricted three-body problem	A
CR3BP-LT	Low-thrust circular restricted three-body problem	A
FC	Floquet controller	A
H-L	Horizontal Lyapunov	
l.p.o	libration point orbit	A
NR	Newton-Raphson	A
RKF78	Runge-Kutta-Fehlberg 7(8)	A
SPM	State propagation matrix	C
STM	State transition matrix	C
TLT	Two-level targeter	A
TUDAT	TU Delft Astrodynamical Toolbox	A

List of symbols

Symbol	Description	Equation of first appearance
α	Low-thrust acceleration orientation	C.6
α_i	Runge-Kutta nodes	B.3
β_{ij}	Runge-Kutta internal weights	B.5
γ_j	External weights of the Runge-Kutta scheme	B.3
Δ	Difference	B.10
ϵ_{tol}	Local truncation error tolerance	B.6
ϵ_m	Machine epsilon	A.3
η_k	Two-level targeter constraint at node k	C.32
θ	Angle of the equilibrium point with respect to the positive x-axis of the synodic frame	C.19
ζ	Defect constraint	B.12
ι_j	Floquet targeter coefficients	C.14
κ	Line search attenuation parameter	C.47
μ	Mass parameter	A.1
ξ	Eighth-order derivative estimate	B.16
Π	Mesh of the collocation procedure	B.15
σ	Complex step increment	C.46
τ	Normalized segment time	B.9
ϕ	Orbital phase	C.49
Φ	State transition matrix	C.10
A_x	In-plane amplitude	C.19
\bar{a}_k	Acceleration vector at node k	C.29
a_{lt}	Low-thrust acceleration magnitude	C.6

B_i	Polynomial time matrix	B.11
\mathbf{b}	Last column of the inverse of B_i	B.18
b_j^i	Constants for defect computation	B.12
C	Computable constant for error control	B.16
C_i	Polynomial coefficient matrix	B.11
DF	Jacobian	C.3
\bar{e}_i	i^{th} column of the Floquet modal matrix	C.11
e	Local truncation error estimate	B.6
F	Defect vector	C.1
\bar{f}_i	Field vector evaluation	B.10
$G(t)$	Perturbation decomposition matrix	C.12
\bar{g}_i	i^{th} column of the perturbation decomposition matrix	C.11
H_{lt}	Low-thrust Hamiltonian	C.38
h	Step size in explicit propagation schemes	B.1
I	Collocation error integral	B.19
l	Relaxation parameter	C.8
l_*	Characteristic length	A.2
n	Number of nodes	B.15
p	Piecewise polynomial	B.9
\bar{R}	Position vector	
r_{ij}	Distance from body i to body j	C.6
T	Orbital period	C.18
t_*	Characteristic time	A.2
S	Eigenvector matrix	C.13
\bar{V}	Position vector	C.14
w_j^i	Constants for defect computation	B.12
X	Design vector	C.1
Z_j	Runge-Kutta local function evaluation	B.3
$*$	Constraint reference value	C.39
$+$	Incoming quantity	B.10
$-$	Outgoing quantity	B.10
T	Matrix transpose	B.9
$ $	Absolute value	B.6
$ \cdot $	Euclidian norm	C.50
$\langle \cdot, \cdot \rangle$	Inner product	C.49
∂	Partial derivative symbol	C.3

1

Journal Article

LOW-THRUST HORIZONTAL LYAPUNOV ORBITS IN THE EARTH-MOON RESTRICTED THREE-BODY PROBLEM

Sjors Martens* and **Kevin J. Cowan†**

Preliminary design of low-thrust trajectories in the circular restricted three-body problem (CR3BP) frequently relies upon ballistic dynamical structures and optimization algorithms. A fundamental understanding of how these dynamical structures change due to presence of a low-thrust force may lead to trajectories that cannot be obtained otherwise. This paper investigates the effect of a constant low-thrust acceleration on the Horizontal-Lyapunov families in the CR3BP. Families of low-thrust periodic solutions are constructed in vicinity of L_1 and L_2 using numerical continuation methods. By either varying the Hamiltonian, acceleration orientation or magnitude along the solution family, the effect of a low-thrust force on Horizontal-Lyapunov orbits is characterized. Identifying the geometry, bifurcations and hyperbolic unwinding behaviour of these families provides insight into the low-thrust periodic solution structure of the Earth-Moon system.

INTRODUCTION

Libration point orbits have been key to the realization of numerous space missions. An increased understanding of Solar winds¹ and the early Universe² are just some of the valuable scientific insights which have been obtained by utilization of these non-Keplerian geometries. The significance of these libration point orbits will only increase in the near-future as NASA aims to deploy the successor of the International Space Station in the vicinity of the Earth-Moon L_2 point.³ Recent advancements in low-thrust propulsion technology have sparked the interest of the scientific community into investigation of non-ballistic libration point orbits. Research efforts have led to the discovery of novel mission concepts like continuous observation of lunar poles via deformed Halo orbits.⁴ These so-called 'pole-sitter' orbits illustrate the possibility to discover new mission concepts by combining low-thrust technology and non-Keplerian geometries.

Initial designs of space missions involving libration point orbits are commonly obtained from low-fidelity multi-body models like the CR3BP. Extensive research towards the dynamical structures of this model has revealed a rich set of periodic solutions in the vicinity of the Lagrangian points.⁵ Furthermore, invariant manifolds emanating from these equilibria have opened up new opportunities for low-energy space travel.⁶ The common approach for preliminary design of missions involving non-ballistic libration point orbits is to specify a ballistic trajectory in the CR3BP and find a control history via trajectory optimization techniques. The mass- or time-optimal trajectories resulting from this design philosophy may satisfy mission specific constraints but fail to provide an understanding how the fundamental flow in the CR3BP changes under influence of a low-thrust force. Such an understanding can be obtained by studying the flow of a multi-body model whose dynamics allow the formulation of a low-thrust force.

*Graduate Student, Aerospace Engineering, Delft University of Technology, Kluiverweg 1, 2629 HS Delft, The Netherlands

†Lecturer, Aerospace Engineering, Delft University of Technology, Kluiverweg 1, 2629 HS Delft, The Netherlands

Investigation of dynamical structures in low-thrust multi-body models is an emerging field of research, especially in the context of solar sailing. Studies towards the deformation of Halo orbits in the Sun-Earth radial solar sail CR3BP⁷ and the existence of libration point orbits in the Earth-Moon solar sail CR3BP⁸ are just some of the examples that have revealed new geometries. Multi-body models which incorporate a low-thrust force via electric propulsion have received far less attention despite the widespread use of this form of propulsion today's space missions. Recent studies that investigate multi-body models that incorporate a low-thrust force in the form of electric propulsion show that key dynamical structures like equilibria, periodic motion and invariant manifolds exist.^{9–11} However, the phase space of this model remains largely unexplored. This paper increases the understanding of dynamical structures in these low-thrust multi-body models by investigating the planar periodic solution structure in the Earth-Moon system.

This article starts with a formulation of the dynamics of the low-thrust multi-body model. Next, the characteristics of the equilibrium solutions within this system are discussed. Three different types of periodic solution families are presented in the vicinity L_1 and L_2 at a variety of thrust parameters. Studying the geometry and linear stability of these low-thrust libration point orbits aids to an increased understanding of the low-thrust multi-body dynamics.

DYNAMICAL MODEL

Before periodic motion in a low-thrust multi-body model can be investigated, it is necessary to formulate the dynamics of such a system. The dynamical model adopted in this investigation is known as the low-thrust restricted three-body problem (CR3BP-LT).¹¹ A graphical representation of this dynamical model is presented in Figure 1.

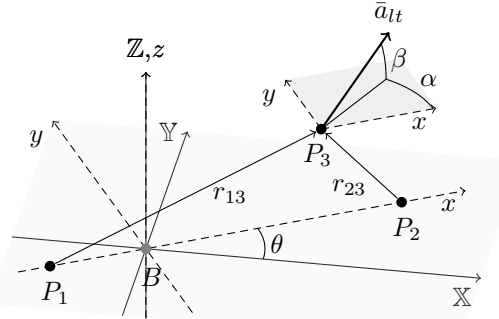


Figure 1. The configuration of the CR3BP-LT. The light-grey shaded area denotes the plane of motion of the two primaries and coincides with the xy and XY -plane. The orientation of the dark-grey shaded area is parallel to the xy plane.

The CR3BP-LT is a combination of CR3BP and a low-thrust acceleration \bar{a}_{lt} provided by a reaction engine. The dynamics of the CR3BP system are explained first followed by a discussion on how these are affected by the introduction of a low-thrust acceleration.

The Circular Restricted Three-Body Problem

The CR3BP concerns the motion of three bodies resulting from their mutual gravitational attraction. The two celestial bodies, from now on referred to as the primary (P_1) and secondary (P_2),

rotate around their mutual barycenter B in a coplanar and circular fashion. The artificial body (P_3) is unrestricted in its movement and has a negligible mass so its gravitational pull can be neglected. It is a common strategy to study the three-body problem in a rotating reference frame (x, y, z) where the x -axis coincides with the primary and secondary. This so-called synodic reference frame removes the time dependency of the dynamics which simplifies its analysis.¹² It is worth noting that the introduction of a rotating reference frame gives rise to a centrifugal force and Coriolis force. Hence, the motion in the synodic frame is the result of the gravitational pull and the two aforementioned forces.

Another standard simplification is the nondimensionalization of the CR3BP which is achieved by assuming three quantities to unity. These quantities are the total mass in the system, the mean motion of the synodic reference frame and the distance between the primary and secondary.¹² The nondimensionalization of system allows full parametrization of the CR3BP via the mass ratio parameter $\mu = \frac{M_2}{M_1+M_2}$. This research assumes $\mu \approx 0.0121506^*$ to simulate motion in the Earth-Moon version of the CR3BP. The position of the primary and secondary are fixed in the synodic reference frame at $(-\mu, 0, 0)$ and $(1 - \mu, 0, 0)$ respectively, so the distances of P_3 with respect to the spacecraft can be calculated according to Eq. (1).

$$r_{13} = \sqrt{(x + \mu)^2 + y^2 + z^2}, \quad r_{23} = \sqrt{(x - 1 + \mu)^2 + y^2 + z^2} \quad (1)$$

The motion of P_3 is defined through three-second order partial non-linear differential equations,¹⁴ which are shown below in Eq. (2).

$$\begin{aligned} \ddot{x} &= 2\dot{y} + x - \frac{1 - \mu}{r_{13}^3}(x + \mu) - \frac{\mu}{r_{23}^3}(x - 1 + \mu) = 2\dot{y} + \Omega_x \\ \ddot{y} &= -2\dot{x} + y - \frac{1 - \mu}{r_{13}^3}y - \frac{\mu}{r_{23}^3}y = -2\dot{x} + \Omega_y \\ \ddot{z} &= -\frac{1 - \mu}{r_{13}^3}z - \frac{\mu}{r_{23}^3}z = \Omega_z \end{aligned} \quad (2)$$

Ω represents the pseudo-potential of the system, which is formed by the sum of the centrifugal force and gravitational potential of P_1 and P_2 as shown in Eq. (3).¹²

$$\Omega = \frac{1}{2}(x^2 + y^2) + \frac{1 - \mu}{r_{13}} + \frac{\mu}{r_{23}} \quad (3)$$

The aforementioned time independence of the CR3BP implies the existence of a first integral in the dynamical model according to Hamiltonian dynamics.¹⁵ The conserved quantity is known as the Jacobi integral and is an important parameter for characterizing motion in the dynamical model. The Jacobi integral is equivalent to the Hamiltonian of the system, as shown in¹¹ and is computed via Eq. (4).

$$C = -2H_{nat} = 2\Omega - V^2 \quad (4)$$

The Low-Thrust Circular Restricted Three-Body Problem

The CR3BP-LT arises from the CR3BP by introducing a dimensionless low-thrust acceleration \bar{a}_{lt} vector to the ballistic model in the form of Eq. (5). The magnitude of this acceleration is

*The exact value of μ is obtained directly from the publicly available TUDAT software package¹³

represented as a_{lt} whereas its orientation is defined via the in-plane angle α and an out-of-plane angle β as shown in Figure 1.

$$\bar{a}_{lt} = \frac{f}{m} \hat{u}, \quad \hat{u} = \begin{bmatrix} \hat{u}_x \\ \hat{u}_y \\ \hat{u}_z \end{bmatrix} = \begin{bmatrix} \cos(\beta)\cos(\alpha) \\ \cos(\beta)\sin(\alpha) \\ \sin(\beta) \end{bmatrix}, \quad f = \frac{Ft_*^2}{l_* M_{3,0}} \quad (5)$$

In Eq. (5), f denotes the dimensionless thrust magnitude and $m = \frac{M_3}{M_{3,0}}$ is the dimensionless spacecraft mass with $M_{3,0}$ defined as the initial spacecraft mass in kilograms. F represents the dimensional thrust force in kilonewtons which is nondimensionalized using l_* and t_* , respectively referred to as the characteristic length and characteristic time.¹¹ The characteristic length represents the distance between P_1 and P_2 in kilometers whereas the characteristic time represents the inverted mean motion of the system in seconds. This research adopts $l_* = 384400$ from which the characteristic time can be computed with Kepler's third law. Furthermore, this research assumes $f \in [0.0, 0.1]$ which is in line with today's low-thrust propulsion technology as shown in Appendix A.

The dynamics of P_3 in the CR3BP-LT can be defined via four second-order differential equations as shown in Eq. (6).¹¹ The first three different equations define the dynamics of P_3 whereas the fourth differential equation governs the dimensionless mass flow of the system. I_{sp} denotes the specific impulse in seconds and $g_0 = 9.80665 m/s^{-2}$ represents the gravitational acceleration at sea level.

$$\begin{aligned} \ddot{x} &= 2\dot{y} + \Omega_x + a_{lt}\hat{u}_x \\ \ddot{y} &= -2\dot{x} + \Omega_y + a_{lt}\hat{u}_y \\ \ddot{z} &= \Omega_z + a_{lt}\hat{u}_z \\ \dot{m} &= \frac{f l_* t_*}{I_{sp} g_0 t_*} \end{aligned} \quad (6)$$

Contrary to the CR3BP, the Hamiltonian of the CR3BP-LT, shown in Equation (7), is not a conserved quantity since it varies with a change in the acceleration vector.

$$H_{lt} = H_{nat} - \langle \bar{r}, \bar{a}_{lt} \rangle, \quad \frac{\partial H_{lt}}{\partial \tau} = \langle \bar{r}, \dot{\bar{a}}_{lt} \rangle \quad (7)$$

The time-varying nature of the spacecraft mass transforms the dynamical model into a non-autonomous system. Dynamical structures in a time-variant system are challenging to characterize due to the absence of a first integral. This research employs three simplifications to transform the CR3BP-LT into an autonomous dynamical system. First of all, the acceleration orientation vector \hat{u} is fixed in the rotating frame. Secondly the thrust magnitude f is held constant. Finally it is assumed that $\dot{m} = 0$. These assumptions constitute to a constant low-thrust acceleration vector in the rotating frame and give rise to an integral of motion in the form of H_{lt} . The remainder of this work considers a_{lt} and H_{lt} as constant quantities since a varying spacecraft mass has a negligible influence in the Earth-Moon system, as suggested in previous literature.¹¹ This section is concluded with the notice that the dynamics of P_3 are constrained to planar motion.

LOW-THRUST EQUILIBRIUM SOLUTIONS

The CR3BP possesses five locations where a spacecraft experiences a net zero acceleration. Analysis of the dynamics around these Lagrangian points reveals the existence of dynamical structures

like libration point orbits and/or invariant manifolds.¹⁶ Hence, investigating the equilibria in the CR3BP-LT allows characterization of the phase space. This section presents the methodology to locate the equilibria and characterize the dynamics around them. Furthermore, it discusses the effect of a constant low-thrust acceleration on the equilibria locations and the surrounding dynamics.

Equilibria localization and characterization methodology

Previous research has shown that the low-thrust acceleration can considerably shift the locations of the equilibria.⁹ These low-thrust equilibrium solutions are located via a multivariate relaxed Newton-Raphson root-finding method¹⁷ which finds a position in the rotating frame that satisfies the conditions of Eq. 8.

$$\begin{aligned}\ddot{x} &= 2\dot{y} + \Omega_x + a_{lt}\cos(\alpha) = 0 \\ \ddot{y} &= -2\dot{x} + \Omega_y + a_{lt}\sin(\alpha) = 0\end{aligned}\tag{8}$$

The multivariate root-finding algorithm is leveraged to compute two types of structures. The first structure comprises the low-thrust equilibrium solutions at a fixed acceleration magnitude a_{lt} over the complete domain of possible acceleration orientations ($\alpha \in [0, 2\pi]$). This structure is referred to as an α -varying zero acceleration contour (ZAC). The second structure, referred to as the a_{lt} -varying ZAC, concerns all low-thrust equilibrium solutions for a fixed acceleration orientation α over the full domain of possible acceleration magnitudes ($a_{lt} \in [0, 0.1]$). These two contours isolate the effect of a_{lt} and α rad so their influence on the equilibrium solutions can be investigated separately.

The multivariate root-finding procedure is initialized with seed solutions that differ per type of contours. For the α -varying ZAC, two types of seed solutions are leveraged. The first type of seed solutions are low-thrust equilibria located at the x-axis of the rotating frame which are straightforwardly calculated via a univariate Newton-Raphson procedure. The second type of seed solutions are non-collinear low-thrust equilibria with $\alpha = 0$ obtained via analytical Eqs. (9-11).¹¹

$$\begin{aligned}\bar{r}_{L_4} &= [-\mu + r_{13}\cos(\kappa) \quad r_{13}\sin(\kappa) \quad 0] \\ \bar{r}_{L_5} &= [-\mu + r_{13}\cos(\kappa) \quad -r_{13}\sin(\kappa) \quad 0]\end{aligned}\tag{9}$$

$$\begin{aligned}r_{13} &= \left[\frac{1-\mu}{1-\mu+a_{lt}} \right]^{\frac{1}{3}} \\ r_{23} &= \left[1 - \frac{a_{lt}}{\mu} \right]^{-\frac{1}{3}}\end{aligned}\tag{10}$$

$$\kappa = \left[\frac{1+r_{13}^2+r_{23}^2}{2r_{13}} \right]\tag{11}$$

In the equations above, κ represents the angle between the positive x -axis and the r_{13} vector. The seed solutions of a_{lt} -varying ZAC's are simply obtained from the Lagrangian points of the CR3BP.

When the position of an equilibrium solution has been computed, the dynamics in the neighbourhood of the equilibrium can be characterized through analysis of the linearized dynamics about the equilibrium location. The linearized dynamics are obtained through a first-order Taylor series approximation about the equilibrium location which is provided in Equation 12.

$$\frac{d}{dt} \begin{bmatrix} x \\ y \\ z \\ \dot{x} \\ \dot{y} \\ \dot{z} \\ f \\ \alpha \\ \beta \\ m \end{bmatrix} = \begin{bmatrix} 0 & 0 & 0 & 1 & 0 & 0 & 0 & 0 & 0 & 0 \\ 0 & 0 & 0 & 0 & 1 & 0 & 0 & 0 & 0 & 0 \\ 0 & 0 & 0 & 0 & 0 & 1 & 0 & 0 & 0 & 0 \\ \Omega_{xx} & \Omega_{xy} & \Omega_{xz} & 0 & 2 & 0 & \frac{C_\alpha C_\beta}{m} & -\frac{f S_\alpha C_\beta}{m} & -\frac{f C_\alpha S_\beta}{m} & -\frac{f C_\alpha C_\beta}{m^2} \\ \Omega_{yx} & \Omega_{yy} & \Omega_{yz} & -2 & 0 & 0 & \frac{S_\alpha C_\beta}{m} & \frac{f C_\alpha C_\beta}{m} & -\frac{f S_\alpha S_\beta}{m} & -\frac{f S_\alpha C_\beta}{m^2} \\ \Omega_{zx} & \Omega_{zy} & \Omega_{zz} & 0 & 0 & 0 & \frac{S_\beta}{m} & 0 & f \frac{C_\beta}{m} & -\frac{f S_\beta}{m^2} \\ 0 & 0 & 0 & 0 & 0 & 0 & 0 & 0 & 0 & 0 \\ 0 & 0 & 0 & 0 & 0 & 0 & 0 & 0 & 0 & 0 \\ 0 & 0 & 0 & 0 & 0 & 0 & 0 & 0 & 0 & 0 \\ 0 & 0 & 0 & 0 & 0 & 0 & 0 & 0 & 0 & 0 \end{bmatrix}_{eq} \begin{bmatrix} x \\ y \\ z \\ \dot{x} \\ \dot{y} \\ \dot{z} \\ f \\ \alpha \\ \beta \\ m \end{bmatrix}_{eq} = \bar{A}|_{eq} \bar{X}(t) \quad (12)$$

\bar{X} denotes the state vector and A represents its Jacobian, commonly referred to as the state propagation matrix (SPM). C_k and S_k refer to sine and cose operator respectively where subscript k denotes the argument of these operators. Since this research assumes a constant thrust magnitude, orientation and spacecraft mass, the dynamics are defined by the upper 4×4 block of the SPM.(or 6×6 block if spatial motion is assumed).¹¹ The four eigenvalues of the upper block, which occur as two pairs, reveal the stability components in the neighbourhood of the equilibrium point. A pair of real eigenvalues with opposite sign indicates a so-called Saddle (S) mode which suggests the existence of hyperbolic invariant manifolds. Secondly, a conjugate pair of purely imaginary eigenvalues gives rise to a center (C) mode which indicates the existence of periodic solutions. Finally, a conjugate pair of complex eigenvalues denote a mixed (M) mode which suggests spiral behaviour. The combination of two stability modes defines the planar linear stability of the equilibrium point.

Low-thrust acceleration effect on the equilibrium solutions

The root-finding method presented in the previous subsection allows the construction of the α -varying ZAC's around different Lagrangian points. An α -varying ZAC that arises from L_i is denoted with E_i and these structures are displayed in Figure 2 for three distinct acceleration magnitudes. In an analogous way, a_{lt} -varying ZAC's are indicated via E_i^α where α indicates the acceleration orientation. These structures are displayed in Figure 3. Both images show the linear planar stability at each location in the rotating frame. The totality of linear stabilities is referred to as the stability portrait.¹¹

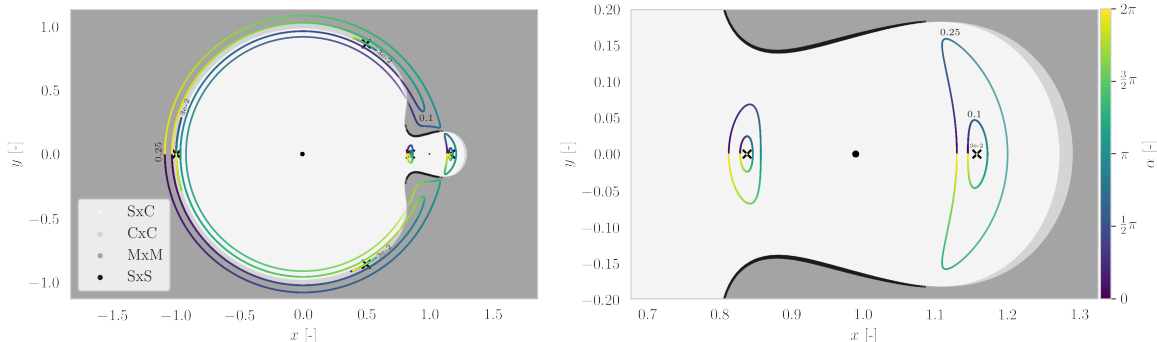


Figure 2. The α -varying ZAC contours at three distinct acceleration magnitude $[0.003, 0.01, 0.025]$ over the complete range of thrust orientations $\alpha \in [0, 2\pi]$. The natural lagrange points are plotted as black crosses whereas the two primaries are symbolized as filled black circles. $a_{lt} = 0.025$ lies outside the feasible range of acceleration magnitudes but is added for visualization reasons.

The stability portrait reveals four the presence of four stability regions in the CR3BP-LT. The neighbourhood around the primary and secondary body are characterized by $S \times C$ stability, indicating that planar periodic solutions and invariant manifolds are present. The $S \times C$ stability realm is surrounded by two small bands characterized by $C \times C$ and $S \times S$ stability. $C \times C$ stability suggests that only bounded motion exists within this field whereas only asymptotic motion can be found within the $S \times S$ realm. An $M \times M$ field encloses these three stability regions.

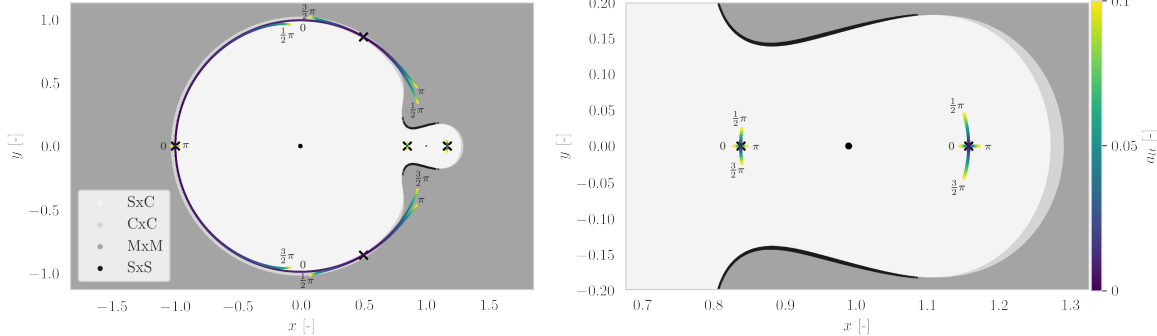


Figure 3. The a_{lt} -varying ZAC contours at four acceleration orientations $[0, \frac{1}{2}\pi, \pi, \frac{3}{2}\pi]$ over the complete range of acceleration magnitude $a_{lt} \in [0, 0.1]$. The equilibria are plotted as black crosses whereas $P_{1,2}$ are shown as black circles.

Figure 2 reveals that a low-thrust acceleration vector can drastically change the location of the equilibrium solution as well as its stability mode. The largest displacements are observed at E_3 followed by the equilateral contours E_4 and E_5 . This effect is so powerful that these three contours merge into a single C-shaped contour ($a_{lt} = 1.05 \cdot 10^{-2}$). Smaller displacements are observed at the E_2 and the low-thrust acceleration has an even more limited effect at E_1 . The varying effect of the low-thrust acceleration is directly attributed to the magnitude of the pseudo-potential at the specific location in the rotating frame. Furthermore, E_1 and E_2 remain in the $S \times C$ stability realm. Figure 3 underpins these conclusions and highlights how the displacement effect is proportional to the acceleration magnitude.

The stability portrait provides qualitative insight into the stability but fails to show how the magnitude of these stability components spatially evolve in the CR3BP-LT. Figure 4 provides such an insight for the saddle component.

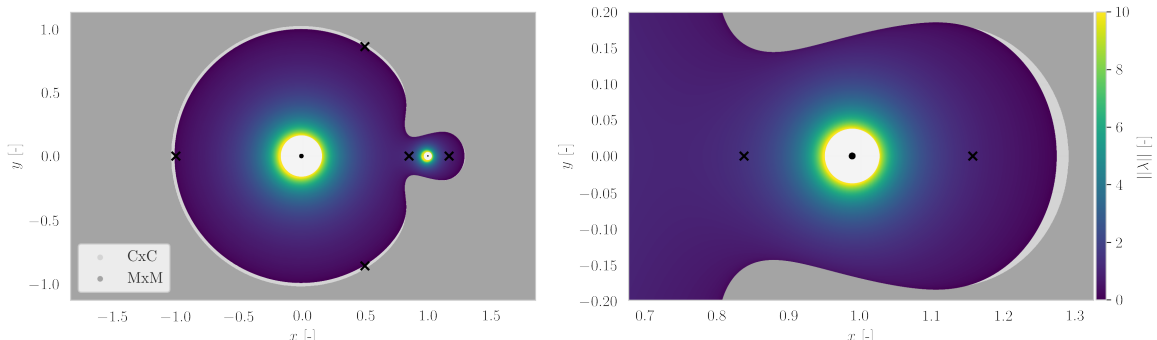


Figure 4. The magnitude of the eigenvalue related to the saddle component of the dynamics as a function of position in the rotating frame. The contour is computed for $\|\lambda\| \leq 10$ for visualization reasons.

The saddle component is represented by the dominant eigenvalue modulus of the eigensystem of Equation 12. This dominant eigenvalue is associated with hyperbolic nature of the dynamics which give rise to the unstable invariant manifold.¹⁶ A larger dominant eigenvalue magnitude is directly linked to a faster rate of hyperbolic unwinding behaviour of the invariant manifolds,¹⁸ possibly creating quicker low-energy transfer opportunities. Figure 4 shows that the unwinding behaviour increases when the equilibrium moves towards the primary or secondary body. Furthermore, the magnitude of the dominant eigenvalue decreases towards zero in the neighbourhood of the $C \times C$ stability realm. These findings are confirmed by Figure 6 which shows the dominant eigenvalue magnitude as a function of the acceleration orientation at two distinct acceleration magnitudes.

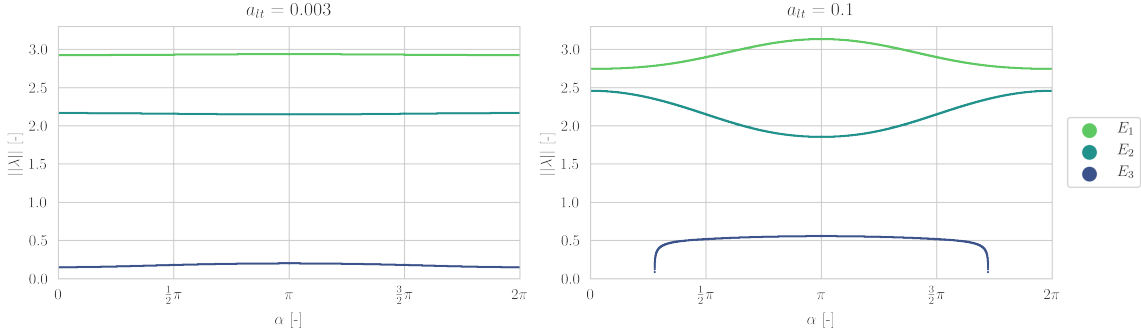


Figure 5. The magnitude of the eigenvalue related to the saddle component of the dynamics as a function of the thrust parameters.

The maximum unwinding behaviour of contour E_1 and E_2 occur at $\alpha = \pi$ rad and $\alpha = 0$ rad since this specific orientation results in an equilibrium location closest to the secondary. In an equivalent way, the maximum unwinding behaviour of the occurs at $\alpha = \pi$ rad since this resonates with the equilibrium closest to the primary. At higher acceleration magnitudes, unwinding behaviour is not guaranteed at E_3 since parts this contour are located in the $C \times C$ and $M \times M$ stability realm.

The final effect of a low-thrust acceleration on the equilibrium solutions concerns the change in Hamiltonian value. Figure 6 shows the integral of motion as a function of the acceleration orientation at two distinct acceleration magnitudes.

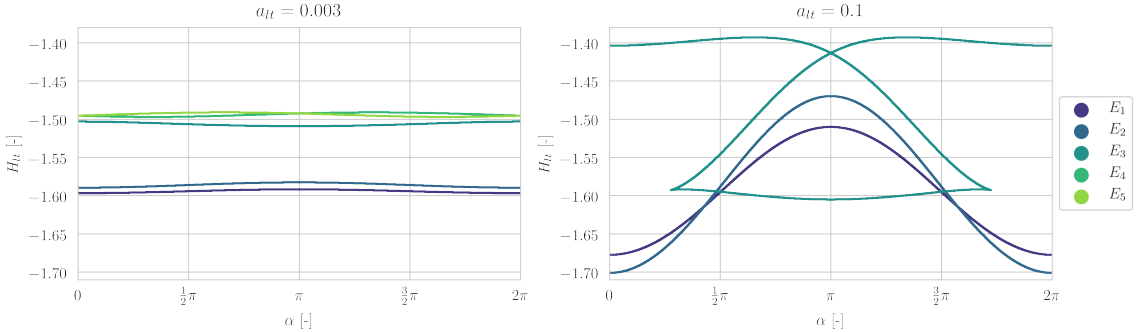


Figure 6. The evolution of the Hamiltonian over the equilibria contours for two distinct thrust magnitudes [0.003,0.1].

These energy curves shows the minimum Hamiltonian value a periodic solution that emanating from that specific equilibrium solution can posses. Hence this plot allows to predict the existence of a_{lt} -varying α -varying families. Unsurprisingly, the change in Hamiltonian is proportional to the acceleration magnitude. Another interesting observation is the varying number of equilibrium solutions which can be attributed to the merge of E_3, E_4 and E_5 .¹¹

The low-thrust acceleration affects the equilibrium solutions in several ways. It can significantly alter the the position of an equilibrium and thereby qualitatively change its stability. Furthermore, the unwinding behaviour can be increased which may give rise to opens up opportunities for faster transfers via invariant manifolds. The totality of the plots in this Section emphasize the existence of a symmetry in the CR3BP-LT. If an equilibrium exists at (x,y,a_{lt},α) , another equilibrium exists at $(x,-y,a_{lt},-\alpha)$.¹¹ The section is concluded with Table 2 which provides the reader with an overview of the key findings of this Section. These findings include the extrema of spatial position, dominant eigenvalue and Hamiltonian of the α -varying contours at $a_{lt} = 0.1$. The properties of the equilibrium solutions of the CR3BP are presented for reference purposes in Table 1.

Variable	L_1	L_2	L_3	L_4	L_5
x	0.836915148369	1.1557821477825	-1.005072643897	0.487854418983	0.487854418983
y	0.0000000000000	0.0000000000000	0.0000000000000	0.866034064038	-0.866034064038
λ	2.932055876779	2.158674362159	0.177875325621	-	-
H_{lt}	-1.594170537701	-1.586080212362	-1.506073573046	-1.493998527801	-1.493998527801

Table 1. An overview of the CR3BP equilibrium solution characteristics. λ denotes the eigenvalue related to the saddle subspace

Variable	E_1	E_2	E_3
x_{min}	0.827608726610	1.143236632185	-1.039291188287
x_{max}	0.845328433899	1.170499045727	0.948146945706
y_{min}	0.024529061495	-0.047042953312	-1.031812984559
y_{max}	-0.024529061495	0.047042953312	1.031812984559
λ_{min}	2.745942677592	1.856372716147	0.089124730775
λ_{max}	3.135841405289	2.459287202304	0.557456692346
$H_{lt,min}$	-1.677404319667	-1.701008408830	-1.604961223715
$H_{lt,max}$	-1.510051094876	-1.469793025395	-1.392875936337

Table 2. An overview of the alpha-varying ZAC properties at $a_{lt} = 0.1$. These properties involve the minimum and maximum positions, Hamiltonians and dominant eigenvalues.

PERIODIC SOLUTIONS

Periodic motion in the CR3BP has been a subject of extensive research which has led to a complete understanding of the periodic solution structure.⁵ The periodic solution structure in the CR3BP-LT on the other hand has been barely investigated. Previous research shows that low-thrust periodic orbits (LTPO) exist¹¹ but the periodic solution structure of the CR3BP-LT is essentially unknown. This section provides an overview of the periodic solutions emanating from E_1 and E_2 in the CR3BP-LT, thereby investigating the effect of a low-thrust acceleration on planar periodic motion in the Earth-Moon system. An overview of the periodic solution structure is effectively achieved by analyzing families of periodic solutions. Families are a set of periodic solutions where points belonging to different family members constitute to a continuous curve in phase space.¹⁹ Individual solutions of these families are uniquely defined by three parameters H_{lt}, a_{lt}, α . Three types

of families are construct in the CR3BP-LT*.¹¹ Along these three families, two of the three aforementioned parameters remain fixed while the other varies over the family. The varying parameter is usually referred to as the bifurcation parameter.²⁰ The remainder of this section is dedicated to the analysis of these families. First of all, the H_{lt} -varying families are investigated to get an initial understanding of the periodic solution structure around E_1 and E_2 . This is followed by analysis of a_{lt} -varying families and α -varying families to explicitly characterize the effect of a low-thrust acceleration on the periodic motion. Before these families are investigated, the underlying methodology for the construction and characterization of these families is presented.

Construction and characterization of periodic solution families

The three types of solution families are generated by employing numerical continuation procedures. The exact numerical continuation procedure varies slightly per family. H_{lt} -varying families are constructed via pseudo-arc length continuation²⁰ algorithm shown in Equation 13. The pseudo-arc length continuation ensures consistent spacing between two family members, symbolized by \mathbf{X}^n and \mathbf{X}^{n+1} . The consistent spacing is achieved by scaling the pseudo-arc length ρ relative to positional increment between the initial states of two family members. The position coordinates of the initial state of a periodic solution are indicated with x_0^n and y_0^n . This research adheres to positional increment of 10^{-4} between two subsequent family members to achieve a near-continuous family of solutions.

$$\mathbf{X}^{n+2} = \mathbf{X}^{n+1} + \rho (\mathbf{X}^{n+1} - \mathbf{X}^n), \quad \rho = \frac{10^{-4}}{\sqrt{(x_0^{n+1} - x_0^n)^2 + (y_0^{n+1} - y_0^n)^2}} \quad (13)$$

The pseudo-arc length continuation procedure is initialised by two periodic solutions. These seed solutions are obtained via a two-step procedure. The first step concerns the construction of approximate periodic solutions via a Floquet controller.^{21,22} During the second step, approximate solutions are transformed into actual periodic solutions via a dual-stage multiple shooting procedure called the two-level targeter.^{23,24} Each guess forwarded by the continuation procedure is solved using a 12th order Legendre-Gauss-Lobatto collocation method²⁵ augmented with Boor's method of mesh refinement for error control purposes.²⁶ The other two family types are constructed via natural parameter continuation.²⁰ Natural parameter continuation requires a start-up solution which is directly obtained from the H_{lt} -varying families. The guess for a new family member is created by slightly incrementing the bifurcation parameter, which is either a_{lt} or α depending on the family type. The aforementioned collocation methods corrects the guess to a truely periodic solution.

Characterization of a periodic solution family is achieved in two distinct ways. First of all, a graphical projection is provided to show the spatial evolution of the family with respect to the continuation parameter. On the other hand, the stability of each family member is mapped with respect to the continuation parameter to detect bifurcations within the dynamical system. Bifurcations are qualitative changes in the dynamics of the system which help identifying topological equivalent regions in the phase space of the CR3BP-LT.²⁷ According to Floquet theory, the stability of a periodic solution can be investigated via the eigensystem of the Monodromy matrix (M).²⁸ The Monodromy matrix maps a state on the periodic solution with period T at time t_i to a new state at time $t_i + T$. Hence, the monodromy matrix is a special case of the state transition matrix and can be obtained via numerical integration from the upper 6×6 block of A and the equations shown in Equation 14.

*In this research, a family type refers to the parameter that varies along the family rather than the type of periodic motion that is observed.

$$M = \Phi(T, 0), \quad \dot{\Phi}(t_{i+1}, t_i) = A_{t_i} \Phi(t_{i+1}, t_i), \quad \Phi(t_i, t_i) = I \quad (14)$$

M adheres to a symplectic map structure since the CR3BP-LT is a Hamiltonian system.⁶ This implies that if λ is an eigenvalue of M (a characteristic multiplier) $\lambda^{-1}, \bar{\lambda}, \bar{\lambda}^{-1}$ are characteristic multipliers as well. Hence, the six characteristic multipliers occur in three reciprocal pairs. The values of these characteristic multipliers reveal the stability of the periodic solution. A pair of (complex) eigenvalues with magnitude one indicates periodicity (or stability). On the other hand, A pair of eigenvalues with magnitude greater (smaller) than one indicates instability. More specifically, a real pair of eigenvalues with a magnitude greater (smaller) than one indicates the existence of stable (unstable) manifolds.⁶ The extent of hyperbolic unwinding behaviour related to these manifolds is captured via a so-called stability index, shown below in Equation 15.

$$\nu_i = \frac{1}{2} \left| \lambda_i + \frac{1}{\lambda_i} \right| \quad (15)$$

A change in the number of unstable eigenvalue pairs, referred to as the order of instability,²⁹ indicates the presence of a bifurcation. The totality of the graphical projection, bifurcation diagram and the Saddle stability index evolution of families allows characterization of the periodic solution structure of the CR3BP-LT.

H_{lt}-varying libration point orbit families

Analyzing H_{lt} -varying families emanating from E_1 and E_2 at different combinations of acceleration magnitude and orientation provides an initial understanding of the CR3BP-LT periodic solution structure. The ballistic families emanating from L_1 and L_2 are presented first for comparison purposes. Periodic families emanating from E_1 and E_2 at three acceleration magnitudes ($a_{lt} = [0.01 \ 0.05 \ 0.1]$) are analyzed subsequently. At each acceleration magnitude, periodic families are presented at six acceleration orientations ($\alpha = [0.0 \ \frac{1}{3}\pi \ \frac{2}{3}\pi \ \pi \ \frac{4}{3}\pi \ \frac{5}{3}\pi]$).

L₁ and L₂ ballistic families It is well-known that the in-plane center modes of L_1 and L_2 give rise to the Horizontal-Lyapunov family.⁶ A graphical projection of them can be found in Figure 7.

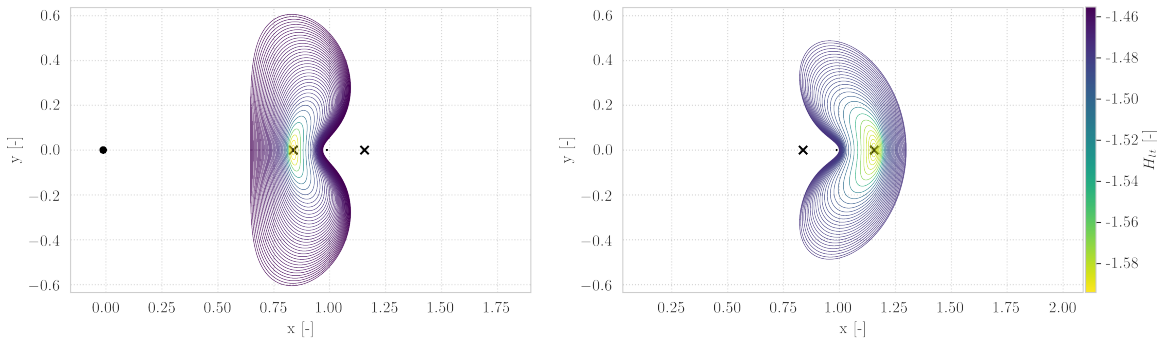


Figure 7. Graphical projection of the L_1 and L_2 H-L families. The left subplot displays the L_1 family whereas L_2 H-L family is shown in the right subplot. The primary and secondary are denoted as black dots whereas the natural lagrangian points are symbolized with black crosses. The colour of the periodic solution indicates the Hamiltonian according to the colourbar depicted on the right. Each 50th member of the family is plotted.

The graphical projections show that the H-L families at L_1 and L_2 differ significantly in shape. The members of the L_2 are heavily curved towards almost engulf the Moon. This can be attributed to the fact that the L_2 family is located to the right side of the Earth and Moon, resulting in a one-sided gravitational potential from the primaries. Furthermore, it can be observed that the members of the L_1 H-L family occupy a larger Hamiltonian range compared to their L_2 counterparts. A bifurcation analysis of the H-L families at L_1 and L_2 is presented in Figure 8.

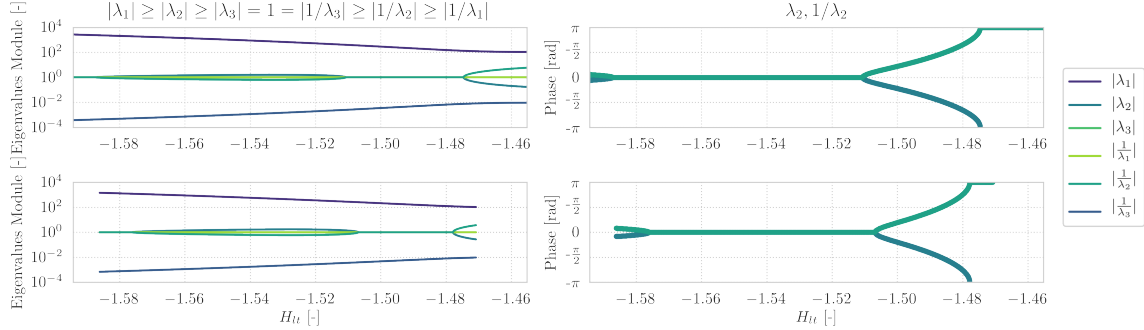


Figure 8. Bifurcation analysis of the L_1 and L_2 H-L families. The left subplots display the characteristic multiplier moduli whereas the right subplots present the phase of the eigenvalue related to the out-of-plane center subspace. The top subplots relate to the L_1 H-L family whereas the bottom subplots represent the L_2 H-L family.

The left subplots reveal the bifurcations by displaying the moduli of the three reciprocal eigenvalue pairs. The $\lambda_1, 1/\lambda_1$ pair relates to the saddle component of the motion which give rise to the unstable(stable) manifold. The $\lambda_2, 1/\lambda_2$ pair denotes the out-of-plane center subspace whereas the $\lambda_3, 1/\lambda_3$ pair relates to the in-plane center subspace from which the H-L family emanates. These left subplots show that three bifurcations occur in both families due to the $\lambda_2, 1/\lambda_2$. From the right subplots it can be observed that the first bifurcation of both families occurs when the $\lambda_2, 1/\lambda_2$ eigenvalue pair leaves the unit circle at the positive x-axis. This behaviour is referred to as a tangent bifurcation and indicates the existence of a new family of solutions; the Halo family.²⁹ The second change in order of instability observed in the H-L families at both L_1 and L_2 is also a tangent bifurcation.²⁹ This tangent bifurcation generates the Axial family that connect the H-L families with the vertical-Lyapunov (V-L) families at the respective Lagrangian point.⁵ The third bifurcation of the H-L families at both L_1 and L_2 occurs when the $\lambda_2, 1/\lambda_2$ leaves the unit circle at the negative x-axis. Such a phenomenon is interpreted as a period doubling bifurcation and is related to periodic solutions with twice the period of the family they emanate from.²⁸ The discussion of the ballistic families is concluded with analysis of the stability index of the unstable eigenvalue pair and the H_{lt} evolution as shown in Figure 9.

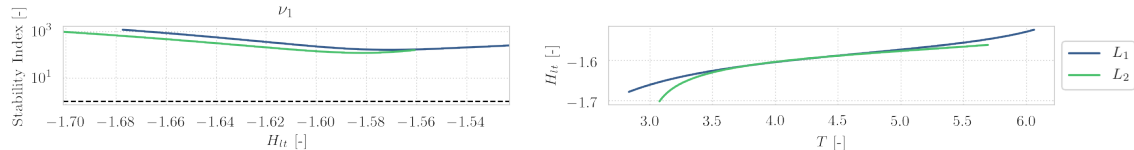


Figure 9. Stability analysis of the L_1 and L_2 H-L families. The left subplot displays the stability index of the eigenvalue related the saddle subspace. The right subplot shows evolution of H_{lt} as a function of the orbital period T .

It can be observed that stability index of the eigenvalue pair related to the Saddle component of the dynamics attains a maximum for periodic solutions situated closest the equilibrium point and

decreases monotonically while the orbits grow in amplitude. Meanwhile, The hamiltonian and orbital period are minimal near the equilibria and increases monotonically over the family.

$a_{lt} = 0.01$ families The effect of a small low-thrust acceleration on the orbit geometry of l.p.o's emanating from E_1 can be observed from Figure 10. At this acceleration magnitude, the characteristic H-L shape is maintained whenever the acceleration is collinear with the x -axis. However, distortions with respect to this H-L geometry occur when the acceleration orientation is not collinear with the x -axis. A lobe appears in orbit geometry in either positive or negative y -direction, depending upon the acceleration orientation. Furthermore, families with acceleration orientation α and $-\alpha$ seem symmetric w.r.t to the x -axis which is expected because of the earlier mentioned symmetry.

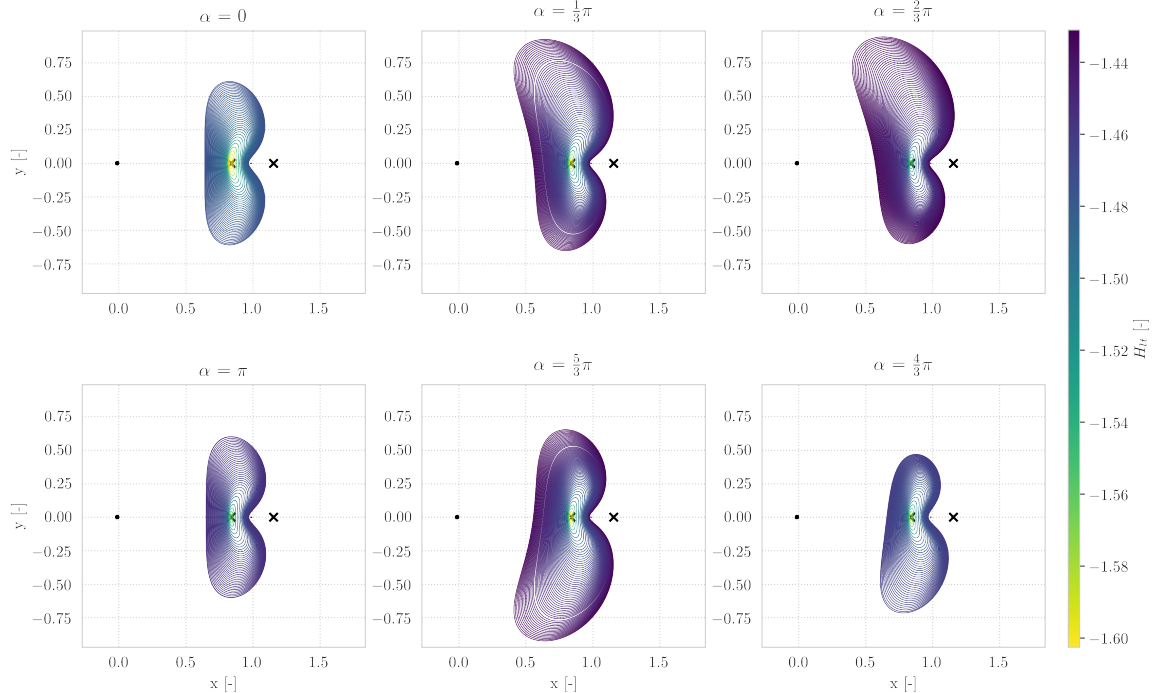


Figure 10. Six H_{lt} -varying families at $a_{lt} = 0.01$ for different α values that emanate from E_1 . The colour of an l.p.o corresponds to its Hamiltonian value according to the colourbar provided on the right side of the Figure. The family with $\alpha = \frac{4}{3}\pi$ is terminated earlier with respect to $\alpha = \frac{2}{3}\pi$ due to instabilities in the collocation algorithm.

The bifurcation diagrams of these H_{lt} -varying families are shown in Figure 11. It can be concluded that for $a_{lt} = 0.01$, the qualitative nature of the bifurcation diagram does not change relative to the bifurcation diagram of the L_1 ballistic family. This implies the existence of the spatial low-thrust Halo, Axial families. Furthermore, the symmetry between families with acceleration orientation α and $-\alpha$ can be observed since the bifurcations of these families happen at identical Hamiltonians. Figure 12 shows that stability index related to the Saddle eigenvalue of these families reveal that the maximum unwinding behaviour can be found near the equilibria. Additionally, the Hamiltonian (orbital period) increase (decrease) monotonically over each family.

Six H_{lt} -varying families with identical thrust parameters are constructed around the E_2 contour. The graphical projection of these families can be found in Figure 13, their bifurcation diagrams are shown in Figure 14 and saddly stability index plus Hamiltonian evolution is shown in Figure 15.

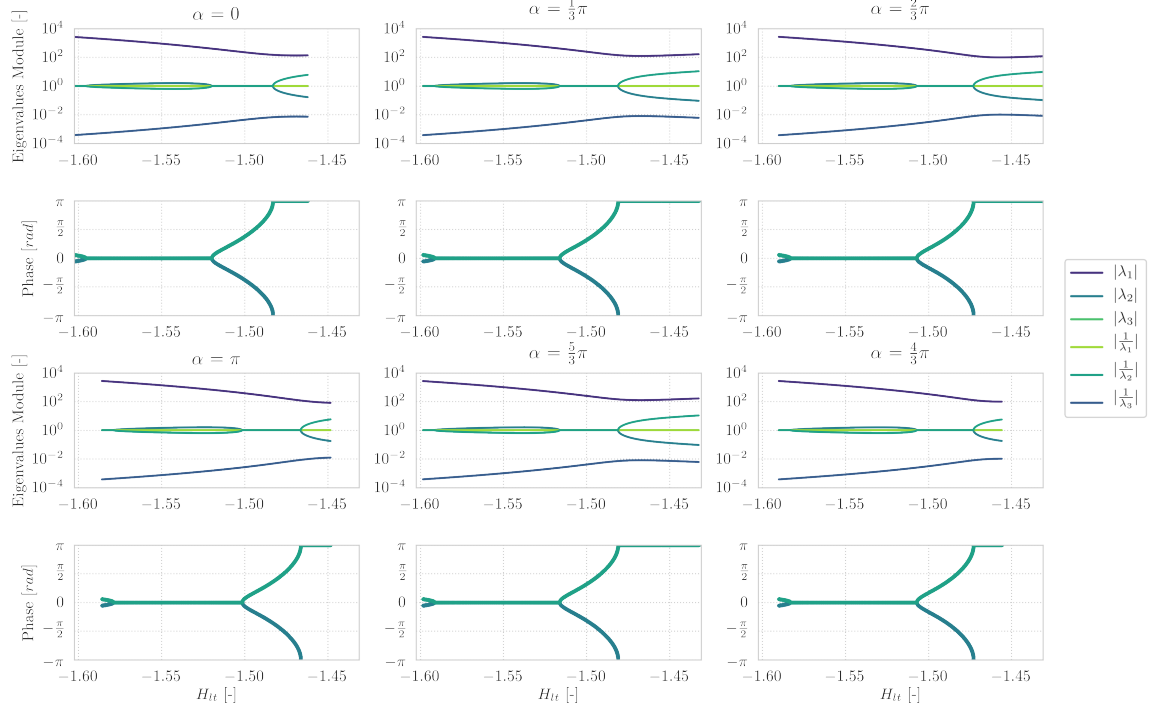


Figure 11. Bifurcation diagram of the six H_{lt} -varying families at $a_{lt} = 0.01$ for different α values that emanate from E_1 . The family with $\alpha = \frac{4}{3}\pi$ is terminated earlier with respect to $\alpha = \frac{2}{3}\pi$ due to instabilities in the collocation algorithm.

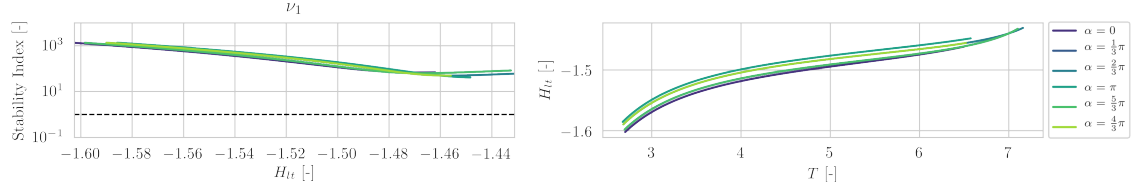


Figure 12. The left subplot displays the stability index of the eigenvalue related the saddle subspace. The right subplot shows evolution of H_{lt} as a function of T .

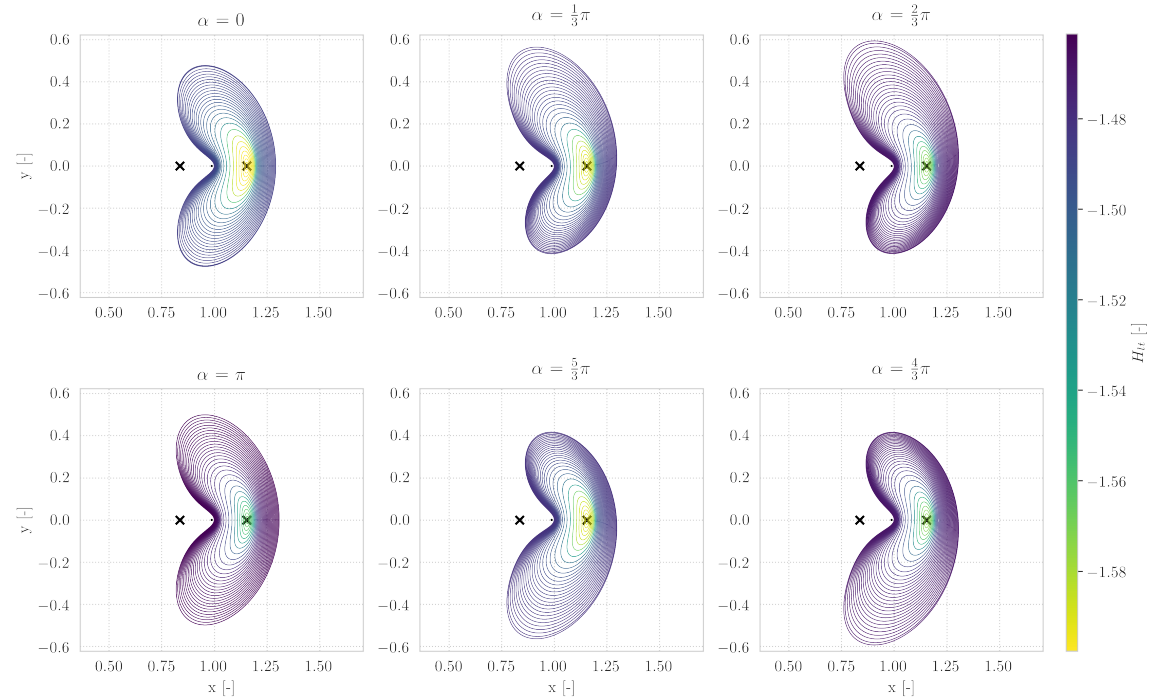


Figure 13. Six H_{lt} -varying families at $a_{lt} = 0.01$ for different α values that emanate from E_2 . The colour of an l.p.o corresponds to its Hamiltonian value according to the colourbar provided on the right side of the Figure.

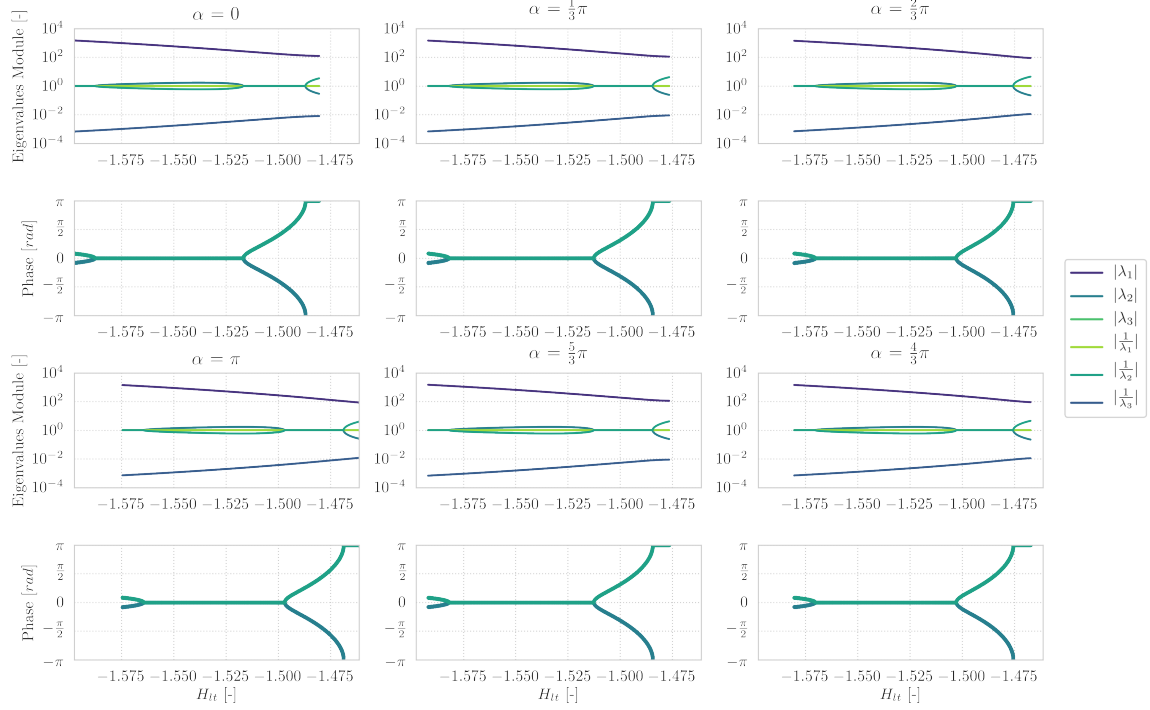


Figure 14. Bifurcation diagram of the six H_{lt} -varying families at $a_{lt} = 0.01$ for different α values that emanate from E_2 .

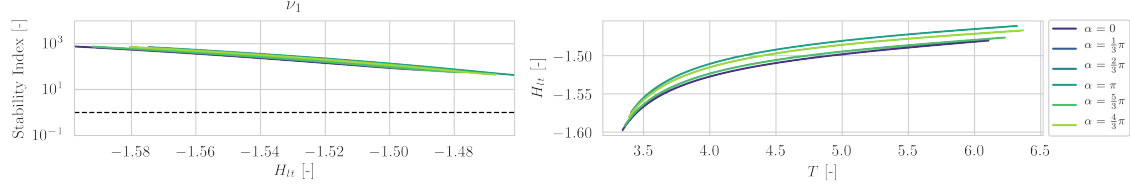


Figure 15. The left subplot displays the stability index of the eigenvalue related the saddle subspace. The right subplot shows evolution of H_{lt} as a function of T .

Inspection of Figures 13–15 reveal that a small acceleration magnitude has an identical effect on families emanating from the E_2 as on families that emanate from the E_1 contour. The geometry of the libration point orbit families is distorted by a lobe whose direction depends upon the orientation of the acceleration. The bifurcation diagram remains qualitatively identical implying that Halo and axial libration point orbits exist around the E_2 contour. The maximum unwinding behaviour is found near the artificial equilibria and the H_{lt} -varying families around E_2 decrease (increase) monotonically in Hamiltonian (orbital period).

$a_{lt} = 0.05$ families The effect of a medium low-thrust acceleration on the orbit geometry of l.p.o.'s emanating from E_1 can be observed from Figure 16. While the acceleration is collinear with the x -axis, no clear differences can be observed with respect to the natural L_1 family in Figure 7. This cannot be said from the H_{lt} -varying families with non-collinear thrust, where the geometry is so distorted the families take on an 'ear-like' shape. For the $\alpha = \frac{5}{3}\pi$ The lobe can even reach twice as far in y -direction relative to the ballistic case. The bifurcation diagrams of these six H_{lt} -varying families can be found in Figure 17 which reveal two interesting phenomena. The first phenomenon is that the qualitative nature of the bifurcation behaviour remains identical with respect to the ballistic families for $\alpha = [0, \frac{1}{3}\pi, \pi, \frac{5}{3}\pi]$ which suggests the existence of Axial and Halo orbits.

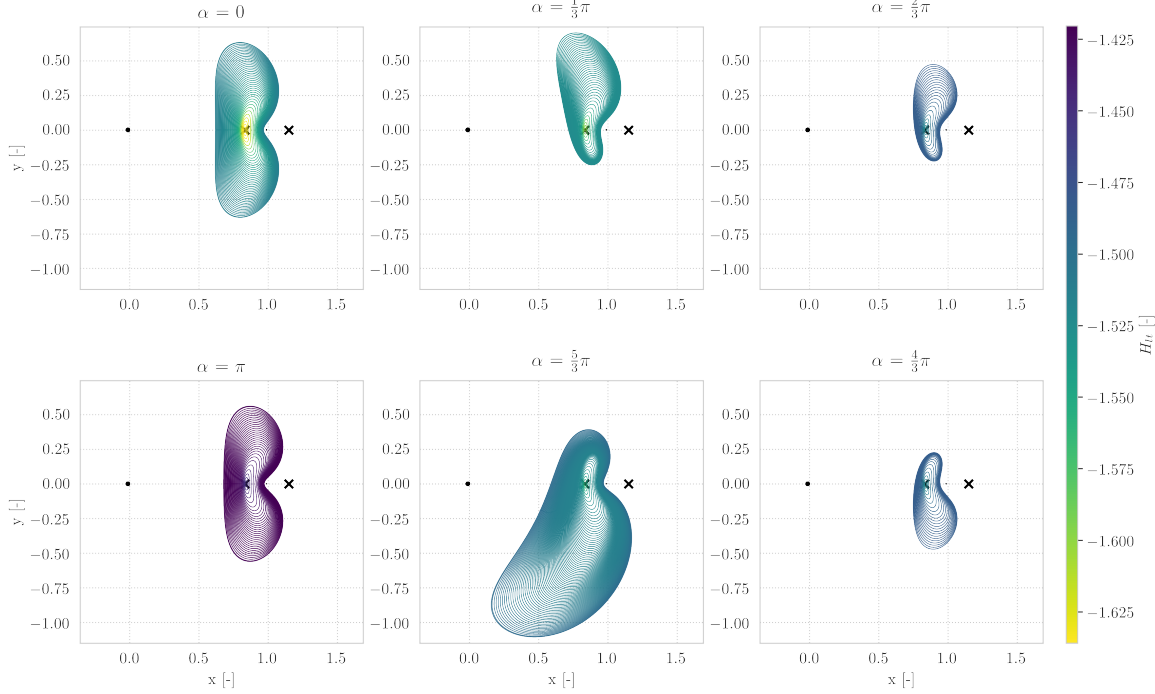


Figure 16. Six H_{lt} -varying families at $a_{lt} = 0.05$ for different α values that emanate from E_1 . The colour of an l.p.o corresponds to its Hamiltonian value according to the colourbar provided on the right side of the Figure. The families with $\alpha = \frac{5}{3}\pi$ are terminated earlier with respect to $\alpha = \frac{5}{3}\pi$ due to instabilities in the collocation algorithm.

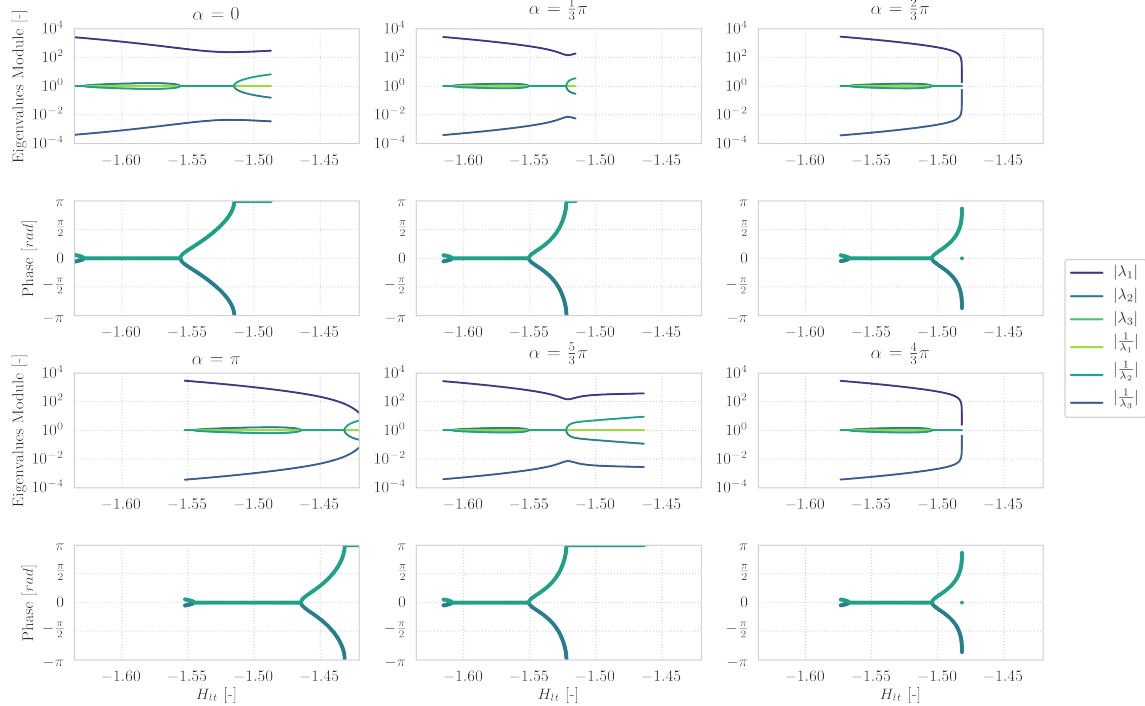


Figure 17. Bifurcation diagram of the six H_{lt} -varying families at $a_{lt} = 0.05$ for different α values that emanate from E_1 . The family with $\alpha = \frac{1}{3}\pi$ is terminated earlier with respect to $\alpha = \frac{5}{3}\pi$ due to instabilities in the collocation algorithm.

The existence of these spatial solutions is also suggested at $\alpha = [\frac{2}{3}\pi, \frac{4}{3}\pi]$ from the two tangent bifurcations. However a period-doubling bifurcation is not observed here. Analysis of the Saddle stability index, displayed in Figure 18 reveals that the maximum hyperbolic unwinding behaviour remains maximum near the equilibria but does not monotonically decrease for the families with $\alpha = [\frac{1}{3}\pi, \frac{5}{3}\pi]$. All six H_{lt} -varying families however decrease (increase) monotonically in Hamiltonian (orbital period).

Six H_{lt} -varying families with identical thrust parameters are constructed around the E_2 contour. The graphical projection of these families can be found in Figure 19, corresponding bifurcation diagrams are shown in Figure 20 whereas the Saddle stability indices and Hamiltonian evolution are shown in Figure 21.

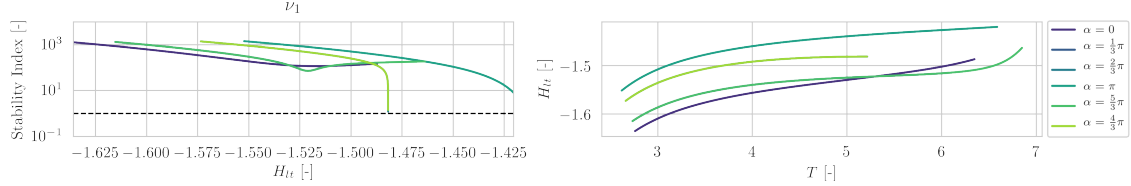


Figure 18. The left subplot displays the stability index of the eigenvalue related the saddle subspace. The right subplot shows evolution of H_{lt} as a function of T .

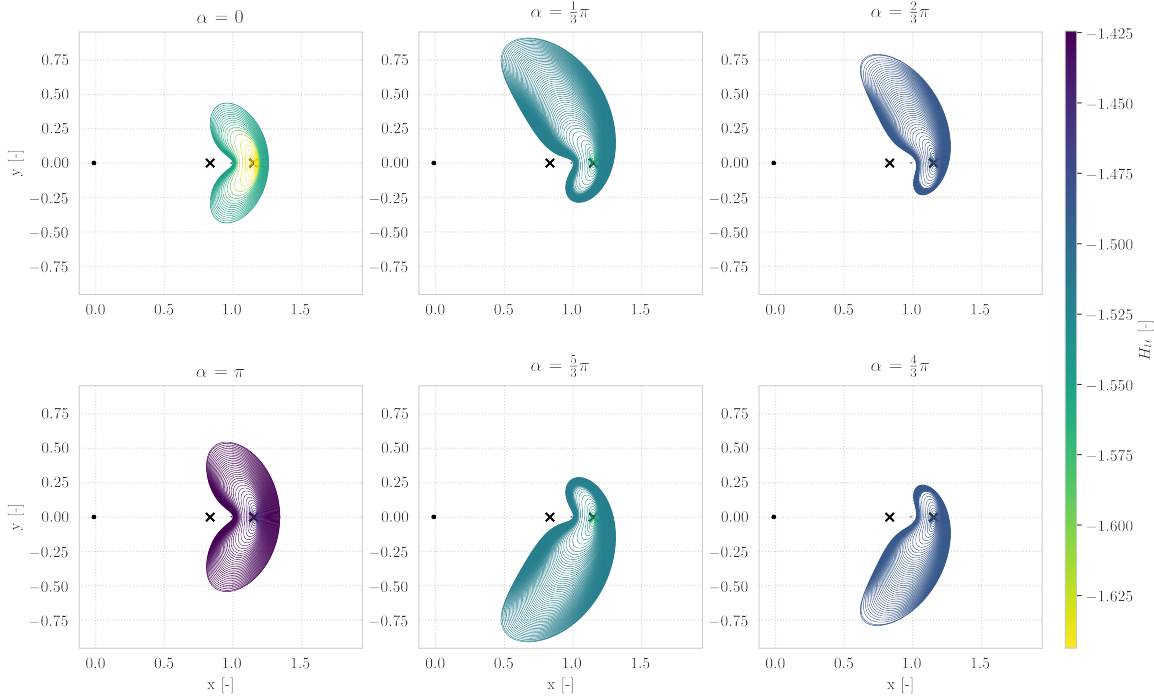


Figure 19. Six H_{lt} -varying families at $a_{lt} = 0.05$ for different α values that emanate from E_2 . The colour of an l.p.o corresponds to its Hamiltonian value according to the colourbar provided on the right side of the Figure.

The medium low-thrust acceleration has a similar effect on H_{lt} families around the E_2 contour as on periodic solutions emanating from the E_1 contour. As long as the acceleration vector remains collinear with the x -axis. The low-thrust periodic solutions remain topological equivalent to the L_2 ballistic family. Off-axis low-thrust orientations give rise to 'ear-shaped' families that curve around the Moon and even the ballistic L_1 Lagrangian point.

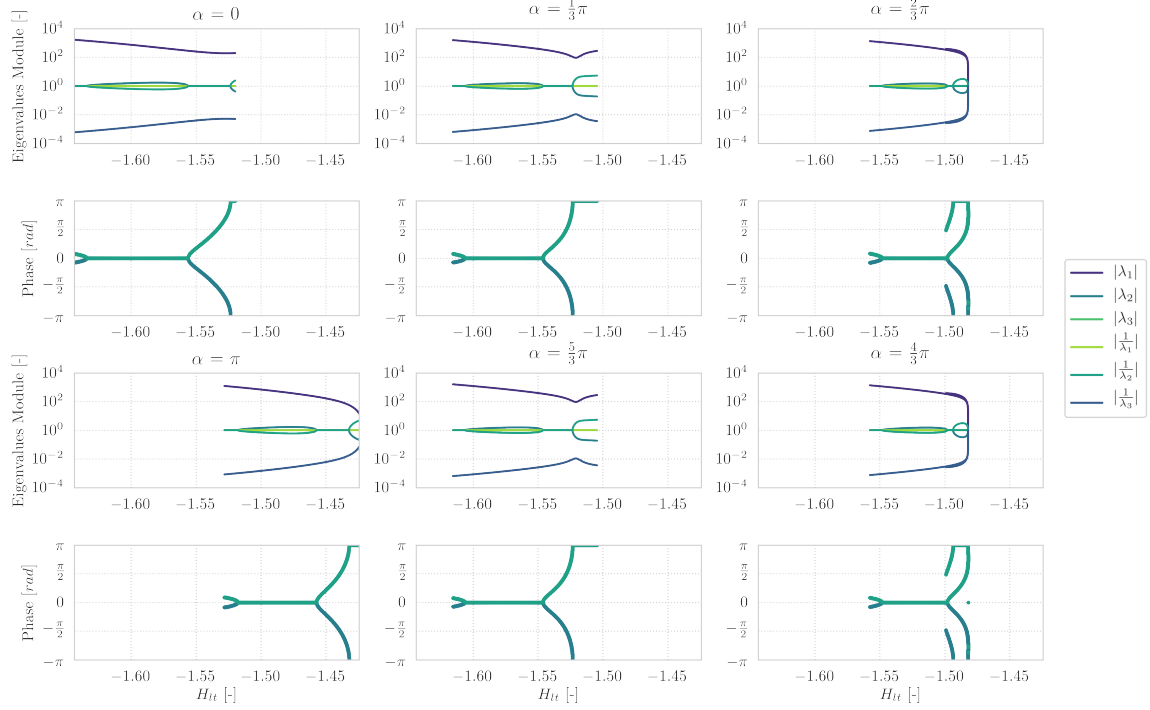


Figure 20. Bifurcation diagram of six H_{lt} -varying families at $a_{lt} = 0.05$ for different α values that emanate from E_2 .

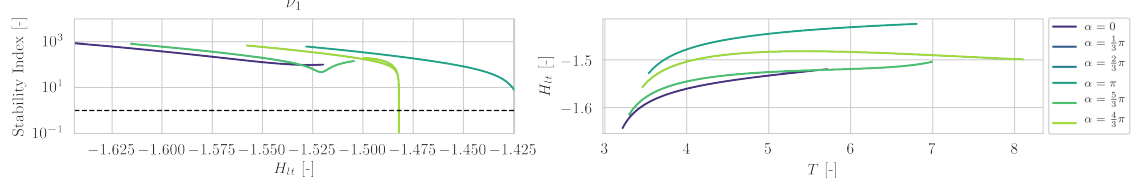


Figure 21. The left subplot displays the stability index of the eigenvalue related the saddle subspace. The right subplot shows evolution of H_{lt} as a function of T .

The bifurcation behaviour of the families with $\alpha = [0, \frac{1}{3}\pi, \pi, \frac{5}{3}\pi]$ remains identical to the ballistic L_2 family since two tangent bifurcations and one period doubling bifurcation is observed, implying the existence of low-thrust Halo and Axial families. This cannot be said for the H_{lt} -varying families with $\alpha = [\frac{2}{3}\pi, \frac{4}{3}\pi]$. Their bifurcation diagrams in Figure 21 reveal that two families possess two tangent fold bifurcation after which the magnitude of all six eigenvalues goes to unity at the extremum of the family Hamiltonian. This indicates a fold bifurcation and although it changes in the order of instability it does not imply a new family of periodic solutions.²⁸ Besides these tangent and fold bifurcations, a period doubling bifurcation occurs towards the end of the families. Analysis of the Saddle stability index, displayed in Figure 21 reveals that the hyperbolic unwinding behaviour remains maximum near the equilibria but does not monotonically decrease for the families with $\alpha = [\frac{1}{3}\pi, \frac{5}{3}\pi]$. The H_{lt} -varying families emanating from E_2 decrease (increase) monotonically in Hamiltonian (orbital period), apart from the families with $\alpha = [\frac{2}{3}\pi, \frac{4}{3}\pi]$. These two families experience an extremum in Hamiltonian but increase monotonically in orbital period.

$a_{lt} = 0.1$ families The effect of a large low-thrust acceleration on the orbit geometry of l.p.o's emanating from E_1 can be observed from Figure 10. At this acceleration magnitude, distortions in geometry happen every acceleration orientation.

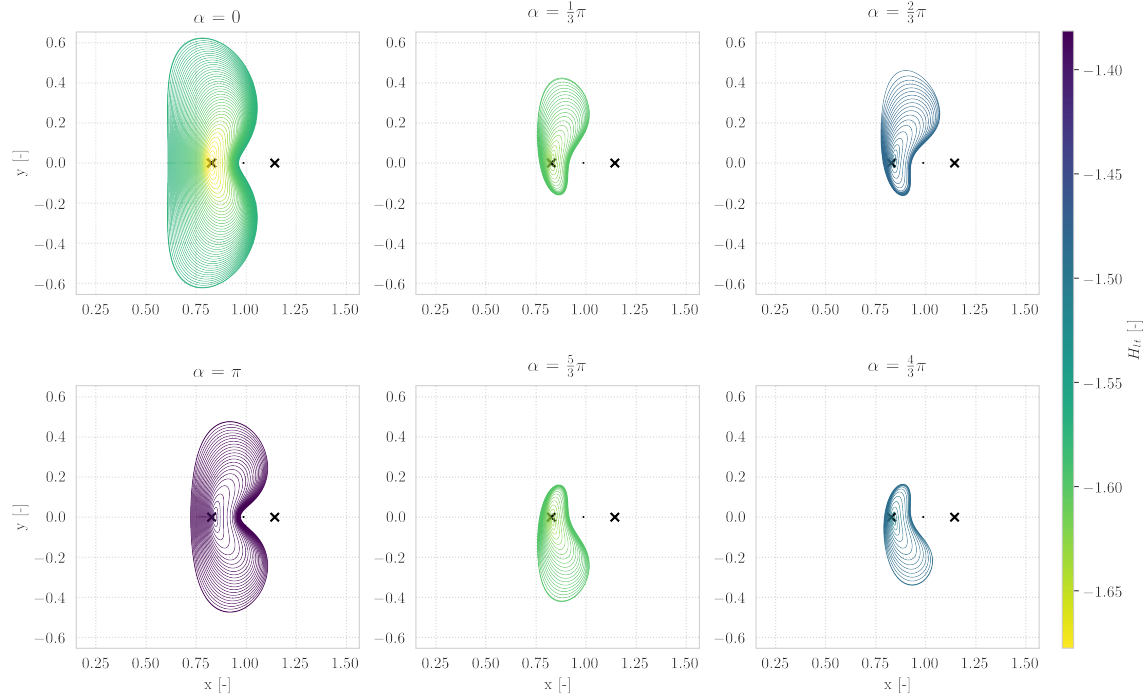


Figure 22. Six H_{lt} -varying families at $a_{lt} = 0.10$ for different α values that emanate from E_1 . The colour of an l.p.o corresponds to its Hamiltonian value according to the colourbar provided on the right side of the Figure. The family with $\alpha = \frac{2}{3}\pi$ is terminated earlier with respect to $\alpha = \frac{4}{3}\pi$ due to instabilities in the collocation algorithm.

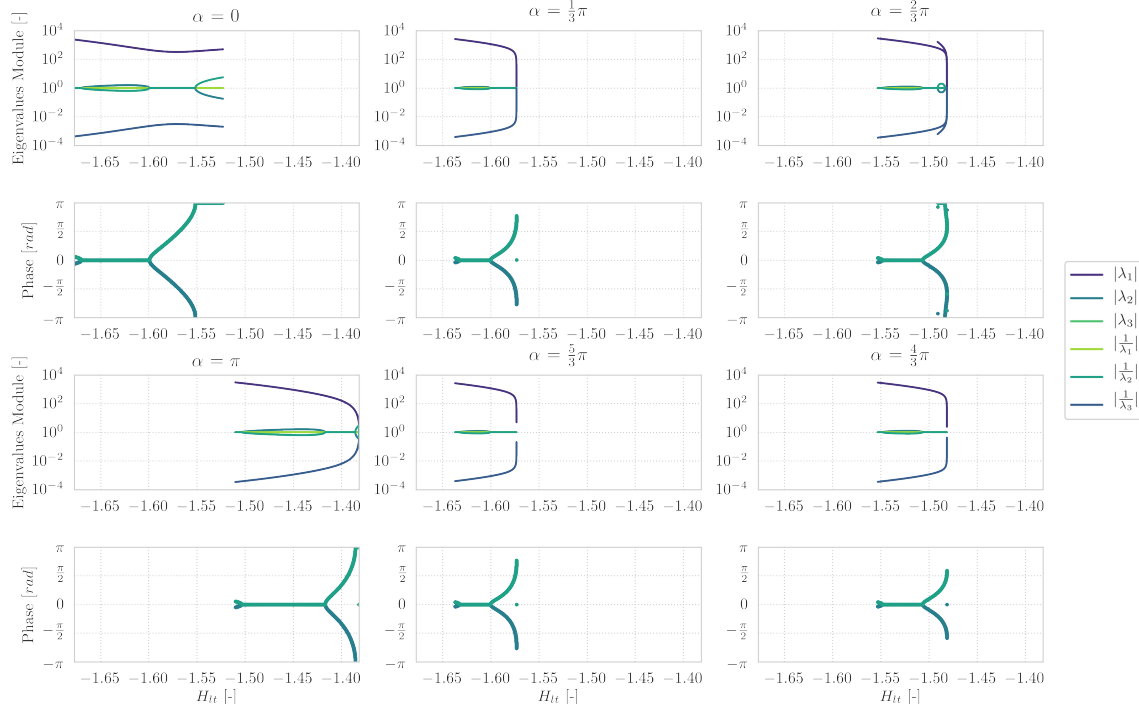


Figure 23. Bifurcation diagram of the six H_{lt} -varying families at $a_{lt} = 0.10$ for different α values that emanate from E_1 . The family with $\alpha = \frac{2}{3}\pi$ is terminated earlier with respect to $\alpha = \frac{4}{3}\pi$ due to instabilities in the collocation algorithm.

A collinear acceleration in the positive x -direction results in a family shape similar to the ballistic L_1 family apart from the fact that the lobes of the orbits extend further in both y -directions. An opposite effect is visible when a collinear acceleration in the negative x -direction is applied. The two lobes of the family are smaller with respect to the ballistic L_1 family and curve further around the Moon like the ballistic L_2 family. For the remaining off-axis acceleration orientations, the orbit geometry transforms into a 'mussel-like' shape. The bifurcation behaviour of families with collinear accelerations remains identical to the ballistic L_1 family as shown in Figure 23. This cannot be said for families with non-collinear accelerations. The H_{lt} -varying families with $\alpha = [\frac{1}{3}\pi, \frac{4}{3}\pi, \frac{5}{3}\pi]$ possess two tangent bifurcations before termination of the collocation procedure whereas the family with $\alpha = \frac{2}{3}\pi$ possesses two tangent bifurcations, one cyclic fold bifurcation and one period doubling bifurcation. The presence of two tangent bifurcations at all families however implies the existence of low thrust Halo and Axial orbits. Analysis of the Saddle stability indices, shown in Figure 24 reveal that maximum unwinding behaviour is maximum near the equilibria. The E_1, H_{lt} -varying families decrease (increase) monotonically in Hamiltonian (orbital period), apart from the $\alpha = \frac{2}{3}\pi$ family.

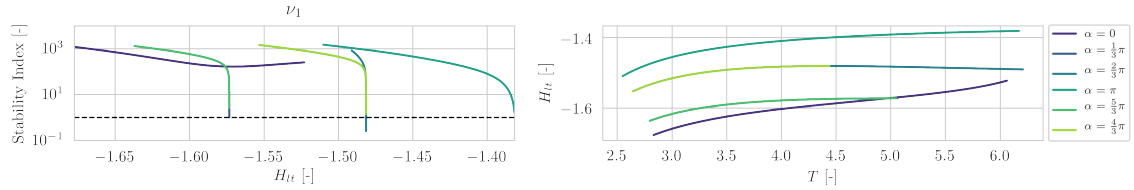


Figure 24. The left subplot displays the stability index of the eigenvalue related the saddle subspace. The right subplot shows evolution of H_{lt} as a function of T .

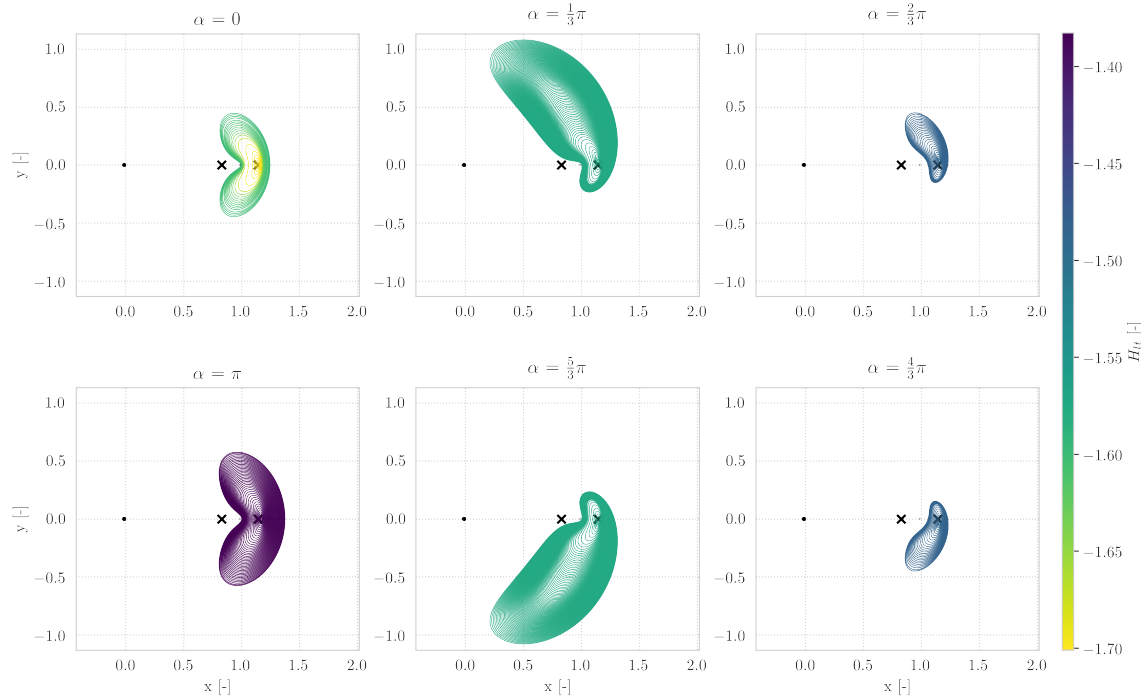


Figure 25. Six H_{lt} -varying families at $a_{lt} = 0.10$ for different α values that emanate from E_2 . The colour of an l.p.o corresponds to its Hamiltonian value according to the colourbar provided on the right side of the Figure.

The final families discussed in this section concern six E_2 , H_{lt} -varying families with $a_{lt} = 0.1$ and varying orientations. Figure 25 shows their geometry whereas their corresponding bifurcation diagrams can be found in Figure 26. Collinear acceleration does not visibly morph the geometry of the L_2 family and the same bifurcations are observed as in the L_2 ballistic families. This this cannot be said for noncollinear acceleration orientations which leads to 'ear-like' shaped families. Intense changes in geometry and bifurcation behaviour are observed for non-collinear accelerations. In the case of $\alpha = [\frac{1}{3}\pi, \frac{5}{3}\pi]$, 'ear-shaped' families arise that curve well beyond the moon. These two families exhibit two extrema in Hamiltonian at which cyclic fold bifurcations occur next to the tangent fold and period doubling bifurcations. 'Ear-shaped' families are likely to exist for $\alpha = [\frac{2}{3}\pi, \frac{4}{3}\pi]$, but the continuation procedure could not compute these family members. These families contain one extremum in Hamiltonian where a cyclic fold bifurcation occurs. Hence, the existence of low-thrust Halo and Axial orbits is implied at all six acceleration orientations. Inspection Saddle stability indices in Figure 27 show that the maximum unwinding behaviour of the family remains near the equilibria.

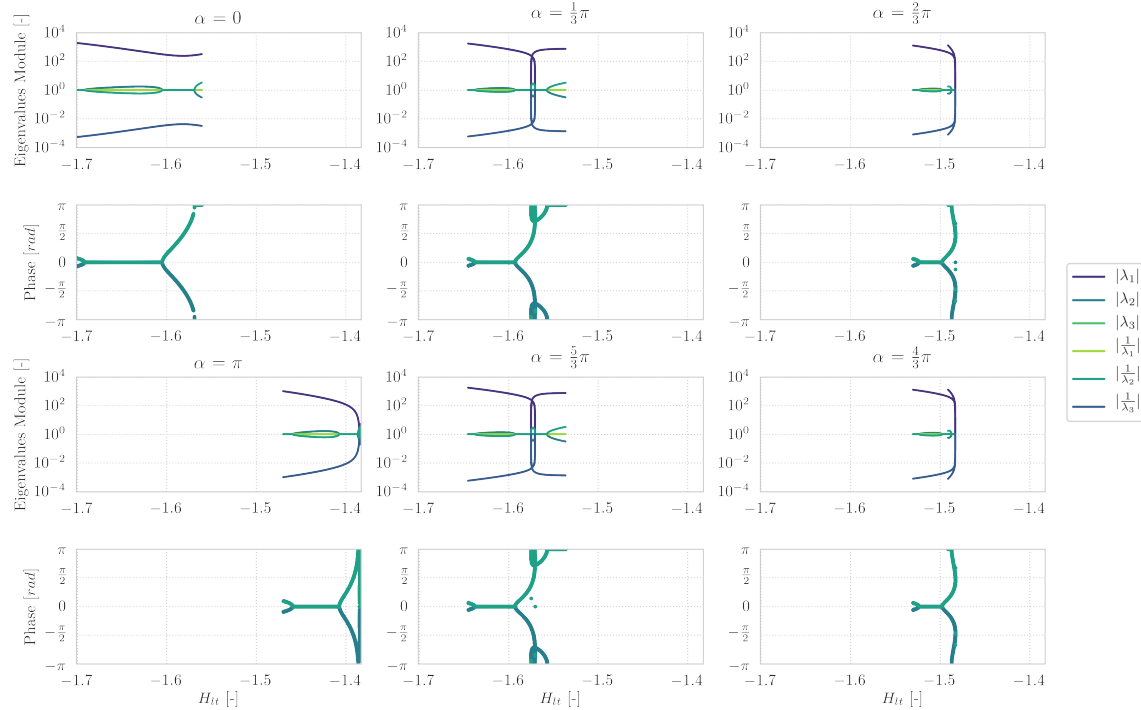


Figure 26. Bifurcation diagram of the six H_{lt} -varying families at $a_{lt} = 0.10$ for different α values that emanate from E_2 . The family with $\alpha = \frac{2}{3}\pi$ is terminated earlier with respect to $\alpha = \frac{4}{3}\pi$ due to instabilities in the collocation algorithm.

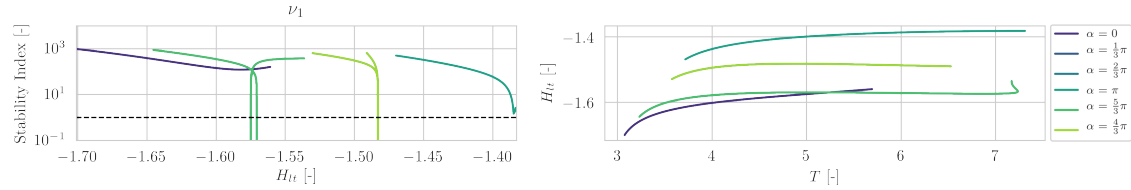


Figure 27. The left subplot displays the stability index of the eigenvalue related the saddle subspace. The right subplot shows evolution of H_{lt} as a function of T .

a_{lt} -varying libration point orbit families

While the H_{lt} -varying families provide an initial understanding of the CR3BP-LT, it remains difficult to characterize the effect of the low-thrust acceleration. To investigate the effect of a low-thrust acceleration magnitude, a_{lt} -varying families are investigated that emanate from the E_1 and E_2 contour for six different acceleration orientations $\alpha = [0, \frac{1}{3}\pi, \frac{2}{3}\pi, \pi, \frac{4}{3}\pi, \frac{5}{3}\pi]$. Every libration point orbit belonging to one of these twelve families has an identical low-thrust Hamiltonian value ($H_{lt} = -1.525$). The graphical projections of six a_{lt} -varying families emanating from the E_1 contour can be found below in Figure 28 whereas the evolution of the saddle stability indices and evolution of T can be found in Figure 29.

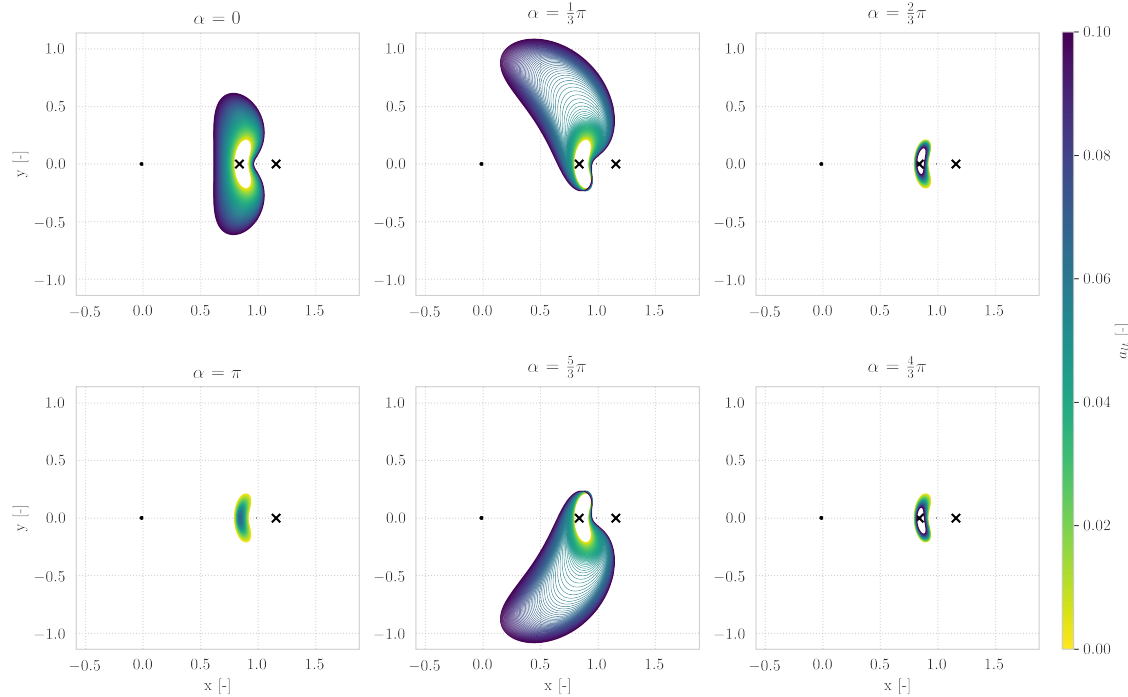


Figure 28. Six a_{lt} -varying families at $H_{lt} = -1.525$ for different α values that emanate from E_1 . The colour of an l.p.o corresponds to its acceleration magnitude according to the colourbar provided on the right side of the Figure.

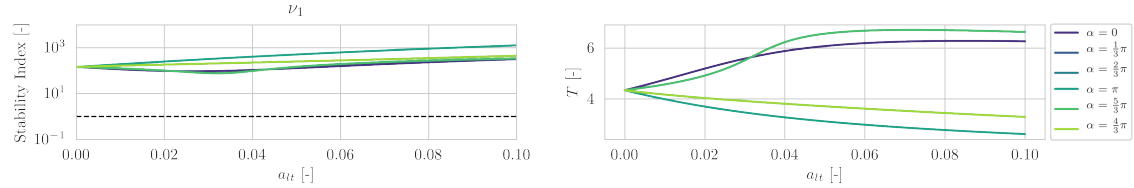


Figure 29. The left subplot displays the stability index of the eigenvalue related to the saddle subspace. The right subplot shows evolution of T as a function of a_{lt} .

The a_{lt} -varying families in Figure 28 reveal that the acceleration magnitude has various effects on the orbit geometry depending upon its orientation. An increase in acceleration aligned with positive x -direction results in a larger libration point orbit. Whereas an increase in acceleration with $\alpha = \pi$ results in a smaller periodic solution. For $\alpha = [\frac{1}{3}\pi, \frac{5}{3}\pi]$, it can be observed how the ballistic H-L orbit morphs into an 'ear-shaped' periodic solution with an increasing acceleration magnitude. These extreme geometry distortions are not observed for $\alpha = [\frac{2}{3}\pi, \frac{4}{3}\pi]$ where an increase

in acceleration magnitude leads to a slight enlargement or shrinking of the periodic solutions. The saddle stability of these families, plotted in Figure 29, show that the rate of the hyperbolic unwinding behaviour monotonically increases with a growing acceleration magnitude for $\alpha = [\frac{2}{3}\pi, \pi, \frac{4}{3}\pi]$. The saddle stability indices of the remaining families decreases to a local minimum for low acceleration magnitudes before increasing. These analyses are repeated for six families emanating from the E_2 contour. Their graphical projections are shown in Figure 30 whereas the evolution of the saddle stability indices and evolution of T can be found in Figure 31.

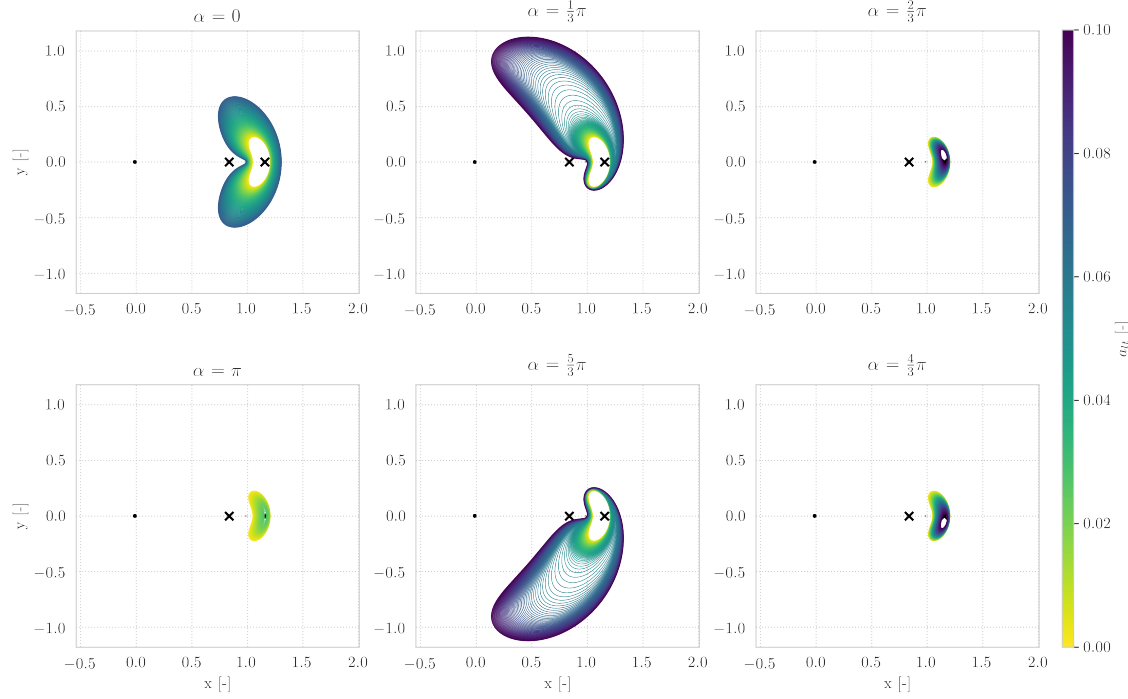


Figure 30. Six a_{lt} -varying families at $H_{lt} = -1.525$ for different α values that emanate from E_2 . The colour of an l.p.o corresponds to its acceleration magnitude according to the colourbar provided on the right side of the Figure. The a_{lt} -varying family with $\alpha = 0$ is not fully computed due to instabilities in the continuation algorithm

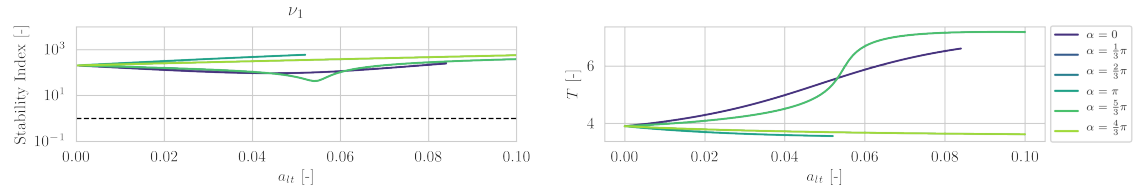


Figure 31. The left subplot displays the stability index of the eigenvalue related the saddle subspace. The right subplot shows evolution of T as a function of a_{lt} .

Inspection of Figures 30 and 31 reveal the the acceleration magnitude has an identical effect on families emanating from the E_2 contour as families emanating from the E_1 contour.

α -varying libration point orbit families

The H_{lt} -varying and a_{lt} -varying family show that the periodic solutions characteristics can widely vary with a change in acceleration orientation. To characterize the effect of the acceleration orien-

tation, α -varying families are constructed at both the E_1 and E_2 contour. Per contour, α -varying families are constructed at three distinct acceleration magnitudes ($a_{lt}=[0.01, 0.05, 0.10]$) and three Hamiltonian values ($H_{lt}=[-1.55, -1.525, -1.50]$) which results in nine periodic solution families per contour. The geometries of these α -varying families emanating from the E_1 contour are shown in Figure 32.

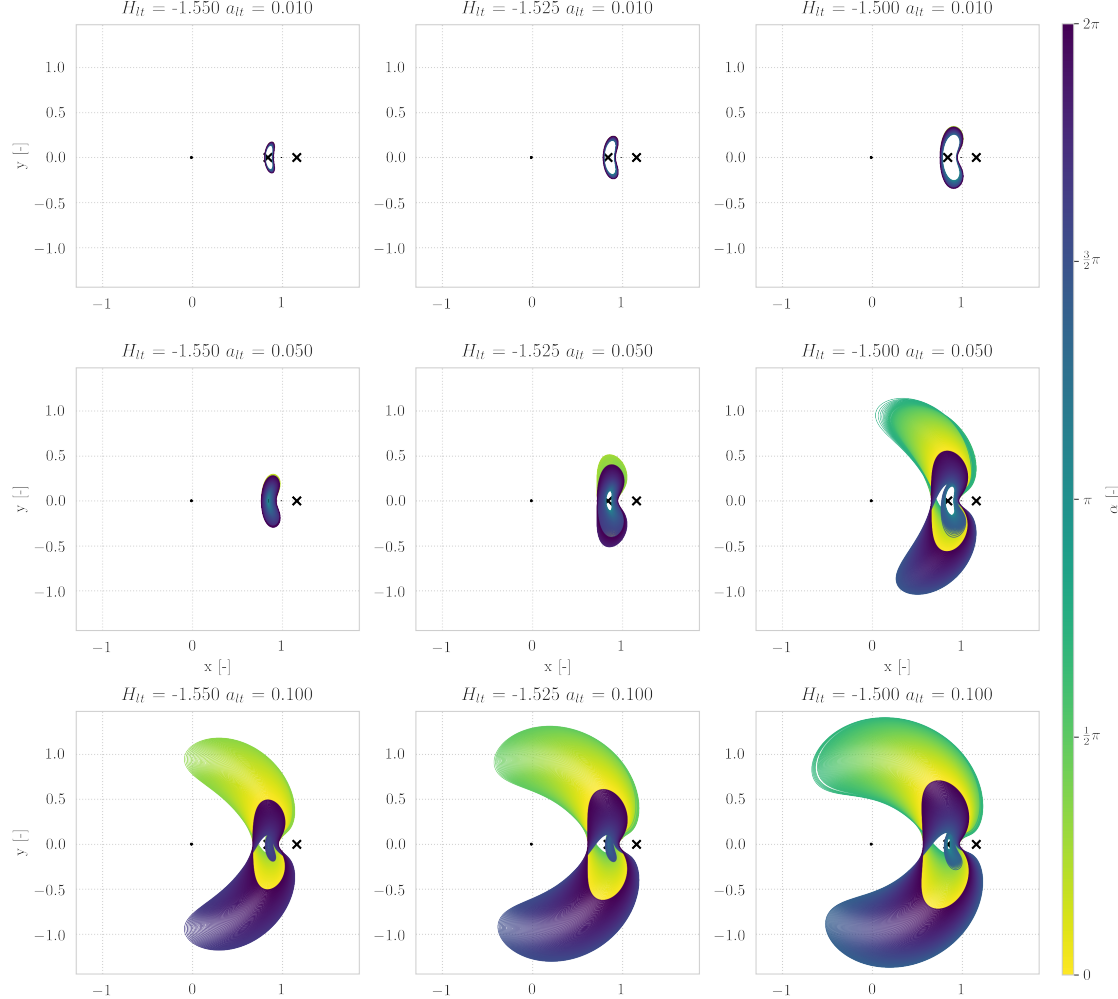


Figure 32. Nine α -varying families at different a_{lt} and H_{lt} values emanating from E_1 . The colour of an I.p.o corresponds to its acceleration magnitude according to the colourbar provided on the right side of the Figure. The asymmetry observed in the middle right and bottom subplots is caused by instabilities in the continuation procedure

The planar projections in Figure 32 confirm the observation from the a_{lt} -varying family subsection that the geometry distortion is proportional to acceleration magnitude. It can also be observed that geometry distortion with respect to the ballistic family becomes more extreme at lower Hamiltonian values. This effect even leads to the 'ear-shaped' periodic which can even curve beyond the Earth. The bottom three subplots and the middle right subplot display asymmetric behaviour which

are caused by instabilities of the collocation procedure and are not a feature of the dynamical model. These asymmetries are also clearly visible in Figure 33. However, it is observed that the stability index consistently reaches a maximum at $\alpha = \pi$ which is also the acceleration orientation where the minimum orbital period is observed for each family.

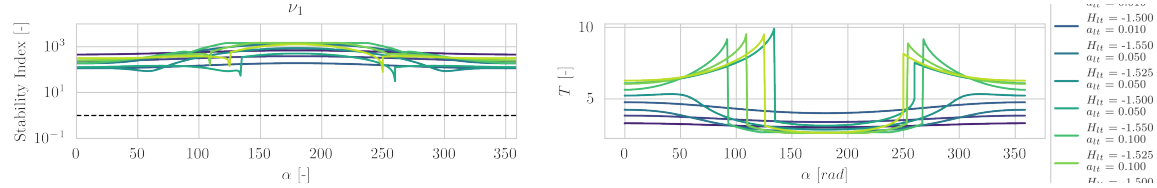


Figure 33. The left subplot displays the stability index of the eigenvalue related the saddle subspace. The right subplot shows evolution of T as a function of a_{lt} .

MISSING RESULTS: The α -varying families of the E_2 contour. These will be added in the final version of the report. The results for these nine families will ultimately be presented at the green light review.

CONCLUSIONS

This paper explores the effect of a constant low-thrust acceleration on the equilibria and Horizontal-Lyapunov orbits in the Earth-Moon CR3BP. These effects can be characterized by investigating the dynamics of a combined multi-body low-thrust model developed in previous work.^{9–11}

The planar low-thrust equilibria, obtained via a multivariate Newton-Rapshon root-finder, show that the low-thrust acceleration vector can significantly shift the position of the low-thrust equilibrium. These translations can cause a qualitative change in the linear stability of the equilibrium and increase (decrease) the rate of hyperbolic unwinding behaviour as the equilibrium moves towards (away from) the secondary body.

Families of low-thrust Horizontal-Lyapunov orbits are constructed via numerical continuation methods that are driven by a 12th order Legendre-Gauss-Lobatto collocation method. Employing the Hamiltonian, acceleration magnitude or acceleration orientation as bifurcation parameter gives rise three family types that allow characterization of their effect on the periodic solution structure in an isolated fashion. A total of thirty-six H_{lt} -varying families have been generated which provide insights on how the geometry, bifurcation behaviour and hyperbolic unwinding behaviour of the ballistic H-L families change due to a low-thrust force. H_{lt} -varying families with collinear thrust do not show any geometry distortions with respect to the ballistic Horizontal-Lyapunov families but this cannot be said for families with non-collinear acceleration orientations. These geometry distortions are proportional with the Hamiltonian and acceleration magnitude and can be so extreme that they result in 'ear-shaped' low-thrust periodic solutions. Analysis of the bifurcation behaviour reveals the existence of low-thrust Halo and Axial periodic solutions for all H_{lt} -varying families. H_{lt} -varying families with $a_{lt} = 0.01$ show identical bifurcation behaviour with respect to the ballistic orbits but additional cyclic fold and period doubling bifurcations are observed at higher acceleration magnitudes. The Saddle stability indices of the H_{lt} -varying families show that maximum hyperbolic unwinding behaviour is consistently found at the periodic solution closest to the equilibrium.

Analysis of the a_{lt} -varying families confirm that the geometry distortion is proportional to the acceleration orientation and heavily depends upon its orientation. A positive collinear acceleration orientation is associated with an increase in amplitude while the opposite orientation is associated

with a decrease in amplitude. This is confirmed by inspection of the α -varying families which show that the maximum geometry distortion occurs between $\alpha = [TBD, TBD]$. Finally, the Saddle stability indices of the a_{lt} -varying families and α -varying families show that unwinding behaviour grows with an increase in acceleration magnitude but that this increase is not necessarily monotonic depending upon the acceleration orientation. The maximum unwinding behaviour at the α -varying families is consistently observed at libration point orbits whose equilibrium point is located in closest proximity to the secondary body.

The families of low-thrust periodic solutions provided in this paper allow initial characterization of the effect of a low-thrust acceleration on Horizontal-Lyapunov orbits in the Earth-Moon system. These families only scratch the surface of the vast low-thrust periodic solution structure of the Earth-Moon CR3BP-LT. Improved continuation algorithms are needed to further explore the vast low-thrust periodic solution of the CR3BP-LT.

NOTATION

α	In-plane angle of the low-thrust acceleration vector	(rad)
β	Out-of-plane angle of the low-thrust acceleration vector	(rad)
θ	In-plane rotation angle between inertial and synodic reference frame	(rad)
κ	Angle between positive x -axis of synodic frame and r_{13} vector	(rad)
λ	Eigenvalue	(–)
μ	Mass ratio parameter of the CR3BP(-LT)	(–)
ν	Stability index	
Φ	State transition matrix	(–)
Ω	Pseudo-potential	(–)
\bar{A}	State propagation matrix	(–)
\bar{a}_{lt}	Acceleration vector	(–)
a_{lt}	Dimensionless acceleration magnitude	(–)
C	Jacobi integral	(–)
E_i	Equilibria contour	(–)
F	Dimensional thrust force	(kN)
f	Dimensionless thrust force	(N)
g_0	Gravitational acceleration at sea-level	(s)
H	Hamiltonian	(–)
\bar{I}	Identity matrix	(–)
I_{sp}	Specific impulse	(s)
L_i	Lagrangian point i of the CR3BP	(–)
l_*	Characteristic length of CR3BP(-LT)	(km)
M_i	Dimensional mass of body i	(kg)
m	Dimensionless mass of P_3	(–)
P_i	Body in the three-body problem	(–)
r_{ij}	Position vector from body i to body j	(–)
T	Orbital period	(–)
t_*	Characteristic time of the CR3BP-(LT)	(s)
\bar{u}	Acceleration orientation vector	(–)
V	Velocity magnitude in the rotating frame	(–)

x, y, z	synodic reference frame position coordinates	(–)
X, Y, Z	Inertial reference frame position coordinates	(–)
$_{eq}$	Equilibrium	
$_{lt}$	Low-thrust	
$_{nat}$	Natural	
x, y, z	Partial derivative with respect to the synodic position coordinates	
\cdot	First time derivative	
$\cdot\cdot$	Second time derivative	
CR3BP	Circular restricted three-body problem	
CR3BP-LT	Low-thrust circular restricted three-body problem	
SPM	State propagation matrix	
ZAC	Zero acceleration contour	

APPENDIX A: LOW-THRUST PROPULSION SYSTEM CHARACTERISTICS

This research considers dimensionless thrust magnitudes $f \in [0.0, 0.1]$ since this is in line with the capabilities of current low-thrust propulsion technology as shown in Table 3.

Table 3. Overview of today's state of low-thrust propulsion technology.

Spacecraft	Propulsion type	F (mN)	$M_{3,0}$ (kg)	f (–)	I_{sp} (s)	\dot{m} (–)
Deep Space ³⁰	Ion thruster	92.0	486	$6.95 \cdot 10^{-2}$	1900 - 3200	$2.61 \cdot 10^{-3}$
Hayabusa ³¹	Ion thruster	72.0	510	$5.17 \cdot 10^{-2}$	2760 - 3000	$1.94 \cdot 10^{-3}$
Hayabusa 2 ³²	Ion thruster	84.0	609	$1.73 \cdot 10^{-2}$	2400 - 2750	$1.90 \cdot 10^{-3}$
Dawn ³³	Ion thruster	92.7	1218	$2.79 \cdot 10^{-2}$	1740 - 3065	$1.04 \cdot 10^{-3}$
NEXT ³⁴	Ion thruster	236	1218	$7.10 \cdot 10^{-2}$	4190	$2.67 \cdot 10^{-3}$
Lunar Icecube ³⁵	Ion thruster	1.0	14	$2.62 \cdot 10^{-2}$	2500	$1.50 \cdot 10^{-4}$
SMART-I ³⁶	Ion thruster	70.0	350	$7.33 \cdot 10^{-2}$	1600	$2.75 \cdot 10^{-3}$
Sunjammer ³⁷	Solar sailing	8.0	32	$9.16 \cdot 10^{-2}$	not applicable	

The Table presented above allows the reader to get an idea of the kind of propulsion systems involved in this study. Looking at the specific impulse column, it can be observed that some missions have a range of possible specific impulses whereas some missions have a fixed specific impulse. This can be addressed to the fact that some propulsion systems have a throttling capability. This addendum is concluded with the note that parts of Table 3 have been obtained from.¹¹

REFERENCES

- [1] R. Bonnet and F. Felici, “Overview of the SOHO mission,” *Advances in Space Research*, Vol. 20, No. 12, 1997. doi: [https://doi.org/10.1016/S0273-1177\(97\)00894-6](https://doi.org/10.1016/S0273-1177(97)00894-6).
- [2] J. Tauber, “The Planck mission,” *Advances in Space Research*, Vol. 34, No. 3, 2004. doi: <https://doi.org/10.1016/j.asr.2003.05.025>.
- [3] R. Whitley and R. Martinez, “Options for staging orbits in cislunar space,” *IEEE Aerospace Conference*, 2016. doi: [10.1109/AERO.2016.7500635](https://doi.org/10.1109/AERO.2016.7500635).
- [4] M. Ozimek and K. H. D. Grebow, “Solar Sails and Lunar South Pole Coverage,” *AIAA/AAS Astrodynamics Specialist Conference*, Honolulu, Hawaii, 2008. doi: <https://doi.org/10.2514/6.2008-7080>.
- [5] E. Doedel, V. Romanov, R. Paffenroth, H. Keller, D. Dichmann, J. Gálán, and A. Vanderbauwhede, “Elemental periodic orbits associated with the libration points in the circular restricted

3-body problem," *International Journal of Bifurcation and Chaos*, Vol. 18, No. 7, 2011. - DOI: 10.1142/S0218127407018671.

- [6] W. Koon, M. Lo, J. Marsden, and S. Ross, *Dynamical Systems, The Three-Body Problem and Space Mission Design*. New-York: Springer-Verlag, 2007. - ISBN: 978-0387495156.
- [7] P. Verrier, T. Waters, and J. Sieber, "Evolution of the L1 Halo family in the radial solar sail CRTBP," *Celestial Mechanics and Dynamical Astronomy*, Vol. 120, No. 4, 2014. doi: 10.1007/s10569-014-9575-2.
- [8] J. Heiligers, M. Macdonald, and J. Parker, "Extension of Earth-Moon libration point orbits with solar sail propulsion," *Astrophysics and Space Science*, Vol. 361, 2016. DOI: 10.1007/s10509-016-2783-3.
- [9] A. Cox, K. Howell, and D. Folta, "Dynamical Structures in a Combined Low-Thrust Multi-Body Environment," *Advances in the Astronautical Sciences Series*, Vol. 162, 2017. ISBN: 978-0-87703-646-3.
- [10] D. F. A. Cox, K. Howell, "Transit and Capture in the Planar Three-Body Problem Leveraging Low-Thrust Dynamical Structures," *AAS/AIAA Space Flight Mechanics Conference*, Honolulu Hawaii, jan 2019.
- [11] A. Cox, K. Howell, and D. Folta, "Dynamical structures in a low-thrust, multi-body model with applications to trajectory design," *Celestial Mechanics and Dynamical Astronomy*, Vol. 131, feb 2019.
- [12] V. Szebehely, *Theory of Orbits*. Academic Press, 1967. - ISBN: 978-0-12-395732-0.
- [13] K. Kumar, Y. Abdulkadir, P. Barneveld, F. Belien, S. Billemont, E. Brandon, M. Dijkstra, D. Dirkx, F. Engelen, D. Gondelach, L. Ham, E. Heeren, E. Iorfida, E. Leloux, J. Melman, E. Mooij, P. Musegaas, R. Noomen, S. Persson, B. Romgens, A. Ronse, T. Secretin, B. Tong-Minh, and J. Vandamme, "Tudat: a modular and robust astrodynamics Toolbox.," *Fifth ICATT, International Conference on Astrodynamics Tools and Techniques*, 2012, pp. 1-8.
- [14] K. Wakker, *Fundamentals of Astrodynamics*. TU Delft Library, 2015. - ISBN: 978-94-6186-419-2.
- [15] E. Ott, *Chaos in Dynamical Systems*. Cambridge University Press, 1993. - ISBN: 978-0521010849.
- [16] G. Gómez, W. Koon, M. Lo, J. Marsden, J. Masdemont, and S. Ross, "Connecting orbits and invariant manifolds in the spatial restricted three-body problem," *Nonlinearity*, Vol. 17, No. 5, 2004. DOI: <https://doi.org/10.1088/0951-7715/17/5/002>.
- [17] C. Kelley, *Solving Nonlinear Equations with Newton's method*. Philadelphia: Society for Industrial and Applied Mathematics, 2003. - ISBN: 0-89871-546-6.
- [18] E. Zimovan-Spreem, K. Howell, and D. Davis, "Near Rectilinear Halo Orbits and Their Application in Cis-Lunar Space," *3rd International Academy of Astronautics Conference on Dynamics and Control of Space Systems*, Moscow, Russia, 2017.
- [19] C. Goudas, "Three-dimensional periodic orbits and their stability," *Icarus*, Vol. 2, 1963, pp. 1–18. doi: [https://doi.org/10.1016/0019-1035\(63\)90003-4](https://doi.org/10.1016/0019-1035(63)90003-4).
- [20] D. Dichmann, E. Doedel, , and R. Paffenroth, "The Computation of Periodic Solutions of the 3-Body Using Numerical Continuation Software AUTO," *Libration Point Orbits and Applications*, 2002. ISBN: 978-981-238-361-1.
- [21] K. Howell and T. Keeter, "Station-keeping strategies for libration point orbits—target point and Floquet mode approaches.," *Advances in the Astronautical Sciences*, Vol. 89, 1995, pp. 1377–1396.
- [22] K. Howell and B. Marchand, "Natural and non-natural spacecraft formations near the L1 and L2 libration points in the Sun–Earth/Moon ephemeris system," *Dynamical Systems: An International Journal*, Vol. 201, mar 2005, pp. 149–173. - doi: <https://doi.org/10.1080/1468936042000298224>.
- [23] B. Marchand, K. Howell, and R. Wilson, "An Improved Corrections Process for Constrained Trajectory Design in the n-Body Problem," *Journal of Spacecraft and Rockets*, Vol. 44, No. 4, 2007. - eISSN: 1533-6794.
- [24] K. Howell and H. Pernicka, "Numerical determination of Lissajous trajectories in the restricted three-body problem," *Celestial Mechanics and Dynamical Astronomy*, Vol. 41, No. 1, 1978, pp. 107–124. - ISSN: 0923-2958.
- [25] A. Herman, *Improved collocation methods with application to direct trajectory optimization*. PhD thesis, University of Illinois at Urbana-Champaign, 1995.
- [26] C. d. Boor, "Good Approximation by Splines with Variable Knots," *Spline Functions and Approximation Theory*, 1973. ISBN: 978-3-0348-5980-6.
- [27] Y. Kuznetsov, *Elements of Applied Bifurcation Theory*. New-York: Springer-Verlag, 2004. ISBN 978-1-4757-3978-7.
- [28] K. Howell and E. Campbell, "Three-dimensional Periodic Solutions that Bifurcate from Halo families in the Circular Restricted Three-Body Problem," *AIAA/AAS Astrodynamics Specialist Conference*, 1998.
- [29] J. Howard and E. Mackay, "Linear stability of symplectic maps," *Journal of Mathematical Physics*, Vol. 28, 1987. - doi: <https://doi.org/10.1063/1.527544>.

- [30] M. Rayman, P. Vargese, D. Lehman, and L. Livesay, “Results From The Deep Space 1 Technology Validation Mission,” *Acta Astronautica*, Vol. 47, 2000, pp. 475–478. doi: [https://doi.org/10.1016/S0094-5765\(00\)00087-4](https://doi.org/10.1016/S0094-5765(00)00087-4).
- [31] H. Kuninaka, K. Nishiyama, Y. Shmimizy, I. Funaki, and H. Koizumi, “Hayabusa Asteroid Explorer Powered by Ion Engines on the Way to Earth,” *The 31st International Electric Propulsion Conference*, 2009.
- [32] K. Nishiyama, S. Hosoda, K. Ueno, and H. Kuninaka, “The Ion Engine System for Hayabusa2,” *32nd International Electric Propulsion Conference*, 2011.
- [33] C. Russell and C. Raymond, *The Dawn Mission to Minor Planets 4 Vesta and 1 Ceres*. New York: Springer-Verlag, 2012. ISBN: 978-1-4614-4902-7.
- [34] G. Schmidt, M. Patterson, and S. Benson, “The Nasa Evolutionary Xenon Thruster (NEXT): The Next Step For U.S. Deep Space Propulsion,” *International Astronautical Congress*, 2008.
- [35] N. Bosanac, A. Cox, K. Howell, and D. Folta, “Trajectory design for a cislunar CubeSat leveraging dynamical systems techniques: The Lunar IceCube mission,” *Acta Astronautica*, Vol. 144, 2018. doi: <https://doi.org/10.1016/j.actaastro.2017.12.025>.
- [36] R. Mackenzie, D. Salvador, and D. Miligan, “Orbit Determination of the SMART-1 Mission,” *Proceedings of the 18th International Symposium on Space Flight Dynamics*, 2004.
- [37] M. Macdonald, *Advances in Solar Sailing*. Berlin: Springer-Verlag, 2014. ISBN: 978-3-642-34906-5.

A

Physical constants and algorithm parameters

This adjunct presents all constants and parameters that have been used to produce the work in Part 1 of this thesis report. Section A.1 discusses all constants that define the dynamics of the physical model while Section A.2 presents the settings of the algorithm that have been used to create the equilibria contours and libration point orbit (l.p.o) families. In case the reader wishes to reproduce the results in the TU Delft Astrodynamics Toolbox (TUDAT) development environment[12], the reader is advised to contact the author or thesis supervisor for a complete copy of the code¹. Given that the reader wishes to reproduce the results outside the TUDAT environment, the remainder of this Chapter provides an exhaustive list of the constants and parameters used in this thesis project.

A.1. Physical constants

The low-thrust circular restricted three-body problem (CR3BP-LT) model is a combination of the natural circular restricted three-body problem (CR3BP) and a low-thrust force. The CR3BP is fully defined by the mass ratio parameter, which can be computed with Equation A.1.

$$\mu = \frac{\mu_{Moon}}{\mu_{Earth} + \mu_{Moon}} \quad (\text{A.1})$$

The symbols on the right hand side denote the gravitational parameters of the primary and secondary body. The values of these parameters are listed in Table A.1.

Due to the presence of a low-thrust force in the CR3BP-LT, three additional physical constant and propulsion system characteristics are required to fully parametrize the dynamical model. Two of these parameters are the characteristic length, (i.e. semi-major axis) and characteristic time (i.e. inverse of the system's mean motion). The latter follows directly from the former via Kepler's Third law, shown below in Equation A.2.

$$t_* = \sqrt{\frac{l_*^3}{\mu_{Earth} + \mu_{Moon}}} \quad (\text{A.2})$$

The final physical constant is the gravitational acceleration at sea-level. The values of these three physical constants can be found in Table A.1 and have been obtained directly from TUDAT and [24]. It should be emphasized that propulsion system characteristics of the spacecraft are also necessary to parametrize the CR3BP-LT model. These variables are regarded as mission-specific variables rather than fundamental physical constants of the CR3BP-LT model. An overview of the adopted propulsion system characteristics can be found in Chapter 1 of this report.

¹S.H.F. Martens: shfmartens@gmail.com

Symbol	Description	Value	Unit
μ	Mass ratio parameter	1.2150581017337	$\cdot 10^{-2}$
μ_{Earth}	Earth gravitational parameter	3.986004418	$\cdot 10^{14}$
μ_{Moon}	Moon gravitational parameter	4.9027988158612	$\cdot 10^{12}$
l_*	Characteristic length	3.84400	$\cdot 10^5$
t_*	Characteristic time	4.354369171925	—
g_0	Gravitational acceleration at sea-level	9.80665	$[m \cdot s^{-2}]$

Table A.1: Fundamental physical constants that define Earth-Moon CR3BP-LT model. All values have been directly adopted from TUDAT or [24].

A common approach to simplify analysis in multi-body models like the Cr3BP-LT is nondimensionalization of the system. For the CR3BP-LT, this is achieved by setting the distance between the two primaries to unity and the synodic period equal to 2π . The disadvantage of nondimensionalization is that results can be difficult to interpret. Hence Table A.2 is provides a relation between the dimensional and dimensionless values.

Symbol	Description	Value	Unit	Dimensionless Value
x	Position	3.84400	$\cdot 10^5$	$[km]$
t	Time	2.7359308403075	$\cdot 10^1$	$[days]$
\dot{x}	Velocity	1.0245468537379	—	$[km \cdot s^{-1}]$

Table A.2: A representation of the dimensionless quantities of position, time, and velocity in the Earth-Moon CR3BP-LT.

The constants summarized in Table A.1 and A.2 fully establish CR3BP-LT dynamical model.

A.2. Algorithm settings for orbit generation

The results presented in Part 1 of this report have been obtained by employing techniques with specific settings. This section provides an exhaustive overview of the adopted settings of these numerical methods.

A.2.1. Integrator settings

The Runge-Kutta-Fehlberg 7(8) (RKF78) method is one of two numerical integration techniques that have been deployed in this thesis project. The RKF78 is an essential techniques in this work since it is used in every step of the construction of l.p.o families. An extensive discussion on the fundamentals of this technique can be found in Appendix B. TUDAT is equipped with a RKF78 integrator so the user is only concerned with selection of the integrator settings. Both the integrator settings and the integrator overshoot procedure are based on the work of [24] and are shown in Table A.3. These settings have proven to allow the construction the l.p.o families in the CR3BP with near machine-precision.

Symbol	Value	Unit	Description
h_0	1.0	$\cdot 10^{-5}$	Initial step-size
h_{min}	ϵ_m	[-]	Minimum step-size
h_{max}	1.0	$\cdot 10^{-4}$	Maximum step-size
ϵ_{abs}	1.0	$\cdot 10^{-24}$	Absolute error tolerance
ϵ_{rel}	ϵ_m	$\cdot 10^2$	Relative error tolerance
Overshoot procedure			
i	$6.0 - 12.0$	[-]	Step size control parameter
h_{min}	1.0	$\cdot 10^{-i}$	Minimum step-size
h_{max}	1.0	$\cdot 10^{-i+1}$	Maximum step-size

Table A.3: Parameter settings for the RKF7(8) Integrator used for propagation in the dynamical model. Obtained from [24].

The Table above ϵ_m denotes the machine epsilon. This variable is defined as the smallest quantity that can be added to number such that the machine interprets it as another number [2]. It's value is given below in Equation A.3

$$\epsilon_m \approx 2.2204460492503 \cdot 10^{-16} \quad (\text{A.3})$$

A 12th order Legendre-Gauss-Lobatto (LGL) collocation scheme is the other numerical integration method that is adopted in this thesis project. An extensive discussion on this method is provided in Appendix B. Contrary to the RK7(8) procedure, this method is built from scratch and the parameter settings, obtained via a trial-and-error procedure, are shown below in Table A.4.

Symbol	Value	Unit	Description
	5	[–]	Initial number of nodes
$e_{i_{max}}$	1.0	$\cdot 10^{-9}$	Maximum error tolerance per segment
Δe_i	1.0	$\cdot 10^{-12}$	Error equidistribution criterium

Table A.4: Parameter settings for the 12th order Legendre Gauss Lobatto collocation methods used for the generation of the l.p.o families

A.2.2. Settings for equilibria generation

The construction of the equilibria contours relies on the multivariate Newton-Raphson (NR) root-finding method. An elaborate discussion on this method is provided in Appendix C. The root-finding procedure parameters have been determined via a trial-and-error procedure and result in robust performance while Equation A.4 is satisfied.

$$a_{lt} \leq 0.25 \quad (\text{A.4})$$

Symbol	Value	Unit	Description
ω	2.0	$\cdot 10^{-1}$	Relaxation parameter
	1.0	$\cdot 10^5$	Maximum number of univariate NR iterations
	8.0	$\cdot 10^4$	Maximum number of multivariate NR iterations
	1.0	$\cdot 10^{-13}$	Maximum potential deviation
$\Delta\alpha$	1.0	$\cdot 10^{-2}$	Step size angle contour
	1.0	$\cdot 10^{-5}$	Step size acceleration contour
Δa_{lt}	10	[–]	Save frequency
	0.1	[–]	Upper acceleration limit
	$\ \alpha_{start} - \alpha\ < 2\pi$	[rad]	Angle stopping condition

Table A.5: Parameter settings for the multivariate root-finding procedure used for computation of the low-thrust equilibria points

A.2.3. Settings for orbit generation

The methodology of constructing the l.p.o families is achieved via a three-step approach as explained in Chapter 1 of this report. The first step concerns the generation of the approximate seed solutions via a Floquet Controller (FC). A detailed discussion and performance analysis of this technique is presented in Appendix C. Its parameters have been determined via a trial-and-error procedure which result in robust performance for in-plane amplitudes values far beyond the required amplitude of the seed solutions. The values of these parameters are shown below in Table A.6.

Symbol	Value	Unit	Description
A_x	1.0	$\cdot 10^{-5}$	Amplitude for first approximate solution
A_x	1.0	$\cdot 10^{-4}$	Amplitude for second approximate solution
	1.0	$\cdot 10^{-13}$	Numerical threshold for motion decomposition
	5.0	$\cdot 10^{-2}$	Time interval between two FC corrections
	1.0	$\cdot 10^{-6}$	Maximum eigenvalue deviation
	1000	[–]	Save frequency

Table A.6: Parameter settings for the Floquet targeter used for computation of the approximate seed solutions of the l.p.o families

The second step in construction of l.p.o families concerns the refinement of the initial guess constructions via a multiple-shooting approach known as the two-level targeter (TLT). An extensive discussion on the workings and performance of this method can be found in Appendix C. The values of the parameters involved in TLT procedure are shown below in Table A.7.

Value	Unit	Description
5	[–]	Number of patch points
10	[–]	Maximum Number of TLT Cycles
1.0	$\cdot 10^{-12}$ [–]	Maximum position deviation
5.0	$\cdot 10^{-12}$ [–]	Maximum velocity deviation
1.0	$\cdot 10^{-12}$ [–]	Maximum period deviation
1000	[–]	Save frequency

Table A.7: Paremeter settings for the TLT algorithm used for the refinement of the approximate seed solutions

The continuation procedure concerns the final step in the construction of the l.p.o families. The parameters of the continuation procedure are shown below in Table A.8 and have been established via a trial-and-error procedure.

Symbol	Value	Unit	Description
	5.0	$\cdot 10^3$ [–]	Maximum number of family members
	1.0	$\cdot 10^{-4}$ [–]	Pseudo-arc length H_{lt} -varying family
Δa_{lt}	1.0	$\cdot 10^{-2}$ [–]	Increment a_{lt} -varying family
$\Delta \alpha$	1.0	$\cdot 10^{-1}$ [–]	Increment α -varying family
κ	[0.1, 0.2, ..., 1.0]	[–]	Line search attenuation parameter
ϵ	1.0	$\cdot 10^{-10}$ [–]	Complex step increment
$\ \mathbf{F}\ $	1.0	$\cdot 10^{-12}$ [–]	Maximum defect vector magnitude
	5.0	$\cdot 10^3$ [–]	Maximum Number of collocation iterations
	1.0	$\cdot 10^{-3}$ [–]	Maximum center eigenvalue deviation
	1.0	$\cdot 10^{-3}$ [–]	Maximum eigensystem determinant deviation
	1.0	$\cdot 10^{-5}$ [-]	Minimum spacing between family members at half-phase
	1.0	$\cdot 10^{-3}$ [-]	Maximum pseudo-arclength before termination
	1.0	$\cdot 10^{-9}$ [-]	Maximum state component discrepancy at full-period

Table A.8: Parameter settings for the continuation procedure of all three types of l.p.o families

The table above completes the set of constants and parameters used in the thesis project. The tables A.1-A.8 allow the reader the reproduce the totality of the results presented in this thesis report.

B

Numerical Integration

This Appendix provides a discussion on the techniques that are used for trajectory propagation in the CR3BP-LT. The propagation of trajectories requires one to find a solution to a set of differential equations subjected to various constraints [22]. In literature, this commonly referred to as a Boundary Value Problem (BVP). Numerical integrators are able to solve these systems of differential equations and two of them are adopted in this thesis project. The remainder of this Addendum presents the principles of both integrators. Section B.1 discusses the fundamentals of the RKF78 integrator while Section B.2 presents the principles of the 12th order Legendre-Gauss-Lobatto collocation method.

B.1. Runge-Kutta Fehlberg 7(8) method

The RKF7(8) integrator belongs to the family of Runge-Kutta methods. These methods are widely used in the scientific community because of their simplicity and capability to straightforwardly control the truncation error [3]. The RKF7(8) integration procedure is a so-called explicit Runge-Kutta method since it uses the current state of the system to approximate the system's solution at another state. The principles of the RK78 method are illustrated on the basis of the system depicted in Equation B.1.

$$\dot{y} = f(x, y), \quad y(x_n) = Y_n, \quad x_{n+1} - x_n = h \quad (\text{B.1})$$

The system's solution (y_n) is known at a particular location (x_n). Suppose one is interested in the solution at a new location x_{n+1} which is separated from x_{n-1} by a distance h , commonly referred to as the step size. Explicit Runge-Kutta methods compute the solution at the new location according to Equation B.2.

$$y_{n+1} = y_n + hF(x_n, y_n, h; f) \quad (\text{B.2})$$

It can be observed that the core principle of Runge-Kutta methods is the approximation of the average slope over the specified increment. This is achieved by computing a weighted averages of slopes at different locations within the increment interval. The procedure for computing the weighted average slope is shown in Equations B.3-B.5 and involves a set of nodes (Z_j) with associated external weights (γ_j). The number of function evaluations per integration step (s) is referred to as stages. For a s-stage Runge-Kutta method, the location of the nodes and their respective weights are fixed on the increment interval.

$$F(x_n, y_n, h; f) = \sum_{j=1}^s \gamma_j Z_j \quad (\text{B.3})$$

$$Z_1 = f(x_n, y_n) \quad (\text{B.4})$$

$$Z_j = f(x + \alpha_j h, y + \sum_i^{j-1} \beta_{ij} Z_i) \quad j = 2, \dots, s \quad (\text{B.5})$$

For sake of accuracy, it is desirable that the local truncation error is constant for each step of the integration process. Embedded Runge-Kutta-Fehlberg methods provide an error estimate by comparing the computed solution of an Runge-Kutta method accurate up to order p with the answer obtained by a Runge-Kutta

method accurate up to order $p+1$. This error estimate can be obtained with little extra computation cost since the higher order method uses the same function evaluations as the lower order method. The RKF7(8) method belongs to this category of Runge-Kutta methods and the exact procedure can be described in a so-called Butcher tableau which is presented below in Table B.1.

α_j	1	2	3	4	5	β_{ij}	6	7	8	9	10	11	12	γ_j	$\hat{\gamma}_j$
0														41/840	0
2/27	2/27													0	0
1/9	1/36	1/12												0	0
1/6	1/24	0	1/8											0	0
5/12	5/12	0	-25/16	25/16										0	0
1/2	1/20	0	0	1/4	1/5									34/105	34/105
5/6	-25/108	0	0	125/108	-65/27	125/54								9/35	9/35
1/6	31/300	0	0	0	61/225	-2/9	13/900							9/35	9/35
2/3	2	0	0	-53/6	704/45	-107/9	67/90	3						9/280	9/280
1/3	-91/108	0	0	23/108	-976/135	311/54	-19/60	17/6	-1/12					9/280	9/280
1	2383/4100	0	0	-341/161	4496/1025	-301/82	2133/4100	45/82	45/164	18/4				41/840	0
0	3/205	0	0	0	0	-6/41	-3/205	-3/41	3/41	6/41	0			0	41/840
1	-1777/4100	0	0	-341/161	4496/1025	-289/82	2193/4100	51/82	33/164	12/41	0	1		0	41/840

Table B.1: The Butcher tableau of the RKF7(8) method as presented in [11]. External weights of the higher order are indicated by $\hat{\gamma}_j$

The difference between the two solutions produced by the p^{th} and $(p+1)^{th}$ order method, provides an estimate of the truncation error ($e(h_i)$). This error estimate together with the error (ϵ_{tol}) tolerance allows adaption of the step size. The step size adaption procedure is outlined in Equation B.6 [27]. The largest of the absolute and relative error provides the error tolerance for the step size adaption procedure. The integration process is repeated with the new step size ($e^*(h_i)$) until the error criteria are satisfied. This procedure leads to a consistent truncation error over the complete integration process.

$$\begin{aligned} e(h_i) &= |\hat{y}_i - y_i| \\ h_i^* &= \sqrt[p+1]{\frac{\epsilon_{tol}}{e(h_i)}} \cdot h_i \end{aligned} \quad (\text{B.6})$$

The methodology outlined in this Section establishes the numerical integration process that is leveraged in the approximation and refinement of the seed solutions for the l.p.o families as well as the verification of the periodic solutions.

B.2. 12th order Legendre-Gauss-Lobatto collocation method

The other numerical integration technique deployed in this thesis is the 12th order Legendre-Gauss-Lobatto collocation method. Subsection B.2.1 explains underlying process of collocation, while Subsection B.2.2 explains the methodology for error control.

B.2.1. Numerical integration through Gauss-Legendre-Lobatto quadrature

Collocation methods approximate the solution to an ordinary differential equation from a set of states via polynomial interpolation. For purpose of illustration, consider the system depicted in Equation B.7 [32]. This problem concerns the identification of a solution to an ordinary differential equation over the time interval $[t_{n-1}, t_n]$ separated by a time increment (h).

$$\begin{aligned} \dot{y} &= f(x, y), \text{ given a set of solutions } y(t_1), y(t_2), \dots, y(t_s) \\ t_i &= t_{n-1} + c_i h, \quad 0 \leq c_1 < c_2 < \dots < c_s \leq 1 \end{aligned} \quad (\text{B.7})$$

The goal of the collocation method is to find a polynomial ϕ up to a degree s which satisfies conditions listed below in Equation B.8. When these conditions are satisfied, the solution to the system in Equation B.7 is known on the entire segment $[t_{n-1}, t_n]$. The reliance of collocation methods on a reference trajectory show that collocation methods are implicit in nature [32].

$$\begin{aligned} \phi(t_{n-1}) &= y_{n-1} \\ \dot{\phi}(t_i) &= f(t_i, \phi(t_i)) \end{aligned} \quad (\text{B.8})$$

Collocation methods are characterized by the way collocation points are distributed over a segment of the reference trajectory. The distribution over a single segment is referred to as the node placement strategy. The node placement strategy of the 12th order Legendre-Gauss-Lobatto collocation method uses seven collocation points. Four of these points are used to construct a seventh order polynomial. The remaining three points are referred to as defect points. At these locations, it is checked whether the dynamics of the polynomial corresponds to the dynamics of the defect points. The thesis project implements collocation by discretizing a reference trajectory into n nodes, resulting in $n - 1$ segments. An illustration of this discretization procedure, together with the 12th order Legendre-Gauss-Lobatto node placement strategy is shown in Figure B.1.

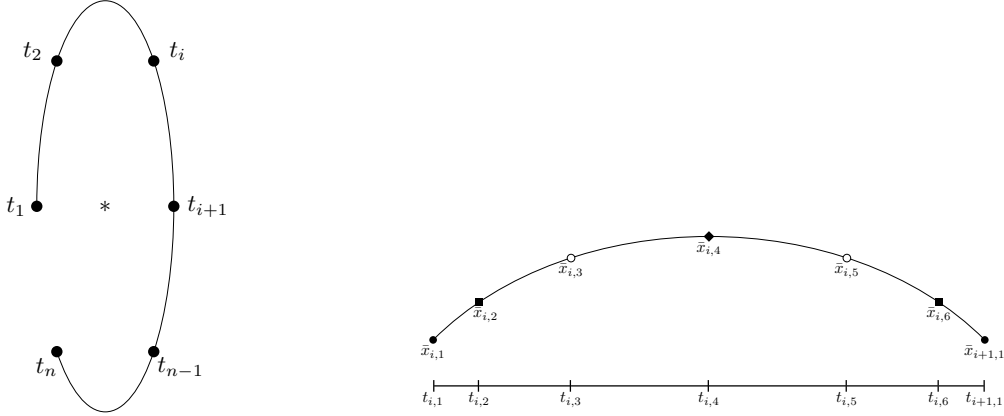


Figure B.1: The left figure shows the discretization of the trajectory into $n - 1$ segments. The right picture shows how a seventh degree polynomial is constructed for a single segment. The bounds of the segment, denoted with black circles, together with the interior points, symbolized by white circles, are used to construct the polynomial. The locations of the defect points are indicated by the black diamonds.

The node placement strategy is defined by the normalized time values of the collocation points. These values for the 12th order Legendre-Gauss-Lobatto collocation method can be found in Table B.2 [14].

node time symbol	normalized time symbol	normalized time value	node type
$t_{i,1}$	τ_1	0	node
$t_{i,2}$	τ_2	8.4888051860717	defect point
$t_{i,3}$	τ_3	2.65575603264643	interior point
$t_{i,4}$	τ_4	5.0	defect point
$t_{i,5}$	τ_5	7.34424396735357	interior point
$t_{i,6}$	τ_6	9.15111948139284	defect point
$t_{i+1,1}$	τ_7	1.0	node

Table B.2: The normalized time values characterizing the node placement strategy of the 12th order Legendre-Gauss-Lobatto collocation method. Values reproduced from [14].

Polynomial interpolation allows the computation of the solution on the entire segment interval via Equation B.9.

$$\bar{x}(\tau) = \mathbf{p}_i(\tau) = C_i \cdot [1 \quad \tau \quad \tau^2 \quad \tau^3 \quad \tau^4 \quad \tau^5 \quad \tau^6 \quad \tau^7]^T \quad \text{on } [t_i, t_{i+1}], \quad 0 \leq \tau \leq 1 \quad (\text{B.9})$$

The piecewise polynomial is defined by the coefficient matrix C_i , which depends upon a constant matrix (B), shown in Equation B.11, the time duration of the segment (Δt), states \bar{x}_i and field vector evaluation ($\bar{f}(\bar{x}_i)$). The coefficient matrix can be computed through Equation B.10.

$$C_i = \begin{bmatrix} \bar{x}_{i,1} & \bar{x}_{i,3} & \bar{x}_{i,5} & \bar{x}_{i+1,1} & \bar{x}'_{i,1} & \bar{x}'_{i,3} & \bar{x}'_{i,5} & \bar{x}'_{i+1,1} \end{bmatrix} \cdot B_i^{-1} \quad \text{where } \bar{x}'_i = \Delta t_i \cdot \bar{f}(\bar{x}_i) \quad (\text{B.10})$$

$$B_i = \begin{bmatrix} 1 & 1 & 1 & 1 & 0 & 0 & 0 & 0 \\ \tau_1 & \tau_3 & \tau_5 & \tau_7 & 1 & 1 & 1 & 1 \\ \tau_1^2 & \tau_3^2 & \tau_5^2 & \tau_7^2 & 2\tau_1 & 2\tau_3 & 2\tau_5 & 2\tau_7 \\ \tau_1^3 & \tau_3^3 & \tau_5^3 & \tau_7^3 & 3\tau_1^2 & 3\tau_3^2 & 3\tau_5^2 & 3\tau_7^2 \\ \tau_1^4 & \tau_3^4 & \tau_5^4 & \tau_7^4 & 4\tau_1^3 & 4\tau_3^3 & 4\tau_5^3 & 4\tau_7^3 \\ \tau_1^5 & \tau_3^5 & \tau_5^5 & \tau_7^5 & 5\tau_1^4 & 5\tau_3^4 & 5\tau_5^4 & 5\tau_7^4 \\ \tau_1^6 & \tau_3^6 & \tau_5^6 & \tau_7^6 & 6\tau_1^5 & 6\tau_3^5 & 6\tau_5^5 & 6\tau_7^5 \\ \tau_1^7 & \tau_3^7 & \tau_5^7 & \tau_7^7 & 7\tau_1^6 & 7\tau_3^6 & 7\tau_5^6 & 7\tau_7^6 \end{bmatrix} \quad (B.11)$$

Defect constraints are critical to construct polynomial that correctly approximates the dynamics over the entire interval. These constraints are computed at each defect points according to Equations B.12-B.14.

$$\begin{aligned} \tilde{\zeta}_{i,2} = & b_i^1 \bar{x}_{i,1} + b_{i,3}^1 \bar{x}_{i,3} + b_{i,5}^1 \bar{x}_{i,5} + b_{i+1,1}^1 \bar{x}_{i+1,1} \\ & + \Delta t_i (w_{i,1}^1 \bar{f}_{i,1} + w_{i,2}^1 \bar{f}_{i,2} + w_{i,3}^1 \bar{f}_{i,3} + w_{i,5}^1 \bar{f}_{i,5} + w_{i+1,1}^1 \bar{f}_{i+1,1}) \end{aligned} \quad (B.12)$$

$$\begin{aligned} \tilde{\zeta}_{i,4} = & b_i^c \bar{x}_{i,1} + b_{i,3}^c \bar{x}_{i,3} + b_{i,5}^c \bar{x}_{i,5} + b_{i+1,1}^c \bar{x}_{i+1,1} \\ & + \Delta t_i (w_{i,1}^c \bar{f}_{i,1} + w_{i,3}^c \bar{f}_{i,3} + w_{i,4}^c \bar{f}_{i,4} + w_{i,5}^c \bar{f}_{i,5} + w_{i+1,1}^c \bar{f}_{i+1,1}) \end{aligned} \quad (B.13)$$

$$\begin{aligned} \tilde{\zeta}_{i,6} = & b_i^6 \bar{x}_{i,1} + b_{i,3}^6 \bar{x}_{i,3} + b_{i,5}^6 \bar{x}_{i,5} + b_{i+1,1}^6 \bar{x}_{i+1,1} \\ & + \Delta t_i (w_{i,1}^6 \bar{f}_{i,1} + w_{i,3}^6 \bar{f}_{i,3} + w_{i,5}^6 \bar{f}_{i,5} + w_{i,6}^6 \bar{f}_{i,6} + w_{i+1,1}^6 \bar{f}_{i+1,1}) \end{aligned} \quad (B.14)$$

The values for the constants b_i^j and w_i^j can be found below in Table B.3.

Parameter	Value		Parameter	Value	
b_i^1	+8.84260109348311	$\cdot 10^{-1}$	b_3^1	-8.23622559094327	$\cdot 10^{-1}$
b_5^1	-2.35465327970606	$\cdot 10^{-2}$	b_{i+1}^1	-3.70910174569208	$\cdot 10^{-2}$
b_i^c	+7.86488731947674	$\cdot 10^{-2}$	b_3^c	+8.00076026297266	$\cdot 10^{-1}$
b_5^c	-8.00076026297266	$\cdot 10^{-1}$	b_{i+1}^c	-7.86488731947674	$\cdot 10^{-2}$
b_i^6	+3.70910174569208	$\cdot 10^{-2}$	b_3^6	+2.35465327970606	$\cdot 10^{-2}$
b_5^6	+8.23622559094327	$\cdot 10^{-1}$	b_{i+1}^6	-8.84260109348311	$\cdot 10^{-1}$
$w_{i,1}^1$	+1.62213410652341	$\cdot 10^{-2}$	$w_{i,2}^1$	+1.38413023680783	$\cdot 10^{-1}$
$w_{i,3}^1$	+9.71662045547156	$\cdot 10^{-2}$	$w_{i,5}^1$	+1.85682012187242	$\cdot 10^{-2}$
$w_{i+1,1}^1$	+2.74945307600086	$\cdot 10^{-3}$	$w_{i,1}^c$	+4.83872966828888	$\cdot 10^{-3}$
$w_{i,3}^c$	+1.00138284831491	$\cdot 10^{-1}$	$w_{i,4}^c$	+2.43809523809524	$\cdot 10^{-1}$
$w_{i,5}^c$	+1.00138284831491	$\cdot 10^{-1}$	$w_{i+1,1}^c$	+4.83872966828888	$\cdot 10^{-3}$
$w_{i,1}^6$	+2.74945307600086	$\cdot 10^{-3}$	$w_{i,3}^6$	+1.85682012187242	$\cdot 10^{-2}$
$w_{i,5}^6$	+9.71662045547156	$\cdot 10^{-2}$	$w_{i,6}^6$	+1.38413023680783	$\cdot 10^{-1}$
$w_{i+1,1}^6$	+1.62213410652341	$\cdot 10^{-1}$			

Table B.3: An overview of the constants for the defect computation for the 12th order Legendre-Gauss-Lobatto collocation method. Data is directly obtained from [14].

If the defect constraints do not meet the tolerance specified in Table A.4, The node and interior points should be altered to improve the polynomial approximation of the dynamics. The procedure for this correction is presented in Section C.5.

B.2.2. Error control via Boor's method

A collocation problem solved via the methodology explained in Sections B.2.1 and C.5 does not necessarily satisfy the tolerances as specified in Table A.8. The root cause of the invalidity of such a solution is that the truncation error can vary widely per over the mesh (i.e the totality of nodes representing the discretization of the trajectory). An ideal mesh equidistributes the truncation error over the segments and keeps the magnitude of this error within bounds as specified in Table A.8. This process is referred to as mesh refinement and is equivalent to the concept of step-size control in explicit integration schemes [8]. The remainder of

this section is dedicated to explaining the Boor's method of mesh refinement [9]. This mesh refinement error method is favoured because no higher-order solution is required for error estimation which makes it a computationally efficient method. The following explanation is based on [8, 9, 14] unless stated otherwise.

The starting point of the error control procedure begins with a discretized trajectory, proposed as a solution by the collocation procedure as outlined in Sections B.2.1 and C.5, with a mesh according to Equation B.15 [8].

$$\Pi : t_1 < t_2 < \dots < t_n \quad (\text{B.15})$$

The error per segment, can be computed according to Equation B.16, where Δt_i denotes the time duration of the segment and ξ_i represents the eighth-order derivative of segment i .

$$\begin{aligned} e_i &= C \Delta t_i^8 \xi_i + \mathcal{O}(\Delta t_i^9), \quad i = 1, \dots, n-1 \\ C &= 2.93579395141895 \cdot 10^{-9} \end{aligned} \quad (\text{B.16})$$

The eighth-order derivative can be computed via a difference scheme, shown below in Equation B.17.

$$\xi_i \approx \left\{ \begin{array}{ll} 2\max \left[\frac{|\mathbf{p}_1^7 - \mathbf{p}_2^7|}{\Delta t_1 + \Delta t_2} \right] & \text{on } (t_1, t_2) \\ \max \left[\frac{|\mathbf{p}_{i-1}^7 - \mathbf{p}_i^7|}{\Delta t_{i-1} + \Delta t_i} \right] + \max \left[\frac{|\mathbf{p}_{i+1}^7 - \mathbf{p}_i^7|}{\Delta t_{i+1} + \Delta t_i} \right] & \text{on } (t_i, t_{i+1}) \text{ for } i = 2, \dots, n-2 \\ 2\max \left[\frac{|\mathbf{p}_n^7 - \mathbf{p}_{n-1}^7|}{\Delta t_1 + \Delta t_2} \right] & \text{on } (t_{n-1}, t_n) \end{array} \right\} \quad (\text{B.17})$$

The differencing scheme involves the seventh order derivatives \mathbf{p}_i^7 which can be computed using Equation B.18, where \mathbf{b} denotes the final column of B_i^{-1}

$$\mathbf{p}_i^7 = 7! \begin{bmatrix} x_{i,1} & x_{i,3} & x_{i,5} & x_{i+1,1} & x'_{i,1} & x'_{i,3} & x'_{i,5} & x'_{i+1,1} \end{bmatrix} \frac{\mathbf{b}}{\Delta t_i^7} \quad (\text{B.18})$$

The differencing scheme involves seventh-order derivatives \mathbf{p}_i^7 which can be computed using Equation B.18, where \mathbf{b} denotes the final column of B_i^{-1} . The new mesh is then recomputed according to Equation B.19.

$$t_{i+1} = I^{-1} \left[\frac{iI(t_n)}{n-1} \right] \text{ for } i = 1, \dots, n-2 \quad (\text{B.19})$$

The quantity $I(t)$ is defined in Equation B.20 and can be computed exactly since it is a piecewise linear function.

$$I(t) = \int_{t_1}^t \xi^{\frac{1}{8}}(s) ds \quad (\text{B.20})$$

The states corresponding to the new mesh are computed via polynomial interpolation. The new trajectory is fed back into the collocation procedure and the solution is refined again. This iterative procedure is repeated until the mesh satisfies the distribution criteria as specified and error tolerances specified in Table A.4. If the segment error does not meet these tolerances, the number of nodes on the trajectory is increased according to Equation B.21 [9].

$$n_{\text{new}} = \text{round} \left[n_{\text{old}} \left(\frac{10e_i}{\text{tol}} \right)^{\frac{1}{8}} + 5 \right] \quad (\text{B.21})$$

The new mesh with the updated number of nodes is subjected to the collocation and mesh refinement procedure until the error is equidistributed again. The procedure of solving via collocation, equidistributing the segment error and adjusting the number of patch points ensures that the solution adheres to the numerical continuation tolerances as specified in Table A.8.

This concludes the discussion on the numerical integration techniques that have been leveraged during the thesis project. Recommendations for improving these techniques can be found in Chapter F.

This page is intentionally left blank.

C

Root-finding algorithms

Root-finding algorithms are the backbone of this thesis project. In conjunction with numerical integrators, these algorithms allow the construction of the equilibria contours and l.p.o families. This addendum provides an overview of all the root-finding algorithms employed during this thesis work. Section C.1 provides the reader with the principles of multivariate root-finding. The root-finder algorithm that computes the artificial equilibria is presented in Section C.2. Section C.3 discusses the targeting scheme that computes the approximate seed solutions. The refinement of these seed solutions is accomplished via the two-level targeter (TLT) which is explained in Section C.4. Finally, the algorithm that constructs the l.p.o families during the numerical continuation procedure is explained in Section C.5.

C.1. Multivariate Newton's method

The multivariate Newton's method is a numerical method which can solve a set of nonlinear equations subjected to multiple nonlinear constraints. It does so by finding the solution \mathbf{X} , commonly referred to as the design vector, such that the residual \mathbf{F} , commonly referred to as the defect vector, at this solution is zero. The mathematical formulation of this objective is shown below in Equation C.1[23].

$$\mathbf{F}(\mathbf{X}) = 0 \quad (\text{C.1})$$

The multivariate Newton's method is initialized with a seed solution, denoted by \mathbf{X}_0 with $\mathbf{F}(\mathbf{X}_0) > 0$. The solution to the system is found through an iterative process where $\mathbf{F}(\mathbf{X}_i) > \mathbf{F}(\mathbf{X}_{i+1}) > 0$. In essence, the solution is updated throughout the iterative process until Equation C.1 is met. The required update can be computed from Equation C.2.

$$\mathbf{F} = D\mathbf{F}\Delta\mathbf{X}, \text{ where } \mathbf{X}_{i+1} = \mathbf{X}_i + \Delta\mathbf{X} \quad (\text{C.2})$$

In the Equation above, $D(\mathbf{F})$ denotes the Jacobian of \mathbf{X} with respect to \mathbf{F} . The Jacobian provides a relationship between the defect vector and design variables which allows one to find the required update to the current solution. For sake of clarity, the Jacobian is displayed in Equation C.3.

$$\mathbf{F} = \begin{bmatrix} \bar{f}_1 \\ \bar{f}_2 \\ \vdots \\ \bar{f}_k \end{bmatrix}, \quad \mathbf{X} = \begin{bmatrix} \bar{x}_1 \\ \bar{x}_2 \\ \vdots \\ \bar{x}_l \end{bmatrix}, \quad D\mathbf{F} = \frac{\partial \mathbf{F}}{\partial \mathbf{X}} = \begin{bmatrix} \frac{\partial x_1}{\partial f_1} & \frac{\partial x_1}{\partial f_2} & \cdots & \frac{\partial x_1}{\partial f_k} \\ \frac{\partial x_2}{\partial f_1} & \frac{\partial x_2}{\partial f_2} & \cdots & \frac{\partial x_2}{\partial f_k} \\ \vdots & \vdots & \ddots & \vdots \\ \frac{\partial x_l}{\partial f_1} & \frac{\partial x_l}{\partial f_2} & \cdots & \frac{\partial x_l}{\partial f_k} \end{bmatrix} \quad (\text{C.3})$$

In case the number of unknowns equals the number of equations ($k = l$). The required update $\Delta\mathbf{X}$ can be computed via Equation C.4.

$$\Delta\mathbf{X} = -(D\mathbf{F})^{-1}\mathbf{F} \quad (\text{C.4})$$

The number of unknowns will often exceed the number of equations ($k > l$). In that event, the update is computed via the Gauss-Newton algorithm, displayed below in Equation C.5 [6].

$$\Delta\mathbf{X} = -D\mathbf{F}^T (D\mathbf{F}D\mathbf{F}^T)^{-1}\mathbf{F} \quad (\text{C.5})$$

The methodology presented in this Section provides the reader with the working principles of the root-finders presented in this Chapter.

C.2. Equilibria root-finding procedure

This section outlines the multivariate root-finding algorithm that computes the artificial equilibria contours. The first type of equilibria contour has a fixed acceleration orientation while the acceleration magnitude varies over the curve. For this type of contour, the natural equilibria are employed as seed solutions. The design and defect vector for this procedure are listed in Equation C.6, whereas the partial derivatives of the Jacobian are presented in Equation C.7.

$$\mathbf{X} = \begin{bmatrix} x \\ y \end{bmatrix} \quad \mathbf{F} = \begin{bmatrix} f_1 \\ f_2 \end{bmatrix} = \begin{bmatrix} x \left(1 - \frac{1-\mu}{r_{13}^3} - \frac{\mu}{r_{23}^3} \right) + \mu \left(-\frac{1-\mu}{r_{13}^3} - \frac{\mu}{r_{23}^3} \right) + \frac{\mu}{r_{23}^3} + a_{lt} \cos(\alpha) \\ y \left(1 - \frac{1-\mu}{r_{13}^3} - \frac{\mu}{r_{23}^3} \right) + a_{lt} \sin(\alpha) \end{bmatrix} \quad (\text{C.6})$$

$$\begin{aligned} D\mathbf{F} &= \begin{bmatrix} \frac{\partial f_1}{\partial x} & \frac{\partial f_1}{\partial y} \\ \frac{\partial f_2}{\partial x} & \frac{\partial f_2}{\partial y} \end{bmatrix} = \begin{bmatrix} D\mathbf{F}_{11} & D\mathbf{F}_{12} \\ D\mathbf{F}_{21} & D\mathbf{F}_{22} \end{bmatrix} \\ D\mathbf{F}_{11} &= \left(1 - \frac{1-\mu}{r_{13}^3} - \frac{\mu}{r_{23}^3} \right) + (x+\mu) \left(3 \frac{1-\mu}{r_{13}^5} (x+\mu) + 3 \frac{\mu}{r_{23}^5} (x-1+\mu) \right) - 3 \frac{\mu}{r_{23}^5} (x-1+\mu) \\ D\mathbf{F}_{12} &= (x+\mu) \left(3 \frac{1-\mu}{r_{13}^5} y + 3 \frac{\mu}{r_{23}^5} y \right) - 3 \frac{\mu}{r_{23}^5} y \\ D\mathbf{F}_{21} &= y \left(3 \frac{1-\mu}{r_{13}^5} (x+\mu) + 3 \frac{\mu}{r_{23}^5} (x-1+\mu) \right) \\ D\mathbf{F}_{22} &= \left(1 - \frac{1-\mu}{r_{13}^3} - \frac{\mu}{r_{23}^3} \right) + y \left(3 \frac{1-\mu}{r_{13}^5} y + 3 \frac{\mu}{r_{23}^5} y \right) \end{aligned} \quad (\text{C.7})$$

The desired increment is computed according to Equation C.4. Correcting the solution in this way did not result in robust behaviour and led to the cyclic and sometimes divergent behaviour of the root-finder. Robust performance has been achieved by the introduction of a relaxation parameter (l), which attenuates the increment of the root-finding procedure [19]. Hence, the solution is updated according to Equation C.8.

$$\mathbf{X}_{i+1} = \mathbf{X}_i + l \cdot \Delta \mathbf{X} \quad (\text{C.8})$$

When an equilibrium is found using the procedure listed in Equations C.6-C.8, the acceleration magnitude is increased and a new equilibrium is found via the root-finding procedure until acceleration magnitude exceeds an upper limit. The values for the acceleration increment, upper limit and relaxation parameter can be found in Table A.5.

The contours with a varying thrust orientation and a fixed acceleration magnitude are initialized from collinear equilibria with the desired acceleration magnitude. The seed solution(s) are found using the a relaxed version of the Newton-Raphson method, shown below in Equation C.9

$$x_1 = x_0 - l \cdot \frac{f(x_0)}{f'(x_0)} \quad (\text{C.9})$$

In the Equation above, $f(x)$ equals f_1 of Equation C.6 and $f'(x)$ equals $D\mathbf{F}_{11}$ of Equation C.7. Th complete equilibria contours are achieved by incrementing the acceleration orientation in both a clockwise and counterclockwise fashion for each seed solution until the angle stopping condition is reached. This stopping condition is listed in Table A.5 is.

The procedure listed above provides robust performance while $a_{lt} \leq 0.25$, which more than twice as high as the maximum assumed acceleration magnitude. In [1], equilibria contours have been presented for $a_{lt} \leq 0.5$. It should be pointed out that for $a_{lt} > 0.25$ the equilibria contours start to merge. This merging phenomenon is likely the root cause for failure of the equilibria root-finding procedure. If one is interested in investigating the merging of these equilibria contours, the reader is referred to Chapter F for suggestions on improving the performance of the equilibria root-finding procedure.

C.3. Floquet targeter

The approximate solutions of the first two members of H_{lt} -varying l.p.o families are constructed through a targeting scheme based on Floquet analysis [20]. This Floquet targeter decomposes the spacecraft motion along the six stability components and determines a velocity correction to cancel out the unwanted motion components. Section C.3.1 explains the fundamentals of the Floquet targeter and how the procedure is adapted to facilitate the construction of libration point orbits. The procedure of constructing approximate seed solutions is presented in Section C.3.2.

C.3.1. Velocity correction via Floquet analysis

To determine the required velocity correction at an arbitrary time, the Floquet controller should be provided with a periodic reference trajectory in the form of a monodromy matrix $M = \Phi(T, 0)$ and an initial deviation with respect to this trajectory $\delta\bar{x}(t_0)$. The deviation at the time of interest is then easily obtained from Equation C.10.

$$\delta\bar{x}(t) = \Phi(t, 0)\delta\bar{x}(t_0) \quad (\text{C.10})$$

The Floquet controller decomposes this deviation into six states which indicate the deviation of spacecraft along each stability components with the help of Equation C.11.

$$\delta\bar{x}_t = \sum_{j=1}^6 \delta\bar{x}_j = \sum_{j=1}^6 \bar{g}_j(t)\bar{e}_j(t) \quad (\text{C.11})$$

In the Equation above, \bar{e}_i symbolizes the columns of the Floquet modal matrix $E(t)$ obtained from Equation C.13, and \bar{g}_j represents the columns of matrix perturbation decomposition $G(t)$ shown in Equation C.12.

$$G(t) = E(t)^{-1}\delta\bar{x}(t) \quad (\text{C.12})$$

The Floquet modal matrix depends upon the eigensystem of the reference trajectory J is a diagonal matrix which hold the complex characteristic multipliers of the monodromy matrix. The eigenvectors related to these characteristic multipliers are stored in Matrix S

$$E(t) = \Phi(t, 0)Se^{-Jt} \quad (\text{C.13})$$

The motion decomposition matrix allows identification of the perturbation contributions of each stability component. Knowing these contributions allows determining of a velocity correction that cancels out the unwanted motion. The mathematical formulation of this problem is presented in Equation C.14 in which ι_j symbolises coefficients of the desired perturbation components.

$$\sum_{j=2,3,4} (1 + \iota_j(t))\delta\bar{x}_j(t) = \sum_{j=1}^6 \delta\bar{x}_j + \begin{bmatrix} 0_3 \\ \Delta\bar{V} \end{bmatrix} \quad (\text{C.14})$$

The above-mentioned procedure was originally designed for station keeping procedures in the vicinity of libration point orbits. However, the procedure can easily be adapted for the construction of approximate periodic solutions. The reference trajectory is a stationary point rather than a periodic orbit. Since periodicity is not defined in a stationary point, The monodromy matrix of an equilibrium does not exist. However, the stability of an equilibrium point can be obtained from the eigensystem of the state propagation matrix (SPM). The deviation at any given time is simply obtained as the state difference between the equilibrium point and the current state of the spacecraft as displace in Equation C.15.

$$\delta\bar{x} = \bar{x}_{eq} - \bar{x} \quad (\text{C.15})$$

It is evident that the deviation in Equation C.15 does not depend on time as opposed to Equation C.10. As a consequence, the Floquet modal matrix is a constant quantity and takes on the form as shown in Equation C.16

$$E = S \quad (\text{C.16})$$

The Floquet targeter algorithm then boils down to Equation C.17.

$$\mathbf{X} = \begin{bmatrix} \dot{x}_3 \\ \dot{x}_4 \\ \dot{x} \\ \dot{y} \end{bmatrix}, \quad \mathbf{F} = \delta\bar{x}_1 + \delta\bar{x}_2 + \delta\bar{x}_5 + \delta\bar{x}_6, \quad D\mathbf{F} = \begin{bmatrix} \delta\bar{x}_{3_r} & \delta\bar{x}_{4_r} & 0_2 \\ \delta\bar{x}_{3_v} & \delta\bar{x}_{4_v} & -I_2 \end{bmatrix} \quad (\text{C.17})$$

The root-finding scheme ignores the out-of-plane stability components and out-of-plane velocity to avoid an underdetermined system. In this way, the required velocity correction can be computed according to Equation C.4.

C.3.2. Construction of approximate periodic solutions

The root-finder algorithms presented in Sections C.4 and C.5 rely on a reference trajectory in the form a a set of nodes with associated times. The approximate seed solutions are defined using an isochronous mesh as defined below in Equation C.18.

$$\Pi: t_1 < \dots < t_i < \dots < t_n, \text{ for } i = 2, \dots, n-1, \text{ where } t_1 = 0, t_i = (i-1) \frac{t_n - t_1}{n-1} \text{ and } t_n = T \quad (\text{C.18})$$

The orbital period of the approximate periodic solution is unknown but Richardson's third-order method [30] provides an analytic expression for approximation of the period. This expression however, can only be used for libration point orbits that emanate from collinear equilibria. In this thesis project, an approximate orbital period is computed by propagating the initial state of the libration point via an RK78 integration scheme until a full revolution has occurred. The initial state of this trajectory is determined in a two-way fashion. First, the initial position of the spacecraft is determined by offsetting it with respect to the equilibrium point according to Equation C.19. This positional offset provides an identical offset as Richardson's third-order method [30] in the case of natural l.p.o families but it extends well to libration point orbits emanating from artificial equilibria not located on the x -axis.

$$\delta \bar{x}_0_{\text{uncorrected}} = \begin{bmatrix} A_x \cos(\theta) \\ A_x \sin(\theta) \\ 0 \\ 0 \\ 0 \\ 0 \end{bmatrix}, \text{ where } \theta = \arctan2(y_{eq}, x_{eq} - (1, 0 - \mu)) \quad (\text{C.19})$$

Secondly, the initial velocity of the spacecraft is computed according to the Floquet targeter specified in Equation C.17. The initial state is then computed via Equation C.20. The methodology pseudo-code for orbital period approximation is presented in Table C.1.

$$\bar{x}_0 = \delta \bar{x}_0_{\text{uncorrected}} + \Delta \bar{V} \quad (\text{C.20})$$

Pseudo-code for orbital period approximation

Input:	(L_p, \bar{x}_0, μ)	
Output:	(T)	
1:	$\theta_0 \leftarrow \text{ComputeOrbitAngle}(L_p, \bar{x}_0, \mu)$	Equation C.19
2:	$\bar{x}_1, t_1 \leftarrow \text{PropagateOrbit}(\bar{x}_0, t_0)$	Section B.1
3:	$\theta_1 \leftarrow \text{ComputeOrbitAngle}(L_p, \bar{x}_1, \mu)$	Equation C.19
4:	if $\theta_1 - \theta_0 > 0$	
5:	$\theta_{sign} = 1$	
6:	else	
7:	$\theta_{sign} = -1$	
8:	$\theta_{change} = 0$	
9:	while $\theta_{change} < 2$	
10:	$\bar{x}_i, t_i \leftarrow \text{PropagateOrbit}(\bar{x}_{i-1}, t_{i-1})$	Section B.1
11:	$\theta_i \leftarrow \text{ComputeOrbitAngle}(L_p, \bar{x}_i, \mu)$	Equation C.19
12:	if $(\theta_i - \theta_0) \cdot \theta_{sign} < 0$	
13:	$\theta_{change}++$	
14:	$T = t_i$	

Table C.1: the subscript p refers to the equilibrium contour instead of the natural libration point. In the case that $p = 1$, the values of the orbit angle are rescaled to the $[0, 2\pi]$ domain to ensure proper functionality. The subscript i denotes a random state along the orbit and is not linked to the mesh as defined in Equation C.18.

With the orbital period known, the node times, as defined in Equation C.18, can be computed while their associated states can be approximated via explicit propagation. This completes the procedure for generating

approximate periodic solution. These start-up arcs serve as input to the two-level targeter algorithm which is described in Section C.4.

C.3.3. Effect of the velocity correction interval

The correction interval parameter of the Floquet targeter allows the user to exert control over the amount of velocity corrections that are performed during one orbital revolution. The effect of varying this parameter is analyzed in Figure C.1, which shows two artificial L_1 families of approximate periodic solutions. The families have identical thrust parameters and in-plane amplitudes but differ in the amount of Floquet corrections which are applied during one orbital revolution. One family uses a correction interval $\Delta t = 50.0$ which means that no velocity corrections are applied during an orbital revolution. The other family uses a correction interval $\Delta t = 0.05$ meaning that a multiple of intermediate velocity corrections are performed to cancel the unstable motion components.

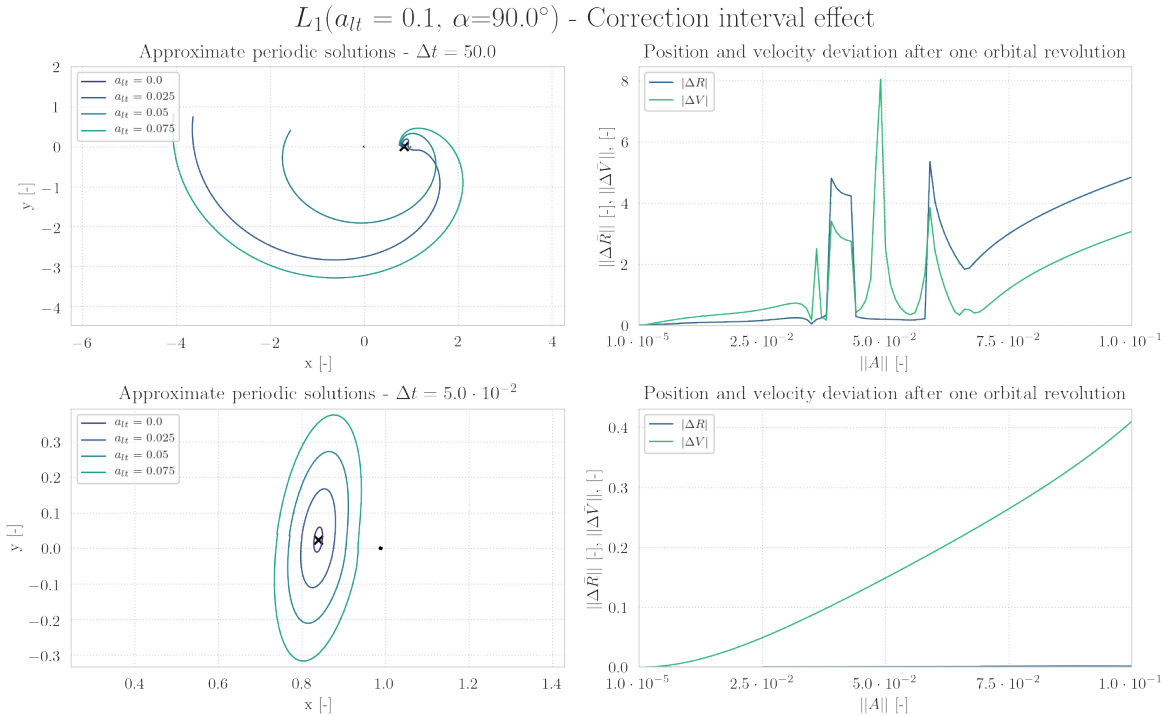


Figure C.1: Two families of approximate libration points generated by the floquet targeter with different correction intervals. The ΔV quantity in the bottom right plot symbolizes the totality of the velocity discrepancy at the full period and the intermediate velocity corrections. The maximum position discrepancy when using a $\Delta t = 5.0 \cdot 10^{-2}$ interval is $\Delta R = 1.9 \cdot 10^{-3}$

Several interesting insights can be extracted from Figure C.1. First of all, the intermediate corrections have a vivid effect on the resulting trajectories. When no intermediate corrections are applied, the chaotic nature of the CR3BP-LT take over, resulting in unpredictable trajectories that do not come close to a periodic orbit. Trajectories that remain bounded near the equilibrium are obtained when applying intermediate velocity corrections. Secondly, the deviation plots show that both the position and velocity discrepancy of the corrected trajectories are an order of magnitude smaller compared to uncorrected trajectories for large amplitudes. Finally, it is worth to note that the corrected trajectories have an elliptical shape and do not posses the typical indent of horizontal Lyapunov orbits.

C.4. Two-level targeter algorithm

A crucial step in the construction of the l.p.o families is the refinement of the approximate seed solutions to actual periodic orbits. Section C.4.1 explains the principles of this refinement procedure whereas the performance of the two-level targeter (TLT) is analysed in Section C.4.2. An extension to the TLT in the form of energy path constraints is discussed in Section C.4.3.

C.4.1. Two-level targeter correction scheme

The input into the TLT algorithm is a trajectory, discretised into a set of n nodes, with multiple velocity and position discontinuities. Each node is subjected to a set of constraints constraints. A visualization of the input trajectory is shown below in Figure C.2

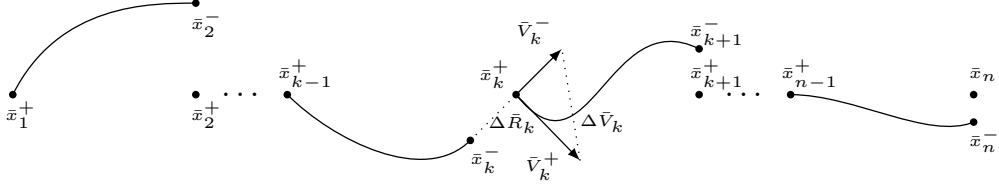


Figure C.2: A discretized trajectory with position and velocity continuous as shown at node k

The discretization transforms the BVP into $n - 1$ two-point boundary value problems (TPBVP). The TLT algorithm constructs a periodic trajectory by solving each TPBVP problem separately. The technique of subdividing a trajectory into smaller subintervals and solving them independently is better known as multiple shooting which a frequently adopted technique in the field spacecraft trajectory design [5]. The TLT owes its name to the two multiple shooting that constitute the algorithm. These shooting schemes are referred to as the level-I corrector and the level-II corrector respectively.

Level-I corrector	A multiple shooting scheme that alters the velocity of the nodes to generate a trajectory that is continuous in position.
Level-II corrector	A multiple shooting scheme that alters the position and time of the nodes to construct a trajectory that is continuous in velocity.

Both the level-I and level-II algorithm correct the state at a certain node based upon the state discontinuities at another node. The relationship between these deviations can be easily obtained from Equation C.21.

$$\delta \bar{x}(t_k) = \Phi(t_k, t_{k-1})\delta \bar{x}(t_{k-1}) \quad (\text{C.21})$$

The deviations presented in the equation above are so-called contemporaneous deviations and do not take into account the deviations due to a change in node times. Since the Level-II corrector alters these times, non-contemporaneous deviation should be taken into account as well, as shown in Equation C.22.

$$\delta \bar{x}' = \delta \bar{x}(t') = \delta \bar{x}(t) + \dot{\bar{x}}\delta t, \text{ where } \delta t = t - t' \quad (\text{C.22})$$

The first term on the right hand side of Equation C.22 represents the contemporaneous deviation whereas the latter term represents the non-contemporaneous variation. Substituting Equation C.22 into C.21 results in the variational equation that serves as the basis for both levels of the TLT algorithm. This variational equation is shown below in Equation C.23.

$$(\delta \bar{x}'(t_k + \delta t_k) - \dot{\bar{x}}(t_k)\delta t_k) = \Phi(t_k, t_{k-1})(\delta \bar{x}'(t_{k-1} + \delta t_{k-1}) - \dot{\bar{x}}(t_{k-1})\delta t_{k-1}) \quad (\text{C.23})$$

The partial derivatives of the state transition matrix (STM) are expressed below in Equation C.24 along with an abbreviated notation to avoid the length expressions later in this subsection.

$$\Phi(t_k, t_{k-1}) = \begin{bmatrix} \frac{\partial x_k}{\partial x_{k-1}} & \frac{\partial x_k}{\partial y_{k-1}} & \frac{\partial x_k}{\partial z_{k-1}} & \frac{\partial x_k}{\partial \dot{x}_{k-1}} & \frac{\partial x_k}{\partial \dot{y}_{k-1}} & \frac{\partial x_k}{\partial \dot{z}_{k-1}} \\ \frac{\partial y_k}{\partial x_{k-1}} & \frac{\partial y_k}{\partial y_{k-1}} & \frac{\partial y_k}{\partial z_{k-1}} & \frac{\partial y_k}{\partial \dot{x}_{k-1}} & \frac{\partial y_k}{\partial \dot{y}_{k-1}} & \frac{\partial y_k}{\partial \dot{z}_{k-1}} \\ \frac{\partial z_k}{\partial x_{k-1}} & \frac{\partial z_k}{\partial y_{k-1}} & \frac{\partial z_k}{\partial z_{k-1}} & \frac{\partial z_k}{\partial \dot{x}_{k-1}} & \frac{\partial z_k}{\partial \dot{y}_{k-1}} & \frac{\partial z_k}{\partial \dot{z}_{k-1}} \\ \frac{\partial \dot{x}_k}{\partial x_{k-1}} & \frac{\partial \dot{x}_k}{\partial y_{k-1}} & \frac{\partial \dot{x}_k}{\partial z_{k-1}} & \frac{\partial \dot{x}_k}{\partial \dot{x}_{k-1}} & \frac{\partial \dot{x}_k}{\partial \dot{y}_{k-1}} & \frac{\partial \dot{x}_k}{\partial \dot{z}_{k-1}} \\ \frac{\partial \dot{y}_k}{\partial x_{k-1}} & \frac{\partial \dot{y}_k}{\partial y_{k-1}} & \frac{\partial \dot{y}_k}{\partial z_{k-1}} & \frac{\partial \dot{y}_k}{\partial \dot{x}_{k-1}} & \frac{\partial \dot{y}_k}{\partial \dot{y}_{k-1}} & \frac{\partial \dot{y}_k}{\partial \dot{z}_{k-1}} \\ \frac{\partial \dot{z}_k}{\partial x_{k-1}} & \frac{\partial \dot{z}_k}{\partial y_{k-1}} & \frac{\partial \dot{z}_k}{\partial z_{k-1}} & \frac{\partial \dot{z}_k}{\partial \dot{x}_{k-1}} & \frac{\partial \dot{z}_k}{\partial \dot{y}_{k-1}} & \frac{\partial \dot{z}_k}{\partial \dot{z}_{k-1}} \end{bmatrix} = \begin{bmatrix} A_{k,k-1} & B_{k,k-1} \\ C_{k,k-1} & D_{k,k-1} \end{bmatrix} \quad (\text{C.24})$$

The remainder of this subsection is dedicated to the explanation of both multiple shooting schemes. The discussion is based upon [4, 7, 21] unless stated otherwise.

Level-I corrector

The objective of the level-I corrector is to remove all position discrepancies. The root-finding scheme for a single segment of this trajectory is provided in Equation C.25.

$$\mathbf{X}_k = \begin{bmatrix} \dot{x}_{k-1}^+ \\ \dot{y}_{k-1}^+ \\ \dot{z}_{k-1}^+ \end{bmatrix} = \bar{V}_k, \quad \mathbf{F}_k = \begin{bmatrix} x_k^+ - x_k^- \\ y_k^+ - y_k^- \\ z_k^+ - z_k^- \end{bmatrix} = \Delta \bar{R}_k, \quad D\mathbf{F}_k = \begin{bmatrix} \frac{\partial x_k^+}{\partial \dot{x}_{k-1}} & \frac{\partial x_k^+}{\partial \dot{y}_{k-1}^+} & \frac{\partial x_k^+}{\partial \dot{z}_{k-1}^+} \\ \frac{\partial y_k^+}{\partial \dot{x}_{k-1}} & \frac{\partial y_k^+}{\partial \dot{y}_{k-1}^+} & \frac{\partial y_k^+}{\partial \dot{z}_{k-1}^+} \\ \frac{\partial z_k^+}{\partial \dot{x}_{k-1}} & \frac{\partial z_k^+}{\partial \dot{y}_{k-1}^+} & \frac{\partial z_k^+}{\partial \dot{z}_{k-1}^+} \end{bmatrix} = \bar{B}_{k,k-1} \quad (\text{C.25})$$

The Level-1 corrector can simultaneously compute velocity corrections for each segment by merging the the $N - 1$ root-finding algorithms into one large root-finding algorithm as shown in Equation C.26. The dimensions of the design vector and defect vector are identical and equal to $(3N \times 1)$. This results in a square Jacobian of dimensions $(3N \times 3N)$ meaning that correction can be computed via Equation C.4.

$$\mathbf{X} = \begin{bmatrix} \Delta \bar{V}_1 \\ \vdots \\ \Delta \bar{V}_{n-1} \end{bmatrix}, \quad \mathbf{F} = \begin{bmatrix} \Delta \bar{R}_1 \\ \vdots \\ \Delta \bar{R}_{n-1} \end{bmatrix}, \quad D\mathbf{F} = \begin{bmatrix} B_{2,1} & & \\ & \ddots & \\ & & B_{n,n-1} \end{bmatrix} \quad (\text{C.26})$$

It is worth to note that [21] uses a different correction scheme than the correction scheme presented above. The difference with respect to [21] being that the node times are allowed to vary. Both versions have been tested during this thesis project but no significant difference in performance was observed. The performance of the implemented Level-I corrector is analyzed in Section C.4.2.

Level-II corrector

The position continuous trajectory arising from the level-I corrector serves as the input for the level-II corrector. The level-II scheme aims to provide an update to the position and times of the nodes such that another level I correction will result in a trajectory that is continuous in both position and velocity. The root-finding scheme of a single segment on the trajectory is presented below in Equation C.27.

$$\mathbf{X}_k = \begin{bmatrix} R_{k-1} \\ t_{k-1} \\ R_k \\ t_k \\ R_{k+1} \\ t_{k+1} \end{bmatrix}, \quad \mathbf{F}_k = \begin{bmatrix} \dot{x}_k^+ - \dot{x}_k^- \\ \dot{y}_k^+ - \dot{y}_k^- \\ \dot{z}_k^+ - \dot{z}_k^- \end{bmatrix} = \Delta \bar{V}_k, \quad D\mathbf{F}_k = \begin{bmatrix} \frac{\partial \Delta \bar{V}_k}{\partial R_{k-1}} & \frac{\partial \Delta \bar{V}_k}{\partial t_{k-1}} & \frac{\partial \Delta \bar{V}_k}{\partial R_k} & \frac{\partial \Delta \bar{V}_k}{\partial t_k} & \frac{\partial \Delta \bar{V}_k}{\partial R_{k+1}} & \frac{\partial \Delta \bar{V}_k}{\partial t_{k+1}} \end{bmatrix} \quad (\text{C.27})$$

To obtain the partial derivatives of the Jacobian in Equation C.27, a relationship that links the design variables to the defect variables is necessary. Such a relationship can be obtained from a first-order expansion as shown in Equation C.28

$$\begin{aligned} \delta \bar{V}_k^- &= \frac{\partial \bar{V}_k^-}{\partial \bar{R}_{k-1}} \delta \bar{R}_{k-1} + \frac{\partial \bar{V}_k^-}{\partial t_{k-1}} \delta t_{k-1} + \frac{\partial \bar{V}_k^-}{\partial \bar{R}_k} \delta \bar{R}_k + \frac{\partial \bar{V}_k^-}{\partial t_k} \delta t_k \\ \delta \bar{V}_k^+ &= \frac{\partial \bar{V}_k^+}{\partial \bar{R}_k} \delta \bar{R}_k + \frac{\partial \bar{V}_k^+}{\partial t_k} \delta t_k + \frac{\partial \bar{V}_k^+}{\partial \bar{R}_{k+1}} \delta \bar{R}_{k+1} + \frac{\partial \bar{V}_k^+}{\partial t_{k+1}} \delta t_{k+1} \end{aligned} \quad (\text{C.28})$$

Leveraging this first-order expression, the elements of the Jacobian in Equation C.27 can be expressed in partial derivatives of velocity states with respect to the design vectors as shown in Table C.2.

Partial derivatives of the Jacobian of the level-II corrector

$$\begin{aligned}\frac{\partial \Delta \bar{V}_k}{\partial \bar{R}_{k-1}} &= -\frac{\partial \bar{V}_k^-}{\partial \bar{R}_{k-1}} & \frac{\partial \Delta \bar{V}_k}{\partial t_{k-1}} &= -\frac{\partial \bar{V}_k^-}{\partial t_{k-1}} & \frac{\partial \Delta \bar{V}_k}{\partial \bar{R}_k} &= \frac{\partial \bar{V}_k^+}{\partial \bar{R}_k} - \frac{\partial \bar{V}_k^-}{\partial \bar{R}_k} \\ \frac{\partial \Delta \bar{V}_k}{\partial t_k} &= \frac{\partial \bar{V}_k^+}{\partial t_k} - \frac{\partial \bar{V}_k^-}{\partial t_k} & \frac{\partial \Delta \bar{V}_k}{\partial \bar{R}_{k+1}} &= \frac{\partial \bar{V}_k^+}{\partial \bar{R}_{k+1}} & \frac{\partial \Delta \bar{V}_k}{\partial t_{k+1}} &= \frac{\partial \bar{V}_k^+}{\partial t_{k+1}}\end{aligned}$$

Table C.2: Partial derivatives that constitute the segment jacobian of the level-II corrector. The data in this table is obtained from [4].

Expressions for the derivatives in Table C.2 can be obtained from the variational equation, as shown in C.23, for segments $k-1 \rightarrow k$ and $k+1 \rightarrow k$. More specifically, a finite differencing method allows the formulation of these partial derivatives. For sake of clarity, the full expressions of these variational equations are shown below in Equation. C.29.

$$\begin{aligned}\begin{bmatrix} (\delta \bar{R}'_k)^- - \bar{V}_k^- \delta t_k^- \\ (\delta \bar{V}_k^-) - \bar{a}_k^- \delta t_k^- \end{bmatrix} &= \begin{bmatrix} A_{k-1,k} & B_{k-1,k} \\ C_{k-1,k} & D_{k-1,k} \end{bmatrix} \begin{bmatrix} (\delta \bar{R}'_{k-1})^+ - \bar{V}_{k-1}^+ \delta t_{k-1}^+ \\ (\delta \bar{V}_{k-1}^+) - \bar{a}_{k-1}^+ \delta t_{k-1}^+ \end{bmatrix} \\ \begin{bmatrix} (\delta \bar{R}'_k)^+ - \bar{V}_k^+ \delta t_k^+ \\ (\delta \bar{V}_k^+) - \bar{a}_k^+ \delta t_k^+ \end{bmatrix} &= \begin{bmatrix} A_{k,k+1} & B_{k,k+1} \\ C_{k,k+1} & D_{k,k+1} \end{bmatrix} \begin{bmatrix} (\delta \bar{R}'_{k+1})^- - \bar{V}_{k+1}^- \delta t_{k+1}^- \\ (\delta \bar{V}_{k+1}^-) - \bar{a}_{k+1}^- \delta t_{k+1}^- \end{bmatrix}\end{aligned}\quad (C.29)$$

The finite differencing approach is a well-known method in the field of engineering for the approximation of partial derivatives [35]. It allows the approximation of a change in the velocity state at node k due to a change in the design variables in a separate fashion. In the context of the level-II corrector, this boils down to nullifying the terms containing other design variables in the Equations of C.29. The results of the finite differencing procedure are presented below in Table C.3.

Partial derivatives of the velocity states at node k with respect to the design variables

$$\begin{aligned}\frac{\partial \bar{V}_k^-}{\partial \bar{R}_{k-1}} &= B_{k-1,k}^{-1}, & \frac{\partial \bar{V}_k^-}{\partial t_{k-1}} &= -B_{k-1,k}^{-1} \bar{V}_{k-1}^+, & \frac{\partial \bar{V}_k^-}{\partial \bar{R}_k} &= -B_{k-1,k}^{-1} \bar{A}_{k-1,k}, & \frac{\partial \bar{V}_k^-}{\partial t_k} &= \bar{a}_k^- - D_{k,k-1} B_{k,k-1}^{-1} \bar{V}_k^- \\ \frac{\partial \bar{V}_k^+}{\partial \bar{R}_k} &= -B_{k+1,k}^{-1} A_{k+1,k}, & \frac{\partial \bar{V}_k^+}{\partial t_k} &= \bar{a}_k^+ - D_{k,k+1} B_{k,k+1}^{-1} \bar{V}_k^+, & \frac{\partial \bar{V}_k^+}{\partial \bar{R}_{k+1}} &= B_{k+1,k}^{-1}, & \frac{\partial \bar{V}_k^+}{\partial t_{k+1}} &= -B_{k+1,k} \bar{V}_{k+1}^-\end{aligned}$$

Table C.3: Expressions for the partial derivatives that constitute the segment jacobian of the level-II corrector. The data in this table is obtained from [4].

The spatial and temporal correction of each node can be computed simultaneously by combining the defects into one vector and all partial derivatives into one matrix. This total root-finding scheme can be found below in Equations C.30 and C.31.

$$DF = \begin{bmatrix} \frac{\partial \Delta \bar{V}_2}{\partial R_1} & \frac{\partial \Delta \bar{V}_2}{\partial t_1} & \frac{\partial \Delta \bar{V}_2}{\partial R_2} & \frac{\partial \Delta \bar{V}_2}{\partial t_2} & \frac{\partial \Delta \bar{V}_2}{\partial R_3} & \frac{\partial \Delta \bar{V}_2}{\partial t_3} & \frac{\partial \Delta \bar{V}_2}{\partial R_4} & \frac{\partial \Delta \bar{V}_3}{\partial t_4} \\ & & \ddots & \ddots & & \ddots & & \ddots & \\ & & & & \ddots & \ddots & & & \\ & & & & & \frac{\partial \Delta \bar{V}_{N-1}}{\partial R_{N-2}} & \frac{\partial \Delta \bar{V}_{N-1}}{\partial t_{N-2}} & \frac{\partial \Delta \bar{V}_{N-1}}{\partial R_{N-1}} & \frac{\partial \Delta \bar{V}_{N-1}}{\partial t_{N-1}} & \frac{\partial \Delta \bar{V}_{N-1}}{\partial R_N} & \frac{\partial \Delta \bar{V}_{N-1}}{\partial t_N} \end{bmatrix} \quad (C.30)$$

$$X = \begin{bmatrix} X_2 \\ \vdots \\ X_{N-1} \end{bmatrix}, \quad F = \begin{bmatrix} \Delta \bar{V}_2 \\ \vdots \\ \Delta \bar{V}_{N-1} \end{bmatrix} \quad (C.31)$$

The level-II correction scheme as presented in Equations C.30 and C.31 provides a correction that diminishes the velocity discontinuity at the interior nodes of the trajectory. The periodic nature of the libration point orbits also requires state continuity between the initial and terminal state of the discretized trajectory. Hence, the level-II corrector needs to be augmented with periodicity constraints. This constraint is denoted as η_k

$$\eta_k = \begin{bmatrix} \bar{R}_1 - \bar{R}_N \\ \bar{V}_1^+ - \bar{V}_N^- \end{bmatrix} \quad (C.32)$$

The scalar constraint as shown in Equation C.32 is used to construct the defect variable [4] which is defined in Equation C.33 where η_k^* is the desired value of the constraint. Defining the constraint in such away allows generalization of the procedure to other types of constraints as will be shown in Section C.4.3. Regarding the periodicity constraint, it is obvious that $\eta_k^* = \bar{0}$.

$$\delta \eta_k = \eta_k^* - \eta_k \quad (C.33)$$

Similar to the derivation of the interior velocity continuity constraints, a first order Taylor series expansion provides a relationship between the constraints and design variables. The Taylor series expansion is shown below in Equation C.34.

$$\begin{aligned}\delta\bar{\eta}_k = & \left(\frac{\partial\eta_k}{\partial\bar{R}_1} + \frac{\partial\eta_k}{\partial\bar{V}_1^+} \frac{\partial\bar{V}_1^+}{\partial\bar{R}_1} \right) \delta\bar{R}_1 + \left(\frac{\partial\eta_k}{\partial t_1} + \frac{\partial\eta_k}{\partial\bar{V}_1^+} \frac{\partial\bar{V}_1^+}{\partial t_1} \right) \delta t_1 + \left(\frac{\partial\eta_k}{\partial\bar{V}_1^+} \frac{\partial\bar{V}_1^+}{\partial\bar{R}_2} \right) \delta\bar{R}_2 + \left(\frac{\partial\eta_k}{\partial\bar{V}_1^+} \frac{\partial\bar{V}_1^+}{\partial t_2} \right) \delta t_2 \\ & + \left(\frac{\partial\eta_k}{\partial\bar{V}_n^-} \frac{\partial\bar{V}_n^-}{\partial\bar{R}_{n-1}} \right) \delta\bar{R}_{n-1} + \left(\frac{\partial\eta_k}{\partial\bar{V}_n^-} \frac{\partial\bar{V}_n^-}{\partial t_{n-1}} \right) \delta t_{n-1} + \left(\frac{\partial\eta_k}{\partial\bar{R}_n} + \frac{\partial\eta_k}{\partial\bar{V}_n^-} \frac{\partial\bar{V}_n^-}{\partial\bar{R}_n} \right) \delta\bar{R}_n + \left(\frac{\partial\eta_k}{\partial t_n} + \frac{\partial\eta_k}{\partial\bar{V}_n^-} \frac{\partial\bar{V}_n^-}{\partial t_n} \right) \delta t_n\end{aligned}\quad (\text{C.34})$$

A change in η_k with respect to \bar{V}_1^+ , \bar{R}_1 , \bar{V}_n^- , \bar{R}_n is obtained via basic differentiation. The result of these derivations are shown in C.35¹

$$\begin{aligned}\frac{\partial\eta_k}{\bar{R}_1} \begin{bmatrix} \bar{I} \\ \bar{0} \end{bmatrix} &= -\frac{\partial\eta_k}{\bar{R}_n} \\ \frac{\partial\eta_k}{\bar{V}_1^+} \begin{bmatrix} \bar{0} \\ \bar{I} \end{bmatrix} &= -\frac{\partial\eta_k}{\bar{V}_n^-}\end{aligned}\quad (\text{C.35})$$

The eight partial derivatives $\frac{\partial\bar{V}_1^+}{\partial\bar{R}_1}$, $\frac{\partial\bar{V}_1^+}{\partial t_1}$, $\frac{\partial\bar{V}_1^+}{\partial\bar{R}_1}$, $\frac{\partial\bar{V}_1^+}{\partial t_2}$, $\frac{\partial\bar{V}_n^-}{\partial\bar{R}_{n-1}}$, $\frac{\partial\bar{V}_n^-}{\partial t_{n-1}}$, $\frac{\partial\bar{V}_n^-}{\partial\bar{R}_n}$ and $\frac{\partial\bar{V}_n^-}{\partial t_n}$ can be easily derived using Table C.3. The complete notation of the periodicity constraint is displayed below in Equation C.42².

$$\begin{aligned}\delta\bar{\eta}_k = & \begin{bmatrix} \bar{I} \\ -B_{21}^{-1}A_{21} \end{bmatrix} \delta\bar{R}_1 + \begin{bmatrix} \bar{0} \\ \bar{a}_1^+ - D_{12}B_{12}^{-1}\bar{V}_1^+ \end{bmatrix} \delta t_1 + \begin{bmatrix} \bar{0} \\ B_{21}^{-1} \end{bmatrix} \delta\bar{R}_2 + \begin{bmatrix} \bar{0} \\ -\bar{B}_{21}\bar{V}_2^- \end{bmatrix} \delta t_2 \\ & + \begin{bmatrix} \bar{0} \\ -B_{n-1,n}^{-1} \end{bmatrix} \delta\bar{R}_{n-1} + \begin{bmatrix} \bar{0} \\ B_{n-1,1}^{-1}\bar{V}_{n-1}^+ \end{bmatrix} \delta t_{n-1} + \begin{bmatrix} -\bar{I} \\ B_{n,n-1}^{-1}A_{n,n-1} \end{bmatrix} \delta\bar{R}_n + \begin{bmatrix} \bar{0} \\ -(\bar{a}_n^- - D_{n,n-1}B_{n,n-1}^{-1}\bar{V}_n^-) \end{bmatrix} \delta t_n\end{aligned}\quad (\text{C.36})$$

The complete level-II correction scheme with periodicity constraints is obtained by simply augmenting the jacobian and defect vector of Equation C.37 with first order Taylor expansion of Equation C.42. The result is shown below in Equation C.37

$$\begin{bmatrix} \mathbf{X} \\ \delta\eta_k \end{bmatrix} = \begin{bmatrix} DF \\ \frac{\partial\eta_k}{\partial\mathbf{X}} \end{bmatrix} \mathbf{X}\quad (\text{C.37})$$

The dimensions of the design and defect vector level-II corrector with periodicity are $4n$ and $3(n-1)+6$ respectively. This results in a Jacobian of size $(3(n-1)+6) \times (4n)$. The inverse of this matrix can easily be solved with standard c++ operations due to the sparsity of the matrix, which is a direct consequence of the decoupling of the multiple shooting segments [4]. The performance of TLT algorithm is presented in Section C.4.2 whereas its veracity is discussed in Section E.3. It should stressed that TLT algorithm can be used to construct H_{lt} -varying l.p.o families. However, the root-finding scheme described in Section C.5 is preferred due to the lower computational cost and its ability to construct the other type of l.p.o families.

¹In [4], the partial derivatives of η_k with respect to \bar{V}_1^+ and \bar{V}_n^- are incorrectly presented as $\frac{\partial\eta_k}{\partial\bar{V}_1^+} = \begin{bmatrix} \bar{I} \\ \bar{0} \end{bmatrix} = -\frac{\partial\eta_k}{\partial\bar{V}_n^-}$. When these partial derivatives were used, the TLT targeter did not converge.

²The sixth term contains the term V_n^+ which should be V_{+n-1} according to [4]. The TLT correction scheme could not find convergence when V_{+n-1} was used.

C.4.2. Two-level targeter performance analysis

The behaviour of the TLT correction procedure is defined by the tolerances, input trajectory and number of nodes. This section is dedicated to investigate the effect of the latter two on the algorithm's behaviour. Figure C.3 presents the convergence behaviour of the algorithm for three different approximate solution of different amplitudes over a wide variety of number of nodes used.

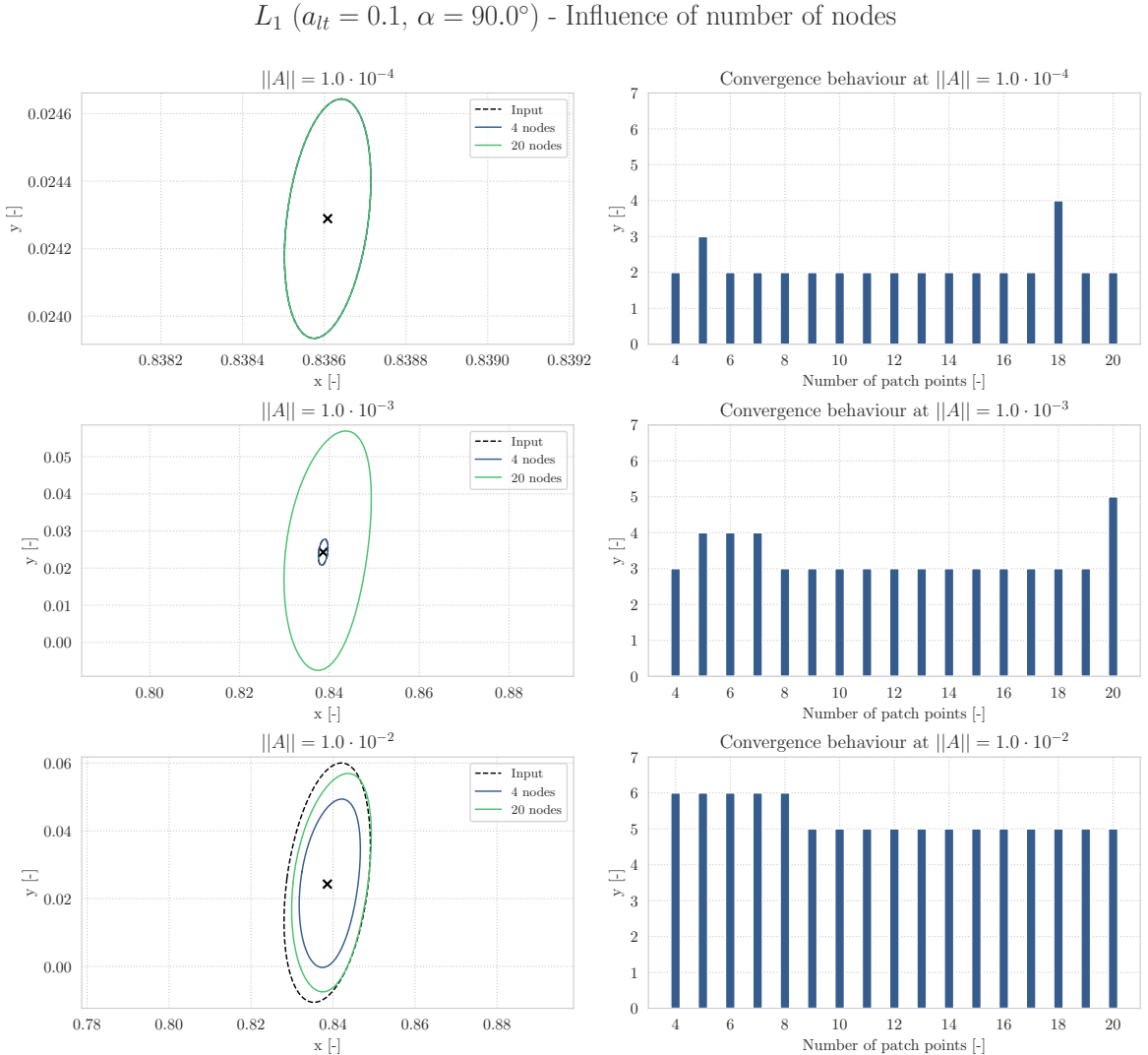


Figure C.3: A comprehensive overview of the TLT behaviour for three different amplitudes and a wide number of nodes.

It can be concluded from Figure C.3 that the number of nodes has little effect on the converged solution for input trajectories with a small amplitude. This is not the case for libration point orbits with larger amplitudes since the shape of the converged solution heavily depends on the number of nodes used to discretize the input trajectory. A higher number of nodes corresponds to a periodic solution that has more similarities with the input trajectory.

An alternative way to ensure that the converged solution closely resembles the input trajectory is to fix the position of one of the nodes. Such an approach has been proposed for the construction of l.p.o families in the natural CR3BP [15]. However, it is not known a-priori at which positions periodic solutions exist and therefore the nodes should remain variable. If the reader desires to use the TLT correction procedure for orbits with large amplitudes, it is advised to carefully check if the periodic solution complies with the desired characteristics.

C.4.3. Hamiltonian path constraints

At the outset of the thesis project the TLT algorithm was the preferred methodology to construct the l.p.o families. The logic behind this line of thought was based on two observations. First of all, shooting algorithms in conjunction with a numerical continuation procedure have proven to be a robust method for the construction of l.p.o families in the natural CR3BP [24], elliptic restricted three-body problem [25] and even in non-ballistic versions of the CR3BP where the propulsive force is generated by a solar sail [16]. Secondly, literature concerning the two-level targeter [4] state that it can be augmented with additional path constraints that depend on a combination of \bar{R}_k , \bar{V}_k and/or t_k . A TLT algorithm with periodicity constraints and Hamiltonian path constraints is able to construct the α -varying and a_{lt} -varying l.p.o families since periodic solutions with specific Hamiltonian values can be generated. The remainder of this section presents the efforts that have been undertaken to implement these path constraints and reports on the performance of the resulting TLT algorithm.

The derivation process of the hamiltonian path constraint is identical to the derivation of the periodicity constraint in Section C.4.1. The constraint is defined below in Equation C.38. Although the thrust parameters influence the Hamiltonian of an orbit, it should be noted these are constant throughout the TLT correction process. Therefore, the constraint's only explicit dependencies are R_k and V_k^+ .

$$\begin{aligned}\eta_k(\bar{R}_k, \bar{V}_k^+, a_{lt}, \alpha) &= H_{lt} = H_{nat} - \bar{R}_k \cdot \bar{a}_{lt} = -\frac{1}{2}C - \bar{R}_k \cdot \langle [a_{lt}\cos(\alpha) \quad a_{lt}\sin(\alpha) \quad 0]^T \rangle \\ &= -\frac{1}{2}(x_k^2 + y_k^2) - \frac{1-\mu}{r_{13}} - \frac{\mu}{r_{23}} + \frac{1}{2}V_k^2 - \langle \bar{R}_k, [a_{lt}\cos(\alpha) \quad a_{lt}\sin(\alpha) \quad 0]^T \rangle = \eta_k(\bar{R}_k, \bar{V}_k^+)\end{aligned}\quad (\text{C.38})$$

Similar to the periodicity constraint described in Section C.4.1, the defect is computed as the difference between the desired Hamiltonian value, denoted as η_k^* and the current value of the hamiltonian as shown in Equation C.39

$$\delta\eta_k = \eta_k^* - \eta_k = H_{lt_k}^* - H_{lt_k} \quad (\text{C.39})$$

The next step in derivation constraint is to relate the design variables to the constraint variables via a first order expansion. This expansion is shown below in Equation C.40.

$$\delta\eta_k = \left(\frac{\partial\eta_k}{\partial\bar{R}_k} + \frac{\partial\eta_k}{\partial\bar{V}_k^+} \frac{\partial\bar{V}_k^+}{\partial\bar{R}_k} \right) \delta\bar{R}_k + \left(\frac{\partial\eta_k}{\partial t_k} + \frac{\partial\eta_k}{\partial\bar{V}_k^+} \frac{\partial\bar{V}_k^+}{\partial t_k} \right) \delta t_k + \left(\frac{\partial\eta_k}{\partial V_k^+} \frac{\partial\bar{V}_k^+}{\partial\bar{R}_{k+1}} \right) \delta\bar{R}_{k+1} + \left(\frac{\partial\eta_k}{\partial\bar{V}_k^+} \frac{\partial\bar{V}_k^+}{\partial t_{k+1}} \right) \delta t_{k+1} \quad (\text{C.40})$$

The partial derivatives in the aforementioned Taylor series expansion can be obtained from Table C.3, except from $\frac{\partial\eta_k}{\partial\bar{R}_k}$ and $\frac{\partial\eta_k}{\partial\bar{V}_k^+}$ which are shown below in Equation C.41.

$$\frac{\partial\eta_k}{\partial\bar{R}_k} = \begin{bmatrix} \frac{\partial\eta_k}{\partial x} \\ \frac{\partial\eta_k}{\partial y} \\ \frac{\partial\eta_k}{\partial z} \end{bmatrix}^T = \begin{bmatrix} -x + \frac{1-\mu}{r_{13}^3}(x+\mu) + \frac{\mu}{r_{23}^3}(x-1+\mu) - a_{lt}\cos(\alpha) \\ -y + \frac{1-\mu}{r_{13}^3}y + \frac{\mu}{r_{23}^3}y - a_{lt}\sin(\alpha) \\ \frac{1-\mu}{r_{13}^3}z + \frac{\mu}{r_{23}^3}z \end{bmatrix}^T, \quad \frac{\partial\eta_k}{\partial\bar{V}_k^+} = \begin{bmatrix} \frac{\partial\eta_k}{\partial\dot{x}} \\ \frac{\partial\eta_k}{\partial\dot{y}} \\ \frac{\partial\eta_k}{\partial\dot{z}} \end{bmatrix}^T = \begin{bmatrix} \dot{x} \\ \dot{y} \\ \dot{z} \end{bmatrix}^T \quad (\text{C.41})$$

The full version of the periodicity constraint is defined below in Equation C.42.

$$\begin{aligned}\delta\eta_k &= \left(\begin{bmatrix} -x + \frac{1-\mu}{r_{13}^3}(x+\mu) + \frac{\mu}{r_{23}^3}(x-1+\mu) - a_{lt}\cos(\alpha) \\ -y + \frac{1-\mu}{r_{13}^3}y + \frac{\mu}{r_{23}^3}y - a_{lt}\sin(\alpha) \\ \frac{1-\mu}{r_{13}^3}z + \frac{\mu}{r_{23}^3}z \end{bmatrix}^T - \begin{bmatrix} \dot{x} \\ \dot{y} \\ \dot{z} \end{bmatrix}^T \cdot B_{k+1,k}^{-1} A_{k+1,k} \right) \delta\bar{R}_k \\ &\quad + \left(\begin{bmatrix} \dot{x} \\ \dot{y} \\ \dot{z} \end{bmatrix}^T \cdot (\bar{a}_k^+ - D_{k,k+1} B_{k,k+1}^{-1} \bar{V}_k^+) \right) \delta t_k + \left(\begin{bmatrix} \dot{x} \\ \dot{y} \\ \dot{z} \end{bmatrix}^T \cdot B_{k+1,k}^{-1} \right) \bar{R}_{k+1} + \left(- \begin{bmatrix} \dot{x} \\ \dot{y} \\ \dot{z} \end{bmatrix}^T \cdot B_{k+1,k} \bar{V}_{k+1}^- \right) \delta t_{k+1}\end{aligned}\quad (\text{C.42})$$

The performance of this constraint is evaluated via a simple test case. The objective is to find natural L_1 H-L orbit with a specific Hamiltonian. The input to the TLT targeter consists of a periodic libration point orbit

with a Hamiltonian that slightly differs from the desired Hamiltonian value according to $\Delta H_{lt} = 1.0 \cdot 10^{-6}$. The Hamiltonian path constraint is enforced at the initial node of the trajectory which leads to the results as presented in Table C.4.

$L_1 (a_{lt} = 0.0, \alpha = 0.0, H_{lt} = -1.594170243726332), n = 10$					
Seed solution	Input deviations	TLT result			
$\ \Delta R\ $	$5.5476770323909 \cdot 10^{14}$	$5.5476770323909 \cdot 10^{14}$	$3.53674153196 \cdot 10^{-10}$		
$\ \Delta V\ $	$1.5003029806242 \cdot 10^{12}$	$1.5003029806242 \cdot 10^{12}$	$8.27673925667 \cdot 10^{-11}$		
$\ \Delta H_{lt}\ $	0.000000000000000	-1.000000000000000	$\cdot 10^{-6}$	$1.80496935643 \cdot 10^{-7}$	

Table C.4: Evaluation of the Hamiltonian path constraints. It should be stressed that the TLT result was obtained after 30 iterations and the TLT process was manually terminated since the algorithm showed cyclic behaviour. 10 nodes were used during the TLT correction process.

The results of the test case show that the Hamiltonian path constraint does not provide the TLT corrector with the ability to find periodic orbits of a desired Hamiltonian. Although the position and velocity discrepancies approach the tolerances as specified in Table A.7, the Hamiltonian of the resulting trajectory does not come close to the desired value. It should be stressed that the state and Hamiltonian discrepancies with the same order of magnitude were already obtained after the third iteration of the TLT algorithm. However the algorithm did not seem to improve after that and therefore the correction process was killed after 30 iterations. A possible cause for the non-convergence is the nonlinear relationship between the Hamiltonian constraints and the design variables which makes the problem difficult to solve [5]. The inability of the TLT algorithm to refine orbits to a desired Hamiltonian solution creates the need for another correction methodology that has the ability to correct orbits to the desired Hamiltonian value. This algorithm is presented in Section C.5.

C.5. Collocation root-finding scheme

The section discusses the root-finding schemes that, in conjunction with numerical continuation algorithms, generate the three types of l.p.o families. Subsection C.5.1 presents the root-finder algorithm for one segment whereas C.5.2 presents additional constraints. The totality of this section with the matter discussed in Section B.2.1 is in literature referred to as the 12th order Legendre-Gauss-Lobatto collocation method.

C.5.1. General collocation root-finding scheme

The design vector, defect vector and jacobian of the root-finding scheme for a single segment can be found below in Equation C.43. Please note that the computation of the design and defect vector are discussed in Section B.2.1.

$$\mathbf{X}_i = \begin{bmatrix} \bar{x}_{i,1} \\ t_{i,1} \\ \bar{x}_{i,3} \\ \bar{x}_{i,5} \\ \bar{x}_{i+1,1} \\ t_{i+1,1} \end{bmatrix}, \quad \mathbf{F}_i = \begin{bmatrix} \bar{\zeta}_{i,2} \\ \bar{\zeta}_{i,4} \\ \bar{\zeta}_{i,6} \end{bmatrix}, \quad D\mathbf{F}_i = \begin{bmatrix} \frac{\partial \bar{\zeta}_{i,2}}{\partial \bar{x}_{i,1}} & \frac{\partial \bar{\zeta}_{i,2}}{\partial t_{i,1}} & \frac{\partial \bar{\zeta}_{i,2}}{\partial \bar{x}_{i,3}} & \frac{\partial \bar{\zeta}_{i,2}}{\partial \bar{x}_{i,5}} & \frac{\partial \bar{\zeta}_{i,2}}{\partial \bar{x}_{i+1,1}} & \frac{\partial \bar{\zeta}_{i,2}}{\partial t_{i+1,1}} \\ \frac{\partial \bar{\zeta}_{i,4}}{\partial \bar{x}_{i,1}} & \frac{\partial \bar{\zeta}_{i,4}}{\partial t_{i,1}} & \frac{\partial \bar{\zeta}_{i,4}}{\partial \bar{x}_{i+1,1}} & \frac{\partial \bar{\zeta}_{i,4}}{\partial t_{i,1}} & \frac{\partial \bar{\zeta}_{i,4}}{\partial \bar{x}_{i,3}} & \frac{\partial \bar{\zeta}_{i,4}}{\partial t_{i+1,1}} \\ \frac{\partial \bar{\zeta}_{i,6}}{\partial \bar{x}_{i,1}} & \frac{\partial \bar{\zeta}_{i,6}}{\partial t_{i,1}} & \frac{\partial \bar{\zeta}_{i,6}}{\partial \bar{x}_{i,3}} & \frac{\partial \bar{\zeta}_{i,6}}{\partial \bar{x}_{i,5}} & \frac{\partial \bar{\zeta}_{i,6}}{\partial \bar{x}_{i+1,1}} & \frac{\partial \bar{\zeta}_{i,6}}{\partial t_{i+1,1}} \end{bmatrix} \quad (C.43)$$

Similar to the TLT corrector, the multivariate root finding scheme can compute the required correction for the complete mesh at once by collecting the design vectors, defect vectors and jacobian of each segments and merge them into a single design vector, defect vector and jacobian according to Equation C.44.

$$\mathbf{X} = \begin{bmatrix} \mathbf{X}_1 \\ \vdots \\ \mathbf{X}_{n-1} \end{bmatrix}, \quad \mathbf{F} = \begin{bmatrix} \mathbf{F}_1 \\ \vdots \\ \mathbf{F}_{n-1} \end{bmatrix} \quad (C.44)$$

$$D\mathbf{F} = \left[\begin{array}{cccccc} \frac{\partial F_1}{\partial \bar{x}_{1,1}} & \frac{\partial F_1}{\partial t_{1,1}} & \frac{\partial F_1}{\partial \bar{x}_{1,3}} & \frac{\partial F_1}{\partial \bar{x}_{1,5}} & \frac{\partial F_1}{\partial \bar{x}_{2,1}} & \frac{\partial F_1}{\partial t_{2,1}} \\ & & & & \frac{\partial F_2}{\partial \bar{x}_{2,1}} & \frac{\partial F_2}{\partial t_{2,1}} \\ & & & & \frac{\partial F_2}{\partial \bar{x}_{2,3}} & \frac{\partial F_2}{\partial \bar{x}_{2,5}} \\ & & & & \frac{\partial F_2}{\partial \bar{x}_{3,1}} & \frac{\partial F_2}{\partial t_{3,1}} \\ & & & & \ddots & \ddots & \ddots \\ & & & & \frac{\partial F_{n-1}}{\partial \bar{x}_{n-1,1}} & \frac{\partial F_{n-1}}{\partial t_{n-1,1}} & \frac{\partial F_{n-1}}{\partial \bar{x}_{n-1,3}} & \frac{\partial F_{n-1}}{\partial \bar{x}_{n-1,5}} & \frac{\partial F_{n-1}}{\partial \bar{x}_{n,1}} & \frac{\partial F_{n-1}}{\partial t_{n,1}} \end{array} \right] \quad (C.45)$$

The partial derivatives that constitute the jacobian in Equation C.43 are approximated via the complex step method [17]. This technique computes the partial derivative of the defect vector \mathbf{F} with respect to a single design variable X_{kj} by re-evaluation of the defect vector with a modified version of the design variable of interest according to $X_{kj,\text{complex}} = X_{kj} + \sigma i$. The partial derivative with respect to X_{kj} is then obtained via Equation C.46.

$$\frac{\partial \mathbf{F}}{\partial X_{kj}} \approx \frac{\text{Im}\left(\mathbf{F}(X_{kj,\text{complex}})\right)}{\sigma} \quad (\text{C.46})$$

The complex step method avoids the need for manual derivation of partial derivatives which is inherent to the finite difference approach as described in Section C.4.1. Furthermore, the quadratic convergence of the complex step method is preserved as long as $\epsilon < 10^{-8}$, resulting in a derivative estimation of $\mathcal{O}(10^{-16})$. At these tiny increments, finite-difference approaches experience subtractive cancellation errors and produce unreliable estimates [18].

The existing solution is updated via a line-search procedure which finds a correction step by reducing the computed correction step with an attenuation factor k according to Equation C.47.

$$\mathbf{X}^{n+1} = \mathbf{X}^n + k \Delta \mathbf{X}^n \quad (\text{C.47})$$

The attenuation factor that provides a correction step resulting the defect vector with the smallest euclidian norm is selected as the new solution. The range of values used for parameter κ can be found in Table A.8.

C.5.2. Additional constraints

Various types of constraints are necessary to enable the collocation algorithm to compute l.p.o families. Regardless of the family that is being generated, the size of the jacobian for a trajectory consisting of n nodes will be $(18(n-1) + 7 \times 19(n-1) + 7)$. The remainder of this section is dedicated to the explanation of these constraints

Periodicity constraint

Periodicity is of the solution is enforced through an equality constraint in the form of the state discrepancy between the initial state. The dimensions of the resulting constraints are $(6 \times 19(n-1) + 7)$, where only the first and final seven columns contain non-zero entries, as shown below in Equation C.48.

$$\mathbf{F}_{\text{periodicity}} = [\delta(\bar{x}_{1,1} - \bar{x}_{n,1})], \quad D\mathbf{F}_{\text{periodicity}} = \begin{bmatrix} \frac{\partial \bar{x}_{1,1} - \bar{x}_{n,1}}{\partial \bar{x}_{1,1}} & \frac{\partial \bar{x}_{1,1} - \bar{x}_{n,1}}{\partial t_{1,1}} & 0 & \dots & 0 & \frac{\partial \bar{x}_{1,1} - \bar{x}_{n,1}}{\partial \bar{x}_{n,1}} & \frac{\partial \bar{x}_{1,1} - \bar{x}_{n,1}}{\partial t_{n,1}} \end{bmatrix} \quad (\text{C.48})$$

Phase constraint for H_{lt} -varying families

The spacing of the members of the H_{lt} -varying l.p.o families are determined via pseudo-arch length continuation procedure. To ensure consistency in the spacing throughout the family, it is necessary that the relative phase drift between orbit members is minimized. Literature suggests the use of a Poincare phase condition in the form of Equation C.49 [10]. It comprises the inner product of the state increment between the family members \bar{x}^{n-1} and \bar{x}^n between their initial states and the state derivative of \bar{x}^n .

$$\delta\phi = \langle \bar{x}_{1,1}^n - \bar{x}_{1,1}^{n-1}, \dot{\bar{x}}_{1,1}^n \rangle \quad (\text{C.49})$$

The disadvantage of the Poincare phase condition is that the phase error propagates over the family [10]. Hence, this thesis project introduces two adaptions to decrease the phase drift over the l.p.o family. First of all, the state increment over the complete becomes constant and is defined as the state discrepancy between the initial state of the first family member and the equilibrium point. Secondly, the initial node state derivative of the already computed member $\dot{\bar{x}}_{1,1}^{n-1}$ is replaced by the state derivative of the to be computed member $\dot{\bar{x}}_{1,1}^n$. The result is shown below in Equation C.50.

$$\delta\phi = k \cdot \frac{(\bar{x}_{1,1}^1 - \bar{x}_{eq})^T \dot{\bar{x}}_{1,1}^n}{||(\bar{x}_{1,1}^1 - \bar{x}_{eq})^T \dot{\bar{x}}_{1,1}^n||} \quad (\text{C.50})$$

It can be observed that the resulting phase constraint is normalized and multiplied by an amplification factor k . The underlying reason for this modification is that it allows the user to control the constraint magnitude and thereby the sensitivity of the collocation procedure to phase constraint. The value of k has been determined through a trial and error procedure and can be found in Equation A.8.

$$\mathbf{F}_{\text{phase}} = [\delta\phi], \quad D\mathbf{F}_{\text{phase}} = \begin{bmatrix} \frac{\partial\phi}{\partial x_{1,1}} & \frac{\partial\delta\phi}{\partial t_{1,1}} & 0 & \dots & 0 \end{bmatrix} \quad (\text{C.51})$$

Hamiltonian constraint for α_{lt} -varying and α -varying families

The members of a specific α_{lt} -varying and α -varying families should have an identical Hamiltonian. This is achieved through an equality constraint at the first node of the trajectory in the form of the discrepancy between the desired Hamiltonian and the actual value of the Hamiltonian of the first node. The dimensions of the resulting constraints are $[1 \times 19(n - 1) + 7]$, where only the first seven columns contain non-zero partial derivatives, as shown below in Equation C.52.

$$\mathbf{F}_{\text{hamiltonian}} = [H_{lt}^* - H_{lt_{1,1}}], \quad D\mathbf{F}_{\text{hamiltonian}} = \begin{bmatrix} \frac{\partial H_{lt}^* - H_{lt_{1,1}}}{\partial x_{1,1}} & \frac{\partial H_{lt}^* - H_{lt_{1,1}}}{\partial t_{1,1}} & 0 & \dots & 0 \end{bmatrix} \quad (\text{C.52})$$

D

Extended analysis of acceleration-varying families

In Chapter 1 of this report, twelve a_{lt} -varying families at $H_{lt} = 1.525$ are presented for different values of the acceleration orientation at both zero acceleration contours. More a_{lt} -varying families have been constructed at other Hamiltonian values ($H_{lt} = [-1.55, -1.50]$) but these are not included in Chapter 1 for sake of conciseness. The remainder of this addendum is dedicated to presenting exactly these a_{lt} -varying families for reasons of completeness. Subsection D.0.1 discusses the a_{lt} -varying families with $H_{lt} = -1.55$ whereas Subsection D.0.2 presents the a_{lt} -varying families with $H_{lt} = -1.50$.

D.0.1. a_{lt} -varying families at $H_{lt} = -1.55$

Figure D.1 shows a planar projection of six a_{lt} -varying families emanating from the E_1 contour whereas Figure D.2 presents the Stability indices of these families as well as the evolution of the orbital period along them.

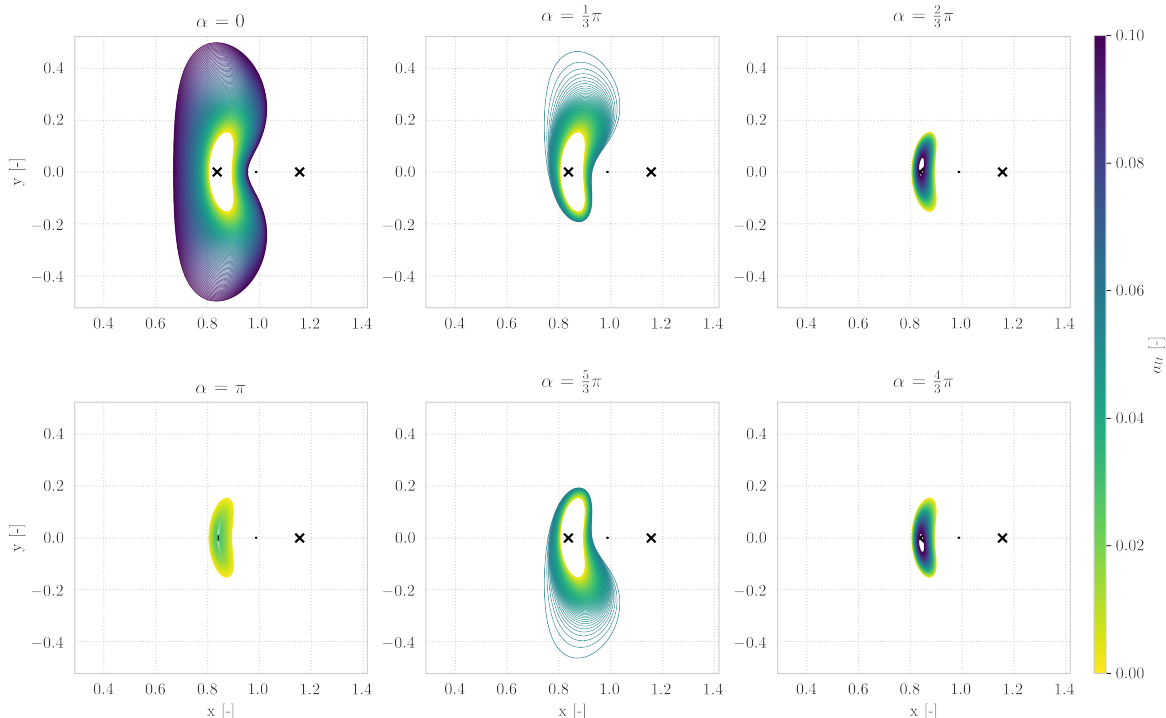


Figure D.1: Six a_{lt} -varying families at $H_{lt} = -1.55$ for different α values that emanate from E_1 . The colour of an l.p.o corresponds to its acceleration magnitude according to the colourbar provided on the right side of the Figure.

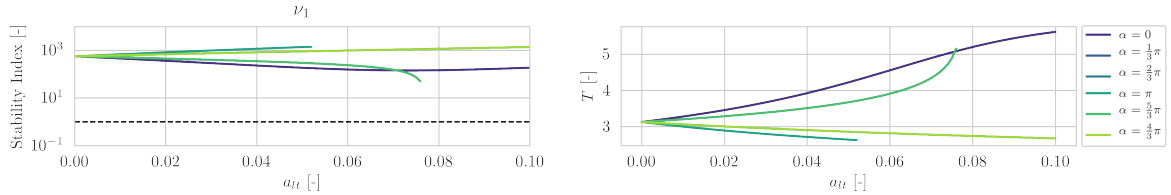


Figure D.2: The left subplot displays the stability index of the eigenvalue related the saddle subspace. The right subplot shows evolution of T as a function of a_{lt} .

The planar projections support the conclusions provided in Chapter 1 of the report which state that a growing acceleration orientation enlarges (shrinks) the orbit size in case of positive (negative) collinear acceleration or distort the orbit geometry into 'ear-shaped' solutions for non-collinear acceleration orientation. The evolution of the stability indices in Figure D.2 supports a different conclusion than presented in Chapter 1. At $H_{lt} = -1.55$ it can be observed that an increase in acceleration orientation either monotonically decreases or increases the Saddle stability index, apart from the $\alpha = 0$ family. Another interesting observation is that the orbital period evolves in an opposite way compared to the saddle stability indices.

These analyses are repeated for a_{lt} -varying families emanating from E_2 . Figure D.3 shows a planar projection of six a_{lt} -varying families emanating from the E_2 contour whereas Figure D.4 presents the Stability indices of these families as well as the evolution of the orbital period along them.

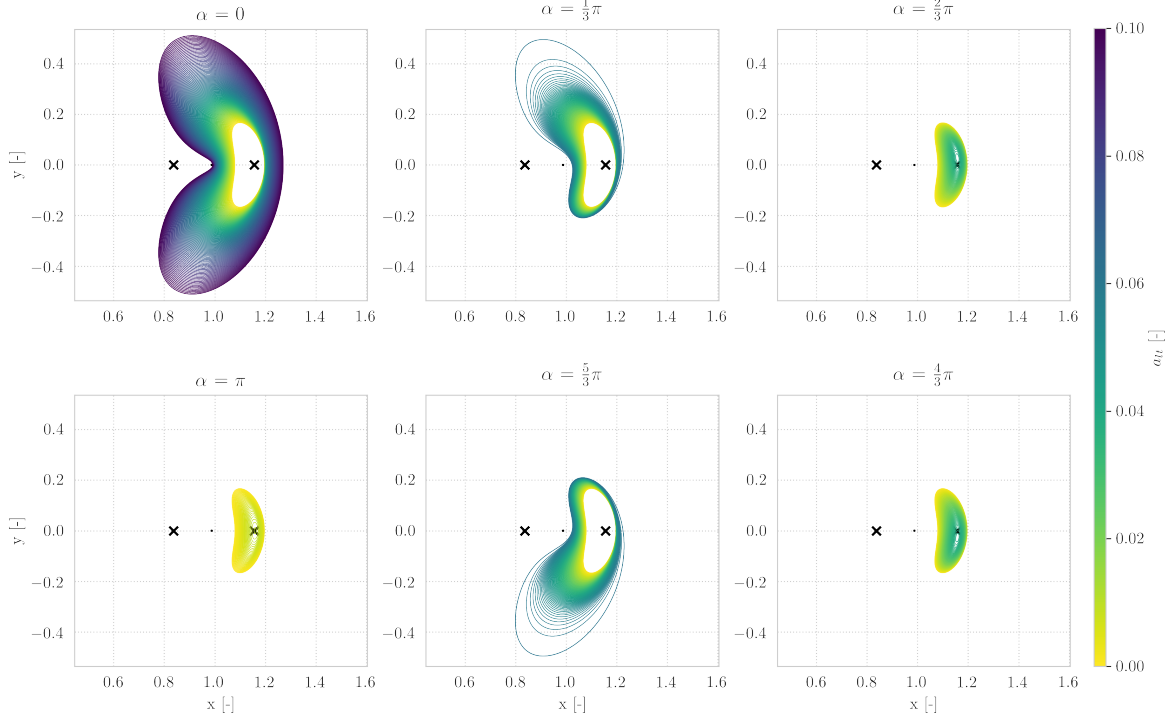


Figure D.3: Six a_{lt} -varying families at $H_{lt} = -1.55$ for different α values that emanate from E_2 . The colour of an l.p.o corresponds to its acceleration magnitude according to the colourbar provided on the right side of the Figure.

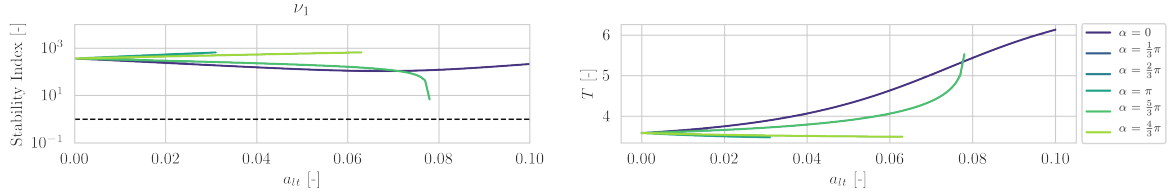


Figure D.4: The left subplot displays the stability index of the eigenvalue related the saddle subspace. The right subplot shows evolution of T as a function of a_{lt} .

Figures D.3 and D.4 show that the acceleration magnitude has the same effect on the geometry, saddle stability index and orbital period of E_2 a_{lt} -varying families as on families arising from E_1 .

D.0.2. a_{lt} -varying families at $H_{lt} = -1.50$

Figure D.5 shows a planar projection of six a_{lt} -varying families emanating from the E_1 contour whereas Figure D.6 presents the stability indices of these families as well as the evolution of the orbital period along them.

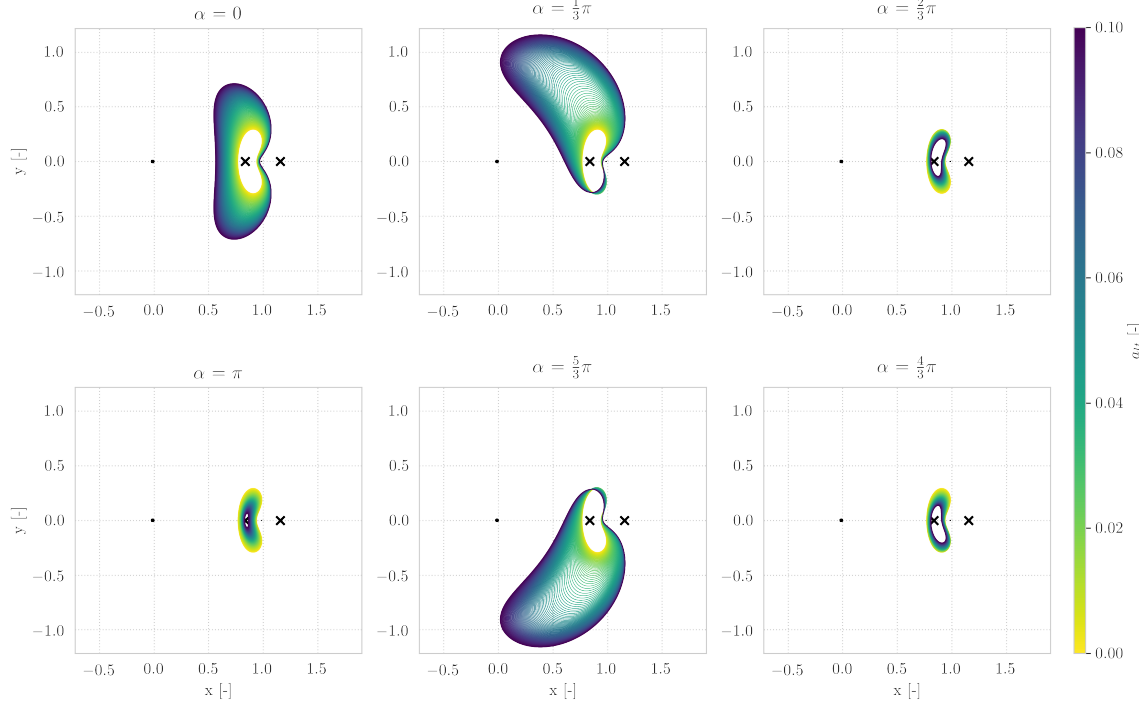


Figure D.5: Six a_{lt} -varying families at $H_{lt} = -1.50$ for different α values that emanate from E_1 . The colour of an l.p.o corresponds to its acceleration magnitude according to the colourbar provided on the right side of the Figure.

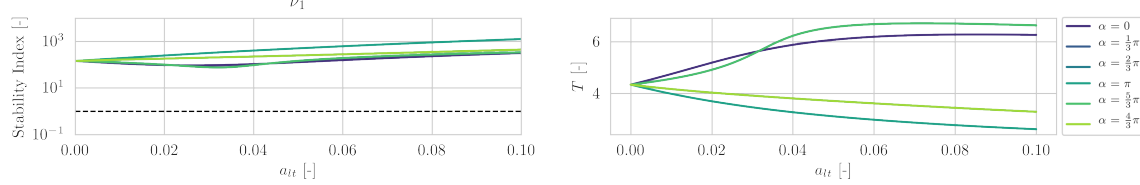


Figure D.6: The left subplot displays the stability index of the eigenvalue related the saddle subspace. The right subplot shows evolution of T as a function of a_{lt} .

The planar projections support the conclusions provided in Chapter 1 of the report. These conclusions state that an increase in acceleration orientation can enlarge (shrink) the orbit size in case of positive (negative) collinear acceleration or distort the orbit geometry into 'ear-shaped' solutions for non-collinear acceleration orientation. The evolution of the stability indices in Figure D.6 also support the conclusions drawn in Chapter 1 and previous Subsection. At $H_{lt} = -1.50$ it can be observed that an increase in acceleration orientation monotonically increases the Saddle stability index, apart from the $\alpha = [0, \frac{1}{3}\pi, \frac{5}{3}\pi]$ families. Furthermore, it can be observed that the orbital period evolves in an opposite way compared to the saddle stability indices. The a_{lt} -varying families emanating from E_2 support these conclusions as well. The graphical projections of the E_2 a_{lt} -varying families can be found in Figure D.8 whereas the evolution of the Saddle stability indices and orbital periods are provided in Figure D.7 and complete the analysis of the a_{lt} -varying families.

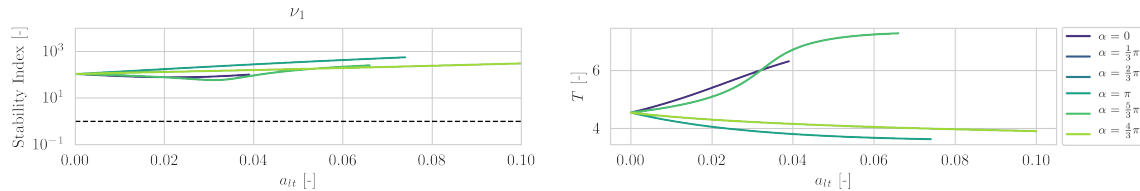


Figure D.7: The left subplot displays the stability index of the eigenvalue related the saddle subspace. The right subplot shows evolution of T as a function of a_{lt} .

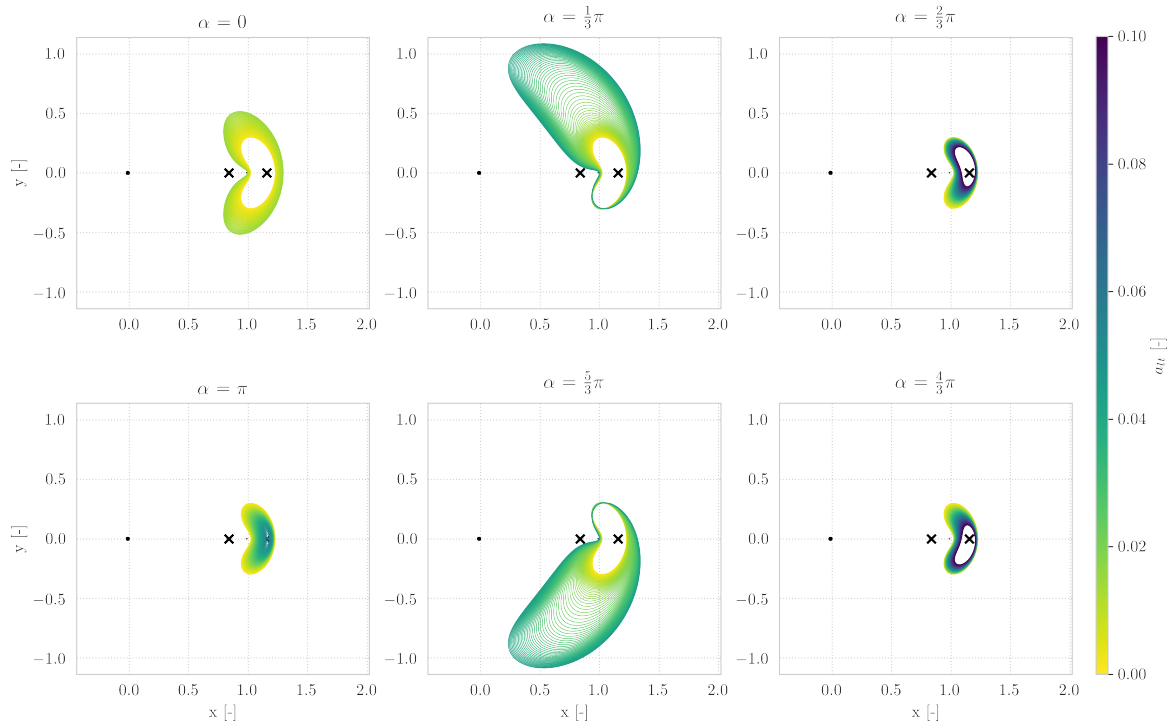
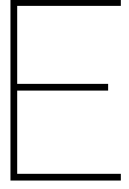


Figure D.8: Six a_{lt} -varying families at $H_{lt} = -1.50$ for different α values that emanate from E_{2t} . The colour of an l.p.o corresponds to its acceleration magnitude according to the colourbar provided on the right side of the Figure.



Verification and Validation

The totality techniques presented in Appendices A-C allow the numerical approximation of equilibria contours and l.p.o families. The purpose of this adjunct is to prove the veracity of these approximation thereby establishing the credibility of the results presented in Chapter 1 and Appendix D. Section E.1 presents the verification procedure for the root-finding algorithms used to create the equilibria contours. The correctness of the Floquet controller is proved in Section E.3. Finally correctness of the collocation algorithm and continuation procedure is discussed in Section E.5.

E.1. Equilibria contour verification

The equilibria contours, presented in Chapter 1, comprise multiple sets of positions where a stationary space-craft experiences a net zero acceleration. Each equilibrium is calculated via the root-finding algorithm as presented in Section C.2. The algorithm's performance is verified by inspecting whether the defect vector of each solution satisfies the tolerances as specified in Table A.8.

Defect vector verification of α -varying equilibria contours

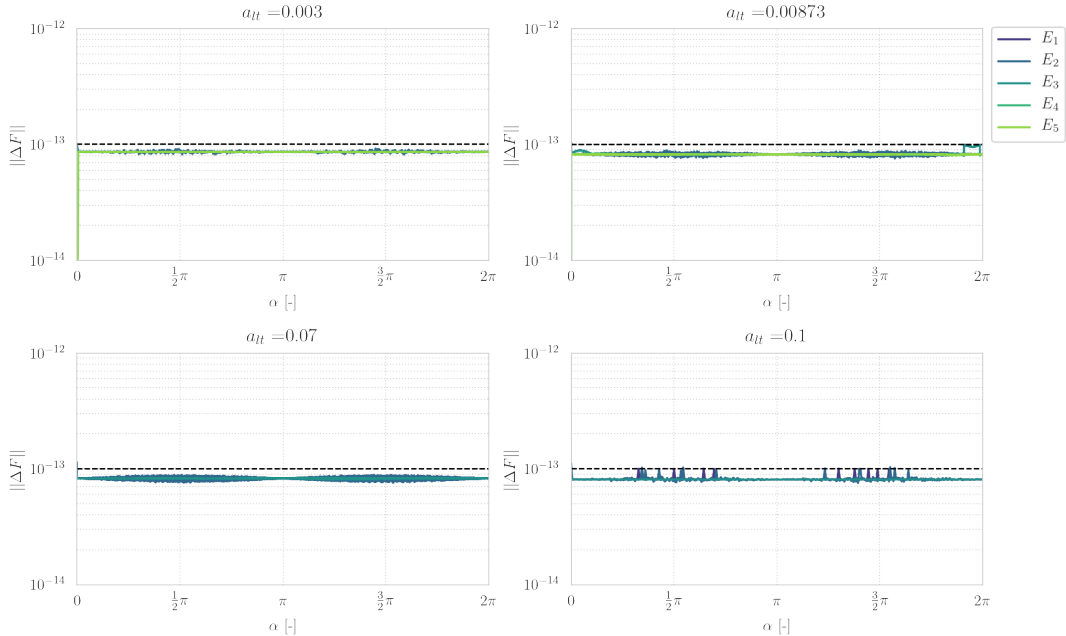


Figure E.1: Each subplot shows the magnitude of defect vector of the complete equilibria contour at a specified acceleration. This Figure proves a robust performance of the root-finding algorithm over the complete range of investigated low-thrust accelerations.

It can be concluded from Figure E.1 that the root-finding algorithm performs as expected since each solution adheres to the defect tolerances.

While Figure E.1 confirms a correct implementation of the multivariate root-finding technique. It does not prove that the positions produced by the algorithm are actually equilibria. According to [34], a spacecraft positioned exactly at a Lagrangian point without any velocity in the rotating reference frame, will forever stay at this Lagrangian point. Validation of the algorithm's solutions are obtained by explicit propagation for half a synodic period. The state deviations with respect to the equilibrium point after propagation are shown below in Figure E.2

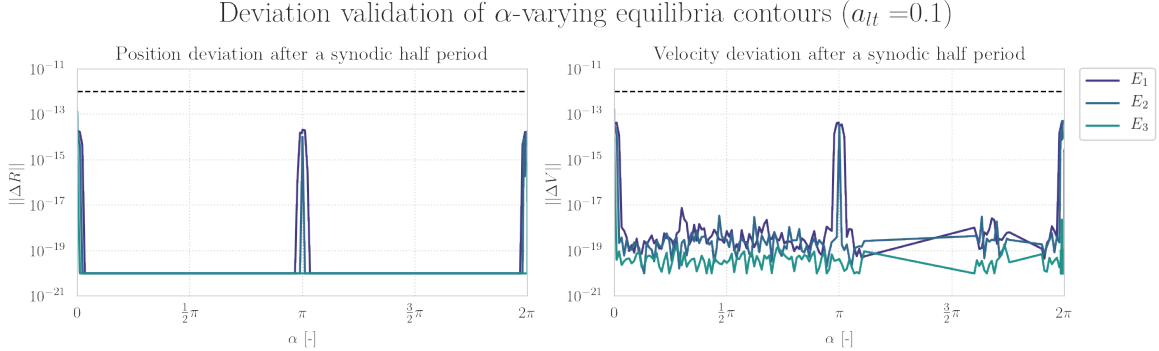


Figure E.2: The left subfigure proves that the positional deviation after a synodic half-period remains near-machine limits. The right subfigure proves that the velocity deviation is negligible. The black dotted line indicates a threshold for machine noise. All deviation smaller than $10 \cdot 1.0^{-20}$ have been set to $1.0 \cdot 10^{-20}$ for visualization purposes.

The data in Figure E.2 shows that position and velocity deviation are negligible after propagation of a synodic half period. These deviations are a result of the errors associated with propagation using explicit integrator scheme of Section B.1 and a near-perfect computation of the equilibrium position via the root-finding algorithm of Section C.2. It is interesting to see that the deviations of the seed solutions are considerably larger compared to the deviations at other contour locations. A possible reason for this phenomenon is that the seed solutions are compute via the univariate Newton-Raphson method instead of a multivariate root-finding method.

Figure E.1 proves a robust performance of the root-finding algorithm over the complete range of acceleration magnitudes whereas Figure E.2 confirms that the solutions provided by the algorithm are in fact libration points of the CR3BP-LT. Together, these figures provide confidence in the veracity of the equilibria contours.

E.2. Floquet targeter verification

The veracity of the Floquet targeter is examined by investigating how the error of the seed solutions evolves over a range of in-plane amplitudes and thrust parameters. These errors should evolve smoothly since the CR3BP-LT is a smooth system. The amplitude range is determined by the maximum amplitude offset as specified in Section A.6. The evolution is checked for all possible values of thrust orientations and the complete range of investigated thrust acceleration as specified in Chapter 1 of this report. The error evolutions of the three aforementioned variables. can be found in Figures E.3-E.5.

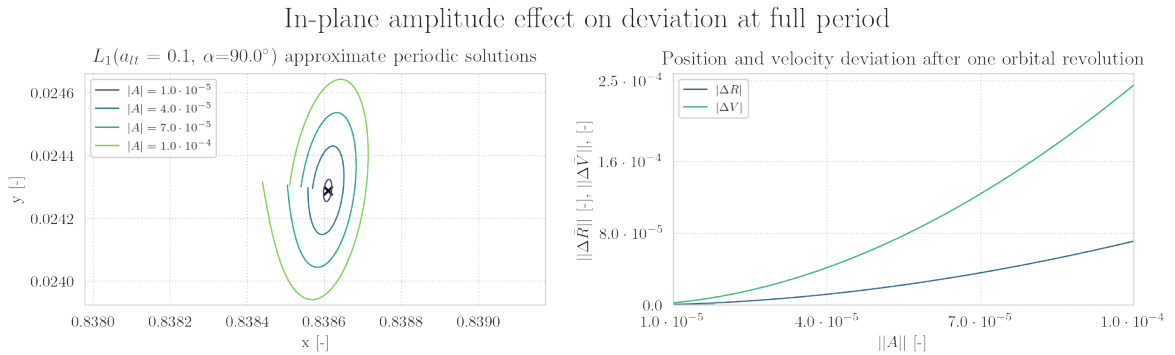


Figure E.3: The evolution of full period deviations of approximate periodic solutions due to a varying offset magnitude.

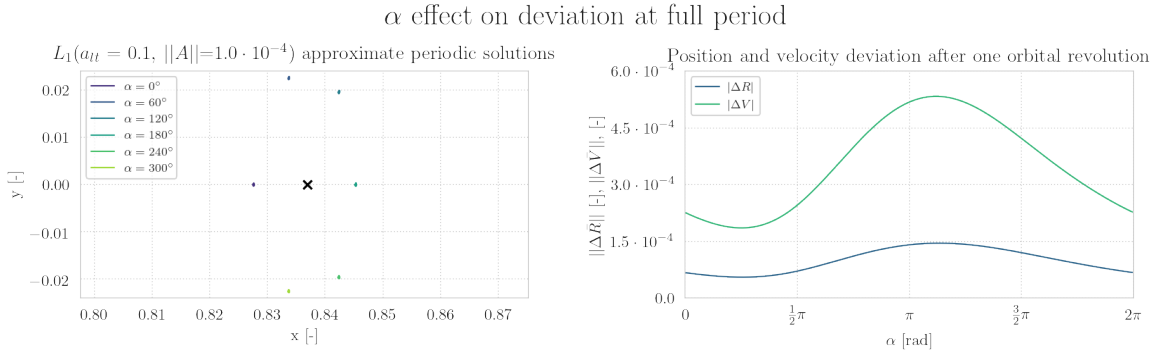


Figure E.4: The evolution of full period deviations of approximate periodic solutions due to a varying acceleration orientation. The natural L_1 point is shown as reference.

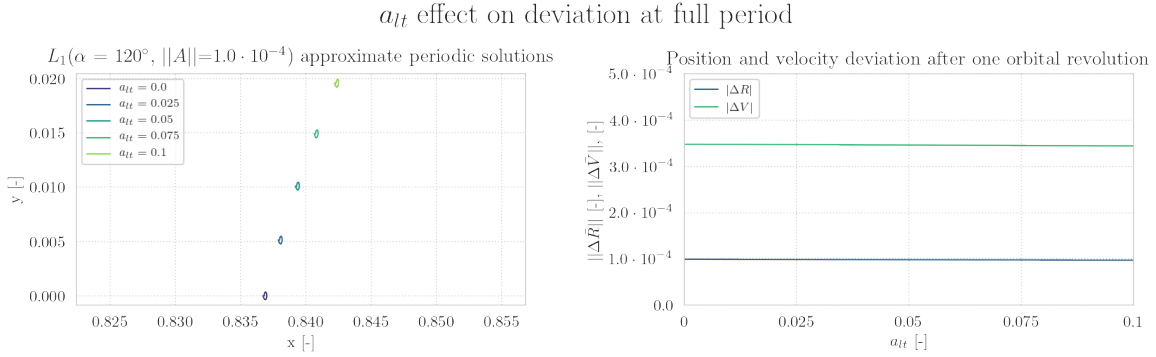


Figure E.5: The evolution of full period deviations of approximate periodic solutions due to a varying acceleration magnitude.

Figures E.3-E.5 show that the error of the approximate seed solutions evolves smoothly over the range of offset amplitudes as specified in Table A.6. Hence a robust performance of the Floquet targeter algorithm is proved within this range of offset amplitudes. Figure E.4 shows that the error seems to grow when the libration point is located closer to the secondary body. This can be explained due to the higher unwinding behaviour that is experienced in regions closer to the Moon. The validation of the Floquet targeter is accomplished by benchmarking its performance against Richardson third order method [30]. Richardson's approximation is a widely used methodology for computation of approximate libration point orbits in the CR3BP [30]. A comparison between the two methods is provided below in Table E.1. The natural H-L orbit around L_1 lagrangian point is selected as a test case. The maximum in-plane amplitude specified in Table A.6 is selected as in-plane amplitude..

State	Floquet Targeter		Richardson Method		Difference	
x	8.368151483688	$\cdot 10^{-1}$	8.368151483689	$\cdot 10^{-1}$	-1.0	$\cdot 10^{-12}$
y	1.2246467991474	$\cdot 10^{-20}$	0.0		-1.2246467991474	$\cdot 10^{-20}$
z	0.0		0.0		0.0	
\dot{x}	0.0		0.0		0.0	
\dot{y}	8.3722730179494	$\cdot 10^{-4}$	8.3784707256357	$\cdot 10^{-4}$	-6.197707686299	$\cdot 10^{-7}$
\dot{z}	0.0		0.0		0.0	
T	2.6915797202527		2.6915816604254		-1.940172699832488	$\cdot 10^{-6}$

Table E.1: Initial states for a natural H-L orbit around L_1 with an in-plane amplitude $A_x = 1.0 \cdot 10^{-4}$. It can be observed that the two methods provide a near-identical position but the methods provide a different starting velocity and estimation of the orbital period. The data regarding Richardson's method has been obtained from [24].

It can be concluded from Table E.1 that the positional difference between the two methods is in the range of machine noise. Furthermore, it is observed that there are significant differences between the Floquet targeter and Richardson's third order method in terms of velocity and orbital period. The velocity difference is

attributed to the different order of the methods. The Floquet targeter determines a velocity correction based upon a first-order linearization of the dynamics whereas Richardson's methods cancels out secular components of the method up to the third order.

Collectively, Figures E.3- E.5 and Table E.1 prove the correctness of the Floquet targeter scheme as described in Section C.4.

E.3. Two-level targeter verification

The TLT algorithm is verified by correcting an approximate solution around an artificial L_1 equilibrium. The characteristics of the specific seed solution are chosen such that the full functionality of the algorithm is tested. The maximum low-thrust acceleration magnitude $a_{lt} = 0.1$ is chosen with an orientation perpendicular to the x-axis of the synodic reference frame ($\alpha = 90^\circ$). This ensures that the approximate seed solution is located well above the collinear equilibria. Furthermore, an in-plane amplitude is chosen that is almost two orders of magnitude larger than the settings specified in Table A.6. These settings establish a test case which allows to test the full functionality of the TLT algorithm. The behaviour of the TLT algorithm during the correction procedure of this orbit is shown below in Figure E.6.

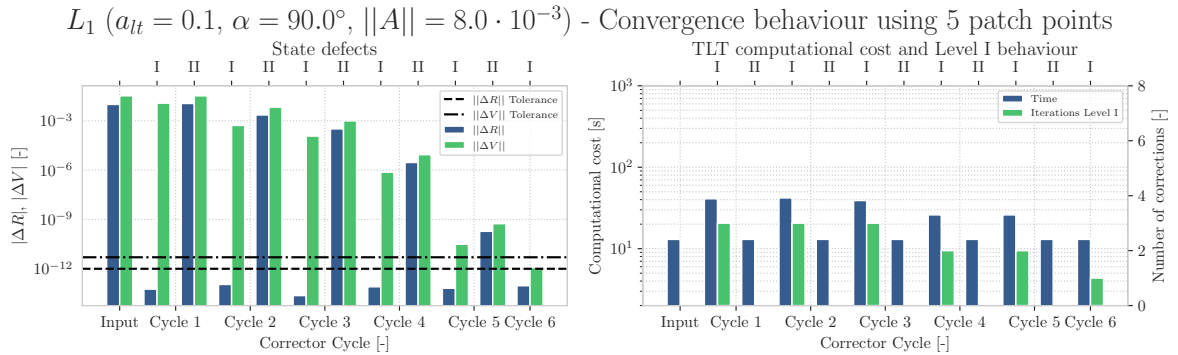


Figure E.6: The left Figure shows the convergence behaviour of the TLT procedure. The Figure on the left shows the behaviour of the computational cost the correction procedure as well as the convergence behaviour of Level I of the TLT procedure.

Figure E.6 proves that the algorithm exhibits monotone convergence and converges in six iterations. Furthermore, it confirms the findings of [4] which state that the corrections provided by the level-II correction procedure should result in a smaller velocity discrepancies once the solution is reconverged with the level-I correction process. A visualization of the process presented in Figure E.6 is shown below in Figures E.7-E.9.

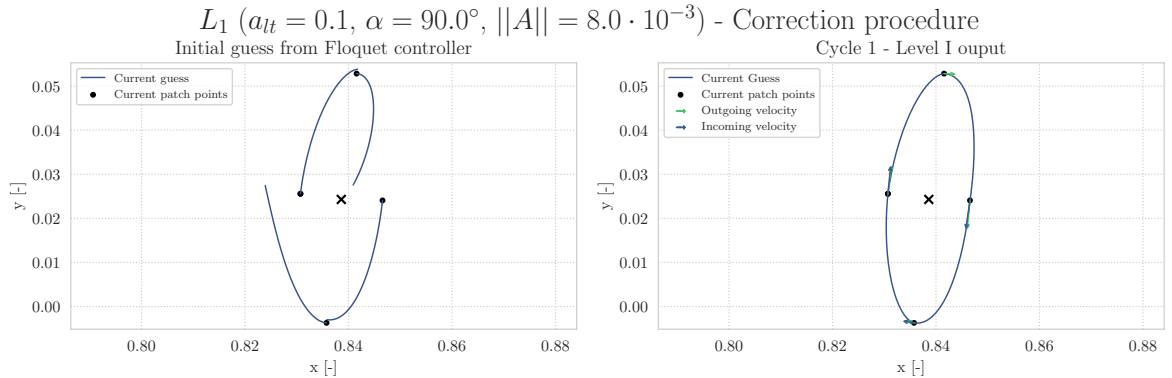


Figure E.7: The input trajectory of the TLT trajectory and the result after the first Cycle Level-I correction procedure.

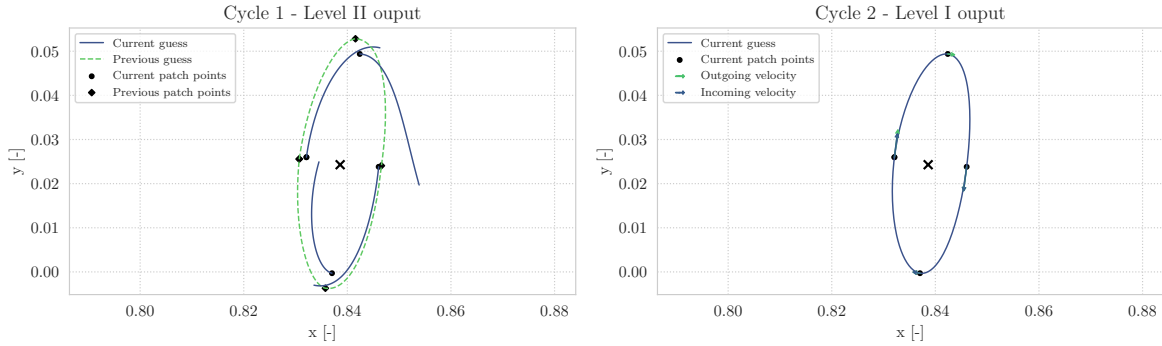


Figure E.8: The trajectory after the Cycle 1 Level-II procedure on the left. The reconverged after the Cycle 2 Level-I trajectory on the right.

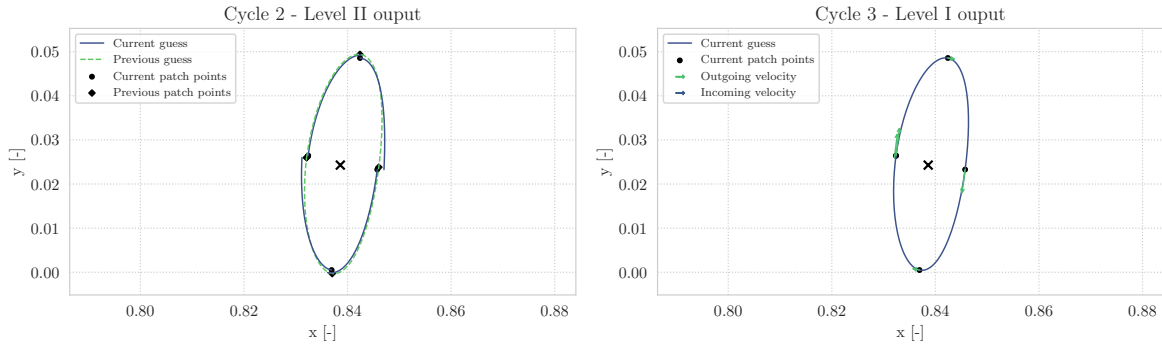


Figure E.9: The trajectory after the Cycle 2 Level-II procedure on the left. The reconverged after the Cycle 3 Level-I trajectory on the right.

Figures E.7-E.9 show only part of the process depicted in Figure E.6. The remainder of the TLT procedure is not visualized since the corrections in the remaining cycles are too small to observe with the naked eye

The TLT correction procedure is validated by propagating the initial states of the input trajectory and converged solution of the orbit for their estimated orbital periods via propagation with the explicit integration scheme of Section B.1. Table E.2 provides an overview of the deviations after one orbital revolution and their respective stability.

	Approximate seed solution		Refined seed solution	
$\ \Delta R\ $	3.8290618036382	$\cdot 10^{-1}$	4.2363516820387	$\cdot 10^{-11}$
$\ \Delta V\ $	0.82710696039002	$\cdot 10^{-1}$	1.2258327370445	$\cdot 10^{-10}$
$\ 1 - \ \lambda_3\ \ $	1.5983036872667	$\cdot 10^{-1}$	1.9085844016331	$\cdot 10^{-12}$
$\ 1 - \det(M)\ $	-4.4061911896875	$\cdot 10^{-9}$	-1.1124317467193	$\cdot 10^{-8}$

Table E.2: Deviations and stability characteristics after propagating for the estimated orbital periods. The data above confirms that the seed solution is indeed corrected to a periodic libration point orbit.

Table E.2 shows the TLT procedure is able to produce an initial state and orbital period that constitute to a periodic libration period once propagated using an explicit propagation scheme.

E.4. Collocation method verification

The veracity of the collocation procedure is achieved by computing the L_1 ($a_{lt} = 0.05$, $\alpha = 0.0^\circ$, $H_{lt} = -1.525$) orbit from a ballistic seed solution L_1 ($a_{lt} = 0.0$, $\alpha = 0.0^\circ$, $H_{lt} = -1.525$). This confirms the capability of the collocation procedure to refine orbits to a desired Hamiltonian, which is crucial capability in computing the a_{lt} - and α -varying types of l.p.o families. The input of the collocation procedure is obtained by providing an acceleration increment $\Delta a_{lt} = 0.05$ to each node. The ballistic, input and converged orbit are depicted in Figure E.10 while the deviations these orbits are presented in Figure E.3

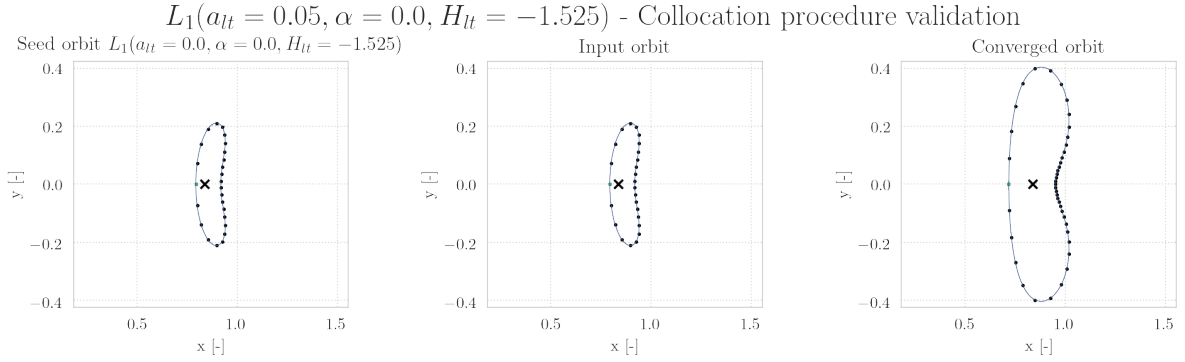


Figure E.10: A visual depiction of the seed orbit, input trajectory and converged solution of the collocation procedure. The totality of the dots constitute the mesh of the algorithm whereas the green dot indicates the initial state.

It should be stressed that the center subfigure in Figure E.10 is nowhere close to a periodic solution. Although it could be interpreted as such from visual inspection. A more reliable way to analyze the trajectories is by checking the state deviations and eigensystem properties. Such an analysis is presented below in Table E.3.

Method	Variable	Seed orbit	Input orbit	Converged orbit
Collocation	$\ \Delta F\ $	$4.3230053967504 \cdot 10^{-13}$	$4.6386010389410 \cdot 10^{-2}$	$3.5152358156095 \cdot 10^{-13}$
	Δe_i	$2.7869117126167 \cdot 10^{-13}$	$1.38974793094065 \cdot 10^{-4}$	$3.6751022289658 \cdot 10^{-13}$
	$\max(e_i)$	$4.6724900286984 \cdot 10^{-10}$	$1.42080133528164 \cdot 10^{-4}$	$1.8799082394172 \cdot 10^{-13}$
	nodes	26	26	43
TLT defects	$\ \Delta R\ $	$1.6005337645492 \cdot 10^{-12}$	$4.4031766961721 \cdot 10^{-3}$	$5.6570955097312 \cdot 10^{-12}$
	$\ \Delta V\ $	$2.9338554376173 \cdot 10^{-12}$	$4.1270508152016 \cdot 10^{-2}$	$5.7516248616859 \cdot 10^{-12}$
	$\ \Delta H_{lt}\ $	$4.4381578877015 \cdot 10^{-13}$	$2.2776414277751 \cdot 10^{-1}$	$5.3794955767292 \cdot 10^{-12}$
Explicit propagation	$\ \Delta R\ $	$7.5734759633996 \cdot 10^{-12}$	1.3671995113793	$6.2045150719090 \cdot 10^{-11}$
	$\ \Delta V\ $	$2.1321116993244 \cdot 10^{-11}$	1.7345934861397	$2.0004908897853 \cdot 10^{-11}$
	$\ \Delta H_{lt}\ $	$9.3258734068512 \cdot 10^{-15}$	$3.9657409547945 \cdot 10^{-2}$	$7.5495165674510 \cdot 10^{-15}$
	$\ 1 - \ \lambda_3\ \ $	$9.8530295034038 \cdot 10^{-11}$	$4.9451492555471 \cdot 10^{-1}$	$5.5449405624963 \cdot 10^{-5}$
	$\ 1 - \det(M)\ $	$4.36806768533415 \cdot 10^{-9}$	$3.6865976937861 \cdot 10^{-10}$	$5.2271951211935 \cdot 10^{-12}$

Table E.3: Validation of the collocation procedure by checking the state deviations of the solution through different defect properties

The Table above ensures the veracity of the collocation procedure in three ways. First of all, the top four rows show whether the converged solution adheres to the collocation tolerances as specified in Table A.4. The middle three rows serve as a consistency check with the TLT root-finding method by computing the TLT defect vector. Finally, the bottom five rows present the state deviations and eigensystem properties of the orbits after propagation of the initial state for estimated orbital period using the RK78 integrator.

Several conclusions can be drawn from Table E.3. First of all, the collocation procedure described in Section C.5 is able to comply with the constraints specified in Table A.4 despite significant deviations of the input trajectory. Secondly, the TLT defect vector that results from the mesh of the converged orbit nearly complies with the criteria as specified in Table A.7. The similarity between the state deviations of both methods establish confidence in a correct implementation of the collocation procedure and an appropriate selection of the tolerances as specified in Table A.4. Thirdly, inspection of the state deviations and eigensystem properties after explicit propagation reveal that collocation procedure is able to produce an initial state and orbital period that constitute to a periodic solution. Finally, it can be concluded that the collocation procedure can refine periodic solutions to a desired Hamiltonian, contrary to the TLT targeter as specified in Section C.4.3.

The converged solution in Figure E.10 shows a peculiar spacing of the nodes over the interval. The mesh is selected by the mesh refinement methodology as explained in Section B.2.2. This error control method is crucial in obtaining a periodic solution that complies with the tolerances as specified in A.8. A visualization of the mesh refinement process associated with the transformation of the input orbit to the converged orbit

as described Figure E.10 and Table E.3 is provided via a collection of bar charts in Figure E.11. The error distribution of single mesh is represented using a bar chart where the width of each bar represents the time duration on the segment and the height indicates the segment error.

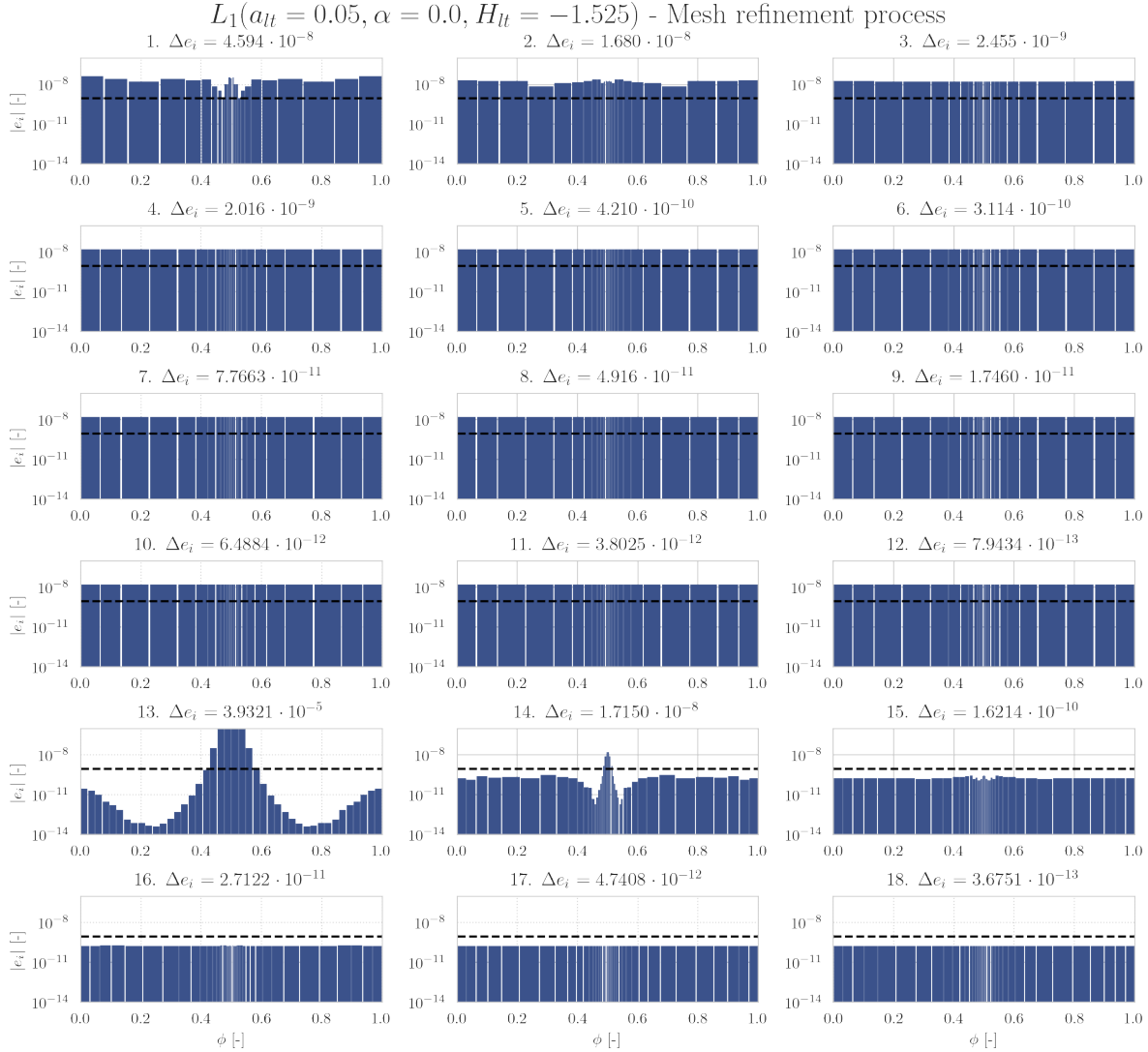


Figure E.11: The mesh refinement procedure associated with the collocation procedure as described in Figure E.10 and Table E.3.

Figure E.11 suggests a correct implementation of Boor's method for error control [9] since the mesh refinement procedure distributes the errors more equally with each iteration and the number of nodes is increased once the equidistributed mesh does not meet the error tolerance as specified in Table A.4.

The totality of Figure E.10, Table E.3 and Figure E.11 establish confidence in a proper implementation of the collocation procedure as explained in Section C.5.

E.5. Libration point orbit families verification

The final section of this addendum discusses the veracity of the l.p.o families as presented in Chapter 1 of this report. The veracity of the l.p.o families is established per type of family. Section E.5.1 presents the veracity of the H_{lt} -varying families. The correctness of the a_{lt} -varying families is discussed in Section E.5.2 whereas the authenticity of the α -varying families is discussed in Section E.5.3. Each Section provides an overview of the termination causes for the continuation associated with construction of each l.p.o family. An exhaustive list of these termination causes is provided in Table E.4.

Label	Termination root cause
A	Full-period Position discrepancy exceeds threshold
B	Full-period Velocity discrepancy exceeds threshold
C	Increment at half-phase below threshold
D ⁿ	Maximum number (n) of family members reached
E	Termination due to reversing of continuation direction
F	Periodic eigenvalue deviation exceeds threshold
G	Acceleration of a_{lt} -varying family exceeds upper limit
H	Orbit hamiltonian below hamiltonian of associated equilibrium
I	Instability in collocation procedure
J	Full revolution of α -varying family reached

Table E.4: An overview of the termination causes of the numerical continuation procedure responsible for the l.p.o family generation.

An instability in the collocation procedure refers to the phenomenon where a node at t_{i+1} is corrected to a time earlier than node t_i . This results in a mesh where a part of the trajectory travels back in time. Consequence of this phenomenon is a collocation problem which is unsolvable. If this instability is encountered. The numerical continuation procedure is terminated.

Besides an understanding of the termination causes, the veracity of a single l.p.o family is then established via three analyses. First of all, it is checked whether each family member satisfies the periodicity tolerances as specified in Table A.4. Secondly, the monodromy eigensystem of each family member is investigated to check whether it adheres to the structure of a symplectic map. Thirdly, the evolution of H_{lt}, a_{lt} and α are investigated to see if a family truly evolves along the H_{lt}, a_{lt} or α branch. The aforementioned three analyses are shown for a subset of all constructed l.p.o families for sake of conciseness.

E.5.1. H_{lt} -varying families

A multitude of H_{lt} -varying families is presented in Chapter 1 of this report and their veracity is established in this Subsection. The termination cause of each numerical continuation procedure associated with construction of a H_{lt} -varying family is presented in Table E.5.

α	[rad]	E_1					E_2						
		0	$\frac{1}{3}\pi$	$\frac{2}{3}\pi$	π	$\frac{4}{3}\pi$	$\frac{5}{3}\pi$	0	$\frac{1}{3}\pi$	$\frac{2}{3}\pi$	π	$\frac{4}{3}\pi$	$\frac{5}{3}\pi$
$a_{lt} = 0.00$	[–]	<u>C</u>	-	-	-	-	-	<u>E</u>	-	-	-	-	-
$a_{lt} = 0.01$	[–]	C	<u>D^{3000}</u>	<u>D^{3000}</u>	C	<u>A</u>	<u>D^{3000}</u>	I	I	I	I	I	I
$a_{lt} = 0.05$	[–]	C	<u>B</u>	F	C	F	<u>I</u>	I	I	I	I	I	I
$a_{lt} = 0.10$	[–]	C	F	<u>I</u>	E	F	<u>I</u>	<u>D^{1000}</u>	<u>I</u>	I	I	I	<u>D^{4500}</u>

Table E.5: An overview of the termination causes of the numerical continuation procedures associated with H_{lt} -varying families. The termination cause of some H_{lt} -varying families is underlined, meaning that proof of their veracity is provided later in this Subsection

Several reasons for termination are observed from Table E.5. Most families with a collinear acceleration orientation are terminated because the spacing between two subsequent family members at the half-phase falls below the threshold specified in Table A.4. Some families have been terminated after reaching a prespecified number of family members. This constraint has been imposed to keep the computational cost of a H_{lt} -varying family bounded to a maximum of ten days. However, the majority of continuation procedures have been terminated because of instabilities in the collocation algorithm which are attributed to the variable node times of the collocation root-finding scheme. The remainder of this section discusses the veracity of the H_{lt} -varying families whose termination code in Table E.5 is shown in underlined.

L₁ ($a_{lt} = 0.0, \alpha = 0.0$ rad) H_{lt} -varying family

The periodicity of each member of the natural L_1 family is verified in Figure E.12. The totality of the subplots of this Figure show that the collocation procedure produces a converged solution with an equidistributed truncation error. The initial state of the resulting solution is explicitly propagated for the estimated orbital period which confirms the periodicity of the family members and validates the correctness of the collocation procedure. Apart from the first few members, all members have a state discrepancy at the full period that satisfy the constraints of Table A.8.

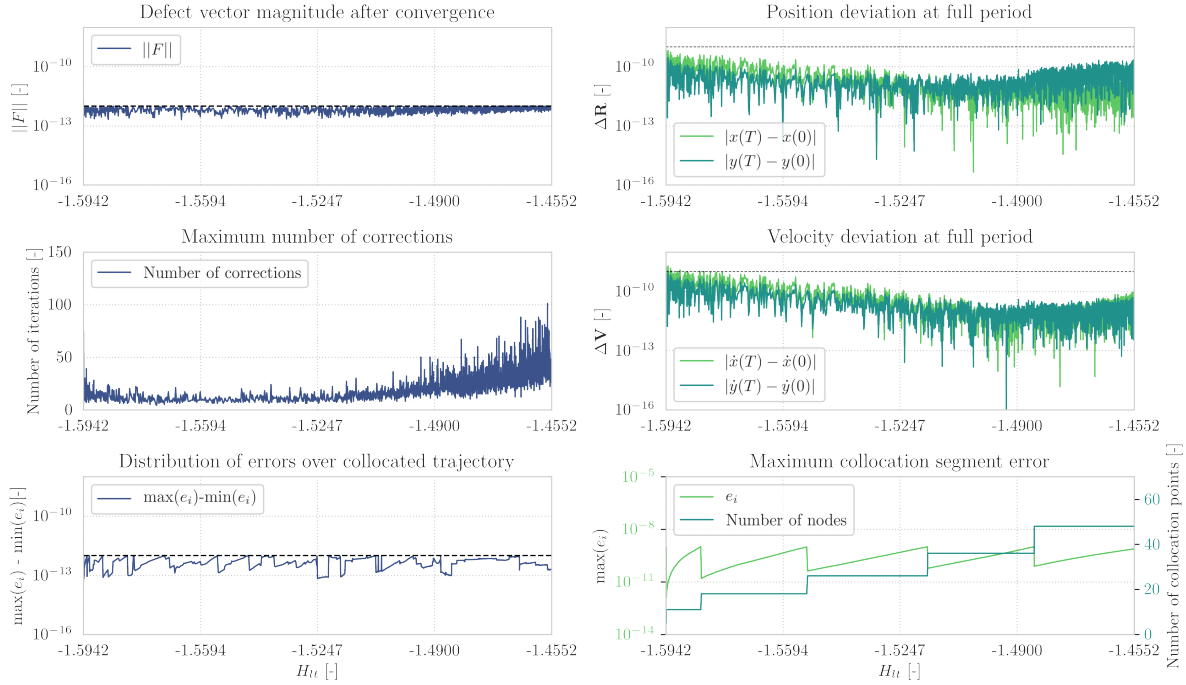
L_1 Horizontal Lyapunov ($a_{lt} = 0.00, \alpha = 0$ rad) - Periodicity constraints verification

Figure E.12: Periodicity verification of the L_1 ($a_{lt} = 0.0, \alpha = 0.0$ rad) family. The three left subplots and the bottom right subplot demonstrate a correct implementation of the collocation procedure. The upper and middle right plot, constructed via explicit propagation of the solution resulting from the collocation procedure, confirm the periodicity of the family members.

As predicted by Floquet theory [33]. The eigensystem of the monodromy matrix of a periodic solution adheres to the structure of a symplectic map. One characteristic of a symplectic map is that its determinant is equal to one. As discussed in Chapter 1 of this report. eigenvalues occur in reciprocal pairs and a periodic solution requires at least one eigenvalue pair with $|\lambda| = 1$. Figure E.13 demonstrates that these properties are satisfied for each member of the ballistic L_1 family.

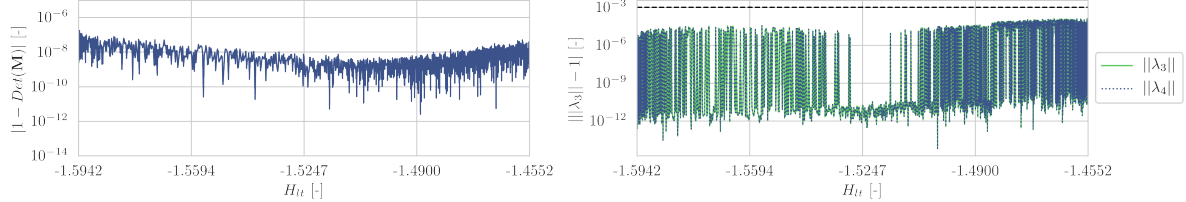
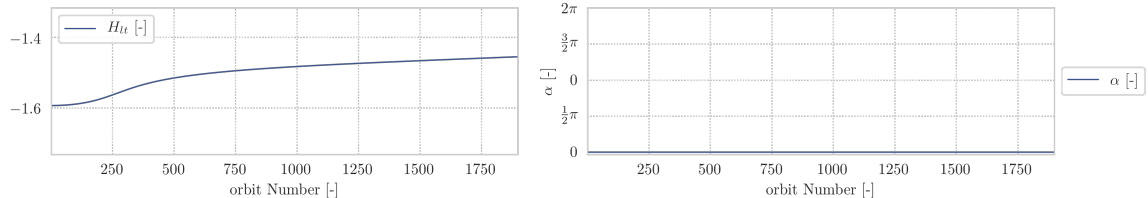
 L_1 Horizontal Lyapunov ($a_{lt} = 0.00, \alpha = 0$ rad) - Monodromy matrix eigensystem validation

Figure E.13: Monodromy matrix eigensystem validation of the L_1 ($a_{lt} = 0.0, \alpha = 0.0$ rad) family. The left subplot shows that the deviation of the monodromy matrix determinant adheres to the constraint as specified in Table A.8 . The right subplot demonstrates the eigenvalue representing the in-plane center subspace adheres to the periodicity constraint as specified in Table A.8.

Figure E.14 demonstrates that the Hamiltonian varies over along the ballistic L_1 family while both thrust parameters are constant. Furthermore, the phase constraint is also satisfied over the complete family.

 L_1 Horizontal Lyapunov ($a_{lt} = 0.00, \alpha = 0$ rad) - Numerical continuation verification

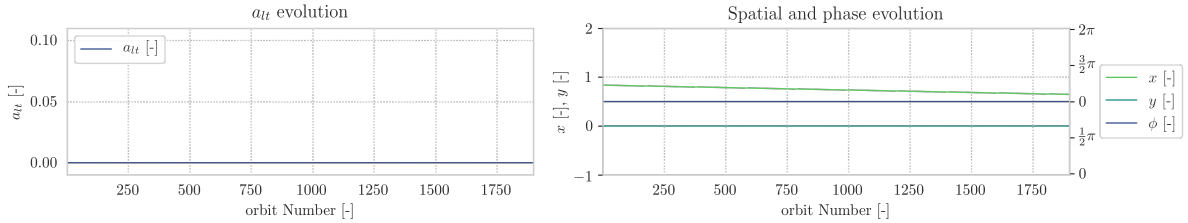


Figure E.14: Numerical continuation verification of the L_1 ($a_{lt} = 0.0, \alpha = 0.0 \text{ rad}$) family. The top subplot and bottom left subplot demonstrate that the l.p.o family unfolds along the Hamiltonian branch. The bottom right subplot shows the spatial evolution and phase drift of the initial condition along the family.

Figure E.15 confirms a consistent spacing between the initial state of two consecutive members of the solution family. The bottom left plot shows that the positional increment between two consecutive members does not adhere to the threshold states in Table A.8 which leads to termination of the continuation procedure.

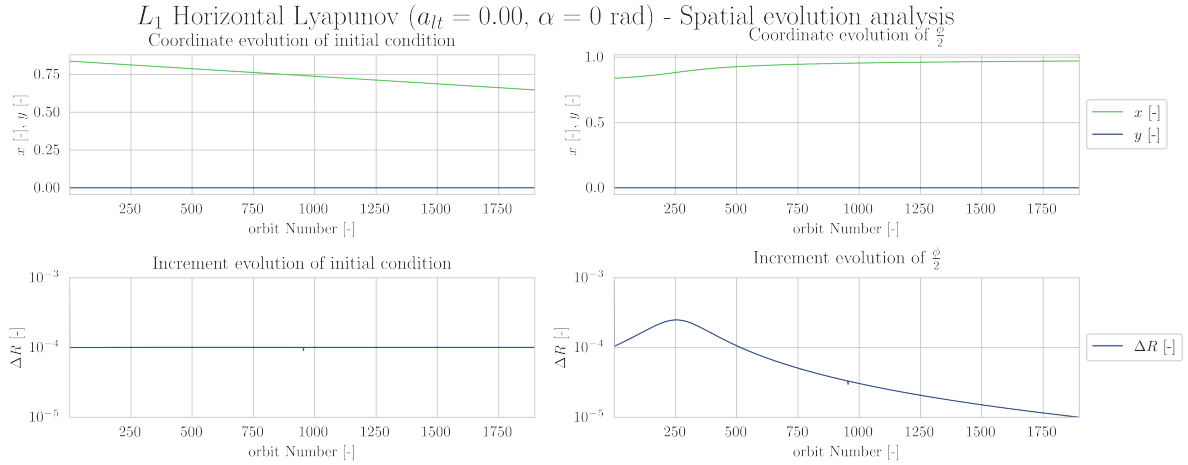
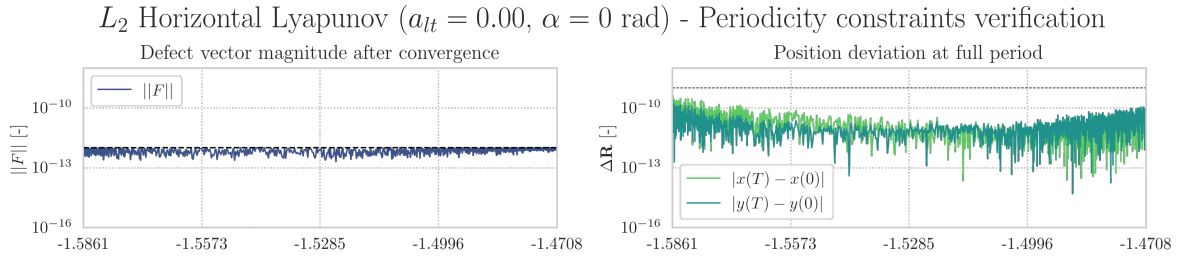


Figure E.15: Spatial evolution of the L_1 ($a_{lt} = 0.0, \alpha = 0.0 \text{ rad}$) family. The two top subplots show the spatial evolution of the initial condition and half-period state. The bottom two subplots show the positional increment between the initial and half-period state between two subsequent family members.

L₂ ($a_{lt} = 0.0, \alpha = 0.0 \text{ rad}$) H_{lt} -varying family

The periodicity of each member of the natural L_2 family is verified in Figure E.16. The totality of subplots show that the collocation procedure produces a converged solution with an equidistributed truncation error. The initial state of the resulting solution is explicitly propagated for the estimated orbital period which confirms the periodicity of the family members and validates the correctness of the collocation procedure.



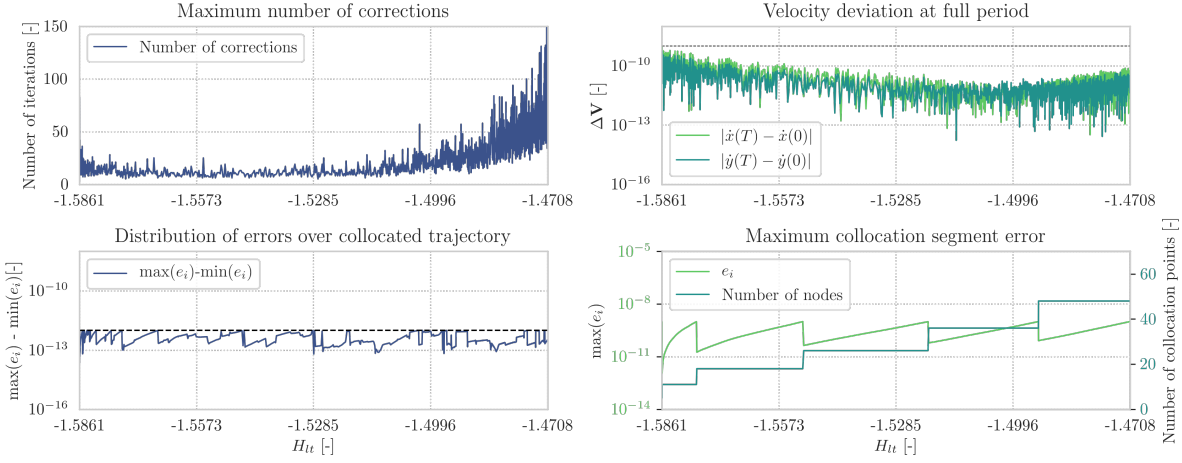


Figure E.16: Periodicity verification of the L_2 ($a_{lt} = 0.0, \alpha = 0.0$ rad) family. The three left subplots and the bottom right subplot demonstrate a correct implementation of the collocation procedure. The upper and middle right plot, constructed via explicit propagation of the solution resulting from the collocation procedure, confirm the periodicity of the family members.

Characteristics of the monodromy eigensystem of each member of the ballistic L_2 family are shown in Figure E.17. It can be concluded that the monodromy eigensystem of each family member adheres to the structure of a symplectic map.

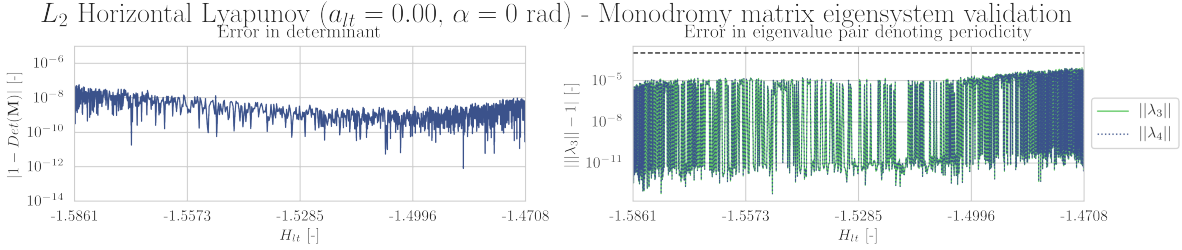
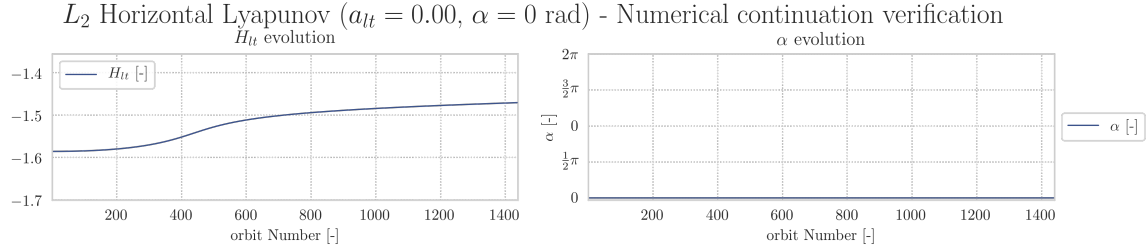


Figure E.17: Monodromy matrix eigensystem validation of the L_2 ($a_{lt} = 0.0, \alpha = 0.0$ rad) family. The left subplot shows that the deviation of the monodromy matrix determinant adheres to the constraint as specified in Table A.8. The right subplot demonstrates the eigenvalue representing the in-plane center subspace adheres to the periodicity constraint as specified in Table A.8.

Figure E.18 proves that the ballistic family is a H_{lt} -varying family since its thrust parameters are constant. Next to that it can be observed that the pseudo-arclength continuation provides a constant spacing between the family members and the phase constraint is also satisfied over the complete family.



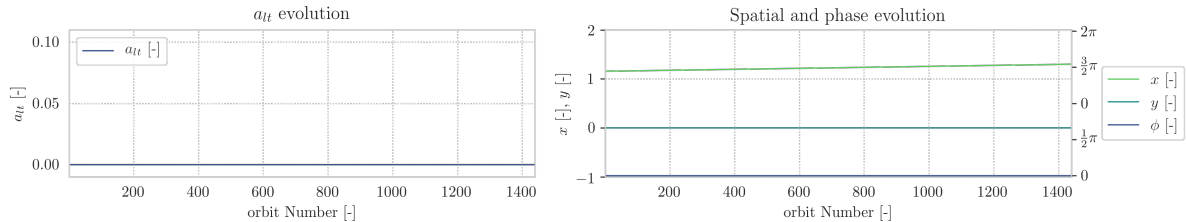


Figure E.18: Numerical continuation verification of the L_2 ($a_{lt} = 0.0, \alpha = 0.0$ rad) family. The top subplots and bottom left subplot demonstrate that the l.p.o family unfolds along the Hamiltonian branch. The bottom right subplot shows the spatial evolution and phase drift of the initial condition along the family.

L1 ($a_{lt} = 0.01, \alpha = \frac{2}{3}\pi$ rad) H_{lt} -varying family

The periodicity of the members that constitute the $L_1(a_{lt} = 0.01, \alpha = \frac{2}{3}\pi$ rad) family are established in Figure E.19. The totality of the subplots of this Figure show that the collocation procedure produces a converged solution with an equidistributed truncation error. The initial state of the resulting solution is explicitly propagated for the estimated orbital period which confirms the periodicity of the family members and validates the correctness of the collocation procedure. The state discrepancy of the first orbits at full period exceeds the thresholds of Table A.8. but termination is intentionally suppressed since the performance of the collocation procedure improves afterwards. Furthermore, it can be observed that at error distribution does not meet the threshold but this does not result in a member with a state discrepancy that violates the periodicity constraints.

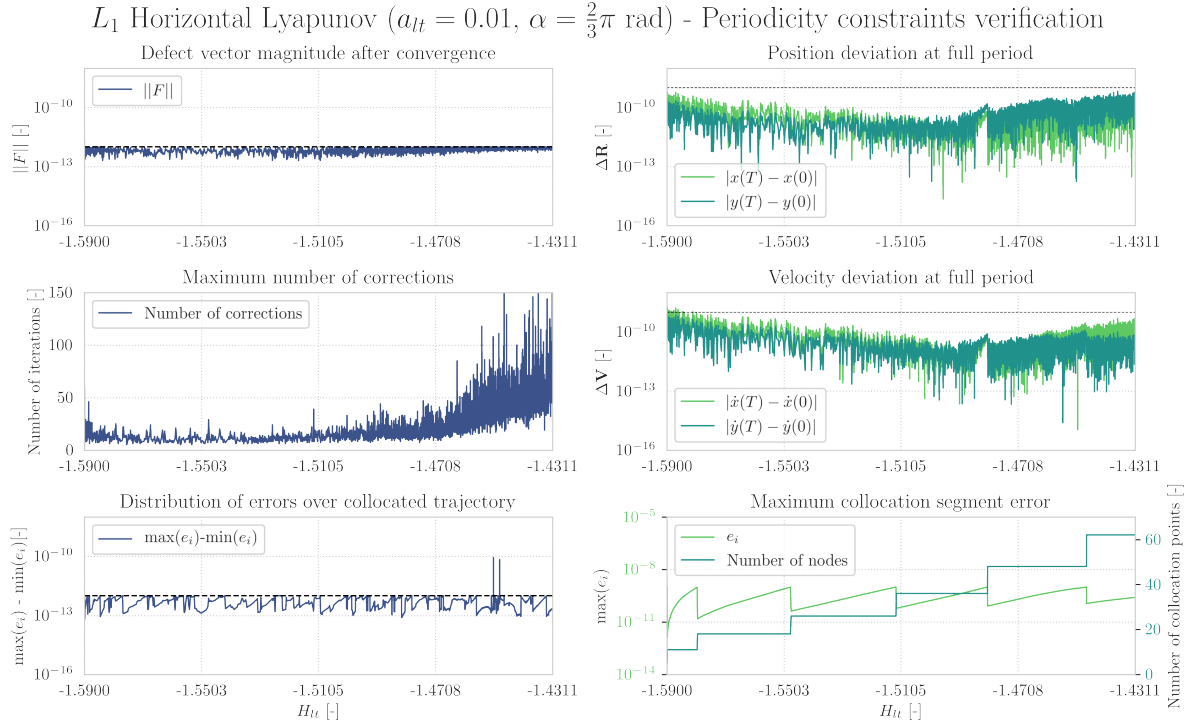


Figure E.19: Periodicity verification of the L_1 ($a_{lt} = 0.01, \alpha = \frac{2}{3}\pi$ rad) family. The three left subplots and the bottom right subplot demonstrate a correct implementation of the collocation procedure. The upper and middle right plot, constructed via explicit propagation of the solution resulting from the collocation procedure, confirm the periodicity of the family members.

Characteristics of the monodromy eigensystem of each member of the L_1 ($a_{lt} = 0.01, \alpha = \frac{2}{3}\pi$ rad) family are shown in Figure E.20. It can be concluded that the monodromy eigensystem of each family member adheres to the structure of a symplectic map.

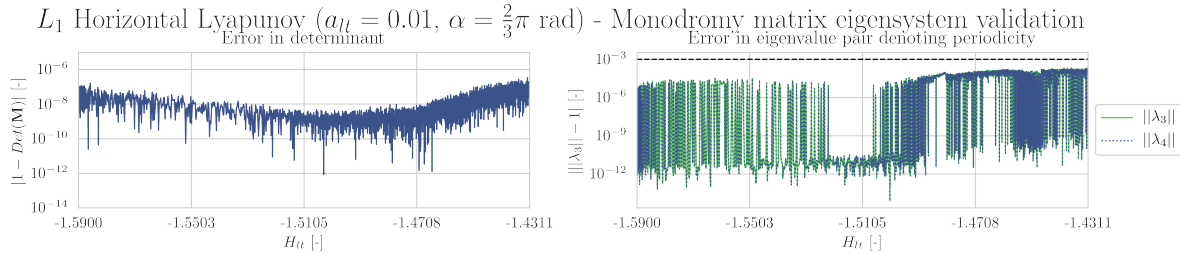


Figure E.20: Monodromy matrix eigensystem validation of the L_1 ($a_{lt} = 0.01, \alpha = \frac{2}{3}\pi$ rad) family. The left subplot shows that the deviation of the monodromy matrix determinant adheres to the constraint as specified in Table A.8. The right subplot demonstrates the eigenvalue representing the in-plane center subspace adheres to the periodicity constraint as specified in Table A.8.

Figure E.21 proves that the L_1 ($a_{lt} = 0.01, \alpha = \frac{2}{3}\pi$ rad) family is a H_{lt} -varying family since its thrust parameters are constant. Next to that it can be observed that the pseudo-arc length continuation provides a constant spacing between the family members. The phase constraint is satisfied for the majority of the family apart from the final members of the family where a slight phase shift is observed.

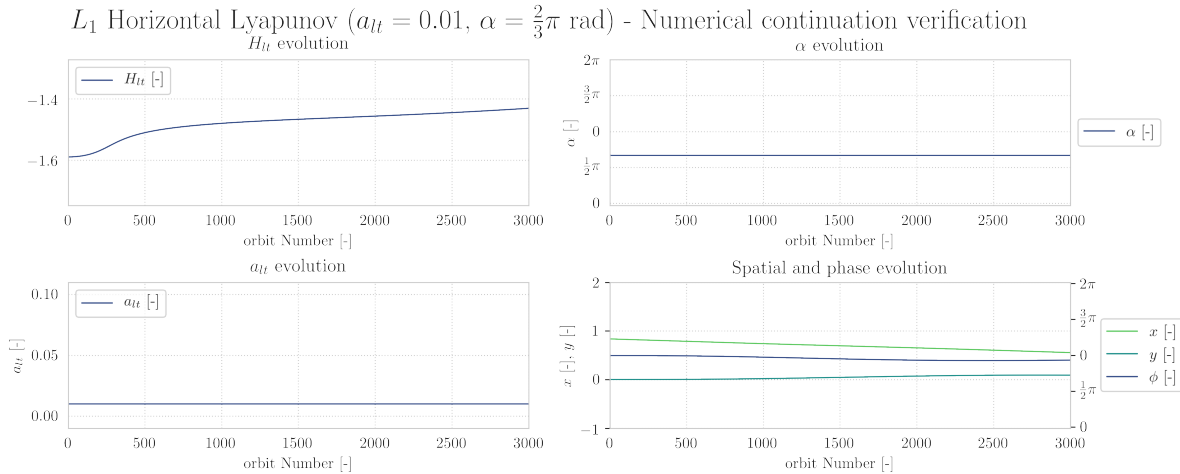
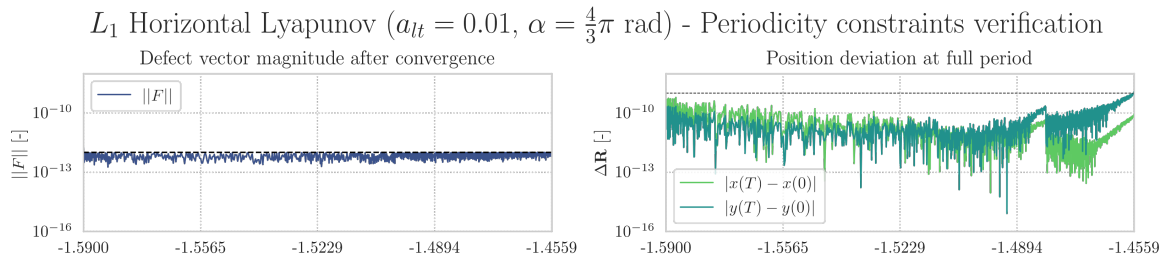


Figure E.21: Numerical continuation verification of the L_1 ($a_{lt} = 0.01, \alpha = \frac{2}{3}\pi$ rad) family. The top subplots and bottom left subplot demonstrate that the l.p.o family unfolds along the Hamiltonian branch. The bottom right subplot demonstrates that pseudo-arc length continuation results in a constant spacing between family members and the phase constraint is satisfied over the complete family. The bottom right subplot shows the spatial evolution and phase drift of the initial condition along the family.

L_1 ($a_{lt} = 0.01, \alpha = \frac{4}{3}\pi$ rad) H_{lt} -varying family

The periodicity of the members that constitute the L_1 ($a_{lt} = 0.01, \alpha = \frac{4}{3}\pi$ rad) family are established in Figure E.22. The totality of the subplots of this Figure show that the collocation procedure produces a converged solution with an equidistributed truncation error. The initial state of the resulting solution is explicitly propagated for the estimated orbital period which confirms the periodicity of the family members and validates the correctness of the collocation procedure. The state discrepancy of the first orbits at full period exceeds the thresholds of Table A.8. but termination is intentionally suppressed since the performance of the collocation procedure improves afterwards. At the end of the family generation procedure, the continuation procedure is terminated since the final member exceeds the position discrepancy threshold at full-period.



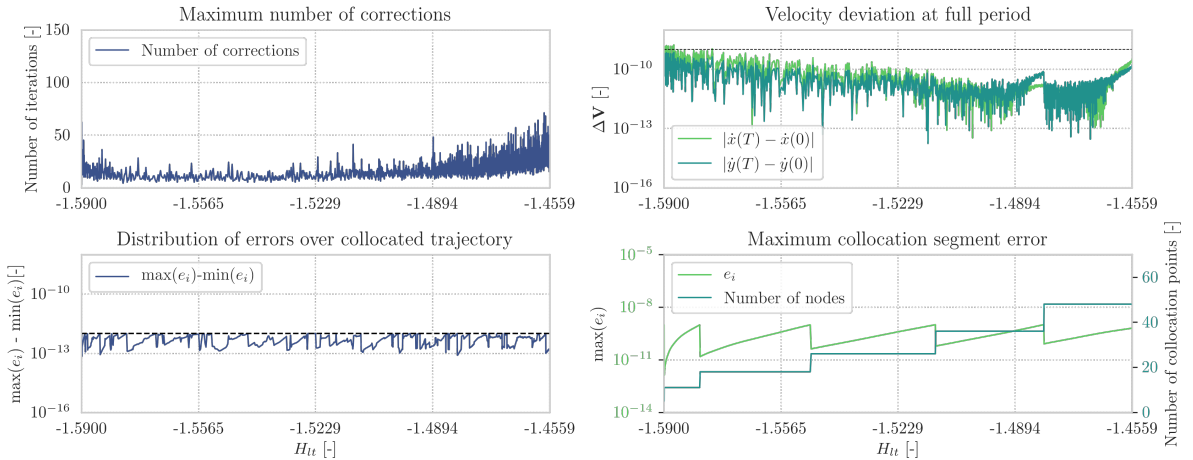


Figure E.22: Periodicity verification of the L_1 ($a_{lt} = 0.01, \alpha = \frac{4}{3}\pi$ rad) family. The three left subplots and the bottom right subplot demonstrate a correct implementation of the collocation procedure. The upper and middle right plot, constructed via explicit propagation of the solution resulting from the collocation procedure, confirm the periodicity of the family members.

Characteristics of the monodromy eigensystem of each member of the L_1 ($a_{lt} = 0.01, \alpha = \frac{4}{3}\pi$ rad) family are shown in Figure E.23. It can be concluded that the monodromy eigensystem of each family member adheres to the structure of a symplectic map.

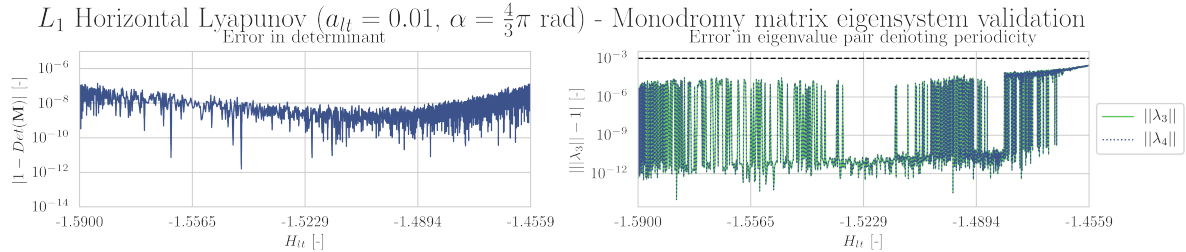
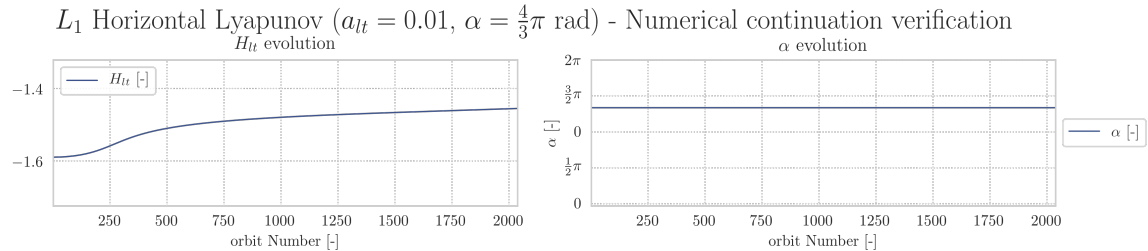


Figure E.23: Monodromy matrix eigensystem validation of the L_1 ($a_{lt} = 0.01, \alpha = \frac{4}{3}\pi$ rad) family. The left subplot shows that the deviation of the monodromy matrix determinant adheres to the constraint as specified in Table A.8. The right subplot demonstrates the eigenvalue representing the in-plane center subspace adheres to the periodicity constraint as specified in Table A.8.

Figure E.24 proves that the L_1 ($a_{lt} = 0.01, \alpha = \frac{4}{3}\pi$ rad) family is a H_{lt} -varying family since its thrust parameters are constant. Next to that it can be observed that the pseudo-arclength continuation provides a constant spacing between the family members. The phase constraint is satisfied for the majority of the family apart from the final members of the family where a slight phase shift is observed. The phase shift is in the opposite direction as the shift observed at the end of the L_1 ($a_{lt} = 0.01, \alpha = \frac{2}{3}\pi$ rad) family.



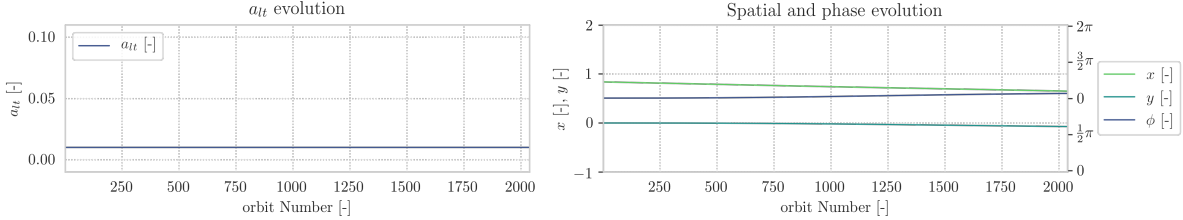


Figure E.24: Numerical continuation verification of the L_1 ($a_{lt} = 0.01, \alpha = \frac{4}{3}\pi$ rad) family. The top subplot and bottom left subplot demonstrate that the l.p.o family unfolds along the Hamiltonian branch. The bottom right subplot shows the spatial evolution and phase drift of the initial condition along the family

L_1 ($a_{lt} = 0.05, \alpha = \frac{1}{3}\pi$ rad) H_{lt} -varying family

The periodicity of the members that constitute the $L_1(a_{lt} = 0.05, \alpha = \frac{1}{3}\pi$ rad) family are established in Figure E.25. The totality of the subplots of this Figure show that the collocation procedure produces a converged solution with an equidistributed truncation error. The initial state of the resulting solution is explicitly propagated for the estimated orbital period which confirms the periodicity of the family members and validates the correctness of the collocation procedure. The state discrepancy of the first orbits at full period exceeds the thresholds of Table A.8. but termination is intentionally suppressed since the performance of the collocation procedure improves afterwards. At the end of the family generation procedure, the continuation procedure is terminated since the final member exceeds the velocity discrepancy threshold at full-period.

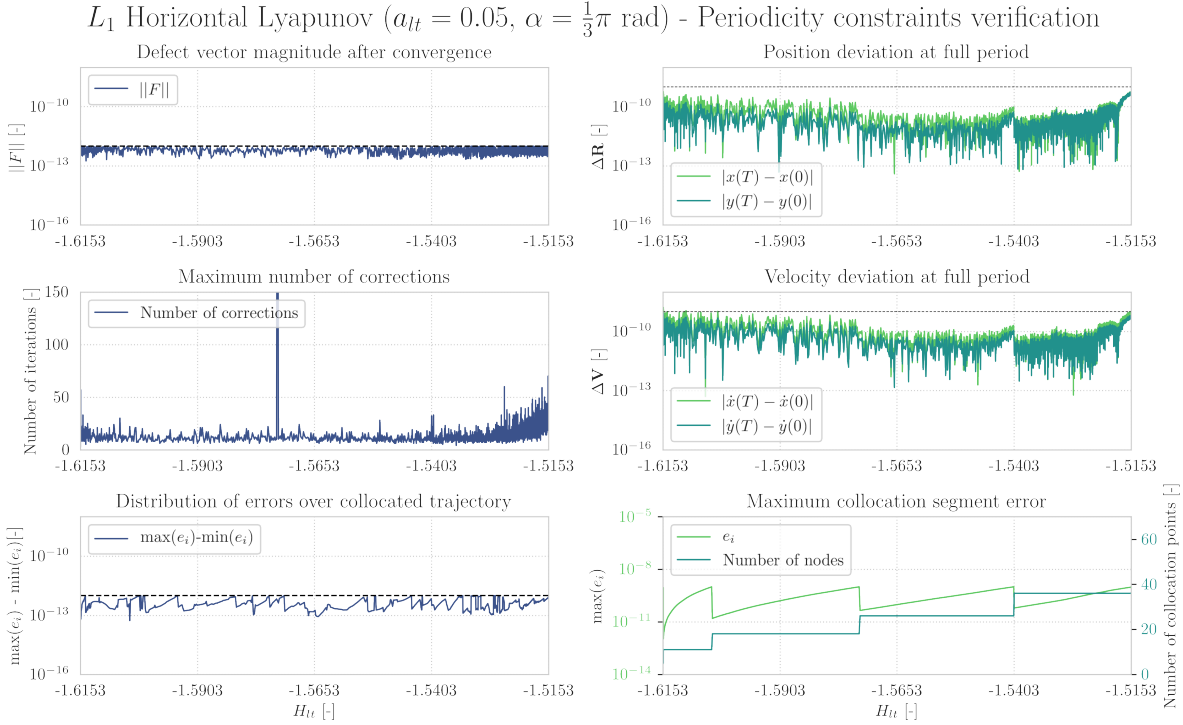


Figure E.25: Periodicity verification of the L_1 ($a_{lt} = 0.05, \alpha = \frac{1}{3}\pi$ rad) family. The three left subplots and the bottom right subplot demonstrate a correct implementation of the collocation procedure. The upper and middle right plot, constructed via explicit propagation of the solution resulting from the collocation procedure, confirm the periodicity of the family members.

Characteristics of the monodromy eigensystem of each member of the L_1 ($a_{lt} = 0.05, \alpha = \frac{1}{3}\pi$ rad) family are shown in Figure E.26. It can be concluded that the monodromy eigensystem of each family member adheres to the structure of a symplectic map.

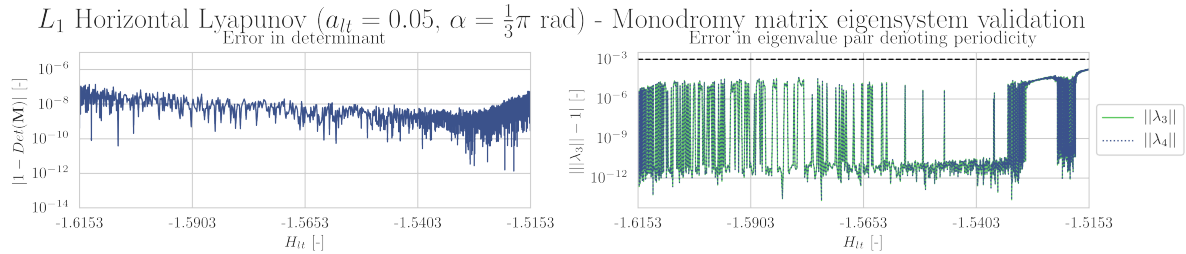


Figure E.26: Monodromy matrix eigensystem validation of the L_1 ($a_{lt} = 0.05, \alpha = \frac{1}{3}\pi$ rad) family. The left subplot shows that the deviation of the monodromy matrix determinant adheres to the constraint as specified in Table A.8. The right subplot demonstrates the eigenvalue representing the in-plane center subspace adheres to the periodicity constraint as specified in Table A.8.

Figure E.27 proves that the L_1 ($a_{lt} = 0.05, \alpha = \frac{1}{3}\pi$ rad) family is a H_{lt} -varying family since its thrust parameters are constant. Next to that it can be observed that the pseudo-arclength continuation provides a constant spacing between the family members. The phase constraint is satisfied for the first half of the family but drifts during the final half of the continuation procedure.

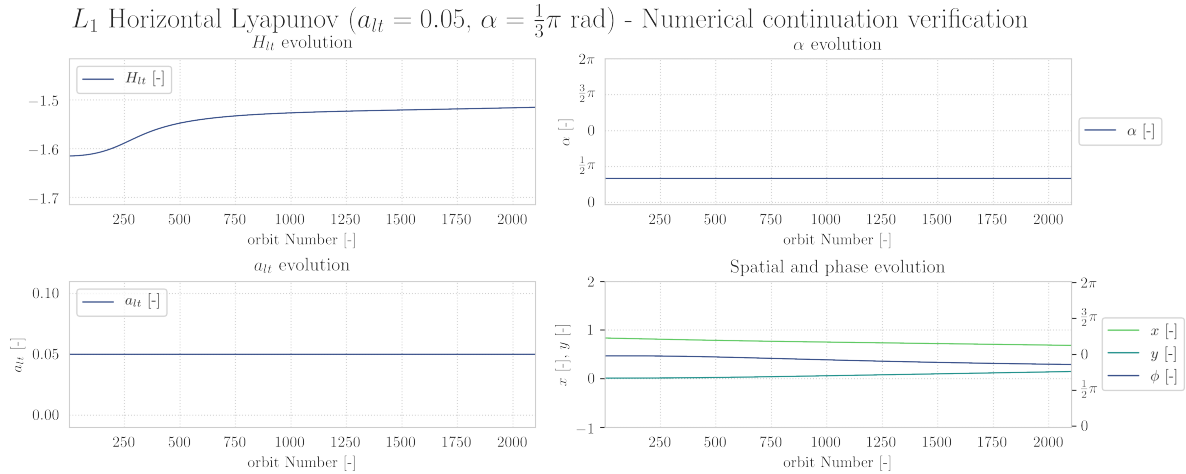
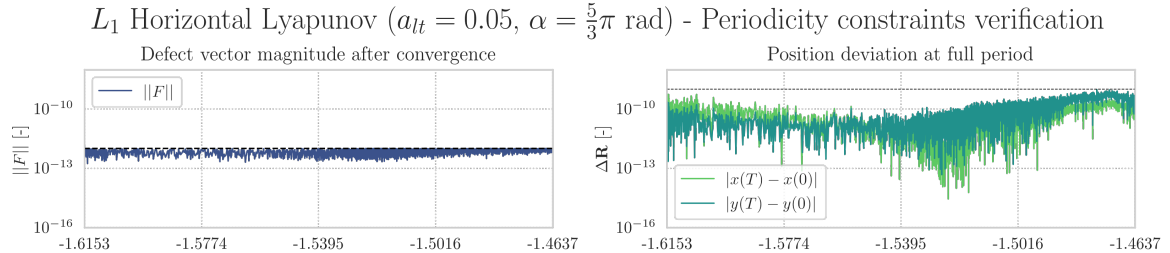


Figure E.27: Numerical continuation verification of the L_1 ($a_{lt} = 0.05, \alpha = \frac{1}{3}\pi$ rad) family. The top subplots and bottom left subplot demonstrate that the l.p.o family unfolds along the Hamiltonian branch. The bottom right subplot shows the spatial evolution and phase drift of the initial condition along the family

L_1 ($a_{lt} = 0.05, \alpha = \frac{5}{3}\pi$ rad) H_{lt} -varying family

The periodicity of the members that constitute the $L_1(a_{lt} = 0.05, \alpha = \frac{5}{3}\pi$ rad) family are established in Figure E.28. The totality of the subplots of this Figure show that the collocation procedure produces a converged solution with an equidistributed truncation error. The initial state of the resulting solution is explicitly propagated for the estimated orbital period which confirms the periodicity of the family members and validates the correctness of the collocation procedure. The state discrepancy of the first orbits at full period exceeds the thresholds of Table A.8. but termination is intentionally suppressed since the performance of the collocation procedure improves afterwards until the end of the family where the members just meet the periodicity criteria.



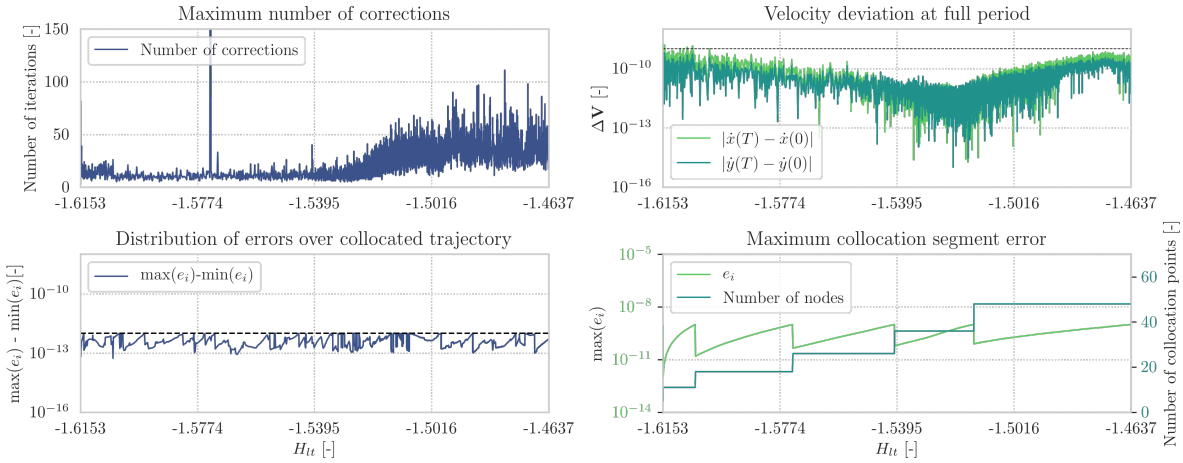


Figure E.28: Periodicity verification of the L_1 ($a_{lt} = 0.05, \alpha = \frac{5}{3}\pi$ rad) family. The three left subplots and the bottom right subplot demonstrate a correct implementation of the collocation procedure. The upper and middle right plot, constructed via explicit propagation of the solution resulting from the collocation procedure, confirm the periodicity of the family members.

Characteristics of the monodromy eigensystem of each member of the L_1 ($a_{lt} = 0.05, \alpha = \frac{5}{3}\pi$ rad) family are shown in Figure E.29. It can be concluded that the monodromy eigensystem of each family member adheres to the structure of a symplectic map.

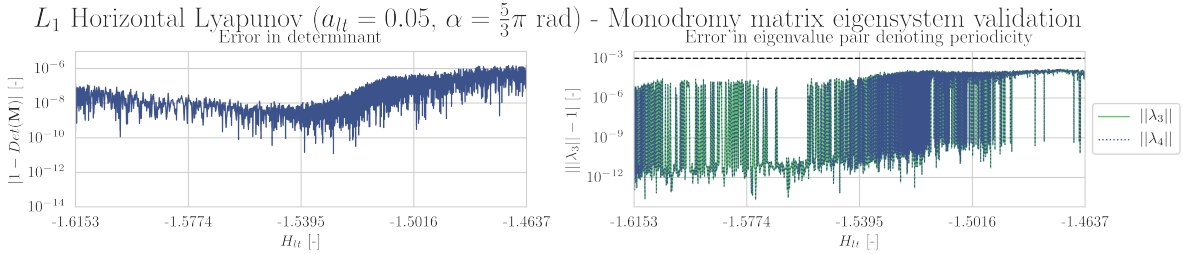
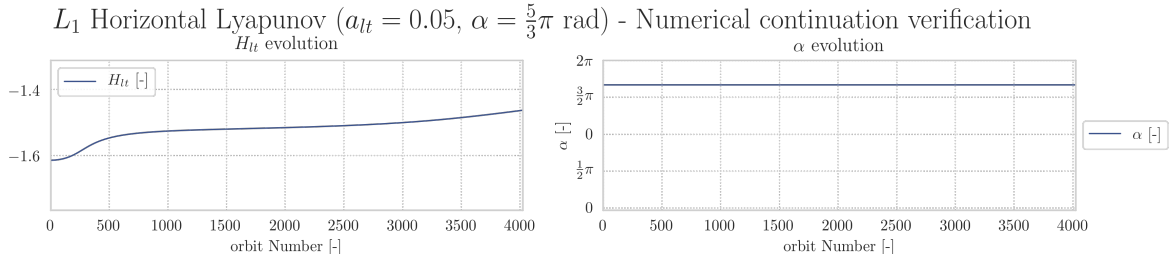


Figure E.29: Monodromy matrix eigensystem validation of the L_1 ($a_{lt} = 0.05, \alpha = \frac{5}{3}\pi$ rad) family. The left subplot shows that the deviation of the monodromy matrix determinant adheres to the constraint as specified in Table A.8. The right subplot demonstrates the eigenvalue representing the in-plane center subspace adheres to the periodicity constraint as specified in Table A.8.

Figure E.30 proves that the L_1 ($a_{lt} = 0.05, \alpha = \frac{5}{3}\pi$ rad) family is a H_{lt} -varying family since its thrust parameters are constant. The phase constraint is satisfied for the beginning of the family but drifts significantly throughout the family.



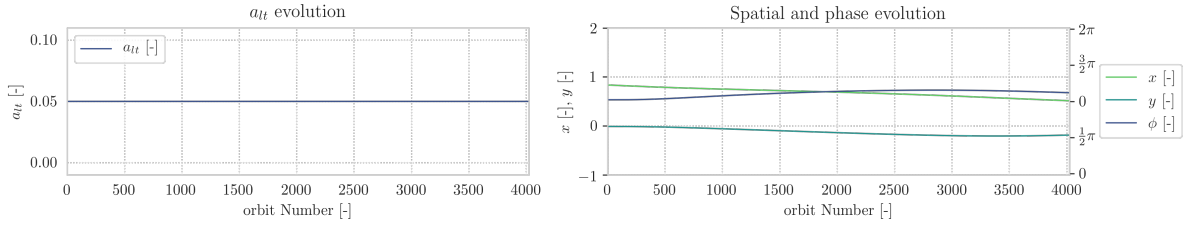


Figure E.30: Numerical continuation verification of the L_1 ($a_{lt} = 0.05, \alpha = \frac{5}{3}\pi$ rad) family. The top subplots and bottom left subplot demonstrate that the l.p.o family unfolds along the Hamiltonian branch. The bottom right subplot shows the spatial evolution and phase drift of the initial condition along the family

L1 ($a_{lt} = 0.10, \alpha = \frac{2}{3}\pi$ rad) H_{lt} -varying family

The periodicity of the members that constitute the $L_1(a_{lt} = 0.10, \alpha = \frac{2}{3}\pi$ rad) family are established in Figure E.31. The totality of the subplots of this Figure show that the collocation procedure produces a converged solution with an equidistributed truncation error. The initial state of the resulting solution is explicitly propagated for the estimated orbital period which confirms the periodicity of the family members and validates the correctness of the collocation procedure. All family members adhere to the periodicity threshold listed in Table A.8. The family is ultimately terminated due to an instability in the collocation procedure. The equidistribution threshold of the truncation error is not satisfied for all members of the family but this does not lead to violation of the periodicity thresholds.

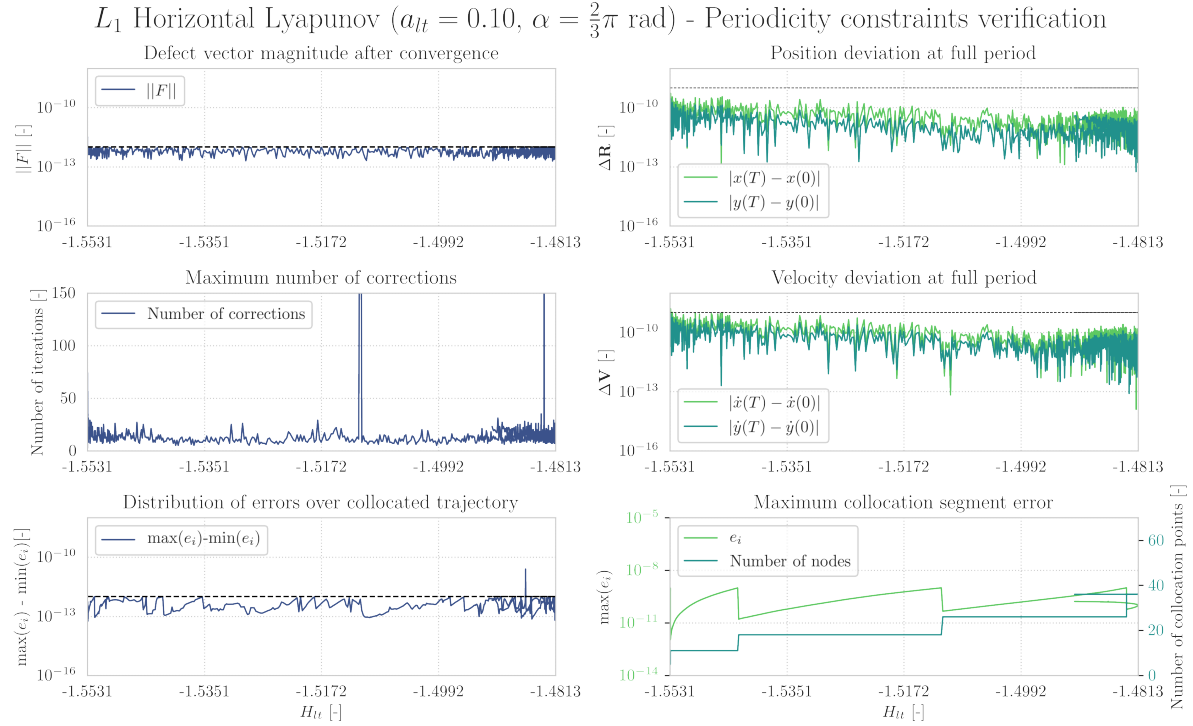


Figure E.31: Periodicity verification of the L_1 ($a_{lt} = 0.10, \alpha = \frac{2}{3}\pi$ rad) family. The three left subplots and the bottom right subplot demonstrate a correct implementation of the collocation procedure. The upper and middle right plot, constructed via explicit propagation of the solution resulting from the collocation procedure, confirm the periodicity of the family members.

Characteristics of the monodromy eigensystem of each member of the L_1 ($a_{lt} = 0.10, \alpha = \frac{2}{3}\pi$ rad) family are shown in Figure E.32. It can be concluded that the monodromy eigensystem of each family member adheres to the structure of a symplectic map.

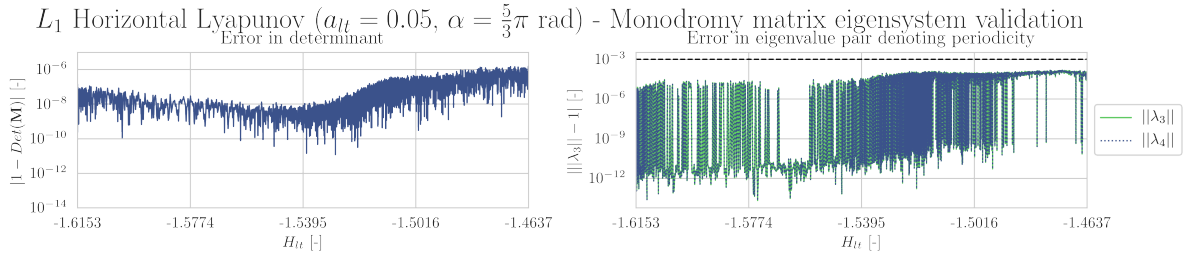


Figure E.32: Monodromy matrix eigensystem validation of the L_1 ($a_{lt} = 0.10, \alpha = \frac{2}{3}\pi$ rad) family. The left subplot shows that the deviation of the monodromy matrix determinant adheres to the constraint as specified in Table A.8. The right subplot demonstrates the eigenvalue representing the in-plane center subspace adheres to the periodicity constraint as specified in Table A.8.

Figure E.33 proves that the L_1 ($a_{lt} = 0.10, \alpha = \frac{2}{3}\pi$ rad) family is a H_{lt} -varying family since its thrust parameters are constant. The phase constraint is satisfied for the beginning of the family but drifts significantly throughout the family.

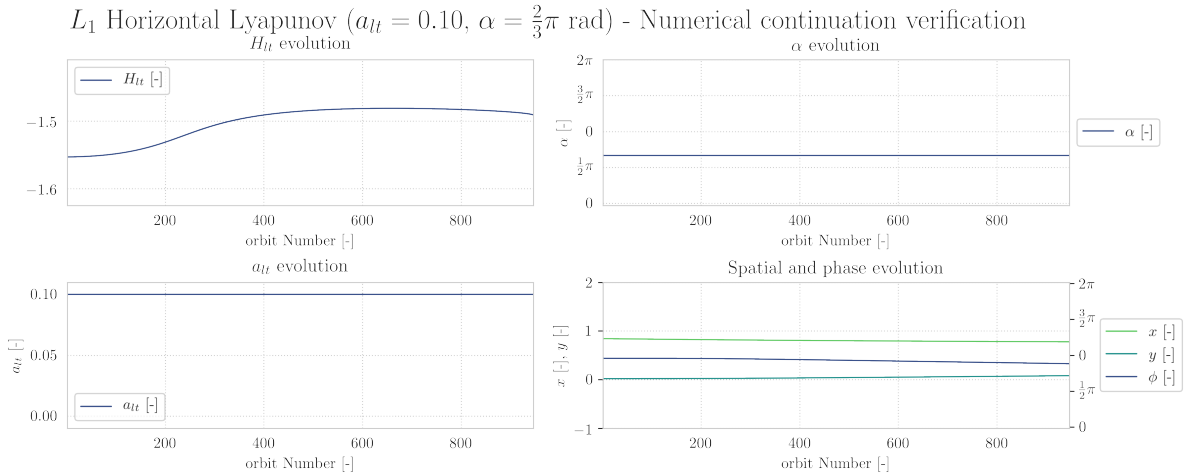
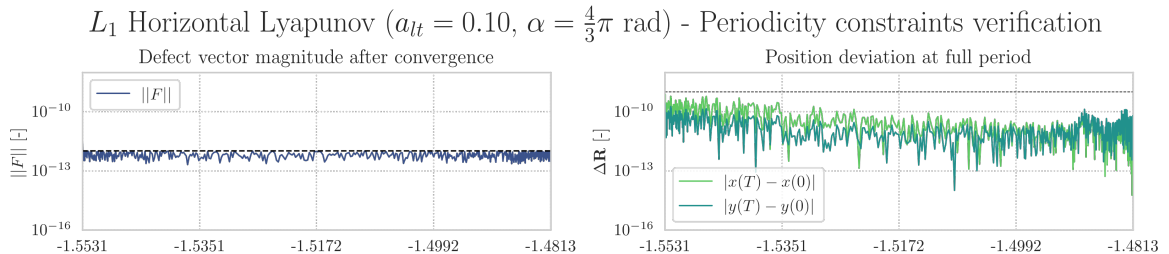


Figure E.33: Numerical continuation verification of the L_1 ($a_{lt} = 0.10, \alpha = \frac{2}{3}\pi$ rad) family. The top subplots and bottom left subplot demonstrate that the l.p.o family unfolds along the Hamiltonian branch. The bottom right subplot shows the spatial evolution and phase drift of the initial condition along the family.

L_1 ($a_{lt} = 0.10, \alpha = \frac{4}{3}\pi$ rad) H_{lt} -varying family

The periodicity of the members that constitute the $L_1(a_{lt} = 0.10, \alpha = \frac{4}{3}\pi$ rad) family are established in Figure E.34. The totality of the subplots of this Figure show that the collocation procedure produces a converged solution with an equidistributed truncation error. The initial state of the resulting solution is explicitly propagated for the estimated orbital period which confirms the periodicity of the family members and validates the correctness of the collocation procedure. All family members adhere to the periodicity threshold and equidistribution criterium listed in Table A.8.



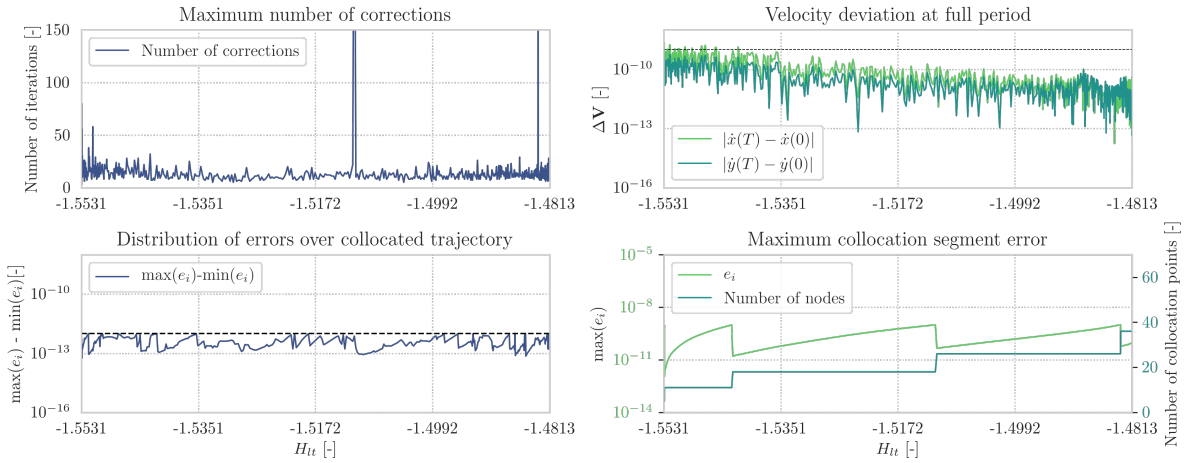


Figure E.34: Periodicity verification of the L_1 ($a_{lt} = 0.10, \alpha = \frac{4}{3}\pi$ rad) family. The three left subplots and the bottom right subplot demonstrate a correct implementation of the collocation procedure. The upper and middle right plot, constructed via explicit propagation of the solution resulting from the collocation procedure, confirm the periodicity of the family members.

Characteristics of the monodromy eigensystem of each member of the L_1 ($a_{lt} = 0.10, \alpha = \frac{4}{3}\pi$ rad) family are shown in Figure E.35. It can be concluded that the monodromy eigensystem of each family member adheres to the structure of a symplectic map.

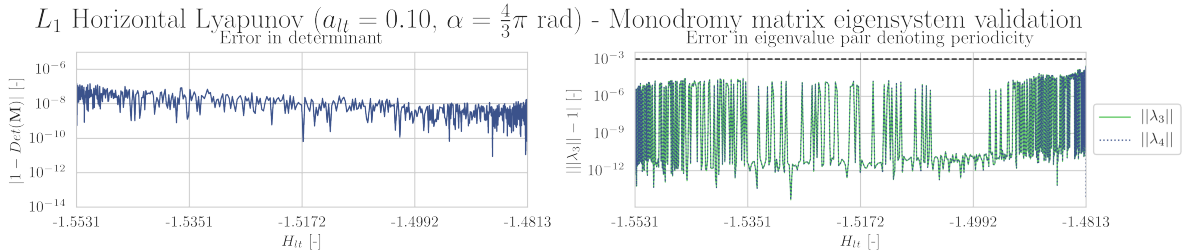
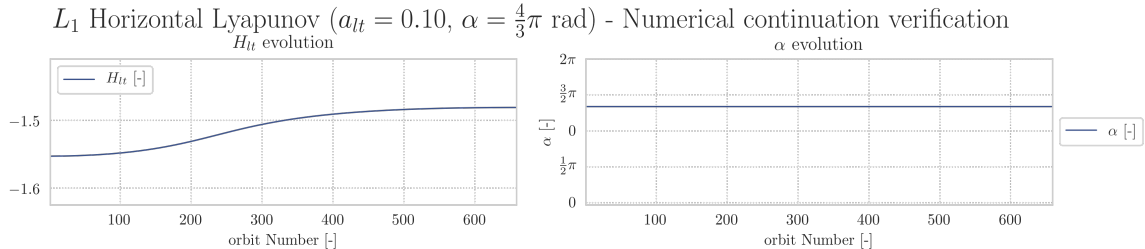


Figure E.35: Monodromy matrix eigensystem validation of the L_1 ($a_{lt} = 0.10, \alpha = \frac{4}{3}\pi$ rad) family. The left subplot shows that the deviation of the monodromy matrix determinant adheres to the constraint as specified in Table A.8. The right subplot demonstrates the eigenvalue representing the in-plane center subspace adheres to the periodicity constraint as specified in Table A.8.

Figure E.36 proves that the L_1 ($a_{lt} = 0.10, \alpha = \frac{4}{3}\pi$ rad) family is a H_{lt} -varying family since its thrust parameters are constant. The phase constraint is satisfied for the first half of the family but shifts slightly during the second half of the family.



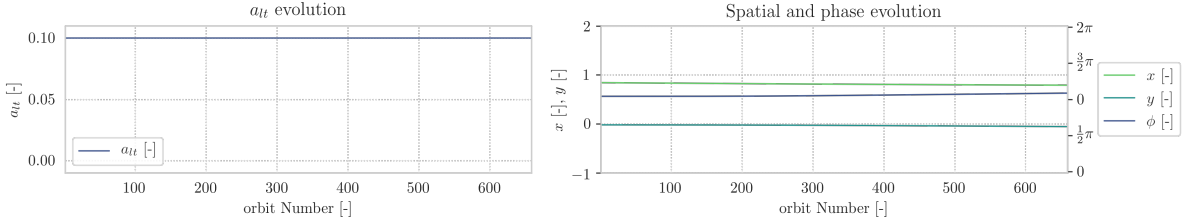


Figure E.36: Numerical continuation verification of the L_1 ($a_{lt} = 0.10, \alpha = \frac{4}{3}\pi$ rad) family. The top subplots and bottom left subplot demonstrate that the l.p.o family unfolds along the Hamiltonian branch. The bottom right subplot shows the spatial evolution and phase drift of the initial condition along the family.

L_2 ($a_{lt} = 0.10, \alpha = \frac{1}{3}\pi$ rad) H_{lt} -varying family

The periodicity of the members that constitute the $L_2(a_{lt} = 0.10, \alpha = \frac{1}{3}\pi$ rad) family are established in Figure E.37. The totality of the subplots of this Figure show that the collocation procedure produces a converged solution with an equidistributed truncation error. The initial state of the resulting solution is explicitly propagated for the estimated orbital period which confirms the periodicity of the family members and validates the correctness of the collocation procedure. All family members adhere to the periodicity threshold despite the fact that some members do not adhere to the equidistribution criterium listed in Table A.8.

L_2 Horizontal Lyapunov ($a_{lt} = 0.10, \alpha = \frac{1}{3}\pi$ rad) - Periodicity constraints verification

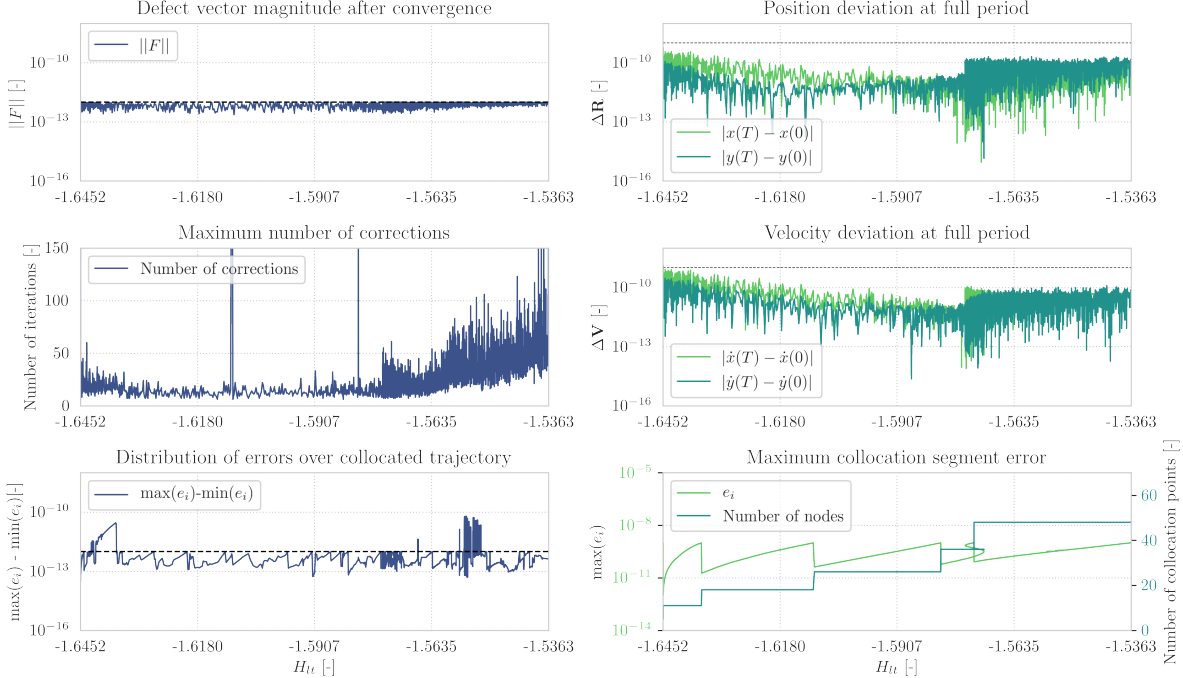


Figure E.37: Periodicity verification of the L_2 ($a_{lt} = 0.10, \alpha = \frac{1}{3}\pi$ rad) family. The three left subplots and the bottom right subplot demonstrate a correct implementation of the collocation procedure. The upper and middle right plot, constructed via explicit propagation of the solution resulting from the collocation procedure, confirm the periodicity of the family members.

Characteristics of the monodromy eigensystem of each member of the L_2 ($a_{lt} = 0.10, \alpha = \frac{1}{3}\pi$ rad) family are shown in Figure E.38. It can be concluded that the monodromy eigensystem of each family member adheres to the structure of a symplectic map although the eigenvalue pair related to the in-plane center subspace is nearly violated at the end of the family.

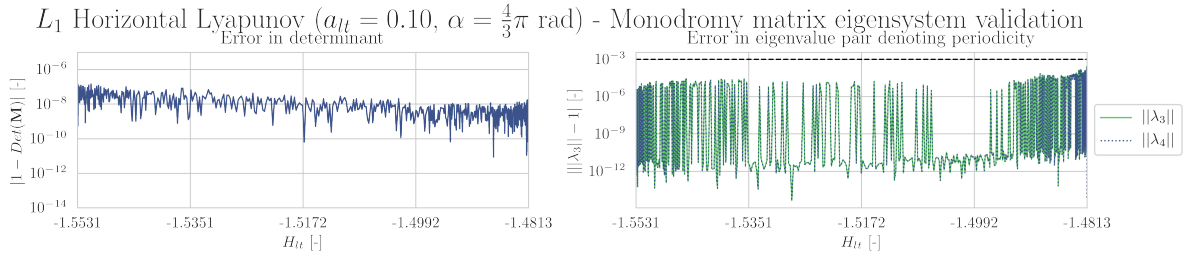


Figure E.38: Monodromy matrix eigensystem validation of the L_2 ($a_{lt} = 0.10, \alpha = \frac{1}{3}\pi$ rad) family. The left subplot shows that the deviation of the monodromy matrix determinant adheres to the constraint as specified in Table A.8. The right subplot demonstrates the eigenvalue representing the in-plane center subspace adheres to the periodicity constraint as specified in Table A.8.

Figure E.39 proves that the L_2 ($a_{lt} = 0.10, \alpha = \frac{1}{3}\pi$ rad) family is a H_{lt} -varying family since its thrust parameters are constant. A phase shift is observed throughout the family which does not affect the periodicity of the family members.

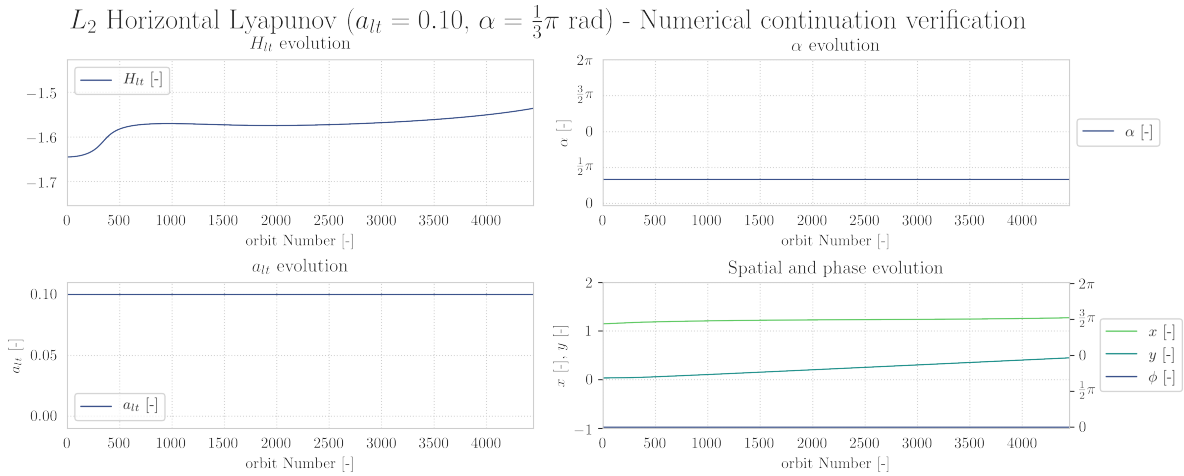
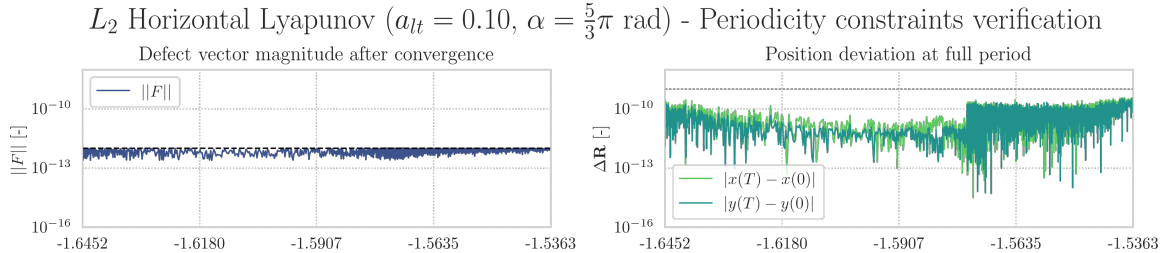


Figure E.39: Numerical continuation verification of the L_2 ($a_{lt} = 0.10, \alpha = \frac{2}{3}\pi$ rad) family. The top subplots and bottom left subplot demonstrate that the l.p.o family unfolds along the Hamiltonian branch. The bottom right subplot shows the spatial evolution and phase drift of the initial condition along the family.

L₂ ($a_{lt} = 0.10, \alpha = \frac{5}{3}\pi$ rad) H_{lt} -varying family

The periodicity of the members that constitute the $L_2(a_{lt} = 0.10, \alpha = \frac{5}{3}\pi$ rad) family are established in Figure E.40. The totality of the subplots of this Figure show that the collocation procedure produces a converged solution with an equidistributed truncation error. The initial state of the resulting solution is explicitly propagated for the estimated orbital period which confirms the periodicity of the family members and validates the correctness of the collocation procedure. All family members adhere to the periodicity threshold despite the fact that some members do not adhere to the equidistribution criterium listed in Table A.8.



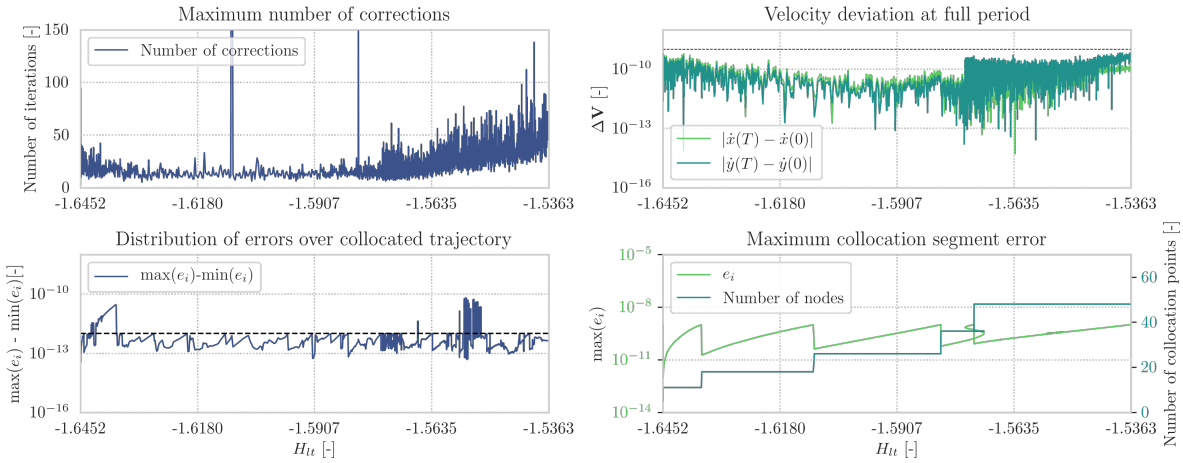


Figure E.40: Periodicity verification of the L_2 ($a_{lt} = 0.10, \alpha = \frac{5}{3}\pi$ rad) family. The three left subplots and the bottom right subplot demonstrate a correct implementation of the collocation procedure. The upper and middle right plot, constructed via explicit propagation of the solution resulting from the collocation procedure, confirm the periodicity of the family members.

Characteristics of the monodromy eigensystem of each member of the L_2 ($a_{lt} = 0.10, \alpha = \frac{5}{3}\pi$ rad) family are shown in Figure E.41. It can be concluded that the monodromy eigensystem of each family member adheres to the structure of a symplectic map apart from the final member who's eigenvalue pair related to the planar center subspace violates the threshold listed in Table A.4. This violation leads to the termination of the continuation procedure.

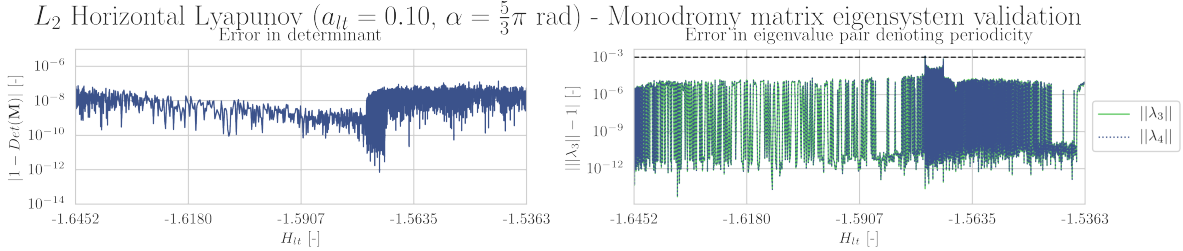
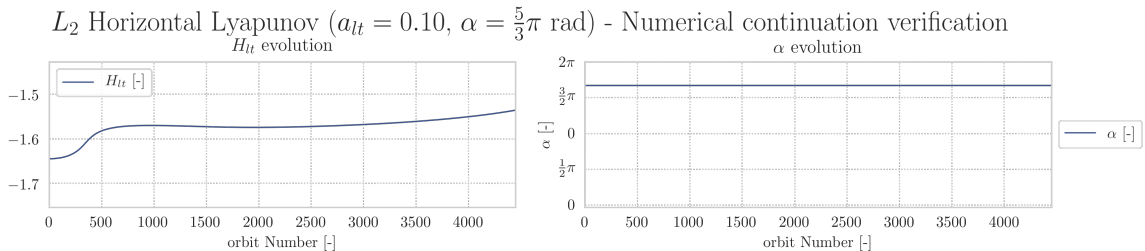


Figure E.41: Monodromy matrix eigensystem validation of the L_2 ($a_{lt} = 0.10, \alpha = \frac{5}{3}\pi$ rad) family. The left subplot shows that the deviation of the monodromy matrix determinant adheres to the constraint as specified in Table A.8. The right subplot demonstrates the eigenvalue representing the in-plane center subspace adheres to the periodicity constraint as specified in Table A.8.

Figure E.42 proves that the L_2 ($a_{lt} = 0.10, \alpha = \frac{5}{3}\pi$ rad) family is a H_{lt} -varying family since its thrust parameters are constant. No phase shift is observed throughout the family.



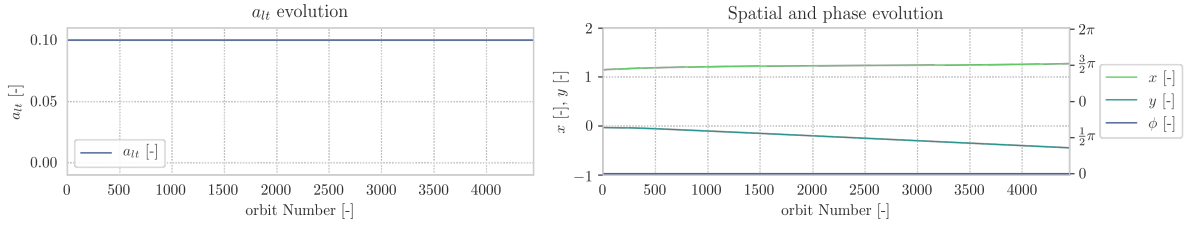


Figure E.42: Numerical continuation verification of the L_2 ($a_{lt} = 0.10, \alpha = \frac{5}{3}\pi$ rad) family. The top subplots and bottom left subplot demonstrate that the l.p.o family unfolds along the Hamiltonian branch. The bottom right subplot shows the spatial evolution and phase drift of the initial condition along the family.

E.5.2. a_{lt} -varying families

A total of thirty-six a_{lt} -varying families have been presented in Chapter 1 and Appendix D of this report and their correctness is discussed in this Subsection. The termination cause of each numerical continuation procedure associated with construction of an a_{lt} -varying family is presented in Table E.6.

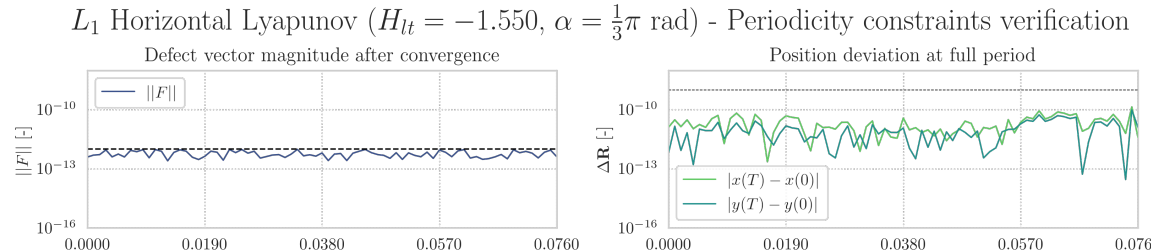
α	[rad]	E_1					E_2					
		0	$\frac{1}{3}\pi$	$\frac{2}{3}\pi$	π	$\frac{4}{3}\pi$	$\frac{5}{3}\pi$	0	$\frac{1}{3}\pi$	$\frac{2}{3}\pi$	π	$\frac{4}{3}\pi$
$H_{lt} = -1.55$	[–]	G	<u>I</u>	G	H	G	<u>I</u>	G	<u>I</u>	H	H	H
$H_{lt} = -1.525$	[–]	G	G	G	H	G	G	D ⁸⁵	G	G	H	G
$H_{lt} = -1.50$	[–]	G	G	G	G	G	G	D ⁴⁰	<u>I</u>	G	G	G

Table E.6: An overview of the termination causes of the numerical continuation procedures associated with a_{lt} -varying families. The termination cause of some a_{lt} -varying families is underlined, meaning that proof of their veracity is provided later in this Subsection. Contrary to the H_{lt} -varying families, the termination causes adhere to the symmetry of the dynamical model.

Table E.6 reveals that the continuation procedures associated with generation of the a_{lt} are terminated due to four different reasons. Most numerical continuation procedures are terminated because the periodic solutions for the complete range of acceleration magnitudes ($0 \leq a_{lt} \geq 0.1$) have been computed, which is indicated with the letter G. Six continuation procedures are terminated before solutions for the complete range of thrust magnitudes are computed since these solutions do not exist. Two continuation procedures have been intentionally terminated before computation of the complete family since the computational cost exceeded the time constraints of this thesis project. Six continuation procedures were terminated due to an instability in the collocation algorithm associated with the numerical continuation procedure. The veracity of these six families will be discussed in the remainder of this Subsection.

L_1 ($H_{lt} = -1.55, \alpha = \frac{1}{3}\pi$ rad) a_{lt} -varying family

The periodicity of the members that constitute the $L_1(H_{lt} = -1.55, \alpha = \frac{1}{3}\pi$ rad) family are established in Figure E.43. The totality of the subplots of this Figure show that the collocation procedure produces a converged solution with an equidistributed truncation error. The initial state of the resulting solution is explicitly propagated for the estimated orbital period which confirms the periodicity of the family members and validates the correctness of the collocation procedure. All family members adhere to the periodicity criteria listed in Table A.8.



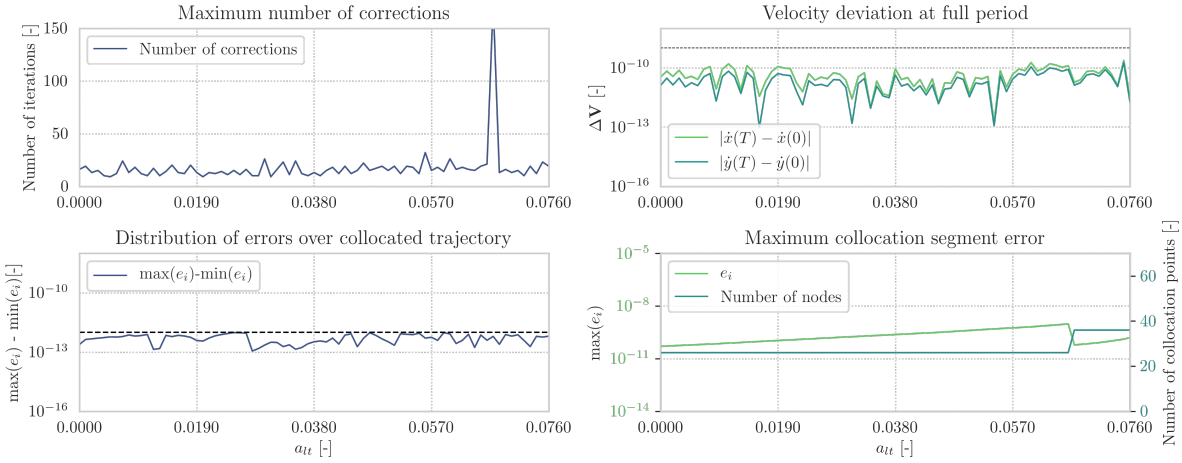


Figure E.43: Periodicity verification of the L_1 ($H_{lt} = -1.55, \alpha = \frac{1}{3}\pi$ rad) family. The three left subplots and the bottom right subplot demonstrate a correct implementation of the collocation procedure. The upper and middle right plot, constructed via explicit propagation of the solution resulting from the collocation procedure, confirm the periodicity of the family members.

Characteristics of the monodromy eigensystem of each member of the L_1 ($H_{lt} = -1.55, \alpha = \frac{1}{3}\pi$ rad) family are shown in Figure E.44. It can be concluded that the monodromy eigensystem of each family member adheres to the structure of a symplectic map.

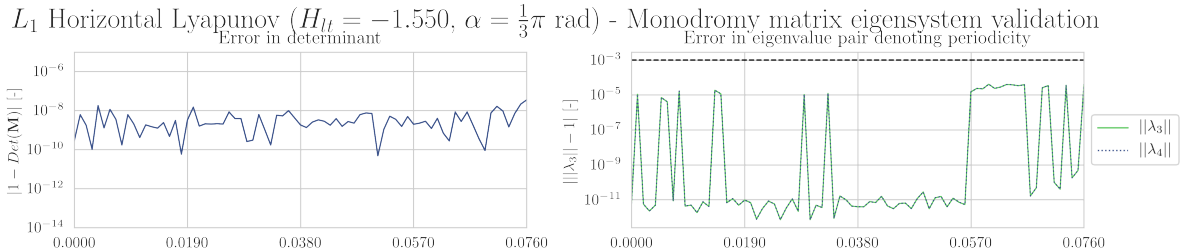
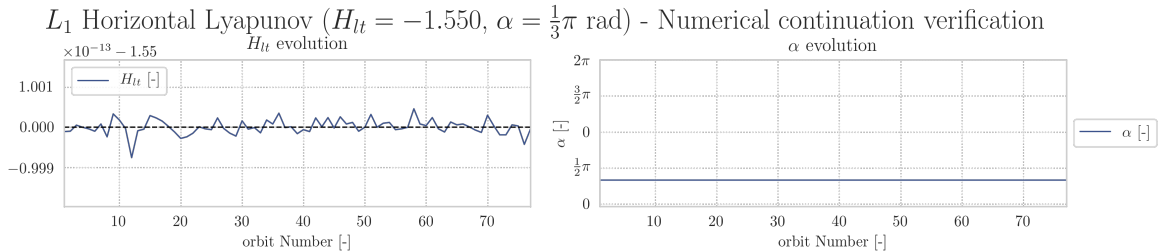


Figure E.44: Monodromy matrix eigensystem validation of the L_1 ($H_{lt} = -1.55, \alpha = \frac{1}{3}\pi$ rad) family. The left subplot shows that the deviation of the monodromy matrix determinant adheres to the constraint as specified in Table A.8. The right subplot demonstrates the eigenvalue representing the in-plane center subspace adheres to the periodicity constraint as specified in Table A.8.

Figure E.45 proves that the L_1 ($H_{lt} = -1.55, \alpha = \frac{1}{3}\pi$ rad) family is an a_{lt} -varying family since the Hamiltonian and acceleration orientation are constant. The phase constraint is not active during construction of this family so the phase drift in the bottom right subplot can be ignored.



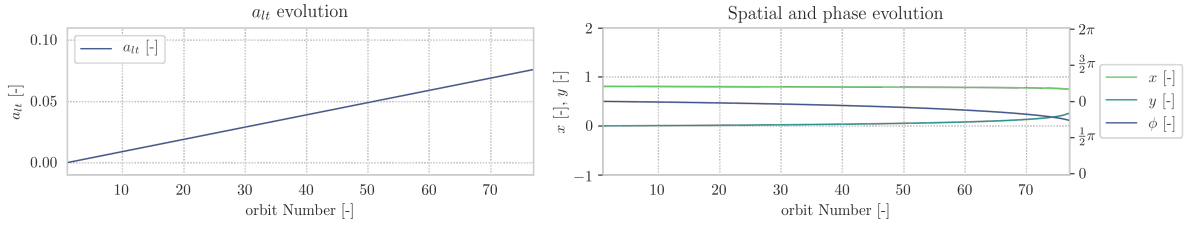


Figure E.45: Numerical continuation verification of the L_1 ($H_{lt} = -1.55, \alpha = \frac{5}{3}\pi$ rad) family. The top subplots and bottom left subplot demonstrate that the l.p.o family unfolds along the acceleration branch. The bottom right subplot shows the spatial evolution and phase drift of the initial condition along the family.

L₁ ($H_{lt} = -1.55, \alpha = \frac{5}{3}\pi$ rad) a_{lt} -varying family

The periodicity of the members that constitute the $L_1(H_{lt} = -1.55, \alpha = \frac{5}{3}\pi$ rad) family are established in Figure E.46. The totality of the subplots of this Figure show that the collocation procedure produces a converged solution with an equidistributed truncation error. The initial state of the resulting solution is explicitly propagated for the estimated orbital period which confirms the periodicity of the family members and validates the correctness of the collocation procedure. All family members adhere to the periodicity criteria listed in Table A.8.

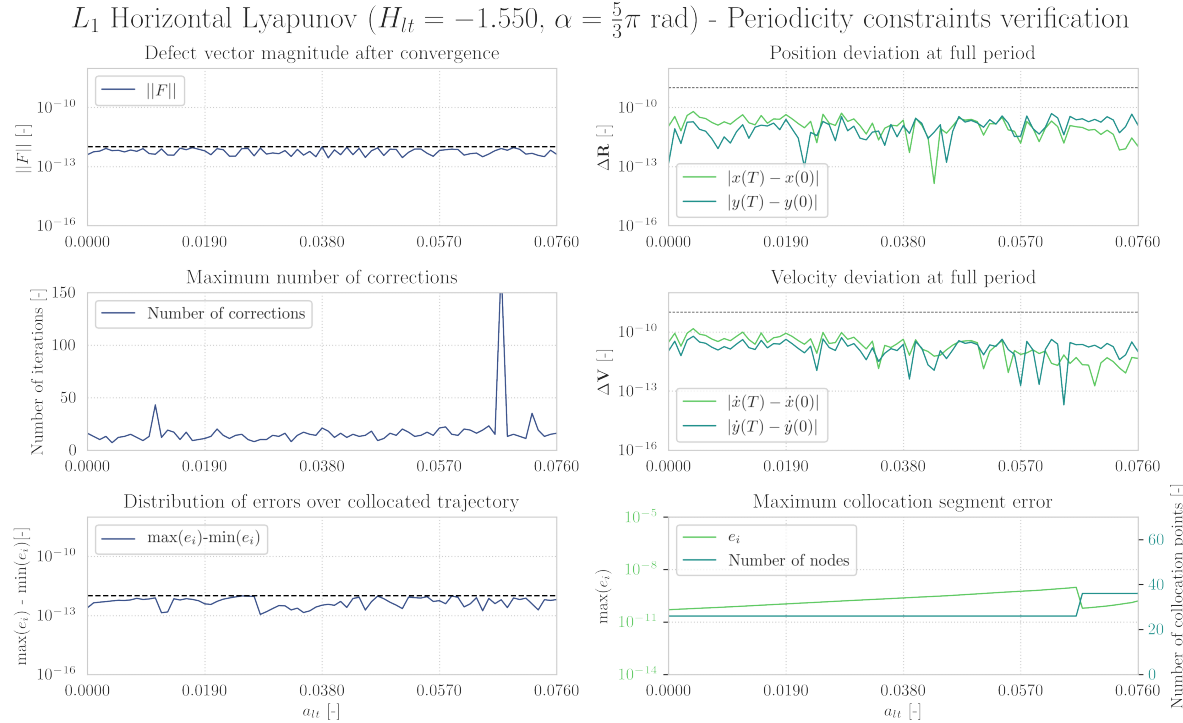


Figure E.46: Periodicity verification of the L_1 ($H_{lt} = -1.55, \alpha = \frac{5}{3}\pi$ rad) family. The three left subplots and the bottom right subplot demonstrate a correct implementation of the collocation procedure. The upper and middle right plot, constructed via explicit propagation of the solution resulting from the collocation procedure, confirm the periodicity of the family members.

Characteristics of the monodromy eigensystem of each member of the L_1 ($H_{lt} = -1.55, \alpha = \frac{5}{3}\pi$ rad) family are shown in Figure E.47. It can be concluded that the monodromy eigensystem of each family member adheres to the structure of a symplectic map.

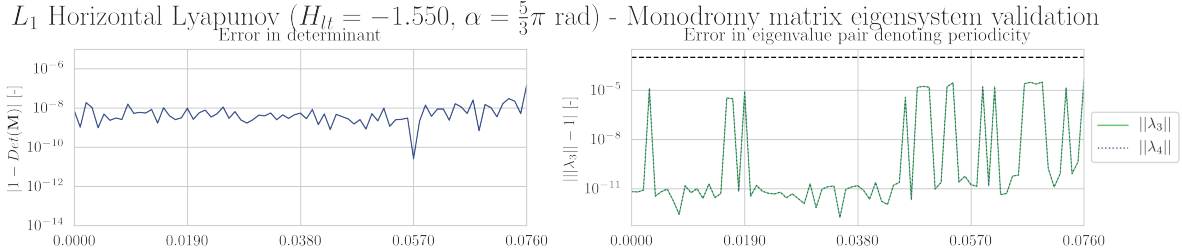


Figure E.47: Monodromy matrix eigensystem validation of the L_1 ($H_{lt} = -1.55, \alpha = \frac{5}{3}\pi$ rad) family. The left subplot shows that the deviation of the monodromy matrix determinant adheres to the constraint as specified in Table A.8. The right subplot demonstrates the eigenvalue representing the in-plane center subspace adheres to the periodicity constraint as specified in Table A.8.

Figure E.48 proves that the L_1 ($H_{lt} = -1.55, \alpha = \frac{5}{3}\pi$ rad) family is an a_{lt} -varying family since the Hamiltonian and acceleration orientation are constant. The phase constraint is not active during construction of this family so the phase drift in the bottom right subplot can be ignored.

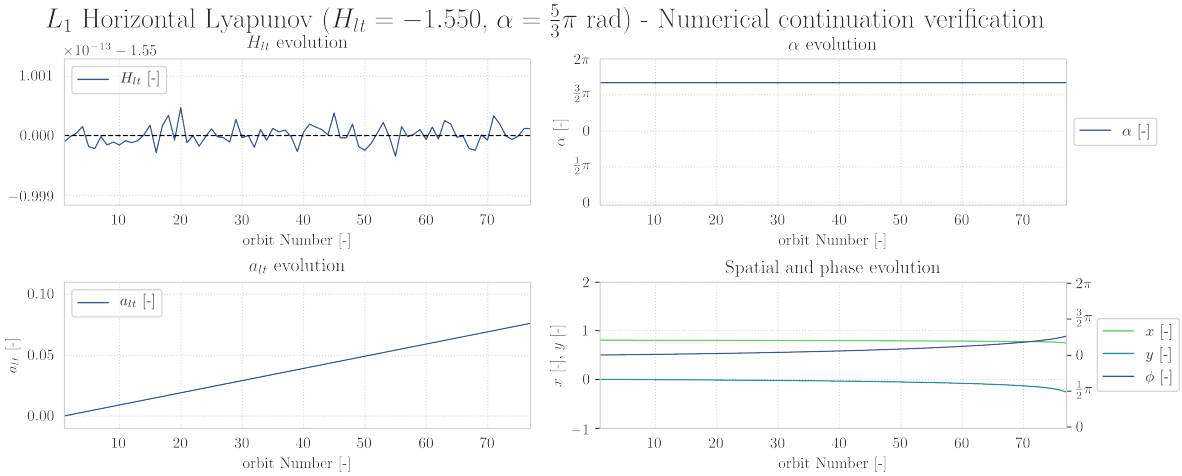
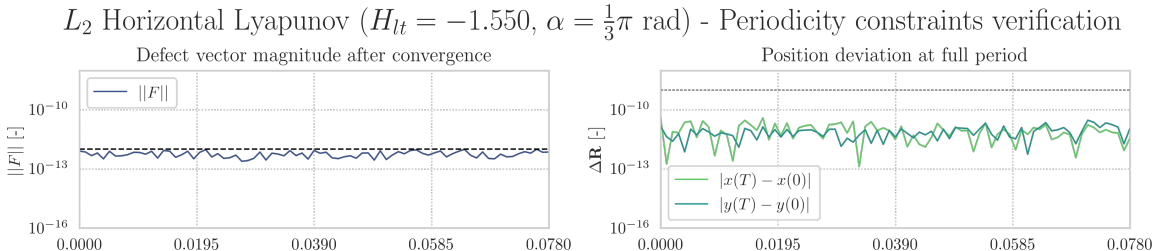


Figure E.48: Numerical continuation verification of the L_1 ($H_{lt} = -1.55, \alpha = \frac{5}{3}\pi$ rad) family. The top subplots and bottom left subplot demonstrate that the l.p.o family unfolds along the acceleration branch. The bottom right subplot shows the spatial evolution and phase drift of the initial condition along the family.

L_2 ($H_{lt} = -1.55, \alpha = \frac{1}{3}\pi$ rad) a_{lt} -varying family

The periodicity of the members that constitute the $L_2(H_{lt} = -1.55, \alpha = \frac{1}{3}\pi$ rad) family are established in Figure E.49. The totality of the subplots of this Figure show that the collocation procedure produces a converged solution with an equidistributed truncation error. The initial state of the resulting solution is explicitly propagated for the estimated orbital period which confirms the periodicity of the family members and validates the correctness of the collocation procedure. All family members adhere to the periodicity and equidistribution criteria listed in Table A.8.



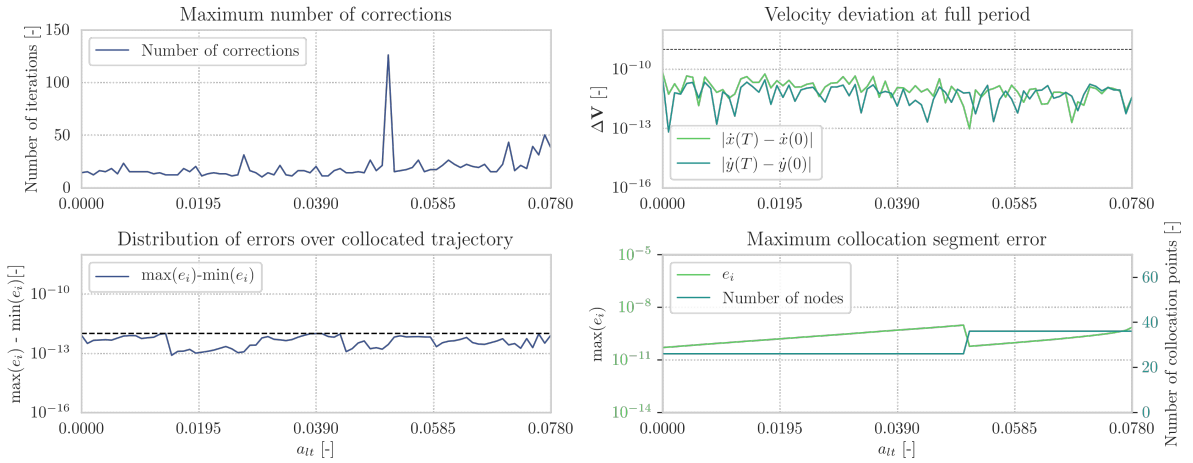


Figure E.49: Periodicity verification of the L_2 ($H_{lt} = -1.55, \alpha = \frac{1}{3}\pi$ rad) family. The three left subplots and the bottom right subplot demonstrate a correct implementation of the collocation procedure. The upper and middle right plot, constructed via explicit propagation of the solution resulting from the collocation procedure, confirm the periodicity of the family members.

Characteristics of the monodromy eigensystem of each member of the L_2 ($H_{lt} = -1.55, \alpha = \frac{1}{3}\pi$ rad) family are shown in Figure E.47. It can be concluded that the monodromy eigensystem of each family member adheres to the structure of a symplectic map.

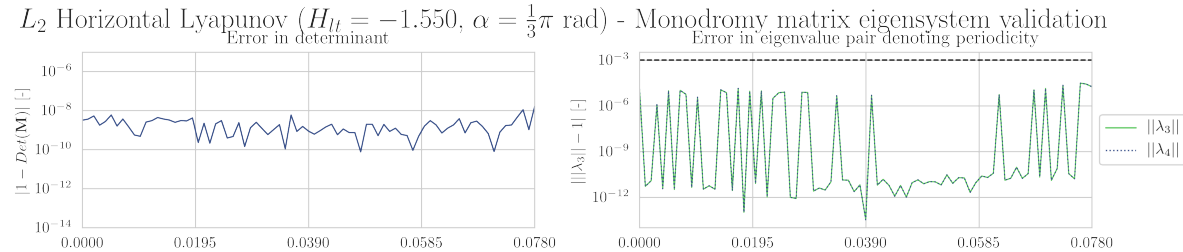
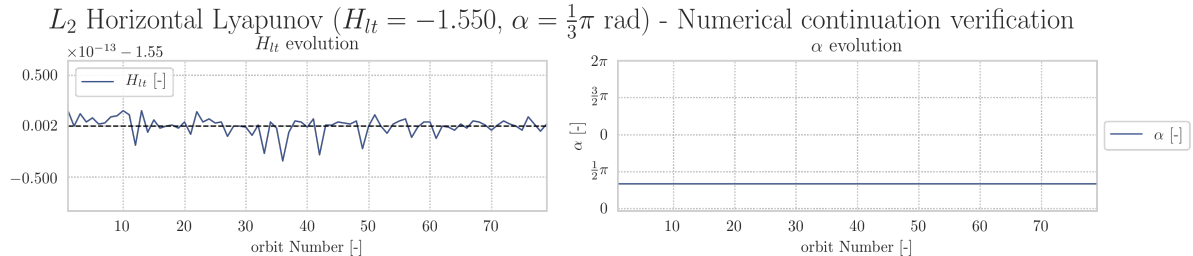


Figure E.50: Monodromy matrix eigensystem validation of the L_{12} ($H_{lt} = -1.55, \alpha = \frac{1}{3}\pi$ rad) family. The left subplot shows that the deviation of the monodromy matrix determinant adheres to the constraint as specified in Table A.8. The right subplot demonstrates the eigenvalue representing the in-plane center subspace adheres to the periodicity constraint as specified in Table A.8.

Figure E.51 proves that the L_2 ($H_{lt} = -1.55, \alpha = \frac{1}{3}\pi$ rad) family is an a_{lt} -varying family since the Hamiltonian and acceleration orientation are constant. The phase constraint is not active during construction of this family so the phase drift in the bottom right subplot can be ignored.



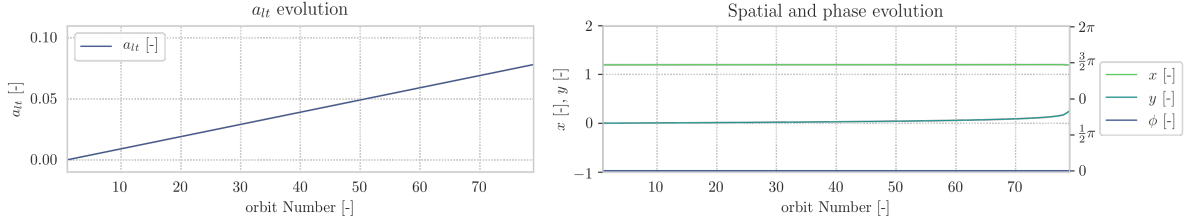


Figure E.51: Numerical continuation verification of the L_2 ($H_{lt} = -1.55, \alpha = \frac{5}{3}\pi$ rad) family. The top subplots and bottom left subplot demonstrate that the l.p.o family unfolds along the acceleration branch. The bottom right subplot shows the spatial evolution and phase drift of the initial condition along the family.

L₂ ($H_{lt} = -1.55, \alpha = \frac{5}{3}\pi$ rad) a_{lt} -varying family

The periodicity of the members that constitute the L_2 ($H_{lt} = -1.55, \alpha = \frac{5}{3}\pi$ rad) family are established in Figure E.52. The totality of the subplots of this Figure show that the collocation procedure produces a converged solution with an equidistributed truncation error. The initial state of the resulting solution is explicitly propagated for the estimated orbital period which confirms the periodicity of the family members and validates the correctness of the collocation procedure. All family members adhere to the periodicity and equidistribution criteria listed in Table A.8.

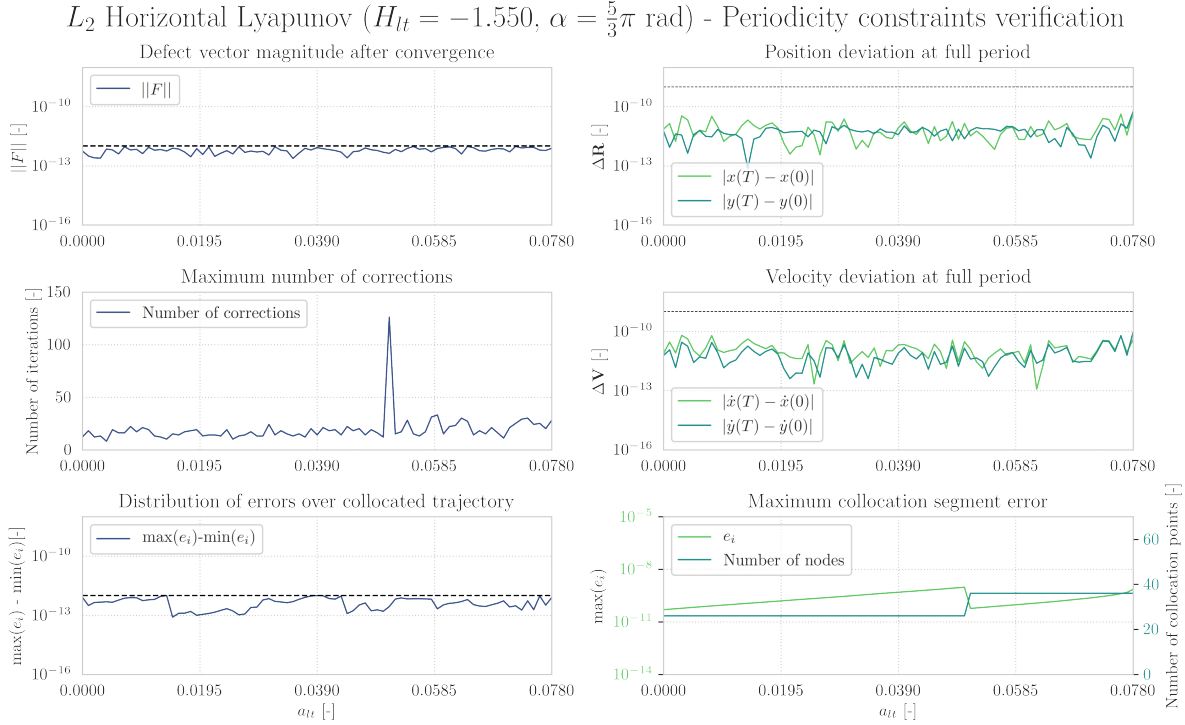


Figure E.52: Periodicity verification of the L_2 ($H_{lt} = -1.55, \alpha = \frac{5}{3}\pi$ rad) family. The three left subplots and the bottom right subplot demonstrate a correct implementation of the collocation procedure. The upper and middle right plot, constructed via explicit propagation of the solution resulting from the collocation procedure, confirm the periodicity of the family members.

Characteristics of the monodromy eigensystem of each member of the L_2 ($H_{lt} = -1.55, \alpha = \frac{5}{3}\pi$ rad) family are shown in Figure E.53. It can be concluded that the monodromy eigensystem of each family member adheres to the structure of a symplectic map.

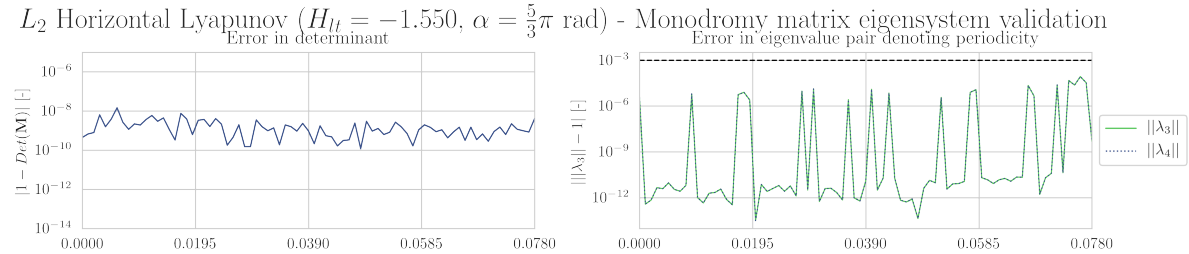


Figure E.53: Monodromy matrix eigensystem validation of the L_2 ($H_{lt} = -1.55, \alpha = \frac{5}{3}\pi$ rad) family. The left subplot shows that the deviation of the monodromy matrix determinant adheres to the constraint as specified in Table A.8. The right subplot demonstrates the eigenvalue representing the in-plane center subspace adheres to the periodicity constraint as specified in Table A.8.

Figure E.51 proves that the L_2 ($H_{lt} = -1.55, \alpha = \frac{5}{3}\pi$ rad) family is an a_{lt} -varying family since the Hamiltonian and acceleration orientation are constant. The phase constraint is not active during construction of this family so the phase drift in the bottom right subplot can be ignored.

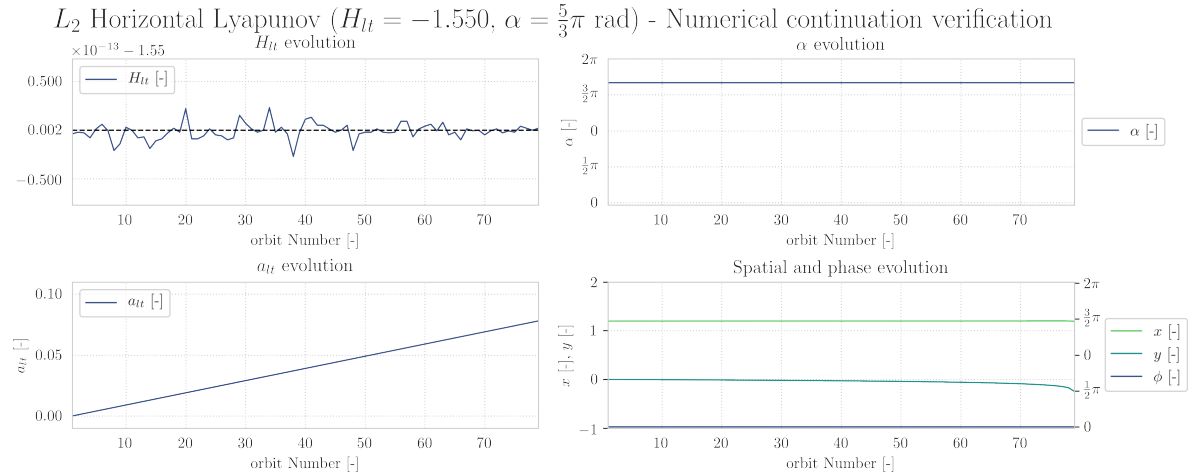
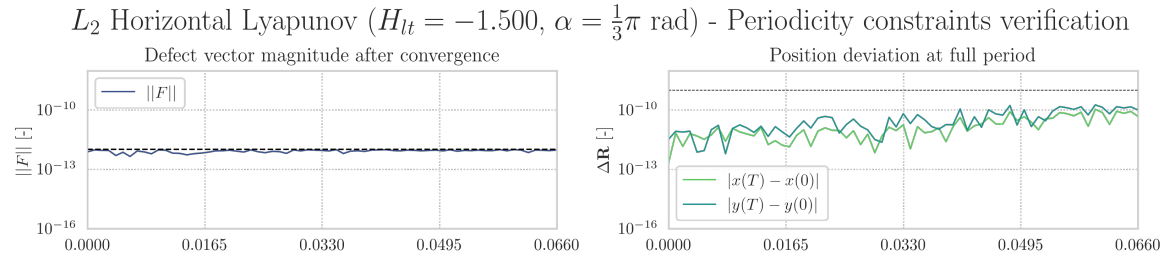


Figure E.54: Numerical continuation verification of the L_2 ($H_{lt} = -1.55, \alpha = \frac{5}{3}\pi$ rad) family. The top subplots and bottom left subplot demonstrate that the l.p.o family unfolds along the acceleration branch. The bottom right subplot shows the spatial evolution and phase drift of the initial condition along the family.

L_2 ($H_{lt} = -1.50, \alpha = \frac{1}{3}\pi$ rad) a_{lt} -varying family

The periodicity of the members that constitute the $L_2(H_{lt} = -1.50, \alpha = \frac{1}{3}\pi$ rad) family are established in Figure E.55. The totality of the subplots of this Figure show that the collocation procedure produces a converged solution with an equidistributed truncation error. The initial state of the resulting solution is explicitly propagated for the estimated orbital period which confirms the periodicity of the family members and validates the correctness of the collocation procedure. All family members adhere to the periodicity and equidistribution criteria listed in Table A.8.



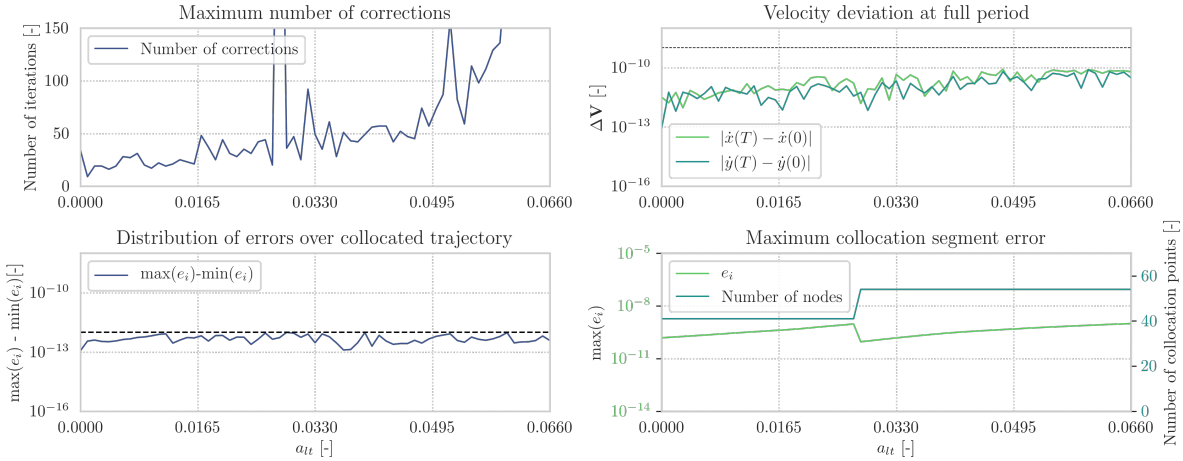


Figure E.55: Periodicity verification of the L_2 ($H_{lt} = -1.50, \alpha = \frac{1}{3}\pi$ rad) family. The three left subplots and the bottom right subplot demonstrate a correct implementation of the collocation procedure. The upper and middle right plot, constructed via explicit propagation of the solution resulting from the collocation procedure, confirm the periodicity of the family members.

Characteristics of the monodromy eigensystem of each member of the L_2 ($H_{lt} = -1.50, \alpha = \frac{1}{3}\pi$ rad) family are shown in Figure E.56. It can be concluded that the monodromy eigensystem of each family member adheres to the structure of a symplectic map.

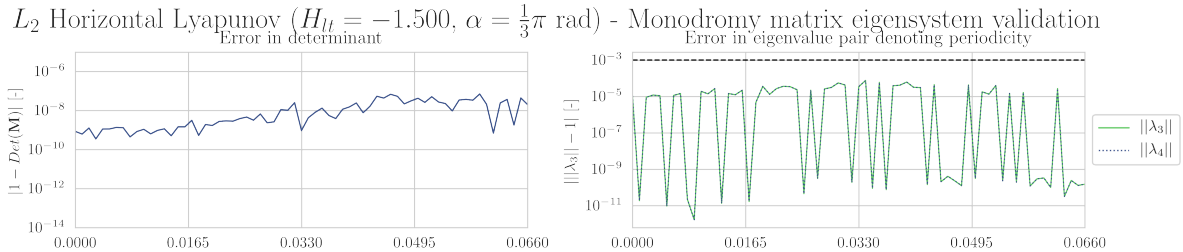
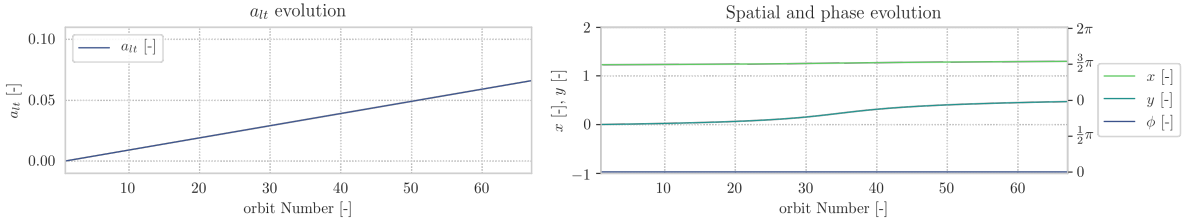


Figure E.56: Monodromy matrix eigensystem validation of the L_2 ($H_{lt} = -1.50, \alpha = \frac{1}{3}\pi$ rad) family. The left subplot shows that the deviation of the monodromy matrix determinant adheres to the constraint as specified in Table A.8. The right subplot demonstrates the eigenvalue representing the in-plane center subspace adheres to the periodicity constraint as specified in Table A.8.

Figure E.57 proves that the L_2 ($H_{lt} = -1.50, \alpha = \frac{1}{3}\pi$ rad) family is an a_{lt} -varying family since the Hamiltonian and acceleration orientation are constant. The phase constraint is not active during construction of this family so the phase drift in the bottom right subplot can be ignored.



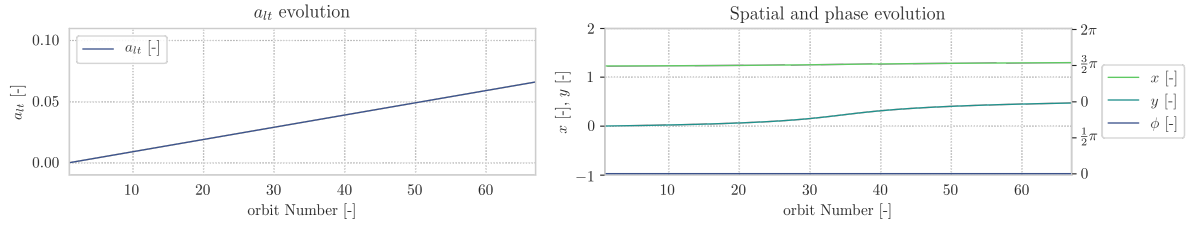


Figure E.57: Numerical continuation verification of the L_2 ($H_{lt} = -1.50, \alpha = \frac{5}{3}\pi$ rad) family. The top subplots and bottom left subplot demonstrate that the l.p.o family unfolds along the acceleration branch. The bottom right subplot shows the spatial evolution and phase drift of the initial condition along the family.

L_2 ($H_{lt} = -1.50, \alpha = \frac{5}{3}\pi$ rad) a_{lt} -varying family

The periodicity of the members that constitute the $L_2(H_{lt} = -1.50, \alpha = \frac{5}{3}\pi$ rad) family are established in Figure E.58. The totality of the subplots of this Figure show that the collocation procedure produces a converged solution with an equidistributed truncation error. The initial state of the resulting solution is explicitly propagated for the estimated orbital period which confirms the periodicity of the family members and validates the correctness of the collocation procedure. All family members adhere to the periodicity and equidistribution criteria listed in Table A.8.

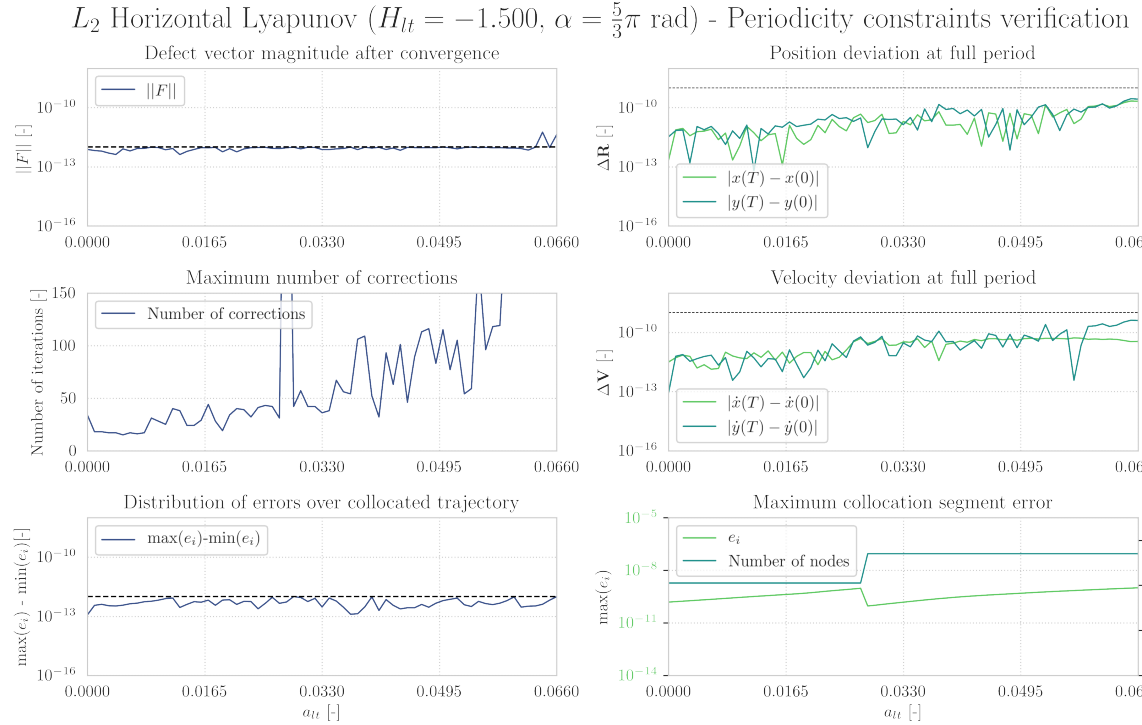


Figure E.58: Periodicity verification of the L_2 ($H_{lt} = -1.50, \alpha = \frac{5}{3}\pi$ rad) family. The three left subplots and the bottom right subplot demonstrate a correct implementation of the collocation procedure. The upper and middle right plot, constructed via explicit propagation of the solution resulting from the collocation procedure, confirm the periodicity of the family members.

Characteristics of the monodromy eigensystem of each member of the L_2 ($H_{lt} = -1.50, \alpha = \frac{5}{3}\pi$ rad) family are shown in Figure E.59. It can be concluded that the monodromy eigensystem of each family member adheres to the structure of a symplectic map.

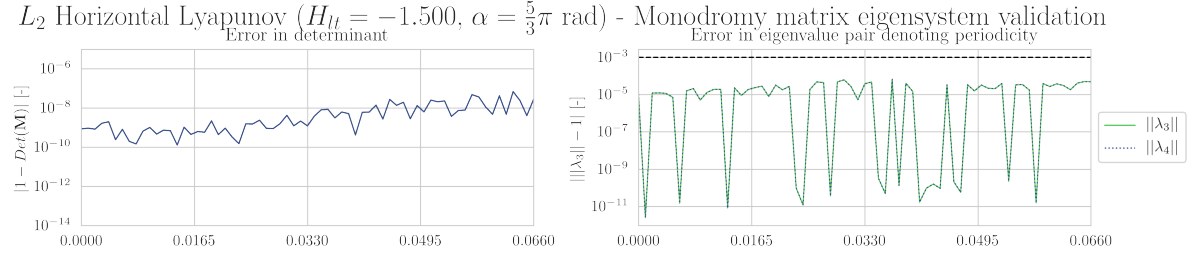


Figure E.59: Monodromy matrix eigensystem validation of the L_2 ($H_{lt} = -1.50, \alpha = \frac{5}{3}\pi$ rad) family. The left subplot shows that the deviation of the monodromy matrix determinant adheres to the constraint as specified in Table A.8. The right subplot demonstrates the eigenvalue representing the in-plane center subspace adheres to the periodicity constraint as specified in Table A.8.

Figure E.60 proves that the L_2 ($H_{lt} = -1.50, \alpha = \frac{5}{3}\pi$ rad) family is an a_{lt} -varying family since the Hamiltonian and acceleration orientation are constant. The phase constraint is not active during construction of this family so the phase drift in the bottom right subplot can be ignored.

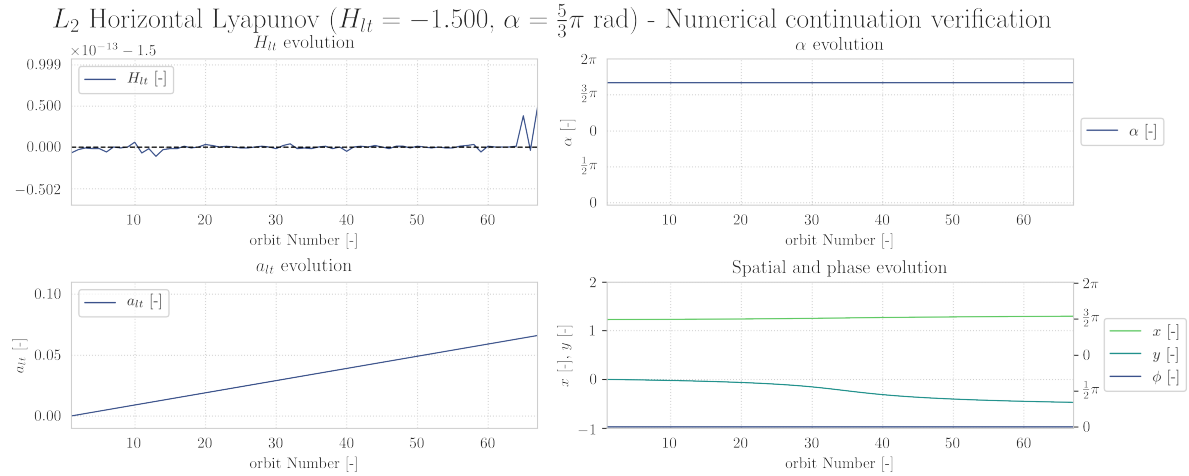


Figure E.60: Numerical continuation verification of the L_2 ($H_{lt} = -1.50, \alpha = \frac{5}{3}\pi$ rad) family. The top subplots and bottom left subplot demonstrate that the l.p.o family unfolds along the acceleration branch. The bottom right subplot shows the spatial evolution and phase drift of the initial condition along the family.

E.5.3. α -varying families

A total of eighteen α -varying families have been presented in Chapter 1 of this report. The correctness of them is discussed in this Subsection. The termination cause of each numerical continuation procedure associated with construction of an α -varying family is presented in Table E.7.

a_{lt}	[-]	E ₁			E ₂		
		0.01	0.05	0.10	0.01	0.05	0.10
$H_{lt} = -1.55$	[-]	J	J	H	J*	H	TBD
$H_{lt} = -1.525$	[-]	J	J	H	J*	J	TBD
$H_{lt} = -1.50$	[-]	J	J*	J*	J	TBD	TBD

Table E.7: An overview of the termination causes of the numerical continuation procedures associated with α -varying families. The termination cause of some α -varying families is underlined, meaning that proof of their veracity is provided later in this Subsection. Families whose termination codes are augmented with an asterisk subscript are generated via multiple continuation procedures.

The continuation procedures responsible for construction of the α -varying families are terminated due to various reasons. Most continuation procedures are terminated because the complete family has been calculated. Some families have been constructed via multiple continuation procedures that leverage different seed solutions. The remaining families could not be fully computed due to instabilities in the collocation procedure. The veracity of the families constructed by continuation procedures terminated due to the latter two reasons are discussed in the remainder of this Subsection.

L₁ ($a_{lt} = 0.05, H_{lt} = -1.50$) α -varying family

The degree of periodicity of the members that constitute the $L_1(a_{lt} = 0.05, H_{lt} = -1.50)$ family is shown in Figure E.61. The totality of the subplots of this Figure show that the collocation procedure produces a converged solution whose truncation error is not always equidistributed. The initial state of the resulting solution is explicitly propagated for the estimated orbital period. One member of the family does not meet the periodicity thresholds at full period but termination of the continuation procedure is due to this violation is intentionally suppressed since α -varying families would otherwise be large to obtain. The family has been constructed via three continuation procedures where the first procedure has produced the partial family for $\alpha \in [0^\circ, 134^\circ]$. The second continuation procedure has computed the partial family for $\alpha \in [135^\circ, 260^\circ]$ and the third continuation procedure computes the partial family for $\alpha \in [261^\circ, 359^\circ]$. The piecewise construction is clearly observed in the right subplots of E.61. A shift in full period state discrepancies and patch points is visible at 135° and 261° .

L_1 Horizontal Lyapunov ($H_{lt} = -1.500, a_{lt} = 0.05$) - Periodicity constraints verification

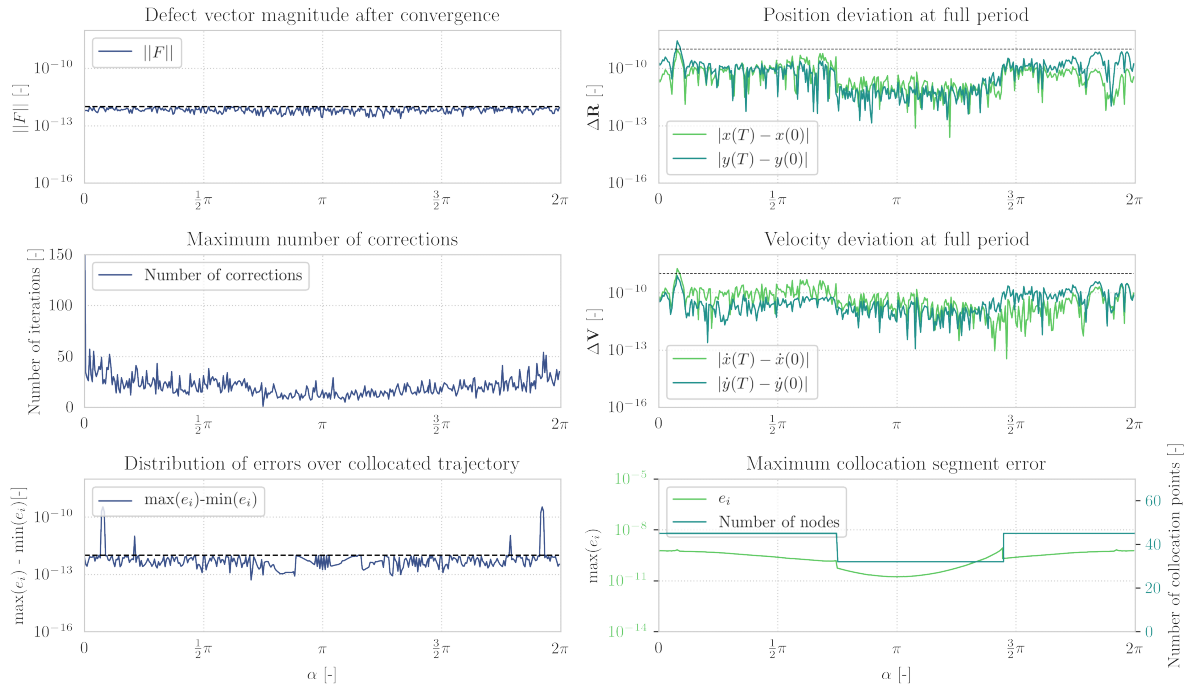


Figure E.61: Periodicity verification of the L_1 ($a_{lt} = 0.05, H_{lt} = -1.50$) family. The three left subplots and the bottom right subplot demonstrate a correct implementation of the collocation procedure. The upper and middle right plot, constructed via explicit propagation of the solution resulting from the collocation procedure, present the state deviation of the family members at full-period.

Characteristics of the monodromy eigensystem of each member of the L_1 ($a_{lt} = 0.05, H_{lt} = -1.50$) family are shown in Figure E.62. It can be concluded that the monodromy eigensystem of each family member adheres to the structure of a symplectic map. The piecewise construction of the family is also visible in the monodromy eigensystem deviations. A shift in the magnitude eigensystem deviations occur at 135° and 261° .

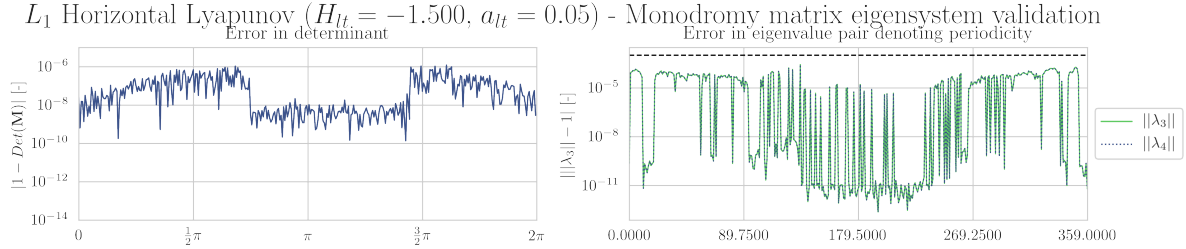


Figure E.62: Monodromy matrix eigensystem validation of the L_1 ($a_{lt} = 0.05, H_{lt} = -1.50$) family. The left subplot shows that the deviation of the monodromy matrix determinant adheres to the constraint as specified in Table A.8. The right subplot demonstrates the eigenvalue representing the in-plane center subspace adheres to the periodicity constraint as specified in Table A.8.

Figure E.63 proves that the L_1 ($a_{lt} = 0.05, H_{lt} = -1.50$) family is an α -varying family since the Hamiltonian and acceleration magnitude are constant. The phase constraint is not active during construction of this family so the phase drift in the bottom right subplot can be ignored. The piecewise construction of the family is also visible in the continuation verification since the deviation in Hamiltonian increases at the end of the first collocation procedure ($\alpha = 134^\circ$) and at the beginning of the third collocation procedure ($\alpha = 135^\circ$).

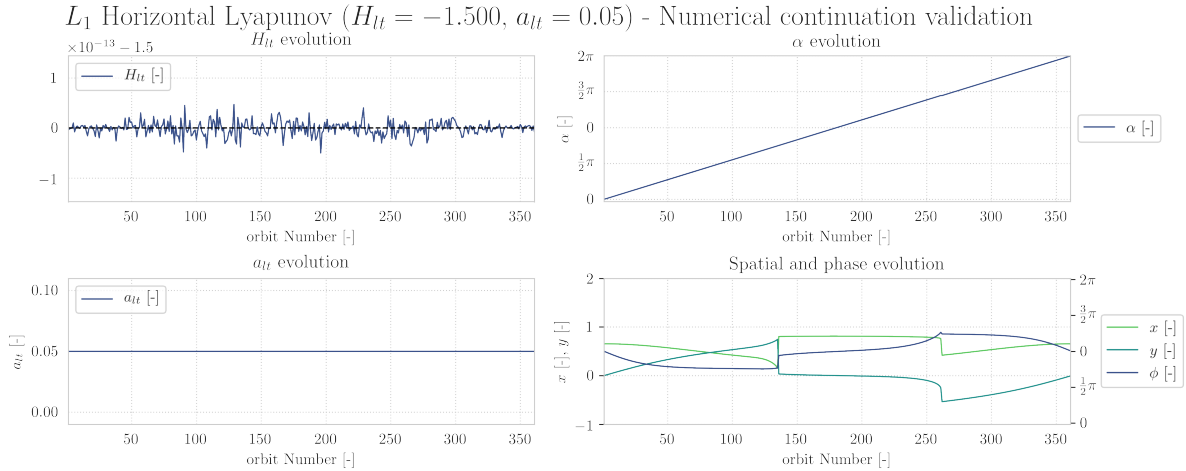


Figure E.63: Numerical continuation verification of the L_1 ($a_{lt} = 0.05, H_{lt} = -1.50$) family. The top subplots and bottom left subplot demonstrate that the l.p.o family unfolds along the acceleration branch. The bottom right subplot shows the spatial evolution and phase drift of the initial condition along the family.

It is unlikely that the asymmetries observed in the L_1 ($a_{lt} = 0.05, H_{lt} = -1.50$) family are correct since symmetry exists in the CR3BP-LT[1]. Hence, the observed asymmetries are a faulty numerical approximation of the family members. Figures E.61-E.63 do not provide a clear explanation since the members adhere to the periodicity eigensystem deviation tolerances. A possible root cause for the asymmetries is that the order of the collocation scheme is not high enough to accurately approximate the family members which extend furthest into the negative x -direction ($\alpha = 135^\circ$). The insufficient order of the collocation procedure causes a lack of robustness which explains why a different seed solution allows computation of the remainder of the family.

L_1 ($a_{lt} = 0.10, H_{lt} = -1.55$) α -varying family

The degree of periodicity of the members that constitute the L_1 ($a_{lt} = 0.10, H_{lt} = -1.55$) family is shown in Figure E.61. This particular family exists for $\alpha \in [-122^\circ, 122^\circ]$ which explains the straight line segment in each plot. The totality of the subplots of this Figure show that the collocation procedure produces a converged solution whose truncation error is not always equidistributed. The initial state of the resulting solution is explicitly propagated for the estimated orbital period. Several members of the family do not meet the periodicity thresholds at full period but termination of the continuation procedure is due to this violation is intentionally suppressed since otherwise construction of α -varying families would not be possible. The family has been constructed via four continuation procedures where the first procedure has produced the partial family for $\alpha \in [0^\circ, 92^\circ]$. The second continuation procedure has computed the partial family for $\alpha \in [93^\circ, 122^\circ]$ whereas the third and fourth continuation procedure compute parts of the family for $\alpha \in [238^\circ, 267^\circ]$ and

$\alpha \in [268^\circ, 359^\circ]$. The piecewise construction is clearly observed in the right subplots of E.64. A shift in full period state discrepancies and patch points is visible at 93° and 268° .

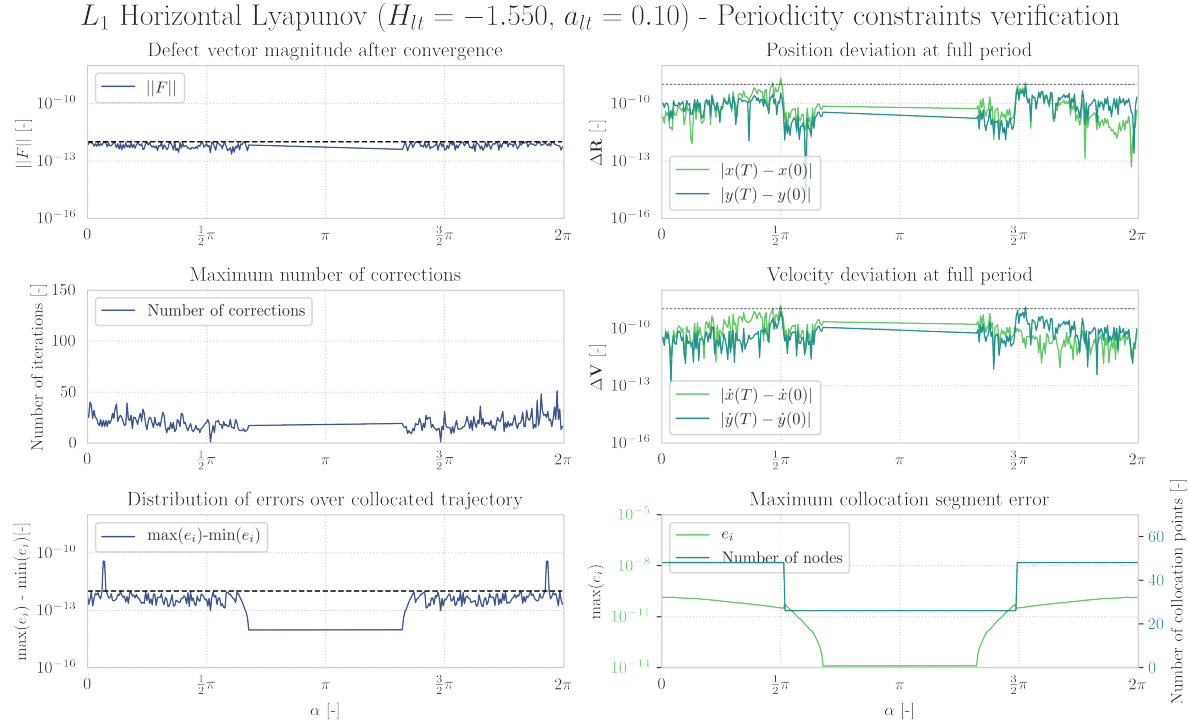


Figure E.64: Periodicity verification of the L_1 ($a_{lt} = 0.10, H_{lt} = -1.55$) family. The three left subplots and the bottom right subplot demonstrate a correct implementation of the collocation procedure. The upper and middle right plot, constructed via explicit propagation of the solution resulting from the collocation procedure, present the state deviation of the family members at full-period.

Characteristics of the monodromy eigensystem of each member of the L_1 ($a_{lt} = 0.10, H_{lt} = -1.55$) family are shown in Figure E.65. It can be concluded that the monodromy eigensystem of each family member adheres to the structure of a symplectic map. The piecewise construction of the family is also visible in the monodromy eigensystem deviations. A shift in the magnitude eigensystem deviations occur at 93° and 268° .

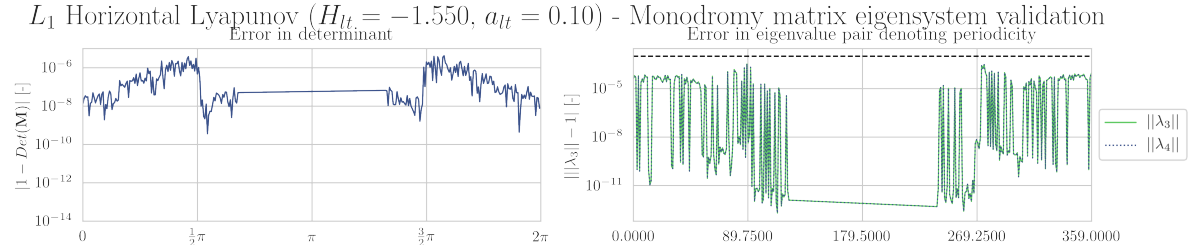


Figure E.65: Monodromy matrix eigensystem validation of the L_1 ($a_{lt} = 0.10, H_{lt} = -1.55$) family. The left subplot shows that the deviation of the monodromy matrix determinant adheres to the constraint as specified in Table A.8. The right subplot demonstrates the eigenvalue representing the in-plane center subspace adheres to the periodicity constraint as specified in Table A.8.

Figure E.66 proves that the L_1 ($a_{lt} = 0.10, H_{lt} = -1.55$) family is an α -varying family since the Hamiltonian and acceleration magnitude are constant. The phase constraint is not active during construction of this family so the phase drift in the bottom right subplot can be ignored. The piecewise construction of the family is also visible in the continuation verification since the deviation in Hamiltonian increases at the end of the first collocation procedure ($\alpha = 93^\circ$) and at the beginning of the fourth collocation procedure ($\alpha = 268^\circ$).

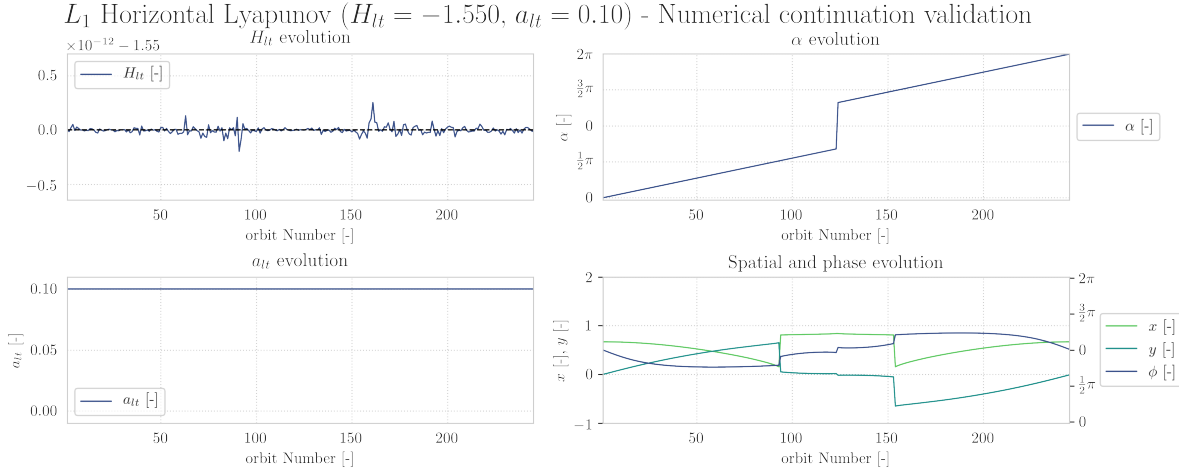


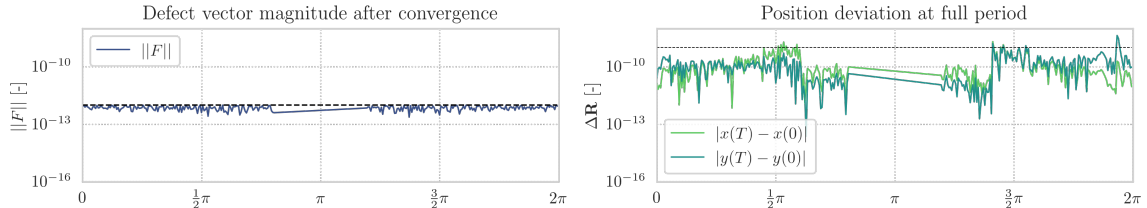
Figure E.66: Numerical continuation verification of the L_1 ($a_{lt} = 0.10, H_{lt} = -1.55$) family. The top subplots and bottom left subplot demonstrate that the l.p.o family unfolds along the acceleration branch. The bottom right subplot shows the spatial evolution and phase drift of the initial condition along the family.

It is unlikely that the asymmetries observed in the L_1 ($a_{lt} = 0.10, H_{lt} = -1.55$) family are correct since symmetry exists in the CR3Bp-LT[1]. Hence, the observed asymmetries are a faulty numerical approximation of the family members. Figures E.64-E.66 do not provide a clear explanation since the members adhere to the periodicity eigensystem deviation tolerances. A possible root cause for the observed symmetries is that the order of the collocation scheme is not high enough to accurately approximate the family members which extend furthest into the negative x -direction. The insufficient order of the collocation procedure causes a lack of robustness which explains why a different seed solution allows computation of the remainder of the family.

L_1 ($a_{lt} = 0.10, H_{lt} = -1.525$) α -varying family

The degree of periodicity of the members that constitute the $L_1(a_{lt} = 0.10, H_{lt} = -1.525)$ family is shown in Figure E.67. This particular family exists for $\alpha \in [-145^\circ, 145^\circ]$ which explains the straight line segment in each subplot. The totality of the subplots of this Figure show that the collocation procedure produces a converged solution whose truncation error is not always equidistributed. The initial state of the resulting solution is explicitly propagated for the estimated orbital period. Several members of the family do not meet the periodicity thresholds at full period but termination of the continuation procedure is due to this violation is intentionally suppressed since otherwise construction of α -varying families would not be possible. The family has been constructed via four continuation procedures where the first procedure has produced the partial family for $\alpha \in [0^\circ, 109^\circ]$. The second continuation procedure has computed the partial family for $\alpha \in [110^\circ, 145^\circ]$ whereas the third and fourth continuation procedure compute parts of the family for $\alpha \in [215^\circ, 253^\circ]$ and $\alpha \in [254^\circ, 359^\circ]$.

L_1 Horizontal Lyapunov ($H_{lt} = -1.525, a_{lt} = 0.10$) - Periodicity constraints verification



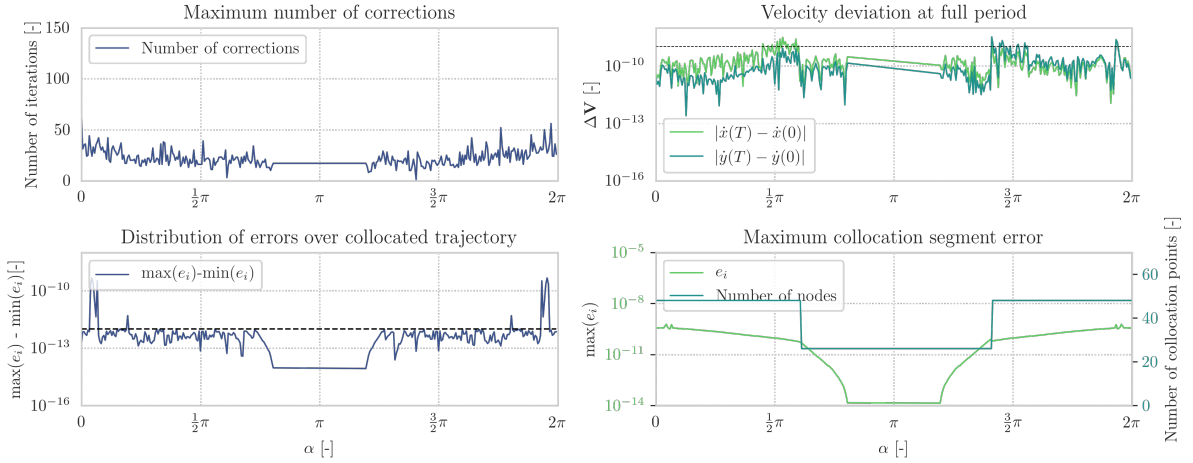


Figure E.67: Periodicity verification of the L_1 ($a_{lt} = 0.10, H_{lt} = -1.525$) family. The three left subplots and the bottom right subplot demonstrate a correct implementation of the collocation procedure. The upper and middle right plot, constructed via explicit propagation of the solution resulting from the collocation procedure, present the state deviation of the family members at full-period.

Characteristics of the monodromy eigensystem of each member of the L_1 ($a_{lt} = 0.10, H_{lt} = -1.525$) family are shown in Figure E.68. It can be concluded that the monodromy eigensystem of each family member adheres to the structure of a symplectic map. The piecewise construction of the family is also visible in the monodromy eigensystem deviations. A shift in the magnitude eigensystem deviations occur at 110° and 254° .

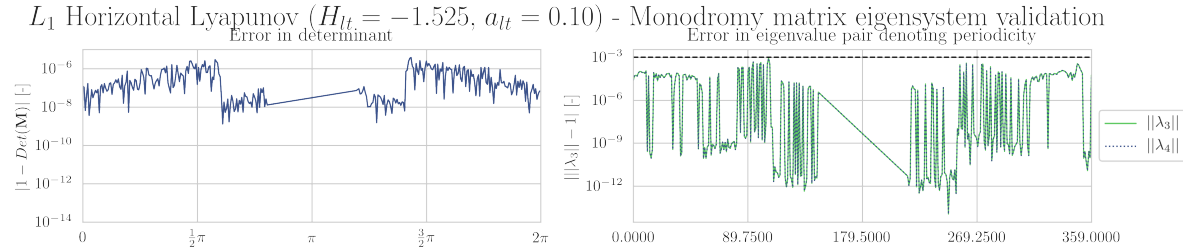
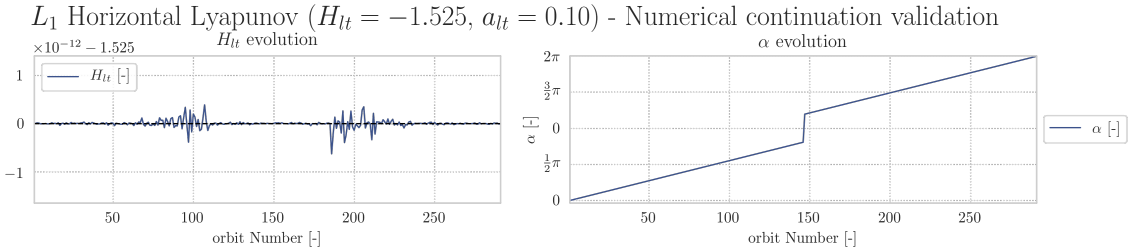


Figure E.68: Monodromy matrix eigensystem validation of the L_1 ($a_{lt} = 0.10, H_{lt} = -1.525$) family. The left subplot shows that the deviation of the monodromy matrix determinant adheres to the constraint as specified in Table A.8. The right subplot demonstrates the eigenvalue representing the in-plane center subspace adheres to the periodicity constraint as specified in Table A.8.

Figure E.69 proves that the L_1 ($a_{lt} = 0.10, H_{lt} = -1.525$) family is an α -varying family since the Hamiltonian and acceleration magnitude are constant. The phase constraint is not active during construction of this family so the phase drift in the bottom right subplot can be ignored. The piecewise construction of the family is also visible in the continuation verification since the deviation in Hamiltonian increases at the end of the first collocation procedure ($\alpha = 110^\circ$) and at the beginning of the fourth collocation procedure ($\alpha = 254^\circ$).



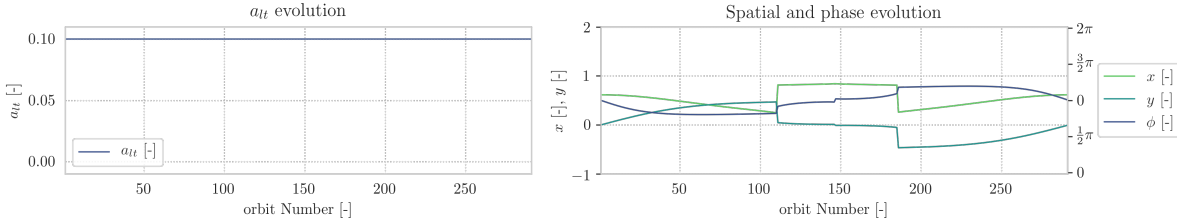


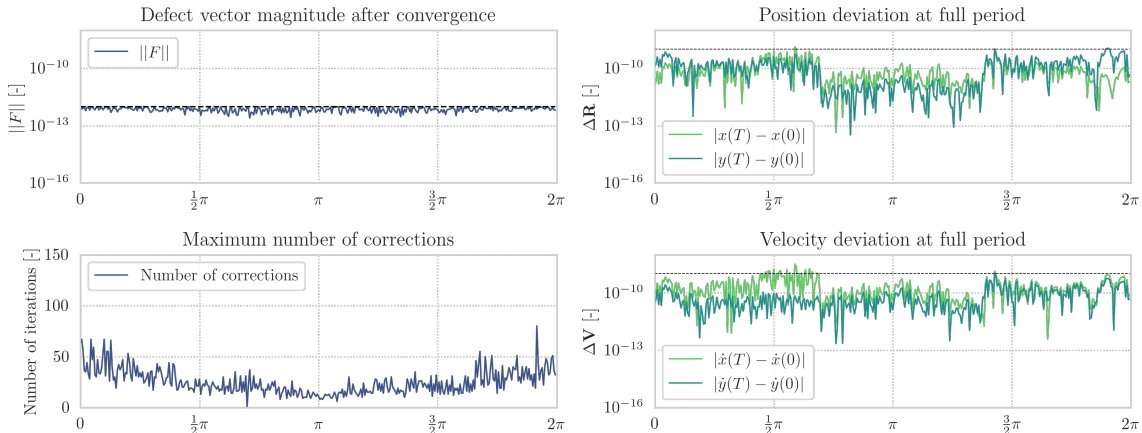
Figure E.69: Numerical continuation verification of the L_1 ($a_{lt} = 0.10, H_{lt} = -1.525$) family. The top subplots and bottom left subplot demonstrate that the l.p.o family unfolds along the acceleration branch. The bottom right subplot shows the spatial evolution and phase drift of the initial condition along the family.

It is unlikely that the asymmetries observed in the L_1 ($a_{lt} = 0.10, H_{lt} = -1.525$) family are correct since symmetry exists in the CR3Bp-LT[1]. Hence, the observed asymmetries are a faulty numerical approximation of the family members. Figures E.67-E.69 do not provide a clear explanation since the members adhere to the periodicity eigensystem deviation tolerances. A possible root cause for the observed symmetries is that the order of the collocation scheme is not high enough to accurately approximate the family members which extend furthest into the negative x -direction. The insufficient order of the collocation procedure causes a lack of robustness which explains why a different seed solution allows computation of the remainder of the family.

L_1 ($a_{lt} = 0.10, H_{lt} = -1.50$) α -varying family

The degree of periodicity of the members that constitute the L_1 ($a_{lt} = 0.10, H_{lt} = -1.50$) family is shown in Figure E.70. The totality of the subplots of this Figure show that the collocation procedure produces a converged solution whose truncation error is not always equidistributed. The initial state of the resulting solution is explicitly propagated for the estimated orbital period. Several members of the family do not meet the periodicity thresholds at full period but termination of the continuation procedure is due to this violation is intentionally suppressed since otherwise construction of α -varying families would not be possible. The family has been constructed via four continuation procedures where the first procedure has produced the partial family for $\alpha \in [0^\circ, 125^\circ]$. The second continuation procedure has computed the partial family for $\alpha \in [126^\circ, 250^\circ]$ whereas the third computes the family for $\alpha \in [251^\circ, 359^\circ]$.

L_1 Horizontal Lyapunov ($H_{lt} = -1.500, a_{lt} = 0.10$) - Periodicity constraints verification



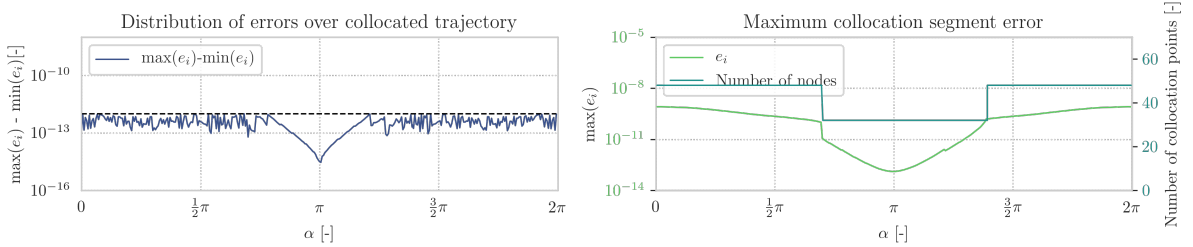


Figure E.70: Periodicity verification of the L_1 ($a_{lt} = 0.10, H_{lt} = -1.50$) family. The three left subplots and the bottom right subplot demonstrate a correct implementation of the collocation procedure. The upper and middle right plot, constructed via explicit propagation of the solution resulting from the collocation procedure, present the state deviation of the family members at full-period.

Characteristics of the monodromy eigensystem of each member of the L_1 ($a_{lt} = 0.10, H_{lt} = -1.50$) family are shown in Figure E.68. It can be concluded that the monodromy eigensystem of each family member adheres to the structure of a symplectic map. The piecewise construction of the family is also visible in the monodromy eigensystem deviations. A shift in the magnitude eigensystem deviations occur at 126° and 251° .

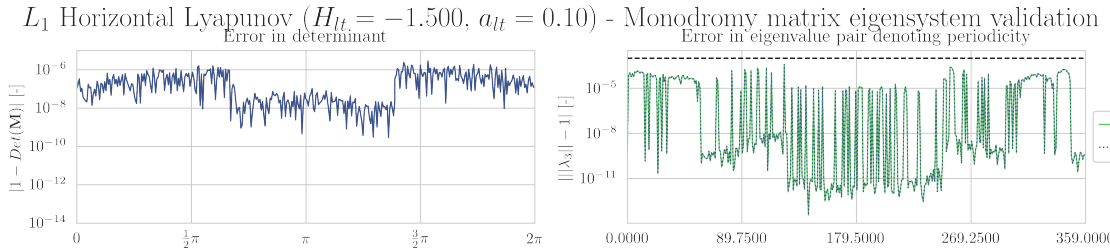
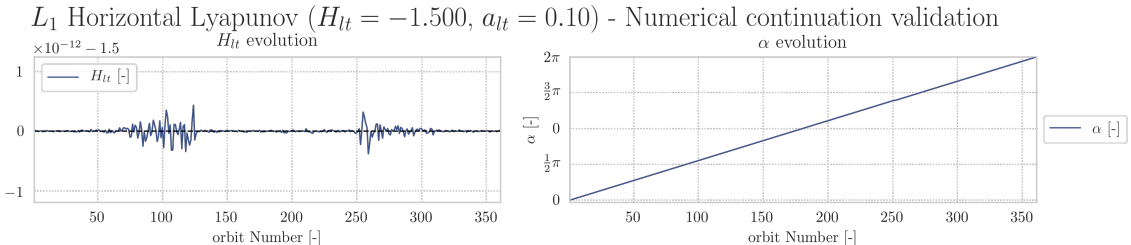


Figure E.71: Monodromy matrix eigensystem validation of the L_1 ($a_{lt} = 0.10, H_{lt} = -1.50$) family. The left subplot shows that the deviation of the monodromy matrix determinant adheres to the constraint as specified in Table A.8. The right subplot demonstrates the eigenvalue representing the in-plane center subspace adheres to the periodicity constraint as specified in Table A.8.

Figure E.72 proves that the L_1 ($a_{lt} = 0.10, H_{lt} = -1.50$) family is an α -varying family since the Hamiltonian and acceleration magnitude are constant. The phase constraint is not active during construction of this family so the phase drift in the bottom right subplot can be ignored. The piecewise construction of the family is also visible in the continuation verification since the deviation in Hamiltonian increases at the end of the first collocation procedure ($\alpha = 126^\circ$) and at the beginning of the third collocation procedure ($\alpha = 251^\circ$).



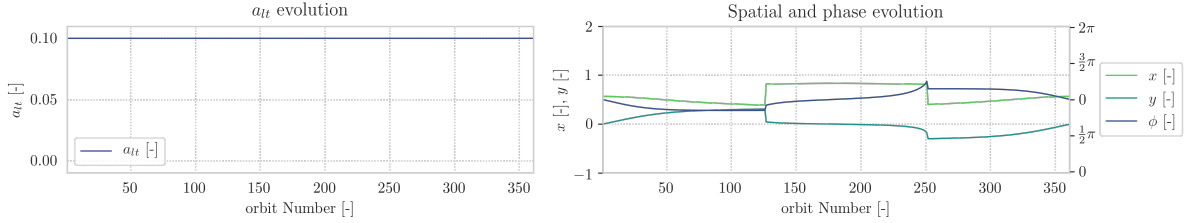


Figure E.72: Numerical continuation verification of the L_1 ($a_{lt} = 0.10, H_{lt} = -1.50$) family. The top subplots and bottom left subplot demonstrate that the l.p.o family unfolds along the acceleration branch. The bottom right subplot shows the spatial evolution and phase drift of the initial condition along the family.

It is unlikely that the asymmetries observed in the L_1 ($a_{lt} = 0.10, H_{lt} = -1.50$) family are correct since symmetry exists in the CR3Bp-LT[1]. Hence, the observed asymmetries are a faulty numerical approximation of the family members. Figures E.70-E.72 do not provide a clear explanation since the members adhere to the periodicity eigensystem deviation tolerances. A possible root cause for the observed symmetries is that the order of the collocation scheme is not high enough to accurately approximate the family members which extend furthest into the negative x -direction. The insufficient order of the collocation procedure causes a lack of robustness which explains why a different seed solution allows computation of the remainder of the family.

This page is intentionally left blank.

F

Recommendations

A multitude of ideas for improved construction of low-thrust equilibria and libration point orbits arose during this thesis project. Next to that, the insights generated during this thesis project open up numerous opportunities for research efforts. The majority of these ideas and research directions could not be implemented in this thesis work due to time constraints. This addendum provides the reader with an overview of these ideas. Section F.1 provides recommendations that concern the improvement of the numerical model as presented in Appendices A-C. Recommendations for new research directions can be found in Section F.2.

F.1. Technical recommendations

Stochastic equilibria root-finding	The equilibria root-finding procedure provides robust performance while the equilibria contours remain separated but fails when the contours merge. Stochastic root-finding procedures might provide more a reliable alternative with lower computational cost compared to classic multivariate root-finding procedures [29]. Alternatively, heuristic algorithms may provide additional seed solutions which could enable the equilibria root-finding procedure to fully compute merged equilibria contours.
Perturbation based Floquet correction	The floquet targeter scheme, as explained in Section C.3, provides a velocity correction after passing of a time interval as specified in Table A.6. Alternatively, a correction manoeuvre can be executed each time the perturbation along the unwanted motion components exceeds a certain threshold.
Extend Floquet-controller to other family types	The current implementation of the floquet targeter scheme generates approximate solutions for H-L type of libration point orbits. According to [4], Floquet targeter schemes can also be used to generate vertical Lyapunov orbits (V-L). If the floquet targeter scheme is augmented with this capability, l.p.o families of the V-L type can be investigated. It remains to be seen if approximate Halo orbits can be generated with the Floquet controller since this type of orbits is not a principle form of motion around the equilibria of the CR3BP-LT.
Variable number of nodes for the TLT correction procedure	The TLT correction procedure does not guarantee that its solution resembles the characteristics of the input trajectory. The robustness of the algorithm could be improved by automatically checking whether the converged solution complies with the desired characteristics, like amplitude or distance with respect to one of the primaries. If these constraints are not satisfied. The algorithm should automatically increase the number of nodes and correct the solution until it complies with the user-specified tolerances.

Legendre Gauss node placement strategy	The choice of a Gauss-Legendre-Lobatto node placement strategy gives rise to an l.p.o family continuation procedure that takes from a few hours to a more than 10 days. The high computational cost is attributed to the number of nodes required to achieve the orbits with the desired accuracy. A higher-order method like the Legendre-Gauss node placement strategy will require less nodes to achieve the desired accuracy thereby lowering computational cost associated to the numerical continuation procedure. It is also expected that a higher order node placement strategy will result in a more robust mesh refinement process since fewer nodes have to be used in order to obtain the desired accuracy.
Collocation using fixed node times	A common approach in collocation is to fix the node times and update them via mesh refinement techniques once the collocation problem has been solved [8]. This thesis uses a variable node time collocation procedure to allow the estimation of the orbital period. A disadvantage of this approach is that algorithm shifts the sequence of the nodes, thereby creating an unsolvable problem which was the root cause for the majority of the continuation procedures. Fixed node times will circumvent this error but this does not allow computation of the unknown orbital period of the solution. A possible solution might be fixing the time of all nodes apart from the final node. It remains to be seen how such a collocation scheme will produce a solution with an equidistributed error.
Extend TUDAT with implicit integration	One of the bottlenecks that prevents near-instant computation of l.p.o families is the use of the RK7(8) integrator in the verification procedure. Replacing the RK(7)8 integrator with an implicit integrator will significantly reduce the computational load of l.p.o family construction. In combination with a higher order node placement strategy, near-instant construction of l.p.o families might be achieved [28].

F.2. Scientific recommendations

Investigate l.p.o families at large acceleration values	In, [1], equilibria contours are presented for currently unfeasible low-thrust acceleration magnitudes. These contours fully encircle the Moon and the periodic solutions emanating from them might open up new opportunities for a wide variety of space missions.
Analytical l.p.o approximation	Approximate solutions for libration point orbits are usually obtained via analytical expressions. Such expressions exist for natural libration point orbits [30], solar-sail assisted libration point orbits [13] and even low-thrust libration point orbits [26, 31]. All methods have the restriction that they can only generate periodic solutions that emanate from equilibria located on the x -axis of the dynamical model. Literature suggests that an analytical expression for off-axis low-thrust libration point orbits exists [1]. To the best of the author's knowledge, such an expression has not been published yet.

Investigate spatial periodic solutions in the CR3BP-LT

Results in Chapter 1 imply that Halo, Axial and vertical-Lyapunov family exist. At the moment of writing this thesis, these spatial families have not been investigated yet and provide an exciting topic for future research efforts. The implementation TLT-algorithm and continuation procedure developed during this thesis are already equipped to compute spatial libration point orbits. This cannot be said for the current implementation of the equilibria root-finding procedure and the Floquet targeter.

Investigate hyperbolic invariant manifolds emanating from low-thrust periodic solutions

The results of this thesis project show that some low-thrust periodic solution have a higher rate of hyperbolic unwinding behaviour compared to the ballistic periodic solutions. Investigating the hyperbolic flow emanating from low-thrust periodic solutions might lead to identification of more time-optimal transfer opportunities in the Earth-Moon system.

This page is intentionally left blank.

Bibliography

The list below is an exhaustive list of references for the sources used the appendices A-F. A reference list for the citations in Chapter 1 can be found at the end of Chapter itself

- [1] D. Folta A. Cox, K. Howell. Dynamical structures in a low-thrust, multi-body model with applications to trajectory design. *Celestial Mechanics and Dynamical Astronomy*, 131(12), 2019. - ISBN: 0923-2958.
- [2] F. Saleri A. Quarteroni, R. Sacco. *Numerical Mathematics*. Springer-Verlag, Berlin, 2001. - ISBN 978-0-387-95116-4.
- [3] K. Atkinson. *An Introduction To Numerical Analysis*. John Wiley & Sons, Canada, 1978. - ISBN: 0-471-62489-6.
- [4] R. Wilson B. Marchand, K. Howell. An improved corrections process for constrained trajectory design in the n-body problem. *Journal of Spacecraft and Rockets*, 44(4), 2007. - eISSN: 1533-6794.
- [5] J. Betts. Survey of numerical methods for trajectory optimization. *Journal of Guidance, Control and Dynamics*, 21(2), 1998.
- [6] A. Björk. *Numerical methods for least squares problems*. Society for Industrial and Applied Mathematics, Philadelphia, 1998. -ISBN 0-89871-360-9.
- [7] K. Howell C. York. A two-level differential corrections algorithm for low-thrust spacecraft trajectory targeting. In *Spaceflight Mechanics Meeting*, volume 168 of *Advances in Astronautical Sciences*, 2019. - ISBN: 978-0-87703-660-9.
- [8] T. Pavlak D. Grebow. Mcoll: Monte collocation trajectory design tool. In *Astrodynamic Specialist Conference 2017*, volume 162 of *Advances in the Astronautical Sciences Series*, pages 677–696, 2017. - ISBN: 978-0-87703-646-3.
- [9] C. de Boor. Good approximation by splines with variable knots. In Springer-Verlag, editor, *Spline Functions and Approximation Theory*, pages 57–72, Basel, 1973. - ISBN: 978-3-0348-5979-0.
- [10] H. Keller D. Dichmann-J. Galan-Vioque A. Vanderbrauwhe E. Doedel, R. Paffenroth. Continuation of periodic solutions in conservative systems with application to the 3-body problem. *International Journal of Bifurcation and Chaos*, 13(6):1353–1381, jan 2003.
- [11] G. Wanner E. Hairer, S. Nørset. *Solving Ordinary Differential Equations I*. Springer-Verlag, Berlin, 1993. - ISBN: 3-540-56670-8.
- [12] K. Kumar et al. Tudat: a modular and robust astrodynamics toolbox. In *Fifth ICATT, International Conference on Astrodynamics Tools and Techniques*, pages 1–8, 2012.
- [13] C. McInnes H. Baoyin. Solar sail halo orbits at the sun-earth artificial l1 point. *Celestial Mechanics and Dynamical Astronomy*, 94(2), 2006. - ISSN: 0923-2958.
- [14] J. Herman. *Improved Collocation Methods to Optimize Low-thrust, Low-Energy Transfers in the Earth-Moon System*. PhD thesis, University of Colorado, Boulder, 2015.
- [15] K. Howell. Three-dimensional, periodic, ‘halo’ orbits. *Celestial Mechanics & Dynamical Astronomy*, 32 (1):51–73, 1984. - ISSN: 0923-2958.
- [16] M. Macdonald J. Heiligers, J. Parker. Extension of earth-moon libration point orbits with solar sail propulsion. *Astrophysics and Space Science*, 361(241), jun 2016.
- [17] C. Moler J. Lyness. Numerical differentiation of analytic functions. *SIAM Journal on Numerical Analysis*, 4(2):202–210, 1967. - ISSN: 0036-1429.

- [18] J. Alonso J. Martins, P. Sturda. The complex-step derivative approximation. *ACM Transactions on Mathematical Software*, 29(3), sep 2003. - ISSN: 0098-3500.
- [19] W. Rheinboldt J. Ortega. *Iterative Solution of Nonlinear Equations in Several Variables*. Academic Press, 1970. - ISBN: 1483244334.
- [20] B. Marchand K. Howell. Natural and non-natural spacecraft formations near the l1 and l2 libration points in the sun-earth/moon ephemeris system. *Dynamical Systems: An International Journal*, 201(1):149–173, mar 2005.
- [21] H. Pernicka K. Howell. Numerical determination of lissajous trajectories in the restricted three-body problem. *Celestial Mechanics and Dynamical Astronomy*, 41(1):107–124, 1978. - ISSN: 0923-2958.
- [22] H. Keller. *Numerical Methods for Two-Point Boundary-Value Problems*. Dover, New York, 1992. - ISBN 13: 9780486669250.
- [23] C. Kelley. *Solving Nonlinear Equations with Newton's method*. Society for Industrial and Applied Mathematics, Philadelphia, 2003. - ISBN: 0-89871-546-6.
- [24] K. Langemeijer. Connecting hyperbolic invariant manifolds at variations of the poincaré section orientation. Master's thesis, TU Delft, 2018.
- [25] L. Massarweh. Linear stability and bifurcations of periodic lagrange orbits in the elliptic restricted 3-body problem. Master's thesis, Delft University of Technology, 2016.
- [26] M. Morimoto. Periodic orbits with low-thrust propulsion in the restricted three-body problem. *Journal of Guidance, Control and Dynamics*, 29(5), 2006. - eISSN: 1533-3884.
- [27] E. Gill O. Montenbruck. *Satellite Orbits: Models, Methods and Applications*. Springer-Verlag, Berlin, 2000. - ISBN: 978-3540672807.
- [28] A. Humphries A. Lemus-Rodríguez E. Oldeman R. Calleja, E. Doedel. Boundary-value problem formulations for computing invariant manifolds and connecting orbits in the circular restricted three body problem. *Celestial Mechanics and Dynamical Astronomy*, 114(12):77–106, 2012. - ISSN: 0923-2958.
- [29] S. Kim R. Pasupathy. The stochastic root-finding problem: Overview, solutions, and open questions. *ACM Transactions on Modeling and Computer Simulation*, 21, 2011. - ISSN: 1049-3301.
- [30] D. Richardson. Analytic construction of periodic orbits about the collinear points. *Celestial Mechanics and Dynamical Astronomy*, 22:241–253, 1980. - ISSN: 0008-8714/80/0223-0241.
- [31] C. McInnes S. Baig. Artificial halo orbits for low-thrust propulsion spacecraft. *Celestial Mechanics and Dynamical Astronomy*, 104:321–355, 2000. ISSN: 0923-2958.
- [32] L. Petzold U. Ascher. *Computer Methods For Ordinary Differential Equations and Differential-Algebraic Equations*. Society for Industrial and Applied Mathematics, Philadelphia, 1998. - ISBN: 0-89871-412-5.
- [33] S. Ross W. Koon. M. Lo, J. Marsden. *Dynamical Systems, the Three-Body Problem and Space Mission Design*. Springer-Verlag, New York, 2007. - ISBN: 978-0387495156.
- [34] K. Wakker. *Fundamentals of Astrodynamics*. TU Delft Library, 2015. - ISBN: 978-94-6186-419-2.
- [35] P. Zhou. *Numerical Analysis of Electromagnetic Fields*. Springer-Verlag, Berlin, 1993. - ISBN: 978-3-642-50321-4.